Site C0020[1]

Expedition 337 Scientists[2]

Chapter contents

Introduction

Marine subsurface hydrocarbon reservoirs and the associated microbial life in continental margin sediments are among the least characterized systems on Earth that can be accessed by scientific ocean drilling. Our scientific knowledge of the biological and abiotic processes associated with hydrocarbon production is limited because of the highly limited opportunities to conduct scientific ocean drilling initiatives using deep-riser drilling in natural gas and oil fields. A number of fundamentally important questions regarding deep subseafloor hydrocarbon systems have remained unanswered. For example,

- What role does subsurface microbial activity play in the formation of hydrocarbon reservoirs?
- Do the deeply buried hydrocarbon reservoirs such as natural gas and coalbeds act as geobiological reactors that sustain subsurface life by releasing nutrients and carbon substrates?
- Do the conversion and transport of hydrocarbons and other reduced compounds influence biomass, diversity, activity, and functionality of deep subseafloor microbial communities?
- What are the fluxes of both thermogenically and biologically produced organic compounds, and how important are these for the carbon budgets in the shallower subsurface and the ocean?

To address these important scientific questions, Integrated Ocean Drilling Program (IODP) Expedition 337 aimed to drill and study a hydrocarbon system associated with deeply buried coalbeds off the Shimokita Peninsula, Japan, in the northwestern Pacific using the riser drilling system of the D/V *Chikyu*. For more information regarding research backgrounds, scientific objectives, and hypotheses, see the **"Expedition 337 summary"** chapter (Expedition 337 Scientists, 2013a).

Operations

The *Chikyu* left Hachinohe Port at 1200 h on 26 July 2012 and arrived at IODP Site C0020 after 7.5 h of transit. The corrosion cap of Hole C9001D, which was drilled to 647 m drilling depth below seafloor (DSF) and cased to 511 m DSF during the *Chikyu* shakedown cruise in 2006, was retrieved at the surface by 2400 h on 27 July. Ten transponders were installed on the seafloor by the remotely operated vehicle (ROV) on 28 July, and failure mode effect

[1] Expedition 337 Scientists, 2013. Site C0020. *In* Inagaki, F., Hinrichs, K.-U., Kubo, Y., and the Expedition 337 Scientists, *Proc. IODP,* 337: Tokyo (Integrated Ocean Drilling Program Management International, Inc.). doi:10.2204/iodp.proc.337.103.2013
[2] **Expedition 337 Scientists' addresses.**

doi:10.2204/iodp.proc.337.103.2013

analysis for the Acoustic Position Reference System was completed on 29 July.

While conducting a surface pressure test of the blowout preventer (BOP), the science party was shuttled aboard by helicopter flights on 31 July. Technical problems ensued during the BOP function test, and troubleshooting continued until the function test was completed at 1330 h on 6 August.

After a successful pressure test, the BOP was transferred to the well center at 0130 h on 7 August and was lowered to the moonpool. However, the BOP control system did not function correctly, so the BOP was picked up on the cart. Incorrect connection of the control line conduit manifold was rectified on 8 August. Running of the BOP and riser started at 1300 h on 8 August.

BOP landing was attempted at ~2130 h on 11 August, but the ROV image was lost just before the moment of landing. A successful landing was confirmed before 2200 h when the ROV image was recovered.

Extensive BOP tests were carried out after the landing until completion of the pressure test on 14 August. Cement was drilled out with a 17½ inch bottom-hole assembly (BHA), and seawater was evacuated starting at 1515 h on 14 August and reached 1854.5 m drilling depth below rig floor (DRF), 1 m above the bottom of the cement. Calcium carbide was added to the drilling mud in order to check the annulus volume. Old mud in the hole and riser was displaced with 1.06 sg KCl-NaCl/polymer/PPG (KNPP) mud. A formation integrity test at the 20 inch casing shoe (1719.5 m DRF) was carried out.

Drilling into fresh formation started on 15 August. Drilling a 17½ inch hole from 1854 to 2171 m DRF (645.5–962.5 m DSF, 317 m) was achieved at an average rate of penetration (ROP) of 1.23 m/min. A maximum mud-gas concentration of 18.94% was observed at 1991 m DRF. After circulation and bottoms up, drilling resumed from 2171 to 2208.5 m DRF (962.5–1000 m DSF, 37.5 m) at 0115 h on 16 August. The average ROP was 1.38 min/m. A high mud-gas concentration (>10%) was occasionally observed. Drilling from 2208.5 to 2375 m DRF (1000–1166.5 m DSF, 166.5 m) proceeded at an average ROP of 1.45 min/m.

At 2200 h on 16 August, we encountered total mud loss at 2375 m DRF. The mud loss rate decreased with time to 8.5 m^3/h at 2400 h. Lost circulation material (LCM) was spotted (12 m^3) at 0230 h on 17 August. The mud loss rate decreased to 0.8 m^3/h after the second spotting of LCM at 1200 h but continued through the day. A decision was made to continue drilling with seawater gel mud.

Drilling resumed at 0515 h on 18 August from 2375 to 2400 m DRF (1166.5–1191.5 m DSF, 25 m). The average ROP was 1.78 min/m. Mud return was confirmed and the pump rate was adjusted. Drilling continued to 2453.5 m DRF (1245 m DSF), and then to 2471.5 m DRF (1263 m DSF) with a sweep of hi-vis mud and circulation bottoms up.

The drilling BHA was pulled to the surface at 1500 h on 19 August. The nominal seat protector was retrieved at 2100 h, and preparation of 13⅜ inch casing began. Running 13⅜ inch casing started at 0400 h on 20 August, and running of the casing hanger with running strings started at 1630 h. However, the casing hanger was pulled back to the surface because it was improperly made up. The casing hanger landed on the wellhead at 0015 h on 21 August. Cementing of the casing began at 0515 h. The pressure test of the BOP was completed on a second attempt, after the seal-retrieving tool was set.

A 12¼ inch drill-out cement BHA was made up at 2030 h on 22 August and run into the hole to 2384 m DRF. Casing pressure tests were carried out twice, and cement was drilled out to reach 2.5 m into new formation at 1830 h on 23 August. A leak-off test was completed after drilling fluid was displaced from seawater gel to KNPP mud. Preparation for a 10⅝ inch rotary core barrel (RCB) BHA was started at 1600 h on 24 August and running into the hole to 2444 m DRF was finished at 0700 h on 25 August. After circulation and bottoms up, the center bit was dropped and a 10⅝ inch hole was drilled 11 m into the formation to reach 2485 m DRF (1278.5 m DSF).

Coring operations started at 1600 h. Core 337-C0020A-1R was recovered on deck at 1822 h, with 2.23 m of recovery from 9.5 m of drilling advance. The following core (2R) was recovered at 2123 h, with improved recovery of 4.08 m. Core 3R was cut after drilling to 2578.5 m DRF (1370 m DSF). A short advance of 5.0 m was attempted to improve core recovery and quality. A good 3.68 m core was recovered at 0929 h on 26 August. Core 4R recovered 3.75 m from 9.5 m of advance. After reviewing the core recovery and quality, short advances were employed thereafter. Core 5R was cut after drilling to 2698.5 m DRF (1490 m DSF). The 2.7 m long core was on deck at 0504 h on 27 August. The following core (6R) was a successful recovery of 4.12 m from 5.0 m advance. After Core 6R, drilling was intended to reach 2841.5 m DRF (1633.0 m DSF), but before reaching the target depth, a low-ROP interval was encountered, and the decision was made to core to determine the material of the hard formation. Core 7R was cut from 2807.5 to 2812.5 m DRF (1599.0–1604.0 m DSF) and 1.15 m was recovered at 1915 h.

The core included gravel of volcanic origin and showed a different lithology from previous cores. The Co-Chief Scientists decided to take a large-diameter coring (LDC) system core at this depth, targeting the presumed Oligocene/Eocene boundary that was observed in the low-ROP interval in a nearby well.

The RCB BHA was pulled to the surface at 0830 h on 28 August. Running the Baker Hughes INTEQ 8½ inch industrial coring BHA started at 1500 h. LDC cutting started at 1045 h on 29 August. Coring operations were stopped at 2834 m DRF at 1530 h (before reaching 27 m of drilling advance in the original plan) because core jamming was suspected when an increase in pump pressure and no penetration were observed. The LDC core was recovered on deck at 0730 h on 30 August. Core 8L recovered 10.0 m from 21.5 m of advance. The core was cut into 1.0 m long sections at the middle pipe rack and transferred to the laboratory.

As LDC did not reach the target depth, it was decided to take the next core at 2834 m DRF. Running a 10⅝ inch RCB BHA started at 1115 h. The LDC interval was opened from 8½ inches to 10⅝ inches, and RCB coring resumed at 0545 h on 31 August. Slow penetration continued, and drilling advance was stopped at 4 m for Core 9R, which was 3.95 m long and was recovered on deck at 0813 h. Core 10R was on deck at 1140 h, and 5.41 m was recovered from 9.5 m of advance. Based on a preliminary inspection of the sample, no particular change in lithology and age was inferred. The Co-Chief Scientists decided to stop coring and drill instead to 1760 m DSF.

Before reaching the next coring interval, an increase in ROP was observed, suggesting a change in lithology. Three consecutive RCB cores were cut from 1737.5 m DSF with full 9.5 m of advance. Cores 11R–13R were recovered on deck on 1 September and showed good recovery. Core 14R was cut after drilling to 1820 m DSF and was recovered at 1843 h. Again, there was not a notable change in lithology. The Co-Chief Scientists decided to drill to 1919 m DSF, at which depth the coal-bearing interval was considered to start in the revised interpretation of seismic profiles based on the observed drilling parameters and cuttings.

Four consecutive RCB cores were cut from 1919 m DSF. Core 15R was on deck at 1230 h on 2 September and contained a thick coal layer. The following Cores 16R (with advance of 7.5 m) and 17R (with full advance) were mainly loose sand. During cutting of Core 18R, the drill bit was suspected to be worn out, and the core was recovered on deck at 2153 h after a drilling advance of 4.5 m. It was decided to pull out of the hole, and the drill bit was retrieved on the surface at 1330 h on 3 September. Three nozzles were plugged in the drill bit.

After Core 18R, it was also decided that RCB coring would continue and LDC would be canceled. The reasons for the change in plans were that (1) RCB coring had shown unexpectedly high core recovery in coal-bearing lithology, at least as high as LDC, (2) core quality of coal recovered by the RCB was good enough to fulfill our scientific objectives, (3) uncertainties in LDC operations risked jeopardizing the expedition goals in the limited time remaining for the site operations, and (4) quicker RCB operations allowed for a longer total coring interval and more flexibility in the future analyses of the cores.

A new drill bit was installed and run into the hole starting at 1430 h. Coring operations resumed at 1000 h on 4 September and continued smoothly to take seven consecutive RCB cores from 3158.5 to 3212.0 m DRF (1950–2003.5 m DSF). Core recovery was high, and coal-bearing sequences were obtained. As various lithologies within and around the coal-rich formation were available for sampling, the Co-Chief Scientists concluded that we had fulfilled our operational mission in this interval. They decided to drill deeper to investigate the broader range of the hydrocarbon system and to explore the limits of life.

Drilling with a center bit from 2003.5 m DSF started at 0715 h on 5 September. Core 26R was cut from 3318.5 to 3328 m DRF (2110–2119.5 m DSF; 9.5 m). At 2111 m DSF, Hole C0020A became the deepest hole in scientific ocean drilling. On 6 September, we celebrated drilling a record-breaking core with >100% recovery of 9.58 m. Spot coring continued at 100 m intervals, and Cores 27R, 28R, and 29R were taken from 2200, 2300, and 2400 m DSF, respectively.

The final total depth (TD) was anticipated at 2460 m DSF, and the Co-Chief Scientists requested to take the last pair of cores with 9.5 m and 4.0 m advances. While cutting the last core (31R), jamming was suspected at 0.5 m of advance. The Operations Superintendent (OSI) decided to retrieve the core at that point. While waiting for recovery of the short core, scientists observed unique features in the X-ray computed tomography (CT) image of Core 30R. The Co-Chief Scientists and OSI decided to take another full core from 2456.5 m DSF. At 0354 h on 9 September, the last core (32R) was on deck. TD of Hole C0020A was 2466 m DSF.

After pulling out of the hole, wireline logging operations started. Logging Run 1 (Platform Express–High-Resolution Laterolog Array–Hostile Environment Natural Gamma Ray Sonde) started at 0200 h on 10 September. Data quality was very good, and the cali-

per showed that the hole condition was good through the entire interval. Logging Runs 2 (Formation MicroImager–Dipole Sonic Imager–Environmental Measurement Sonde [EMS]–gamma ray [GR]) and 3 (combinable magnetic resonance-GR) followed. High-permeability layers were selected for use of the Modular Formation Dynamics Tester (MDT) based on the results from the first three runs. After a wiper trip, logging Run 4 (MDT-GR) started at 2230 h on 12 September. Pretests for fluid mobility and formation pressure measurements were carried out at 31 horizons. Formation fluid samples were taken at six horizons of high mobility, and the six bottles were recovered on deck at 0510 h on 14 September. The sample bottles were delivered to the laboratory during logging Run 5 (vertical seismic profile [VSP]-GR). The last run was finished at 1815 h, ending scientific operations on the rig floor.

This expedition was originally scheduled for March–May 2011 but was postponed because of the Tohoku-oki earthquake and the following tsunami hazard that hit the eastern coast of Japan, including Hachinohe Port. The *Chikyu* suffered damage on the ship body and lost one of the thrusters during emergency evacuation from the port. Repair and reinstallation of the thruster were completed in June 2012, and this expedition was rescheduled for implementation in July 2012.

Lithostratigraphy

In general, drilling in Hole C0020A was divided into two phases of drilling operations. The first phase covered the depth interval from 636.5 to 1256.5 m mud depth below seafloor (MSF), from which only cuttings samples were retrieved, and the second drilling phase covered the depth interval from 1256.5 to 2466 m MSF, in which both core and cuttings samples were collected.

Cuttings observations

Cuttings samples from 636.5 to 926.5 m MSF were composed mainly of dark olive to olive-gray silty claystone with abundant diatoms, common volcanic glasses, common quartz, few feldspars, and few lithic fragments (Fig. **F1**). The first cuttings sample was highly contaminated by cement. Few palagonite and opaque minerals (e.g., pyrite or other iron sulfide) were identified in smear slides along with common sponge spicules and few shell fragments. Rare semiconsolidated fine sandstone fragments were visible in >4 mm cuttings samples. Semiconsolidated silt grains in smear slides were poorly sorted with moderate to subangular roundness.

Cuttings recovered from 926.5 to 1116.5 m MSF were dominated by diatom-bearing clayey siltstone with abundant lithic fragments, quartz, and feldspar. In some samples, volcanic glass and sponge spicules were common, whereas pyrite or other iron sulfides and shell fragments were present in only minor amounts. Semiconsolidated siltstone and fine sandstone in smear slides were subangular to rounded with moderate to poor sorting. Fragments of sandstone were identified in all cuttings samples. In addition, plant remains were rarely visible in cuttings. The sandstone content in the cuttings ranged between 5% and 15%. Colors observed in cuttings from this depth interval corresponded frequently to lithology. For example, well-cemented siltstone fragments were light in color (5Y 5/2) and clayey siltstone and clayey siltstone with fine sandstone (5Y 4/2) were dark olive.

Cuttings samples from 1116.5 to 1236.5 m MSF consisted mainly of medium silt to sand with very common wood fragments found most frequently between 1206.5 and 1226.5 m MSF (as much as 15% of the total material). Sand and silt grains in smear slides were rounded to moderate and were poor to moderately sorted. Siliceous microfossil remains were also common, often as broken fragments. Volcanic glass and iron sulfides were also present.

Only one cuttings sample (337-C0020A-92-SMW) was recovered from 1116.5 to 1186.5 m MSF. The material from this interval consisted of loose, fine to coarse sand grains and was highly contaminated with drilling mud. A rare amount of silty fragments were observed. Loose, fine to medium sand was present in samples from 1186.5 to 1236.5 m MSF. Moreover, lithic fragments, pumice, sulfides, and clayey siltstones were also observed. The amount of clayey silt increased slightly and became more consolidated with depth to a more semiconsolidated consistency (cuttings Samples 92-SMW through 95-SMW).

Cuttings samples from 1236.5 to 1256.5 m MSF consisted mainly of semiconsolidated clayey siltstone with fine sand. In clay-rich layers, diatom fossils were well preserved; however, in coarser fractions, fractured diatoms and shells along with volcanic glass were more frequently observed (Fig. **F2A**). Wood fragments were also observed, although less commonly than from 1186.5 to 1236.5 m MSF. Silt grains in smear slides were rounded to subrounded in poorly sorted material.

In cuttings samples between 1256.5 and 1506.5 m MSF, the clay fraction generally increased from 10%–30% to 50%, whereas the sand fraction varied between 0% and 30% over the same interval (Fig. **F1**). Higher sand fractions in the cuttings corresponded

to the increased prevalence of sandstones at the same core depths. Between 1506.5 and 1696.5 m MSF, the clay fraction increased to 60%–75%, whereas the sand fraction varied between 5% and 35%. This interval demonstrated a transition from a silt-dominated grain size distribution to one that was bimodally dominated by clay and silt. Between 1696.5 and 1826.5 m MSF, clay generally decreased to 30%, silt increased to 50%, and sand varied between 5% and 30%. Wood fragments were observed in most samples between 1186.5 and 1826.5 m MSF in abundances classified as rare or few (Fig. F1). In some sand-rich intervals, common wood and lignite fragments were observed. In general, smear slides were dominated by clay minerals, quartz, lithic fragments, and volcanic glass. Feldspar, mica, ferromagnesian silicates, and organic matter were also frequently observed in this interval. Smear slide observations indicated that the amount of biosiliceous material decreased with depth over this interval, with diatoms and sponge spicules present only in rare to few amounts below 1366.5 m MSF, with no diatoms observed below 1786.5 m MSF (see **"Cuttings contamination"**). In contrast, glauconite increased with depth from rare to absent above 1536.5 m MSF to common to dominant between 1886.5 and 1916.5 m MSF (Fig. F1).

Cuttings samples between 1826.5 and 2046.5 m MSF were dominated by fragments of coal. Silt content was relatively high and ranged between 40% and 70%, except for one sample with only 10% silt. Sand content is <25%. Glauconite was visible in almost all cuttings samples in this interval.

Olive-black silty shale is the most common lithology in cuttings samples between 2046.5 and 2396.5 m MSF. Fine sandstone laminations, few volcanic ash components, pumice, rare to common coal fragments, and some shell fragments are also present within the samples. Clay content is low at 2046.5 m MSF (~25%) and increases downhole (70%–80%). Clay content is nearly constant to 2246.5 m MSF and decreases downhole to 45% at 2396.5 m MSF. Glauconite is visible in varying amounts in smear slides. Quartz, lithic fragments, clay minerals, and volcanic glass are also observed in smear slides.

In cuttings samples between 2396.5 and 2466.5 m MSF, silty mudstone with fine sandstone containing authigenic carbonates was common to abundant. These authigenic carbonate fragments reacted slowly with hydrochloric acid and produced a yellow fluid during reaction, suggesting possible siderite. Smear slides from these samples also contained fine-grained siderite. Abundant lithic fragments, common quartz, few volcanic glass, rare glauconite, and few organic matter were observed in smear slides. Between 2426.5 and 2466 m MSF, clay and silt are the dominant size fraction in cuttings samples with dominant coal fragments.

Core observations

Cores 337-C0020A-1R, 2R, 5R, and 6R largely comprised fine to medium sandstone (Fig. F3A) and less common siltstone, whereas Cores 3R and 4R consist mainly of siltstone (Fig. F3). Plant debris and shell fragments were commonly observed. Planar laminations were common throughout these cores. A coarsening-upward interval and smaller fining-upward intervals were observed in Cores 5R and 6R. Consolidated siltstones showed higher X-ray CT values than semiconsolidated sandstones, corresponding to higher densities of consolidated siltstones. Pebbles display higher CT values than the surrounding sandstone. Clay, quartz, and lithic fragments are common to abundant in nearly every smear slide. Minor amounts of feldspar, volcanic glass, pyrite, mica, and glauconite were visible in some samples. Glauconite observed in these cores indicates reworking of original shelf sediment. Dolomitic cements and a few dolomitic concretions are sometimes also observed. Diatom-bearing mudstones are present in a very rare amount, possibly as contaminations from drilling mud (Fig. F2B).

Cores 337-C0020A-7R and 8L contained shale, conglomerate, siltstone, and sandstone (Fig. F3C). The conglomerate intervals contained rounded volcanic rocks, which were identified as gabbro and altered tuffite by examination of thin sections. Shells and plant fragments were commonly observed in these cores, along with planar and wavy laminations. Slight to heavy bioturbation was commonly observed in Core 8L. Section 8L-2 contained two carbonate nodules. Smear slides taken from these nodules contained dominantly dolomite. Both bioturbation and carbonate nodules are visible in the X-ray CT scan image. Quartz, clay, and volcanic glass are exhibited in nearly every sample of these cores. Lithic fragments, mica, and a few iron sulfides are observable in the smear slides.

Cores 337-C0020A-9R through 14R contained sandstone, siltstone, and shale. Planar, wavy, and cross-laminations were common throughout these cores, more frequently than in Cores 1R through 8L. Bioturbation was also more common in Cores 9R through 14R (e.g., Fig. F3E). X-ray CT scan images showed the morphology and orientation of the burrows that were horizontal and vertical. Mud clasts and upward-fining and upward-coarsening intervals were common. Glauconite was observed in sediments as faint green bands in cores and as sharp thin laminations such as in Core 14R. Sediments were

generally rich in quartz. They showed a certain amount of clay minerals, lithic fragments, volcanic glass, and organic matter (Fig. F2). Olivine was present in some smear slides. A thin coal layer appeared in Core 14R, which may indicate the presence of more terrigenous organic material in the sequence. Lithogenic grains were subangular to subrounded and moderate to poorly sorted. In some depth intervals, siltstones were also aragonitic. Shell fragments and wood fragments were the most common fossils. These fragments were observed in intermittent layers throughout the sections. Parallel laminations were the main sedimentary structure observed in Cores 11R through 14R.

Cores 337-C0020A-15R through 25R were dominated by several coal horizons with intervening coaly shales, siltstones, and sandstones. The description of the coal was also based on X-ray CT images because different lithotypes were difficult to differentiate using the split surface of sections. Almost all coal horizons consisted of detritic to xylo-detritic coal with some layers of xylitic coal. Shaly coal was also observed. Water content, color, and vitrinite reflectance measurements of the coal suggested that the coal showed low maturity (R_o = 0.36%; see "Physical properties"). Amber and pyrite were visible in the coal layers. Pyrite occasionally developed as veins but also appeared more frequently as a series of disseminated crystals scattered within coal and coaly shale layers (Fig. F3G). The boundary between the underlying sediments and the coal above was represented most frequently by a gradational transition between organic-rich shale or less frequently by organic-rich sandstone and coal. Contacts between coalbeds and sediment above the coal were usually sharp and dominated by sand. These sandstones were fine to medium grained and often well sorted. Sediments between the coal horizons in Cores 15R through 19R consisted primarily of fine sandstone. Cores 20R and 21R were dominated by shale and siltstone, followed by a succession of fine sandstone, siltstone, and shale with coal horizons. In general, clay minerals, quartz, and lithic fragments were common in microscopic observations. Glauconite was rare in the entire interval (1959.5–1967.79 m core depth below seafloor, Method B [CSF-B]). Grains in smear slides were mostly moderate to subrounded and were moderately sorted, with a few well-sorted samples. Authigenic carbonate occurred as cement within Cores 15R through 25R (Figs. F2, F3). Bands of carbonate cementation and carbonate nodules that included siderite were visible. Glauconite was present in Cores 15R through 20R but was not observed in Cores 21R through 23R. The sandstones in Cores 21R through 24R have common olivine content.

Major sedimentary structures were observed visually as well as in the X-ray CT scans. Common structures in Cores 337-C0020A-15R through 25R were fining- and coarsening-upward sequences often associated with parallel and/or wavy laminations. Flaser and lenticular bedding and cross-lamination were only common in shale or silty intervals such as Core 21R.

Shells or marine fossiliferous material were observed only in Core 337-C0020A-21R. However, plant remains, present as wood fragments and organic-rich layers, were abundant in Cores 15R through 25R (Fig. F2E, F2F). Burrows, indications of bioturbation, were present in this interval. The shape and orientation of burrows were visible in the X-ray CT scans. In Cores 15R through 17R and 21R, horizontal burrows were present in sandstones. Horizontal burrows were also observed in shales and siltstones.

Cores 337-C0020A-27R and 28R were dominated by silty shale intercalated with thin siltstone layers in the cores. In Core 27R, shale was present as massive, homogeneous, and consolidated material. Grains were subangular to rounded and moderate to well sorted. Core 28R also contained fine to medium dolomitic sandstone intercalated with siltstone layers. Grains were moderate to poorly sorted. Abundant carbonate banding and nodules and glauconitic cement were observed in Core 28R. Carbonate bands and nodules were visible in both X-ray CT scan images (as high CT values) and split core sections (Fig. F3I). Figure F2G shows a photomicrograph from a smear slide of a carbonate band, which consisted of dominant siderite. Carbonate-cemented layers and nodules appear as shades of very light gray in the X-ray CT scan images. Plant remains and shell fragments were the most common fossils found. Gastropods were commonly observed in Core 27R, whereas only a few bivalves and sponge spicules were visible. Sediments of these cores were rich in quartz, clay minerals, and lithic fragments. Mica was visible in few amounts. Parallel laminations were the major sedimentary structure observed in both Cores 27R and 28R. Wavy laminations were found in Core 28R along with coarsening- and fining-upward successions and many carbonate bands. Bioturbation (i.e., vertical and horizontal burrows) was observed in Core 28R.

Cores 337-C0020A-29R through 32R consisted of fine to medium sandstone with minor shale layers associated with coalbeds and coaly material. The upper cores contained shale intercalated with fine sandstone and siltstone. Section 30R-2 contained

one coal horizon with an organic-rich shaly parting (shaly or sandy layer within a coal horizon). Sandstone was often intercalated with thin carbonaceous siltstone and shale layers, and organic and coal material were common in these cores. Grains were subangular to well rounded and moderate to well rounded. Sandstone layers were often dolomite and glauconite rich (Fig. F2I). Lithic fragments were also a dominant component in the smear slides. Few bivalves were observed. Lenticular and wavy bedding along with parallel laminations and coarsening- and fining-upward successions were common.

Scanning electron microscopy

Observations of selected coal and carbonate layers from Cores 337-C0020A-18R, 29R, and 30R were performed on board with a scanning electron microscope with energy dispersive spectrometry (Fig. F4). Pyrites, which were mostly framboidal, siderite, dolomite, and naturally formed barite particles were observed in Core 18R. The presence of barite particles, however, needs further verification because of a possibility of barite contamination from the riser drilling mud. The structure of FeS_2 in the coal of Core 18R showed marcasite.

Mineralogical and geochemical analyses

Semiquantitative X-ray diffraction

Cuttings

Semiquantitative X-ray diffraction (XRD) analysis provided a measure of downcore changes in the relative abundance of four major mineralogical components (i.e., total clay, quartz, plagioclase, and calcite) and was not an absolute percentage of the total sediment, as it did not include some major components (e.g., volcanic glass and biogenic silica) and minor components that generally comprise <10% of marine sediments (e.g., sulfides, oxides, and ferromagnesian silicates). However, semiquantitative XRD measurements provided a good measure of relative lithologic changes, such as the relative changes in the amount of sand and clay. Analysis of cuttings material between 636.5 and 1116.5 m MSF showed a relative dominance of total clay minerals (62%–78%) with lower, but significant, fractions of plagioclase and quartz (15%–20% and 13%–20%, respectively; Fig. F5). Between 950 and 1070 m MSF, relative abundance of quartz and plagioclase increased, which is in contrast to a decline in total clay mineral content at the same depths. The increase in quartz and plagioclase agreed well with the increase in sand content observed below 920 m MSF. Among this four-component semiquantitative analysis, clays, plagioclase, and quartz constitute almost all of the material, whereas calcite is below detection by XRD in each sample above 1116.5 m MSF. The low abundance of calcite over this depth interval as measured by XRD agreed well with the general lack of biogenic calcareous material observed in smear slides.

XRD measurements of cuttings samples below 1296.5 m MSF, which were measured at an approximate resolution of 50 m, support the overall downcore trends determined from macroscopic and microscopic observations of cuttings. The relative abundance of total clay decreased between 1331.5 and 1451.5 m MSF and then increased again to 1701.5 m MSF (Fig. F5) in a pattern that agreed well with the visual estimates of clay. Over the same interval, quartz and plagioclase followed a pattern inverse to total clay, which correlated well with the silt and sand content in the visual estimates. The relative abundance of calcite was below detection in all cuttings samples below 1446.5 m MSF, which was <5% of the four-component mixture in cuttings Sample 337-C0020A-136-SMW (1446.5–1456.5 m MSF).

Cuttings XRD measurements between 1696.5 and 2466.5 m MSF show 54%–73% total clay with 25%–30% quartz and 10%–15% plagioclase. These measurements demonstrate an appreciable decrease in plagioclase relative to cuttings samples above 1696.5 m MSF. XRD measurements in cuttings between 2046.5 and 2466 m MSF show a consistent pattern of 54%–73% total clay with 8%–37% quartz and 10%–31% plagioclase. Calcite was below detection in all cuttings samples across this depth interval.

Core

XRD measurements from core samples showed more pronounced downcore variation between samples than in cuttings because of the higher resolution and discrete sampling that captured individual lithologies (Fig. F5). XRD measurements provided semiquantification that confirmed the visual and smear slide descriptions of lithologies. Total clay content increased systematically from sandstone to siltstone to silty shale to shale. Likewise, plagioclase content systematically decreased between sandstone, siltstone, silty shale, and shale. Quartz was generally higher in sandstone than in shale; however, there was no clear difference in relative quartz abundance between siltstone or silty shale and any other lithology. Calcite was generally below detection in siltstone and shale, present in amounts <5% in sandstone, or up to 47% in calcite-cemented sandstone.

Between 1276 and 1371 m CSF-B, quartz and plagioclase combined were ~60% of the four-component system and decreased between 1371 and 1604 m CSF-B, associated with an increase in total clay over

the same depth interval from 20%–30% to >80%. This pattern generally matched that observed in the cuttings with a trend of increasing shale relative to sandstone with depth. Calcite in this interval was either below detection or 1% and 7% in two samples.

XRD measurements from Cores 337-C0020A-15R through 25R (1919–2002.345 m CSF-B) capture the variation between sandstone (17%–27% total clay and 26%–56% quartz) and shale (70%–82% total clay and 18%–31% quartz) (Fig. F5). As in the cuttings samples, plagioclase was lower when compared to Cores 1R through 14R. Two samples, from very hard carbonate-cemented sandstone, contained calcite relative abundance of 23% and 47%.

XRD samples between 2002 and 2462 m CSF-B in Cores 337-C0020A-25R through 29R were composed of 60%–80% total clay with 5%–25% each of plagioclase and quartz, in agreement with analysis of the cuttings samples. Increases in quartz and plagioclase to 25%–75% were observed in Cores 30R through 32R and associated with an increased prevalence in sandstone. As observed in the cuttings samples, plagioclase is lower relative to quartz compared to the shallower cores. In Cores 25R through 32R, calcite was below detection in all samples except for one sample from carbonate-cemented sandstone, which contained 13% calcite.

Qualitative X-ray diffraction

Cuttings

Qualitative analysis of °2θ peaks in diffraction patterns showed a broadly consistent mineral assemblage, which supports the selection of the four components used in semiquantitative analysis. Quartz, plagioclase, pyrite, and illite/muscovite were present in all or the vast majority of the cuttings samples. No specific clay mineralogical analyses were conducted; therefore, clay mineralogy was only presented in a general discussion, as bulk analysis presents significant errors in analysis of specific clay minerals. Illite was the most common clay mineral present in the cuttings, and has an overlapping peak with muscovite in bulk analysis. In addition, peaks associated with chlorite and smectite group minerals were commonly observed. This agrees well with the regional assessment that illite, chlorite, and smectite clays are dominant along the northern Japan margins (Rateev et al., 1969) and further confirmed by Deep Sea Drilling Project (DSDP) and Ocean Drilling Program (ODP) drilling near the Shimokita region (Kurnosov et al., 1980; Mann and Müller, 1980; Shipboard Scientific Party, 2000). The dominant presence of these minerals suggests that the illite-smectite-chlorite clay, quartz, and plagioclase contained in the standards used for semiquantification in this analysis that were originally selected for the Nankai Trough (e.g., Underwood et al., 2003) are appropriate for semiquantitative analysis of Shimokita sediments.

Peaks associated with pyrite were observed in nearly every sample above 1336.5 m MSF. Above 1056.5 m MSF, clay minerals and micas (usually illite and muscovite) appeared regularly, but clays and micas were observed less frequently, especially in the deeper sediments. Plagioclase was the dominant feldspar, with less frequent occurrence of alkali feldspars; however, alkali feldspar peaks were frequently observed between 691.5 and 741.5 m MSF and between 1801.5 and 2351 m MSF. Cuttings below 920 m MSF were also marked by the appearance of peaks associated with dolomite, likely authigenic carbonate. This is consistent with observations in several smear slides (e.g., 337-C0020A-129-SMW through 131-SMW). Peaks associated with cristobalite were commonly observed, possibly present with volcanic glass or from conversion of amorphous biosiliceous material during drying.

Core

XRD analysis from cores was largely similar to the cuttings, with quartz, plagioclase, illite, and muscovite observed in almost every core sample. Alkali feldspar peaks were frequently observed, correlating with the increased presence of alkali feldspars observed in cuttings samples from the same intervals. Chlorite peaks were only observed in Cores 337-C0020A-15R through 20R and 23R through 24R. Peaks of siderite, dolomite, calcite, or aragonite were observed frequently in samples from Cores 1R, 16R, 19R through 22R, 24R, 26R through 29R, and 32R in intervals near observed carbonate nodules, bands, or cement. Pyrite was commonly observed, especially in Core 15R and shallower. Pyroxene minerals were frequently observed in samples from Cores 13R through 32R. A minority of XRD samples contained peaks associated with amphiboles, olivine, or heavy minerals. Table T1 shows the summary of qualitative XRD data from cores.

X-ray fluorescence

Cuttings

Many samples contained >60% SiO_2 and, together with Al_2O_3, decrease continuously between 824 and 1050 m MSF (Fig. F6). This decrease was associated with the simultaneous decrease of clay and diatoms over this interval, as observed in smear slides and XRD (Fig. F5). High SiO_2 in Hole C0020A was influenced by the high silica content of diatoms and quartz, with additional silica from plagioclase, and clay minerals. High values of Si/Al (a proxy for sands

because sands are rich in silica and clays are rich in aluminum) were consistent with high values of quartz from the XRD data. This was in good agreement with our visual description of cuttings that also showed sand between 636.6 and 1236.6 m MSF. The high biogenic silica content can increase Si/Al, adding uncertainty to the use of Si/Al as a sand proxy; however, the incorporation of X-ray fluorescence (XRF) Si/Al with observations such as sand/silt content from visual observations or XRD data (Figs. **F1, F4**) suggests this proxy is effective in this environment.

Calcium values were consistently low above 1106.5 m MSF, apart from one value at ~1050 m MSF that indicated possible authigenic carbonate. Dolomite is thought to have first-order control on Mg/Al values (Limmer et al., 2012). Given that dolomite is present in multiple cuttings samples (e.g., Sample 337-C0020A-74-SMW [1056.5–1066.5 m MSF]), the high Mg/Al value could be linked to the authigenic precipitation of dolomite in cuttings samples. Mg/Al also showed a strong positive correlation with both CaO and Ti/Ca. Authigenic carbonate nodules observed in cores near the Shimokita region during DSDP Leg 56 and ODP Leg 186 were primarily dolomitic (Okada, 1980; Ijiri et al., 2003). Therefore, increases in Mg/Al in Hole C0020A can indicate, and potentially identify, intervals in which authigenic dolomite was present in cuttings. However, one particularly high Mg/Al ratio was noted at 1050 m MSF corresponding to the appearance of the Mg-rich olivine (i.e., forsterite) (Fig. **F6**) in the qualitative XRD data (Table **T2**). The chemical index of alteration (CIA) (Nesbitt and Young, 1982), using the correction of Singh et al. (2005), in which CaO* is replaced by CaO/Na_2O, was also measured. The CIA value showed a significant correlation with Mg/Al and CaO, suggesting a further proxy for carbonate weathering. The relationships between CaO, CIA, and Mg/Al have been confirmed by the cross-plots (Fig. **F7**).

Below 1106.5 m MSF, Si/Al is generally lower than above this depth, most likely as a result of the general decrease in diatoms and sponge spicules; however, variation within this unit serves as a sand proxy. In cuttings samples, Si/Al increases in intervals with higher sand content, and core samples collected from sandstone have increased Si/Al. There is a good correlation between XRF Si/Al and quartz content between 1296.5 and 1946.5 m MSF, although overall quartz content and Si/Al values are not statistically significant. K/Al values are lower in the shale-rich layers at the bottom of this depth interval, which is consistent with increased chemical weathering in the finer, more clay-rich sediments.

Between 1256.5 and 1826.5 m MSF, the CIA shows little fluctuation, with an increase in K/Al and Si/Al at ~1400 m MSF, where the CIA declines. This drop in Al_2O_3 matches an increase in the proportion of lithic fragments observed in the cuttings. Also, an increase in the CaO ratio is found above 1400 m MSF, where an increase in carbonate is observed in the cuttings samples. In cuttings, a consistent inverse relationship between CaO and the CIA is seen (Fig. **F7**).

Only four cuttings samples were analyzed between 1826.5 and 2046.5 m MSF, although they cover three different lithologies. The uppermost sample (337-C0020A-226-SMW) is a silty shale, and as a result has low K/Al, Si/Al, Ti/Al ratios. In contrast, Sample 242-SMW, taken from a coal, has the highest K/Al and Ti/Al values from the hole. Sample 254-SMW, taken from a coal-rich sand, has very low SiO_2 and Al_2O_3 values.

Cuttings samples below 2046.5 m MSF show a sharp increase in K/Al and Si/Al between the hole bottom and ~2200 m MSF as the lithology becomes sandier. The remaining element ratios appear relatively stable, although sodium fluctuates, which also corresponds to aluminum above 2200 m MSF.

Core

In comparison to cuttings, the geochemistry record for cores is slightly more diverse between 1256.5 and 1826.5 m MSF. Many elements and ratios fluctuate in value, especially between 1600 and 1800 m CSF-B. This region is an area where faulting is observed and perhaps more importantly marks the first appearance of carbonate nodules within the sediments. The declines in K/Al and Si/Al are consistent with an increase in the relative proportion of shale within the sediment.

Core data from 1826.5 to 2046.5 m MSF show a relative increase in Ti/Ca and substantially lower K/Al values than the cuttings samples. Analysis of element values suggests this is due to fluctuations in aluminum, probably linking to the change between sand, silt, and coal. Also, one very high Mg/Al value was observed that is linked to a sharp increase in Fe/Al and Ca/Al. This value is associated with a siderite nodule observed in Core 337-C0020A-24R. Fe/Al and Mg/Al have a consistent positive statistical relationship because iron and magnesium both increase when aluminum declines. Mg/Al values increase consistently wherever dolomite is observed.

Both element values and ratios in cores closely follow the pattern of the cuttings. The differences occur at the bottom of the hole, where values for potas-

sium, sodium, and silica are lower, resulting in a decrease in the K/Al ratio. Small increases in Ti/Ca, Ca/Al, and Mg/Al at 2400 m CSF-B are probably linked to more siderite production. The CIA value slightly declines from 77% to 70% during this interval.

Some elemental geochemical ratios have been used as proxies for chemical weathering based on the relative mobility of some chemical elements relative to others (Duzgoren-Aydin et al., 2002; Wei et al., 2006). For example, the K/Al ratio has been widely used as a proxy for chemical weathering, based on the principle that potassium is highly mobile in water and will therefore be lost under intense chemical weathering (e.g., Nesbitt et al., 1980; Derry and France-Lanord, 1996; Limmer et al., 2012). Therefore, a decreasing K/Al ratio in cores between 1256.5 and 2046.5 m CSF-B indicates more chemical weathering. A general increase of Ti/Ca is visible in cores between 1256.5 and 2046.5 m CSF-B. The Ti/Ca ratio has been applied as a proxy for the relative amount of terrigenous input, assuming that Ti is sourced from coarse-grained sediments. Overall, the only statistically significant correlations occur in proxies used for either carbonate weathering or carbonate precipitation. This means that the composition of sediments at Site C0020 is strongly influenced by these processes. Chemical weathering and terrigenous input show a minor influence on the proxies (Fig. F7).

Interpretation of units

Based on macroscopic and microscopic descriptions of cuttings and core samples, XRD, and XRF data, we defined four different lithologic units at Site C0020. To obtain a more precise interpretation, some of the units were divided into subunits. The units are summarized in Table T3.

Unit I

Interval: cuttings Samples 337-C0020A-25-SMW through 98-SMW

Depth: 647–1256.5 m MSF

Unit I consists primarily of diatom-bearing silty clay. The interval between 1116.5 and 1236.5 m MSF is an exception. The upper part (1116.5–1216.5 m MSF) of this interval consists of loose sand, and the lower part (1216.5–1236.5 m MSF) consists of semiconsolidated sandstone. The lithology of Unit I was observed only from the cuttings samples available from the first phase of riser drilling during Expedition 337. Cuttings samples were taken at 10 m depth intervals from 636.5 to 1256.5 m MSF with a gap of 70 m between 1116.5 and 1186.5 m MSF. A total of 56 cuttings were available and subjected to macroscopic (visual and binocular) and microscopic (smear slides) observations, as well as XRD and XRF analyses. However, because of high contamination from the drilling mud ingredients (e.g., walnut shells, mica, and metal shards) associated with the mud-loss countermeasure, XRD and XRF analyses for the cuttings samples between 1116.5 and 1256.5 m MSF were not conducted.

To obtain a more precise interpretation, we divided this unit into four subunits. Subunit Ia is characterized by semiconsolidated and consolidated diatom-bearing clayey siltstone to silty shale with volcanic glass (647–926.5 m MSF; cuttings Samples 25-SMW through 58-SMW). The Subunit Ia/Ib boundary is defined by the top of the first occurrence of fine sand in cuttings samples (between Samples 58-SMW and 59-SMW). Subunit Ib consists of semiconsolidated diatom-bearing clayey siltstone with common fine sandstone (926.5–1116.5 m MSF; Samples 59-SMW through 88-SMW). At the top of Sample 92-SMW (1116.5 m MSF), cuttings consist mainly of unconsolidated to semiconsolidated sandstone and silty sandstone with rare clayey siltstone. This lithologic unit (Subunit Ic; 1116.5–1236.5 m MSF) is visible to 1236.5 m MSF (Sample 95-SMW). The Subunit Ic/Id boundary was characterized by a change in lithology to semiconsolidated clayey siltstone (1236.5–1256.5 m MSF; Samples 97-SMW through 98-SMW).

Unit II

Intervals: cuttings Samples 337-C0020A-105-SMW through 216-SMW; Cores 337-C0020A-1R through 14R

Depth: 1256.5–1826.5 m MSF

The Unit I/II boundary is defined by lithologic changes found in cuttings samples (between Samples 337-C0020A-98-SMW and 105-SMW). A rapid decrease of sand content is visible at this boundary. The boundary is also characterized by the first occurrence of rare glauconite in cuttings samples (1266.5–1276.5 m MSF; Sample 111-SMW). In addition, the amount of biosiliceous material decreases, whereas the amount of plant remains increases. Unit II consists mostly of silty shale, with some intervals of sandstone and siltstone. The interval between 1256.5 and 1826.5 m MSF was characterized at the top by a relatively high silt content (70%–90%) (Fig. F1). The silt content decreases to the middle part of the unit and shows the lowest content at 1556.5 m MSF (15%). Silt content then increases again to the bottom of this unit (50%).

To obtain a more precise interpretation, this unit was divided into two subunits. Subunit IIa includes mainly shale, siltstone, and sandstone associated with marine fossiliferous material (1256.5–1506.5 m

MSF; Samples 105-SMW through 153-SMW and Cores 337-C0020A-1R through 6R). Subunit IIb consists of organic-rich shales and sandstone with plant remains (1506.5–1826.5 m; Samples 154-SMW through 216-SMW and Cores 7R through 14R).

The principal difference between Subunits IIa and IIb is the presence of abundant organic material mostly in the form of wood/lignite fragments and glauconite in cuttings samples in Subunit IIb. The sand fraction generally increases to the bottom of Subunit IIb, whereas the amount of biosiliceous material decreases. Organic-rich silty shale with abundant volcanic glass comprises the upper part of this subunit, with grains that were mostly moderate to subangular and moderate to well sorted. The lower part of this subunit was dominated by fine to medium sandstone with few silt and shale intercalations. Grains were moderate to subangular and moderately to well sorted. Parallel and wavy laminations are commonly observed throughout Subunit IIb, whereas cross- and ripple cross-lamination as well as coarsening- and fining-upward intervals were only observed in some parts of Subunit IIb. Joint, normal fault, and mineral-filled fractures were found in the middle part of this subunit. Bioturbation ranged from slight to moderate and was common throughout this subunit. Unit II demonstrated a transition from a siltstone-dominated lithology in Subunit IIa to one that is bimodally dominated by clay and sandstone in Subunit IIb.

Unit III

Intervals: cuttings Samples 337-C0020A-217-SMW through 260-SMW; Cores 337-C0020A-15R through 25R

Depth: 1826.5–2046.5 m MSF

The Unit II/III boundary was selected at the point where plant remains and lignite were the dominant fraction in the cuttings samples. However, the first occurrence of coal in cores appears in the lower part of Core 337-C0020A-14R (1824.6 m CSF-B). To be consistent with defining unit boundaries on the basis of cuttings samples, it was decided to set the boundary below cuttings Sample 216-SMW. The lithology of Unit III was determined from macroscopic and microscopic observations on 11 cores (337-C0020A-15R through 25R) and 22 cuttings samples (337-C0020A-217-SMW through 261-SMW) available from the second phase of drilling operations. This unit is dominated by several coal horizons that are divided by coaly shales, siltstones, and sandstones.

Unit IV

Intervals: cuttings Samples 337-C0020A-261-SMW through 391-SMW; Cores 337-C0020A-26R through 32R

Depth: 2046.5–2466 m MSF

The Unit III/IV boundary was selected at the base of the last dominant occurrence of plant remains/lignite in cuttings samples (337-C0020A-260-SMW). The absence of thick coal layers differentiates this unit from Unit III. Unit IV covered the deepest part of Hole C0020A. The identification of the lithology in this unit was supported by the recovery of seven cores (337-C0020A-26R through 32R) and 42 cuttings samples (261-SMW through 391-SMW). Unit IV was dominated by silty shales in the upper part, sandstone intercalated with siltstone in the middle part, and shales associated with sandstone, siltstone, and a thin coal layer in the lower part.

Unit IV is divided into two subunits. The boundary between these two subunits is drawn by the first common occurrence of plant remains/lignite in a cuttings sample (384-SMW). Shale and sandstone associated with carbonate and glauconitic material characterize Subunit IVa (2046.5–2426.5 m MSF; cuttings Samples 261-SMW through 371-SMW and Cores 26R through 29R). Subunit IVb shows clay and silt as the dominant size fraction in cuttings samples (2426.5–2466 m MSF; cuttings Samples 384-SMW through 391-SMW and Cores 30R through 32R). Coal fragments are also dominant. Clay and silt are the dominant size fraction in cuttings samples. Coal fragments are also dominant in the cuttings samples. In cores of Unit IV, fine to medium sandstone with minor shale layers with one coal layer is visible.

Depositional environment

In general, sand-sized lithic fragments and biotite occur throughout the hole. Furthermore, sediments are often poorly to moderately sorted and grains are often moderate to subangular rounded (except the deeper parts in the hole). These details suggest short and/or sometimes fast transport distances of the sediments.

The interpretation of Unit I is limited to only cuttings samples because no cores were collected until 1276.5 m CSF-B. Diatom-bearing clay- and siltstones are interpreted as hemipelagic sediments representative of a slope to abyssal plain setting. Toward the top of Unit II, the occurrence of sponge spicules and diatoms decreases, whereas rare glauconite was observed. Glauconite is a hydrated illite-group mica mineral that typically forms in water depths of 5–

500 m in the presence of high biological activity (Cloud, 1955; McRae, 1972). Thus, glauconite is an indicator for shallow-marine environments, typical of continental shelf settings. Glauconite formation is limited by high sedimentation rates. In the uppermost part of Unit II, sediments are likely still deposited in a deep-marine setting but with a position nearer to the shelf margin. Occurrence of abundant and dominant glauconite is probably caused by transport from the shelf to the slope by mass flows (cf. Core 337-C0020A-2R).

The first occurrence of bioturbation appears in Core 337-C0020A-6R (1495–1499.135 m CSF-B). In addition, cross-laminae that are convex-upward are visible in this core. These laminae could be interpreted as hummocky cross-stratification, which is typical for storm sediments. In Core 8L and deeper, bioturbation and glauconite are very common. Burrows in this area are normally horizontal and often occur in shales and siltstones. Detailed ichnofacies studies were not conducted, but with the observation of glauconite in the sediments, we suggest that the burrows belong to the *Cruziana* ichnofacies, which is typical for continental shelf environments. Symmetric cross-stratifications, which are visible in this part of the hole, are typical for low-energy and shallow-marine environments. Therefore, we conclude that sediments from the end of Subunit IIa to the middle part of Subunit IIb (1495–1634.905 m CSF-B; Cores 6R through 10R) were deposited on the shelf between the fair-weather wave base and the storm wave base (Fig. **F8**).

Horizontal and vertical burrows occur in the lower part of Subunit IIb (1737.5–1828.095 m CSF-B; Cores 11R through 14R). Bioturbation is observed in clayey, silty, and sandy sediments. Parallel and cross-lamination as well as wavy bedding are visible in Cores 11R through 14R. Several shell fragment–rich layers are observable in Core 12R, and some shell fragments, likely of the genus *Ostrea*, appear in Core 13R. Greater diversity of different burrows in different types of sediments and the sedimentary structures suggest deposition in an intertidal and lagoonal environment.

In the middle of Core 14R, the depositional environment changes slightly. Organic-rich shales enclose a thin coal horizon. Asymmetric cross-stratification above the coal layer suggests a high-energy nearshore environment. Several coal horizons and organic-rich shales are present in Unit III until Core 25R (1995–2002.345 m CSF-B). High gelification of the coal, no inertinite (inert component in the coal), and areas with high clay and sand content in coal horizons suggest very wet conditions in the swamp. Glauconite, mostly horizontal burrows, and different types of sedimentary structures are visible in Unit III. Cores 15R through 19R (1919–1960.295 m CSF-B) are sand dominated and show coarsening- and fining-upward cycles and parallel laminations. Cores 20R and 21R (1959.5–1972.71 m CSF-B) are rich in shale and siltstone with flaser and lenticular bedding, wavy bedding, and coarsening- and fining-upward cycles. Core 22R (1973–1979.19 m CSF-B) contains planar bedding and cross-bedding within sandstones, whereas Core 23R (1981.5–1991.25 m CSF-B) is again shaly with authigenic carbonate bands possibly containing siderite. Authigenic carbonate bands are also visible in Cores 24R (sandstone rich; 1991–1994.965 m CSF-B) and 25R (mostly fine grained; 1995–2002.345 m CSF-B). Lenticular bedding is typical for tidal flats. The absence of carbonate bands in the upper part of Unit III suggests a tidal flat environment with cycles of changing environments from intratidal to supratidal (marsh and swamp). Sandstones immediately above the coal seams could be related to deltaic environments (channels of an estuary or of a fluvial-dominated delta). Siderite bands and nodules are typical for euxinic environments (brackish) and can be found in back-barrier marine environments with lagoons, tidal flats, tidal channels, and flood tidal deltas (Boggs, 2006). Initial XRD, XRF, and smear slide results suggest that siderites are a common constituent in observed carbonate bands. No glauconite was observed near siderite bands. Cycles of frequently changing environments from back-barrier to wetland are also interpreted for this interval. Burrows and glauconite in Unit III show the presence of marine conditions. It is not known if these frequent changes in depositional environment are caused by sea level fluctuations. Sediments of Unit IV look very homogeneous over wide parts of the hole (cuttings and cores). Carbonate bands, horizontal burrows, fining- and coarsening-upward cycles, cross-bedding, and lenticular and flaser bedding are visible throughout Unit IV. Therefore, the depositional environment of this unit is similar to that of Unit III. Wetland conditions are only observable in the lowermost part of this unit (coal and organic-rich shale). Siderite layers are again an indicator for a back-barrier environment with tidal flats (lenticular bedding) and tidal channels. Sandy distributary channels from deltas are also possible environments preserved in Unit IV. The coal horizon in the lowermost part of this succession is similar to the coal layers in Unit III, suggesting a similar depositional environment.

Units III and IV are ~700 m thick in total. These parts of the hole were deposited in almost the same depositional environment, showing fluctuations between intertidal and wetland (marine/brackish influence) conditions. This also suggests that the sediment accumulation is in balance with tectonic subsidence, which seems to be high in this area.

Drilling disturbances

Recovery in Hole C0020A was excellent overall, even at such deep penetration depth. Although Cores 337-C0020A-1R through 7R had <50% recovery, core recovery in deeper parts of the hole, especially around the coal formation interval, was high (80%–100%).

Drilling disturbance (Fig. F9) varied depending on core and lithology. Unit II experienced slight disturbance or fracturing, except for Cores 337-C0020A-5R and 6R, where parts of the cores were moderately to heavily fractured. In Unit III, drilling disturbance was also generally low, especially in the shale and silt regions. Semiconsolidated sandstones were more likely to be affected by drilling disturbance. The cores of Unit IV were also mostly found in good condition with minor disturbance throughout. However, moderate to heavy disturbance was found in some sections of Cores 28R and 31R.

Injections of drilling mud and fluid used in riser drilling during Expedition 337 caused complications to visual observations of the cores. Semiconsolidated materials were commonly observed in Hole C0020A, and drilling mud often easily penetrated the rock, causing possible false lamination structure in the cores, which might be misinterpreted as natural sedimentary structure preserved in the cores (Fig. F9). Drilling mud may also contribute additional contamination to smear slide analysis. In this case, it was possible that the mud layers caused by mud injections were observed on smear slides under the microscope, which could also lead to misinterpretation of fossils or other materials present on the slides.

Cuttings contamination

During Expedition 337, drilling mud circulation also caused high contamination of cuttings samples. Cuttings samples were washed to eliminate this contamination. In addition to drilling mud components, other material such as walnut shells and mica from lost circulation material (LCM) and metal shards from drilling equipment were observed in cuttings samples. During the washing process, semiconsolidated material was easily broken, and fractions finer than 250 µm were lost through the mesh. This is one possible reason why cuttings and cores containing a large amount of sandstone were not in good agreement in the lithologic description (e.g., cuttings Sample 337-C0020A-114-SMW and Core 337-C0020A-1R).

Drilling mud may contaminate samples for XRD and XRF analyses as well. For this reason, XRD and XRF analyses were not conducted on the cuttings samples between 1116.5 and 1256.5 m MSF because it was obvious that the samples were highly contaminated with LCM. Although attempts were made to avoid samples with high contamination, in some cases it is evident that the mud penetrated the cutting chips easily and it is extremely difficult to differentiate this type of mud from clay originally present in the cuttings samples. In this case, the contamination can be seen only after measuring XRD and XRF of samples. For example, potassium in cuttings samples was often higher than that observed in the cores, likely due to introduction by drilling fluid. However, overall trends are nearly the same. Therefore, it is suggested that the influence of contamination is only low.

Other than from drilling mud, some of the cuttings samples probably represent a mix from different depths. Poor agreement between XRD and XRF results of cuttings and cores (e.g., 1256.5–1506.5 m MSF) could be due to this mixture of material from a wide range of depth intervals (e.g., recirculated material or cave-in material). On the other hand, washing-out of semiconsolidated and unconsolidated sand in cuttings as well as different lithologies taken from cores can also cause differences in XRD and XRF results. Variability in elements and mineral abundances measured from XRF and XRD are much lower in cuttings than in cores, suggesting the influence of a dominant lithology can overprint the downhole elemental variation in cuttings. In this case, rather than having cuttings or core profiles only, it is quite beneficial to have both sets of analysis to help identify contamination.

Conclusion

Based on macroscopic and microscopic descriptions of cuttings and core samples during Expedition 337, which was supported by XRD and XRF data as well as all available data (e.g., logging, micropaleontology, and physical properties data), we defined four different lithologic units at Site C0020. The succession of lithofacies in Hole C0020A also provides insight into the evolution of depositional environments in the site region.

- Unit I (647–1256.5 m MSF) consists primarily of diatom-bearing silty clay. This unit clearly represents a marine offshore environment.

- Unit II (1256.5–1826.5 m MSF) consists mostly of silty shale with some intervals of sandstone and siltstone. The principal differences between this unit and the upper unit are the tendency for decreasing amounts of biosiliceous material and increasing plant and glauconite material toward the deeper part of the unit. Based on those phenomena, Unit II was divided into two different subunits: sandstone and siltstone associated with marine fossiliferous material and organic-rich shale and sandstone associated with plant remains. This unit reveals more offshore transition environment, which then gradually changes into a shallow-marine setting. The lower part of this unit is situated in the intertidal zone.
- Unit III (1826.5–2046.5 m MSF) is dominated by several coal horizons that are divided by coaly shales, siltstones, and sandstones. Almost all coal horizons consist of detritic to xylo-detritic coal with some layers of xylitic coal. Sometimes shaly coal was observed. Water content, color, and vitrinite reflectance measurements of the coal suggest that the coal has low maturity (R_o = 0.36%). Bioturbation and sedimentary features like flaser bedding, lenticular bedding, or cross-bedding suggest a nearshore depositional environment with tidal flats and tidal channels. The presence of coal, coaly shale, and siderite bands at the bottom of this unit suggest a back-barrier marine environment in combination with wetlands (e.g., salt marsh or swamp). Small terrestrial influence might occur within sand bodies that overlie coal horizons. This could be due to channels from fluvial-dominated or tidal-dominated deltaic estuarine environments.
- Unit IV (2046.5–2466 m MSF) is dominated by silty shales in the upper part, sandstone intercalated with siltstone in the middle part, and shale associated with sand, silt, and a thin coal layer in the lower part. The absence of thick coal layers differentiates this unit from Unit III. Although one coal layer appears again at the bottom of the unit, it is only a thin layer, which may indicate the presence of another coal-rich unit below this interval. Unit IV suggests deposition in the same environment as Unit III. Units III and IV represent high-frequency changes of depositional environment. Within a few meters, sediments indicate tidal flats and tidal channels that are overlain by organic-rich marsh sediments and terminate in the formation of a peat. Often, coal layers are bounded at the top by sandstones that can be interpreted as channel sandstones of a fluviodeltaic system.

Paleontology

During Expedition 337, a succession of different lithologies was penetrated, reflecting environments ranging from warm-temperate coastal backswamps to cool-water continental shelf. These different environments yielded fossil groups with varying degrees of utility for biostratigraphy. Considerable challenges were posed by contamination from drilling mud that affected core samples, core catcher samples, and especially cuttings samples. Large volumes of sand also led to no yield throughout some parts of the hole for palynological investigations. Despite these obstacles, micropaleontology was able to successfully secure an age of late Pliocene at the top of Hole C0020A at 636.5 m MSF and indicate a probable age of late Oligocene–early Miocene at the base of the hole (2466 m MSF).

Shipboard micropaleontology included diatoms, calcareous nannofossils, organic-walled dinoflagellate cysts (dinocysts), pollen, and spores. A range of different sample types was analyzed, including well cuttings, core catcher samples, and discrete samples taken from working halves. In documenting fossil distribution in Hole C0020A, discussion is split into four units: Unit I spans the top of the hole from 647 to 1256.5 m MSF, Unit II ranges from 1256.5 to 1826.5 m MSF, Unit III from 1826.5 to 2046.5 m MSF, and the final unit (Unit IV) ranges from 2046.5 to 2466 m MSF (see **"Lithostratigraphy"**). Calcareous nannofossils are rare and poorly preserved. Calcareous nannofossils do not inform the age model presented here. Preservation varied greatly throughout the hole for the other microfossil groups, but diatoms were best and most abundantly preserved in Unit I together with predominantly heterotrophic dinocysts. Diatom floras indicate a Pliocene cool-water continental shelf succession in Unit I. In contrast, Unit II yielded few identifiable diatoms and poor dinocysts. Pollen and spores are moderately well represented but are abundant near the base of Unit II in the more terrestrial to very shallow marine sediments. Unit III contains excellent pollen and spore assemblages in the coals and associated terrestrial to coastal shallow-marine sediments, but dinocysts are scarce and contain few useful biostratigraphic markers. The same remarks can also be made for Unit IV, which is marked by good pollen and spore assemblages from the cores but contains very few dinocysts. A feature of Units II–IV is that reworked Paleogene dinocysts are encountered that have ranges from early middle Eocene to late Oligocene. Therefore, the pollen floras provide some indication of the age in Units III and IV, indicating a maximum age of

late Oligocene for the base of Unit IV and a likely age of early middle Miocene for Unit III.

Palynology

A total of 101 samples were analyzed for dinocysts, pollen, and spores. Preservation and yield of palynomorphs varied significantly throughout the different units with the greatest yield and abundance of dinocysts from Unit I and greatest abundance and best preservation of pollen and spores in Units III and IV. Clast grain size, as well as depositional environment, plays a major role in determining whether samples yield palynomorphs. Despite the predominance of spores and especially pollen in Units III and IV and a general lack of dinoflagellate cysts, stratigraphic information is provided by the palynomorphs. Reworking is noted throughout the core and mixes Eocene and Oligocene dinoflagellates into Neogene assemblages. Remobilization of palynomorphs in drilling fluid has a significant role in smearing stratigraphic ranges for those palynological data taken from cuttings samples. However, this is a minor issue for core and core catcher samples because they were selected away from the core edge and could be washed effectively. In particular, samples from terrestrial deposits such as lignites in Units III and IV contain pollen and spores in such high concentrations that palynomorph presence totally masks any potential contamination that is remnant even after washing the raw sample.

Unit I (647–1256.5 m MSF)

A total of 41 cuttings samples were analyzed from Unit I and captured a Pliocene sequence of dinocysts and gymnosperm pollen (Table **T4**). Palynomorph abundance was greatest from 636.5 to 846.5 m MSF, but the lower half of Unit I below 846.5 m MSF contained generally poor samples with sparse representation of any palynomorph group. Dinocyst assemblages are dominated by a restricted assemblage of primarily heterotrophic forms such as *Brigantedinium* spp., *Selenopemphix* spp., and *Xandarodinium variabile*. The composition of the assemblages is identical to that of Pliocene samples from ODP Leg 186 Hole 1151A located slightly further south off the Sanriku Coast of northern Japan (Kurita and Obuse, 2003), as well as those from the Bering Sea (Bujak, 1984; Bujak and Matsuoka, 1986). The only notable event is the first downhole occurrence (FDO) of *Capillicysta fusca* at 746.5–756.5 m MSF. The dinocyst flora contains occasional specimens of other dinocysts such as *Operculodinium* spp. together with some reworked Miocene and Paleogene dinoflagellates. The pollen flora is skewed toward large specimens that were trapped in the 20 µm mesh used during the processing of these samples in Unit I. Conifer pollen (including *Tsuga* and gymnosperms) is very common, indicating development of significant coniferous vegetation on nearby land areas. The paleoenvironment of deposition is interpreted as continental shelf with cool water and high productivity that allowed the development of restricted heterotrophic dinocyst communities feeding off diatom blooms.

Unit II (1256.5–1826.5 m MSF)

This unit is represented by 30 samples, of which 12 are barren, and the rest contain moderate to poor palynomorph abundance (Table **T5**). A total of 18 samples are from cuttings, 10 are from core catchers, and 2 are from working halves. The sandy nature of sediment in some parts of this unit results in the poor preservation and abundance of palynomorphs. All samples from Unit II were processed using a 10 µm mesh to enhance the capture of pollen and spores as well as dinoflagellate cysts. Pollen and spores are considerably more abundant than dinoflagellates in this unit, with particularly strong representation of Betulaceae (*Alnus, Betula,* and *Carpinus*). Pollen from other angiosperm trees is frequently encountered, including Juglandaceae (*Juglans* and *Pterocarya*), *Fagus,* deciduous *Quercus* (D. *Quercus*), and *Ulmus/Zelcova*. Gymnosperm pollen are represented by abundant Taxodiaceous pollen (a group that includes *Glyptostrobus, Metasequoia*, and *Taxus* here), bisaccate pollen (that includes undifferentiated Pinaceae grains), and *Tsuga*. Pollen of *Larix* is also encountered, although it is not abundant. The only notable FDOs are evergreen *Quercus* (E. *Quercus*) that first appears at 1546.5 m MSF and *Platanus* at 1816.5 m MSF. The flora is similar to late Neogene assemblages of Japan (Yamanoi, 1978, 1992; Wang et al., 2001) and northeast China (Wang, 2006) but lacks significant quantities of herbaceous taxa. Reduced herb presence may be an artifact of depositional environment that is interpreted as marine shelf environment. The pollen flora suggests the presence of a temperate paleovegetation type dominated by trees in northeast Honshu, Japan, during deposition of Unit II.

Dinocyst assemblages include the presence of reworked *Trinovantedinium boreale* and assemblages that offer limited biostratigraphic information. The last downhole occurrence (LDO) of *Xandarodinium variable* at 1378.83 m MSF may indicate the middle–late Miocene based on Leg 186 Hole 1151A (Kurita and Obuse, 2003) and age ranges from west Japan (Matsuoka et al., 1987). The dominant dinocyst remains *Brigantedinium* spp. in Unit II, with the continued presence of *Lejeunecysta* spp., *Operculodinium* spp., and *Selenopemphix* spp. The presence of *Tubercu-*

lodinium vancampoae is also noted, which supports a middle Neogene age determination. The paleoenvironment of deposition is interpreted as shallow marine and more proximal to land than depositional environments in Unit I. The presence of pyrite damage to some organic matter throughout the unit confirms the likely deposition in or near seawater.

Unit III (1826.5–2046.5 m MSF)

A total of 20 samples from Unit III yield moderate to abundant palynomorphs (Table T6). Only two samples are barren. Five samples are from cuttings, five are from core catchers, and the remaining ten are taken from working halves. Lithologies include fine sand to coal, and the best pollen and spore assemblages are found associated with the coal facies. Dinoflagellates are present in the more clastic samples but are neither diverse nor abundant and capture a range of taxa from the late Eocene and Oligocene (Kurita and Matsuoka, 1994; Kurita, 2004) that are interpreted as reworked. This group includes *Bellatudinium hokkaidoanum, Kallosphaeridium, Phthanoperidinium* spp., *Systematophora ancyrea*, and *Trinovantedinium boreale*. These dinocysts are uniformly poorly preserved and associated with sediments that are not open shelf but rather lagoonal to very shallow marine or even terrestrial deposits. The presence of *Evittosphaerula* sp. A at 1846.5 m MSF may indicate that the sediments are early middle Miocene (Bujak and Matsuoka, 1986; Kurita and Obuse, 2003). This age estimate is further supported by the pollen and spore flora that contain a notable presence of evergreen taxa and thermophilic elements, such as *Engelhardtia, Liquidamber,* Malvaceae/Euphorbiaceae, Myrtaceae, *Pasania,* E. *Quercus*, and *Reevsia*. Pollen of Taxodiaceous plants is very common and so are *Liquidamber, Nyssa,* D. *Quercus*, E. *Quercus*, and *Ulmus/Zelcova*. Frequently encountered pollen includes *Alnus, Carya,* and *Fagus*. Conifers and *Larix* are not present in the coals but are present in clastic sediments. Therefore, conifers, *Larix*, and *Tsuga* are transported into the depositional environment from drier regions, presumably at the basin edge where active uplift and erosion of marine Paleogene strata facilitate the deposition of reworked dinocysts.

The composition of the flora in the terrestrial sediments suggests a warmer climate than that of Unit II, and the flora is comparable to the pollen Zone NP2 of Yamanoi (1978, 1992) that spans the early–middle Miocene (≈13–19 Ma) and to pollen floras from northeastern China that are early–middle Miocene (Wang, 2006). The relative abundance and composition of angiosperm pollen are very similar to those documented for the middle Miocene Sugata Formation of central Japan (Wang et al., 2001). The abundance of *Liquidamber*, Ulmaceae (*Celtis* and *Ulmus/Zelcova*), and also taxodiaceous pollen is a feature of other Miocene swamp deposits in Japan (Shimada, 1967). None of these coalbeds or terrestrial sediments are comparable with the early Oligocene and middle Eocene coal fields of Hokkaido reported by either Sato (1994) or Kurita and Obuse (1994). The presence of unusual Paleogene-type pollen, such as *Taliisipites pulvifluminis*, together with modern genera and families, is a feature shared with lignites within the Taneichi Formation in the Iwate Prefecture, northeast Japan. In the Taneichi Formation, Paleogene dinoflagellates are reworked into clastic sediments and even lignite that contains pollen floras assigned to the late Oligocene–early Miocene (Yagishita et al., 2003). The paleoenvironment of Unit III is interpreted as coastal swamps with associated mosaics of coastal to very shallow marine depositional environments. A notable feature is that pyrite damage to organic matter is observed in many clastic samples, suggesting some deposition in very shallow marine sediments.

Unit IV (2046.5–2446 m MSF)

Pollen and spores are the dominant palynomorphs throughout the nine samples analyzed in Unit IV. All samples are taken from working halves, and most yield abundant fossils (Table T7). Fern spores are present in abundance together with pollen from taxodiaceous trees, *Alnus*, and *Betula*. Throughout Unit IV, pollen from deciduous trees such as *Nyssa, Platanus, Pterocarya*, and *Ulmus/Zelcova* are consistently present. The LDO of *Cathaya* is noted at 2110.5 m MSF, and the LDO of *Larix* is at 2456.5 m MSF. *Cathaya* has been previously reported from the early Miocene of Japan (Wang et al., 2001), and *Larix* is most commonly found in the Neogene as well (Shimada, 1967). The first occurrence (FO) of *Larix* in northern Japan is probably in the late Oligocene based on correlation from eastern Hokkaido between pollen occurrences with dinocysts and diatom stratigraphy (Kurita et al., 1998). Unit IV is no older than late Oligocene based on the presence of these gymnosperms.

Dinoflagellates from Unit IV are poorly represented, although *Batiacasphaera micropapillata* is consistent with an age of late Oligocene–early Miocene (Schiøler, 2005). A similar species, *Batiacasphaera hirsuta*, occurs in the late Oligocene of Japan (Kurita, 2004). The occurrence of *Diphyes latisculum* may indicate early Miocene because this species has biostratigraphic significance (Matsuoka et al., 1987; Kurita, 2004). The presence of reworked Paleogene dinocysts are noted and is in accord with Units II and III, of which *Phthanoperidinium* spp. and *Trivan-*

todinium boreale are most persistent. Both these dinocyst groups are noted from Hokkaido and northeastern Honshu and are reworked into late Oligocene–early Miocene sediments (Kurita et al., 1998; Yagishita et al., 2003). The depositional environment for the majority of Unit IV is interpreted as a shallow- to very shallow marine environment, based on the palynomorph assemblages. The base of the unit contains coal. Therefore, coastal swamps are also encountered.

Diatoms

Diatoms are present and identifiable throughout the entirety of Unit I but are either too poorly preserved throughout Units II, III, and IV to be useful as geologic age indicators or are completely absent. Throughout Hole C0020A, the zonation of Yanagisawa and Akiba (1998) is followed.

Unit I (647–1256.5 m MSF)

In Unit I, diatom samples range from barren to abundant with poor to good preservation (Table **T8**). Samples can be dated and zoned with varying degrees of precision to 1076.5 m MSF. All samples are Pliocene in age. Samples 337-C0020A-24-SMW (636.5–646.5 m MSF) through 55-SMW (886.6–896.5 m MSF) are assigned to the upper Pliocene *Neodenticula koizumii* Zone (North Pacific diatom [NPD] 9), but Samples 25-SMW (646.5–656.5 m MSF) through 45-SMW (846.5–856.5 m MSF) belong to the upper part of this zone based on the FO of *N. seminae*. Samples 56-SMW (896.5–906.5 m MSF) through 61-SMW (946.5–956.5 m MSF) have been assigned to the underlying middle–upper Pliocene *N. koizumii–Neodenticula kamtschatica* Zone (NPD 8) based on an increase in *N. koizumii* abundance. Samples 66-SMW (996.5–1006.5 m MSF) through 75-SMW (1066.5–1076.5 m MSF) have been assigned to the lower Pliocene *Thalassiosira oestrupii* Subzone (NPD 7Bb). Diatoms are identifiable in Samples 79-SMW (1076.5–1086.5 m MSF) through 98-SMW (1246.5–1256.5 m MSF)—the base of Unit I at 1256.5 m MSF—and appear to be Miocene; however, marker species were not identified in any of these samples and the potential exists that specimens in these sediments have been reworked. The early Pliocene/late Miocene boundary is not observed.

Contamination became more apparent at ~1126.5 m MSF, just below the first lost interval near the base of Unit I, with persistent remobilization of Miocene–Pliocene diatoms down the hole. Microfossils polluted the drilling mud as it recirculated through the hole, causing contamination in nearly every sample to the base of the hole despite thorough washing of the sediment. Contamination proved problematic for core samples, core catcher samples, and cuttings samples of all fraction sizes. Samples of the smallest size fraction often contained no rock cuttings and were of a sandy or muddy consistency, therefore completely saturated with the contaminated drilling mud. Most samples taken from the center of the core were free of contamination but contained no diatoms in Units II, III, or IV. Diatoms were observed in deeper parts of the hole (see **"Lithostratigraphy"**) but are restricted to small, uninformative fragments or contaminants. The most prolific contaminants to 2119 m MSF were those of late Miocene and Pliocene age, including such marker species as *N. kamtschatica* and *N. koizumii*. Two Pleistocene diatoms, *Actinocyclus oculatus* and *Proboscia curvirostris*, were also identified as contaminants.

Calcareous nannofossils

Calcareous nannofossils were very low in diversity and rare to absent in all sediments recovered from Hole C0020A. Nannofossils were only observed in the shallower sediments and consisted of younger species of *Reticulofenestra* and *Sphenolithus*—species that tend to be too small for precise identification using a light microscope and, therefore, of little biostratigraphic significance when present.

Downhole logging

Excellent logging data quality, probably due to in-gauge borehole condition and relatively simple lithology consisting of sandstone, siltstone, shale, coal, and conglomerates, made clear identification of lithologic features based on the logging data characteristics. Because most lithology showed typical log response and was found to be intercalated by a number of marker layers (i.e., coals and cemented sandstones), correlation of the logging data to cores was also relatively easy and depth difference between these was 0.7 m or smaller.

Log characteristics suggested that the lithology of Unit I is most likely similar to that of Unit II, which consists of alternation of relatively thick layers of massive sandstones and siltstones (Fig. **F10**). Unit III was characterized by frequent coal layers in a few meters thickness of sandstone and siltstone alternation sequence. Based on correlations to visual core descriptions (VCDs), 7 coal layers, including the thickest two (7.3 and 3.5 m), were acquired in the cores among 13 layers that were >30 cm in thickness. Unit IV consists of thick (~200 m) massive shale in the upper half and alternation of sandstone and shale of a few meters thickness in the lower half, which also includes one thin coal layer (Core 337-C0020A-30R).

Resistivity borehole images suggested that sandstones in Unit II are massive and include granules, pebbles, and mollusks (i.e., Bivalvia), whereas those in Units III and IV consist of thin, a few centimeter thick sandstones or laminae of this scale, suggesting a change in the sedimentary environment at the Unit II/III boundary. By combining the logging data and core descriptions, sandstones that are supposed to be of high permeability were identified in Units II and III.

By using a formation-testing tool, in situ formation fluid samples were acquired from six permeable sandstones. The 35 "pretest" measurements prior to the fluid sampling indicated that formation pore pressure is hydrostatic or elevated by only a few percent of the hydrostatic value to depths of at least 2425 m wireline log matched depth below seafloor (WMSF) (i.e., the depth of the deepest reliable measurement for logging operations).

Borehole temperature was measured by two types of logging tools. The maximum temperature at the bottom of Hole C0020A was also estimated by examining the temperature build-up pattern during logging operations. Conclusively, the estimated temperature gradient is 24.0°C/km or slightly lower (Fig. **F11**).

Preliminary log-seismic integration was carried out based on the time-depth curve derived from vertical seismic profile (VSP) operations and synthetic seismogram calculation. The time-migrated seismic profile for Line ODSR03-BS (Taira and Curewitz, 2005) was converted with the time-depth relationship and compared with logging data. Strong reflectors are basically well correlated with the abrupt change on the logging curves.

Overview of logging results

The geophysical logging data set acquired during Expedition 337 showed characteristic log features corresponding to the lithology confirmed by the cores. The logging data set mainly used for lithology identification included gamma radiation (GR), spontaneous potential (SP), resistivity, density, and neutron porosity. Spectral gamma (uranium, potassium, and thorium) showed little change among the variation of rock types, and thus was not used. The responses of the sedimentary rocks, such as sandstone and shale, to the logging tools were typical, and therefore rock types could be distinguished without particular difficulty in the logging data. There were a number of anomalously high resistive layers, which are coal and mineral-cemented sandstones. These resistive layers can be a good marker to correlate the logging data to cores. Typical responses of major lithologies are summarized in Table **T9.**

Coal layers could be clearly identified, with very low gamma radiation, very high resistivity, exceptionally low density, and exceptionally high neutron porosity (see Table **T10** for major coal layers). Mineral-cemented sandstones also showed a characteristic log response of very high resistivity, but those layers showed very high density and very low porosity, which is the opposite trend of coal layers.

Overall, the logging data showed that sandstones clearly responded to SP as low values, which is probably due to drilling fluid having higher salinity than formation water.

Data quality

Logging data quality is generally excellent, which is probably due to very good borehole condition without elongation or irregularity of the borehole wall. The lithology encountered may also contribute to log data quality, and the relatively simple rock type (e.g., sandstone, siltstone, shale, coal, and conglomerates) made clear identification of lithology based on the logging data characteristics. Because most lithology shows typical log response and is intercalated by a number of marker layers (coal and cemented sandstones), correlation of the logging data to cores is also straightforward.

However, there are some concerns in terms of the data quality. The Formation MicroImager borehole image quality (i.e., resistivity scanning on the borehole wall) might be significantly affected by the contact situation of the electrode pads and flaps. In the images acquired during Expedition 337, noise could be seen only in those taken by the flap edges. This may be due to weaker contact force of the flaps than that of the pads. When any material stuck to the pad and flap, those on the flaps might remain longer before being removed by friction to the borehole wall.

The top part of the logging data was affected by the 17½ inch hole and the 13⅜ inch casing pipe. Before the 10⅝ inch hole was drilled, the 17½ inch hole was drilled to 1263.0 m DSF and the 13⅜ inch casing shoe was installed at 1252.5 m DSF. Therefore, the quality of the logging data is reduced above this depth.

GR, sonic, and VSP were also acquired in the 13⅜ inch casing pipe, and data quality was affected by the size of the borehole (17½ inch) and the situation of the casing cement that fills the gap between the casing pipe and the borehole. GR signals simply weakened because of less gamma ray penetration through the steel casing pipe and the increased distance from the tool to the borehole wall, which decreased the characteristics of the GR pattern. For the sonic measurements performed in the bottom 150 m

part of the cased hole, most of the *S*-wave was not acquired, which may be due to the imperfect contact situation behind the casing pipe. *P*-wave quality was also significantly affected by that situation. VSP signals showed poor quality in the top 100 m interval of the cased hole, most likely due to the "ringing effect" to the shallow 20 inch casing pipe.

Unit descriptions based on wireline logging

Unit boundaries are based on sedimentological observations (shown in MSF), and then the exact depths were determined by log characteristics (shown in WMSF). The depth at the bottom of the hole is in drillers depth (DSF).

Unit I (647~1256.5 m MSF)

GR is the only tool available for the entire interval of this unit, and it shows a log response similar to that of Unit II. GR values are roughly the half of the Unit II GR values, which is likely due to the larger borehole size and effects of the casing pipe (see **"Data quality"**). For the bottom 150 m, Dipole Sonic Imager sonic data are also available, suggesting that this interval may be continuous from Unit II. Based on such limited information, the lithology of Unit I may be similar to that of Unit II.

Unit II (~1825.5 m WMSF)

Log characteristics of Unit II consist of alternation of relatively thick layers of massive sandstones and siltstones. Resistivity borehole images suggest that the sandstones in Unit II are massive and include granules, pebbles, and mollusks (i.e., Bivalvia).

The shallowest interval (~1429.1 m WMSF) of this unit consists of sandstone and siltstone of 60–70 m thickness. Several highly resistive layers (<1 m thickness each) are probably carbonate-cemented layers. Nuclear magnetic resonance (NMR) permeability and SP responses suggest that these sandstones are generally highly permeable (up to 4000 mD).

The middle part (~1617.4 m WMSF) of this unit is a thick (~170 m) sandy sequence, also highly permeable (a few hundreds to 1000 mD), and includes at least three coal layers (see Table **T10**) and frequent cemented resistive layers. This sandy sequence is characterized by a highly resistive zone (1429.1~1437.9 m WMSF) at the top, where a number of highly resistive layers of decimeter thickness each are concentrated. Around the base of this sequence, at least three thick conglomerate layers can be identified at 1592.5~1599.5, 1608.2~1611.2, and 1612.2~1617.4 m WMSF. Relatively low NMR values in these layers (100 mD or less) suggest poor sorting.

The bottom part (~1825.5 m WMSF) of this unit begins as a predominantly silty sequence and gradually changes to sandy layers with depth. Three permeable sandstones of a few meters thickness show 100–2000 mD at their best points. One of these sandstones forms the basal sandstone of this unit.

Unit III (~2055.0 m WMSF)

Unit III is characterized by frequent coal layers in alternation with a sandstone and siltstone sequence of a few meters thickness. Thirteen coal layers of >30 cm thickness were identified in this unit (see Table **T10**) as well as a number of thin coal layers. The sandstone layers are generally permeable (a few hundreds to 1000 mD), based on the NMR, laterolog resistivity, and SP logging data sets. There are also frequent intercalations of highly resistive cemented sandstone layers. As a whole, this unit forms the most colorful interval of this borehole. Resistivity borehole images show that the sandstones of this unit generally consist of a number of thin (centimeter thickness) sandstone layers or include laminae of this scale. Because such features are not commonly observed in the sandstones of Unit II, there may be a change in the sedimentary environment at the Unit II/III boundary.

This unit can be divided into shallow and deep parts at 1916.2 m WMSF, the top horizon of the thickest coal layer in this hole. The shallow part is silty and includes frequent sand layers of a few meters thickness and three coal layers of >30 cm thickness. In the deep part, lithology is more sandy with ten coal layers of >30 cm thickness, including the thickest two horizons (i.e., 7.3 and 3.5 m thick). Based on correlations to VCDs, seven coal layers of the deep part were acquired by coring (see Table **T10** for the Unit III thick coal layers).

Unit IV (~2466 m DSF)

Unit IV consists of thick (~200 m) massive shale in the upper half and alternation of sandstone and shale of a few meters thickness in the lower half, which also includes one thin coal layer (Core 337-C0020A-30R; see Table **T10**). Resistive cemented layers are commonly identified. The sandstone layers are generally not as permeable (100 mD or less) as those above, based on the NMR, laterolog resistivity, and SP logging data sets.

Evaluation of fluid sampling points

Formation fluid sampling points needed to be permeable sandstones. Lithology was identified using the logging data because lithologic characteristics can be distinguished clearly. The first list of 31 candi-

date zones in which sampling points were determined was made based on separation of the five laterolog resistivity measurements that suggested permeable layers. Then borehole resistivity images were used to define the exact depth of the zones. Based on borehole resistivity images, most sandstones consist of fine (centimeter thick) laminated sand layers that are frequently intercalated by electrically resistive layers. The resistive layers possibly have low permeability (e.g., cemented); therefore, those layers were removed from the potential sampling zones. NMR permeability was then examined to identify layers of possible free water. Most zones in the first list show high potential of free water with NMR permeability of 100–400 mD, and the zones were ranked according to the NMR permeability to form a second list. By comparing with VCDs, several zones of clean sandstone layers were replaced (or added as backups) to make the final list of potential fluid sampling points.

Prior to fluid sampling, pretests were conducted in 35 zones based on the final list to measure in situ mobility of the fluid in these zones (see **"Downhole logging"** in the "Methods" chapter [Expedition 337 Scientists, 2013b] for the definition of mobility). Because formation fluid viscosity may not significantly vary, mobility can be used to assess the sandstone permeability. Based on the mobility evaluations, actual formation fluid sampling zones were determined at six points as described in Table **T11.**

Formation pressure

By using the formation testing tool, formation pressure was measured as a part of the fluid sampling pretests. Pressure data at the 35 points indicated that formation pore pressure is hydrostatic or elevated by only a few percent of the hydrostatic value to depths of at least 2425 m WMSF (the depth of the deepest reliable measurement).

Temperature estimation

During logging operations, two types of logging tools (Environmental Measurement Sonde [EMS] and Modular Formation Dynamics Tester [MDT]) measured borehole fluid temperature in situ. The EMS measured the borehole mud temperature in detail, and the MDT recorded the temperature during the pretests and fluid sampling. We also used a method to estimate the bottom-hole static temperature by using the temperature measurements during the first three logging runs. The Horner plot (Dowdle and Cobb, 1975), a method commonly used for computing static formation temperature (Espinosa-Paredes et al., 2009), was applied and the corrected temperature was 63°C, indicating a maximum temperature gradient of 24.0°C/km. The Horner plot result was plotted together with wireline logging temperatures from EMS and the temperature measurements during the pretest (with the single probe) and during the fluid sampling (with Quicksilver probe) with the MDT (Fig. **F11**), and showed that the measured values were all lower than this corrected temperature gradient.

Log-seismic integration

We used the VSP to establish an accurate time-depth relationship. Detailed log-seismic correlation was achieved through the synthetic seismogram calculation and its comparison with the seismic profiles. Synthetic seismograms were calculated using *P*-wave velocity log and density log data (Fig. **F12**). The *P*-wave velocity log data were calibrated with the time-depth relationship derived from VSP data. We used a 30 Hz minimum phase ricker wavelet to generate synthetic seismograms. The seismic section was shifted down 10 ms to align the major reflectors with the synthetic seismograms. The synthetic seismogram matches well with the seismic profile. For example, strong reflections at ~2610–2650 and ~2780–2820 meters below sea level (mbsl) in the synthetic seismogram can be aligned to key reflectors at ~3180–3200 and ~3320–3350 ms two-way traveltime (TWT) on the seismic profile of Line ODSR03-BS, respectively. The synthetic seismogram and the seismic section also generally match at ~3100–3150 mbsl, corresponding to the coal layers. The uppermost part of this depth range in particular shows a good match; however, the reflection pattern in the lower part of this depth range shows some discrepancy between them. In the deeper interval of this borehole, the depths of the synthetic seismogram reflections are not exactly aligned to the seismic profile.

The log data in time domain, converted with the VSP time-depth relationship, can be directly compared with the time-migrated seismic section. Generally, the seismic reflectors are well correlated with the logging data. Figure **F13** shows the gamma ray and resistivity logs in time domain laid on the seismic profile. The reflectors at ~3180, ~3320, and ~3580 ms TWT are correlated with the positive peaks in the resistivity log. The reflector at ~3440 ms TWT coincides with a slight positive shift in GR value. We correlated the lithologic units with the seismic profile (Fig. **F14**). The Unit I/II boundary can be correlated to a relatively strong, continuous reflector at ~3000 ms TWT on the seismic profile; however, the regional unit boundary was supposed to be an unconformity at ~2800 ms TWT. Unit II has two strong reflectors at ~3180 and ~3320 ms TWT, which are

traceable in the regional scale. The top of Unit III might be correlated with a weak reflector at ~3490 ms TWT, but the major reflectors are located within Unit III. The bottom of Unit III is situated slightly below a series of relatively strong reflectors. Unit IV has several reflections; however, the lateral continuity of these reflectors is not well preserved in the regional range.

Physical properties

At Site C0020, a series of physical properties measurements (moisture, density, *P*-wave velocity, electric resistivity, thermal conductivity, anelastic strain recovery [ASR], and vitrinite reflectance) were carried out using core samples and cuttings in the laboratory. All physical properties were measured at room temperature and atmospheric pressure conditions. Depth and lithologic variation effects on the physical properties were investigated. Physical properties of cuttings samples were also compared with those of core samples and with data from sequential core measurements in the multisensor core logger (MSCL).

Whole-round multisensor core logger

Whole-round multisensor core logger (MSCL-W) measurements were carried out on all sections from Units II–IV at Site C0020, with the exception of samples taken for interstitial water analysis. A sensor track of the split core multisensor core logger (MSCL-S) was used for Core 337-C0020A-8L of 10.8 cm industry-type LDC. It should be noted that data from whole-round cores (RCB) and from split cores (LDC) with differing diameters may not be directly comparable.

Results

The gamma ray attenuation (GRA) density values on the MSCL-W are mainly 1.8–2.23 g/cm^3 above 1300 m CSF-B (Fig. **F15**). The main trend is that density decreases to 1.4–1.9 g/cm^3 at ~1600 m CSF-B and increases again to 1.5–2.3 g/cm^3 at ~1800 m CSF-B. In the interval from Cores 337-C0020A-15R through 25R (1921–2002 m CSF-B), density varies between 1.7 and 2.5 g/cm^3. This may be due to variable lithology in this interval. Density of the coal portions in Cores 15R and 19R is 1.5–2.0 g/cm^3 and 1.2–1.5 g/cm^3, respectively, which is lower than in intervals represented by other lithologies, where typical values range from 1.7 to 2.3 g/cm^3 with the exception of some minor deviations. After tight density measurements ranging between 1.7 and 2.1 g/cm^3 in mudstone-dominated intervals of Cores 26R and 27R (2111–2204 m CSF-B), density values range from 1.2 to 2.3 g/cm^3 to the lowermost part of the hole.

Peak magnetic susceptibility is generally 70 × 10^{-5} to 100 × 10^{-5} SI. There are some decreases, such as one drop to 11 × 10^{-5} SI in Cores 9R and 10R at ~1630 m CSF-B and another drop to 12 × 10^{-5} SI in Core 27R at ~2200 m CSF-B. Coal-bearing sediments had a low magnetic susceptibility of <11 × 10^{-5} SI, which is lower than other sediment types.

Natural gamma radiation (NGR) in Unit II generally ranges from 20 to 40 counts per second (cps) and abruptly rises in Unit III, where NGR mainly ranges from 30 to 65 cps. Coal samples range between 6 and 47 cps. In Unit IV, NGR gradually increases from 30–45 cps in Core 28R at ~2300 m CSF-B to 40–62 cps in Core 32R at ~2460 m CSF-B.

Electrical resistivity in Unit II increases with depth from 0.4 to 2.0 Ωm, although Core 8L deviates from the RCB core trend. The resistivity of coal and other sediments is similar in the coaly interval of Core 15R, although coal shows higher resistivity than other sediments in Core 19R. Lower resistivity was observed in Cores 23R and 24R. A slight increase in resistivity was observed below Core 27R.

P-wave velocity was scattered from 1 to 2 km/s in whole-round core (WRC) sections, and lithologic and depth dependence on *P*-wave velocity is not clear. Deviation is small in Core 26R.

Data quality and error

Even though the data were scattered, distributions of GRA density, magnetic susceptibility, and NGR show certain trends. These trends depend on the lithology, mineral contents, degree of consolidation, and pore structures. However, data were also influenced by artificial disturbance during core processing.

Injection of drilling mud and fluid into cores and fracturing by drilling creates additional pore space, and it mainly reduces GRA density and resistivity. We rapidly took measurements with the MSCL-W and the MSCL-S without concern for thermal equilibrium to room temperature. Most of the temperatures measured at the top of each section, which were measured just before the MSCL measurements, were close to room temperature (the greatest observed difference was ~2 K). Therefore, the error caused by the temperature treatment is probably small, even though temperature dependence is high for electrical resistivity. Large deviation in *P*-wave velocity in a core, and with no distinct difference with depth, might be due to poor contact of the *P*-wave sensor with the core liner because the core was wrapped in an ESCAL bag. Expansion of the ESCAL

bag potentially caused by the release of gas from cores also induced poor contact. Different contact conditions between the core and core liner caused by the difference in the actual core diameter that was observed in the X-ray CT images might also lead to a loss in quality for velocity data. Varying quantities of drilling fluid seeping out and filling the core liner as well as varying core diameters are other potential causes of noise in the *P*-wave data.

Magnetic susceptibility, NGR, and electrical resistivity of LDC (Core 337-C0020A-8L) measured by the MSCL-S doesn't match with those of RCB measured by the MSCL-W. The difference of the NGR values between the two procedures can be caused mainly by the difference in core diameter. However, the causes of discrepancy between the other measurements, GRA, magnetic susceptibility, electrical resistivity and *P*-wave velocity, are not clear. The sensitivity of the sensors and different core disturbances mediated by mud/core treatment (larger core is probably associated with less disturbance) may be the cause.

Moisture and density measurements

Moisture and density (MAD) were analyzed on every discrete sample from all recovered cores from Units II–IV. The four categorized cuttings samples (i.e., >>4, >4, 1–4, and <1.0 mm) from Units I–IV were also subjected to MAD analyses. The lithology of discrete samples for MAD analysis was also categorized in four types (sand/sandstone, silt/siltstone/shale, coal, and carbonate-cemented sandstone and siltstone). In discrete core samples, cementation was verified by stereomicroscopic observation and the addition of hydrochloric acid. No lithologic categorization of cuttings samples was made because cuttings are a mixture of various rocks.

Results

Porosity profiles categorized by core/cuttings size are shown in Figure **F16A.** Cuttings samples have generally higher porosity than core samples. Among the four categories of the sieved cuttings, larger size fractions show generally lower porosity. Despite such variations in cuttings size fraction, porosity in each category shows a gradual decrease with depth.

Figure **F16B** shows porosity profiles categorized by lithology. For discrete core sample porosity, sandstone in Unit II mainly ranges 30%–50%, whereas siltstone plots mainly within 34%–42%. In Unit III, siltstone porosity shows a drop to 20%–30%. Sandstone shows a similar minimum porosity of ~2% but ranges up to a maximum of almost 50%. Coal porosity (gray inverted triangle in figure) ranges 24%–38%. Carbonate-cemented sandstone and siltstone show very low porosities of 2%–14%.

In Unit IV, sandstone and siltstone porosities generally range 26%–32% and decrease slightly to 23%–27% in Core 337-C0020A-32R. Carbonate-cemented sandstone is less porous than other lithologies in Unit IV, with values of 14%–17%. A porosity shift in siltstone was observed at the Unit III/IV boundary.

Figure **F17A** shows bulk density profiles of core samples and cuttings. In general, cuttings samples show lower bulk density than core samples. Among the four categories, the larger size fraction shows the highest bulk density. Core samples in Unit II range mainly between 1.9 and 2.3 g/cm^3 with some deviations. In Unit III, core sample bulk density is scattered widely from 1.2 to 2.7 g/cm^3, whereas values in Unit IV are clustered tightly between 2.1 and 2.3 g/cm^3. In the bulk density scatter plots in Unit III, some outliers with high values of 2.5–2.7 g/cm^3 were identified as carbonate-cemented sandstone and siltstone (Fig. **F17B**). On the other hand, coal samples have low density values around 1.2–1.4 g/cm^3. In Unit IV, sandstone and siltstone density narrowly range between 2.2 and 2.3 g/cm^3. Carbonate-cemented sandstone and siltstone have generally higher bulk densities than other lithologies, with values between 2.4 and 2.6 g/cm^3. The relationship of porosity to depth for siltstone decreases in Unit IV (Fig. **F16B**), where only a very slight increase in bulk density is recorded (Fig. **F17B**).

Grain density of core and cuttings samples gradually increases with depth from ~2.5 g/cm^3 at 700 meters below seafloor (mbsf) to ~2.7 g/cm^3 at 2400 mbsf (Fig. **F18A**). Differences in grain density among core samples and sieved cuttings samples are not obvious, although cuttings samples seem to have slightly lower values than core samples and smaller cuttings have more variable grain density values. Grain density values in Unit III cover a particularly wide range (1.3–2.7 g/cm^3). Among different lithologic rock types, coal has a very low grain density of 1.3–1.6 g/cm^3 (Fig. **F18B**).

Discussion

Cuttings samples show higher porosity, lower bulk density, and lower grain density than core samples. These differences are considered to be caused by excess moisture on cuttings surfaces because the ratio of surface area to bulk volume increases with decrease in the fraction. Additional fractures and damage might be formed in cuttings samples during the transfer from depth to the surface, and the damage produces extra pores and increases porosity. Lower

grain density in cuttings samples is also influenced by the deposition of NaCl (solid density = 2.14 g/cm^3) on the surface by drying. The smaller size fraction likely contains excess water that may affect wet mass; therefore, the larger size fraction produces more reliable MAD data. During the treatment of discrete cores, multiple fracturing likely develops parallel to the bedding. This might cause overestimation of porosity and underestimation of bulk and grain density.

Assuming that discrete samples from cores produce more reliable MAD data, we infer that porosity gradually decreases from 60% to 25% with depth. However, carbonate-cemented sediments strongly deviate from the consolidation curve. Cement minerals possibly have a higher density than major minerals (e.g., quartz and feldspar) in the same samples because grain density in several cores is higher than in noncemented sections. These low-porosity cemented rocks are located in units with coal layers. Porosity and bulk density shifts were observed in siltstone at the Unit III/IV boundary. The apparent shift may be caused by undercompaction of sediment because of the generation and maintenance of high pore pressure in Unit IV. Several mechanisms are involved in high pore pressurization in sedimentary basins (Osborne and Swarbrick, 1997), and one of the plausible processes is that the effective sealing of low-porosity layers developed in Unit III prevented fluid flow from depth.

Thermal conductivity

Results

Thermal conductivity was determined on samples from recovered cores in Units II–IV. For the measurements, full-space configuration using a needle probe (standard VLQ probe) was applied to semiconsolidated sediments at two points in the whole cores (337-C0020A-1R and 2R). For other cores, a half-space line source probe (mini-HLQ probe) was applied.

The collected thermal conductivity data gradually increase with greater depth from a range of 1.0–1.8 to 1.5–2.1 W/(m·K) except for Unit III, which shows a wider variation of 0.4–3.5 W/(m·K) (Fig. **F19**). Carbonate-cemented sandstone and siltstone, which were identified by stereomicroscopic observation and hydrochloric acid reaction, have higher values than others (red triangles in figure). The highest thermal conductivity value was 3.473 W/(m·K) in highly carbonate-cemented, hard sandstone in Sample 337-C0020A-22R-2, 77 cm. Thermal conductivity in coal shows lower values in the range of 0.4–1.4 W/(m·K) (solid inverse triangles in figure).

Discussion

The major trend in thermal conductivity is obtained from sandstone and siltstone data, and the increasing thermal conductivity may indicate increasing compaction with depth. The scattered thermal conductivity values in Unit III are caused by more diverse lithologies, which include coal and carbonate-cemented sandstone in addition to sandstone and siltstone. Very low thermal conductivity values observed in coal are lower than that of saline water at room temperature (0.62 W/[m·K] at T = 22°C) (Beardsmore and Cull, 2001). The increase in thermal conductivity with depth is mainly caused by the reduction of porosity in sedimentary rocks because thermal conductivity of porous media is described as the average for pore fluid and lithic material thermal conductivity. High thermal conductivity of carbonate-cemented rock is explained by carbonate materials of high thermal conductivity (>4 W/[m·K]) and less fluid of low thermal conductivity. The sandstone is mostly composed of quartz particles, which have generally higher thermal conductivity (>7 W/[m·K]) than other major rock-forming minerals (Beardsmore and Cull, 2001); therefore, the thermal conductivity variation of sandstone as well as the low thermal conductivity of coal is affected by the quartz contents.

P-wave velocity

The *P*-wave velocity measured in Unit I cuttings, which were measured after preparing the large fraction cuttings cubic samples, ranged from 1.67 to 1.90 km/s (Fig. **F20**). Velocity in this unit averaged 1.81 km/s and decreased with depth. In Unit II, discrete core sample velocity ranged from 1.51 to >3.00 km/s for sandstone and siltstone. A very high velocity of 5.6 km/s was observed in carbonate-cemented sandstone at 1753 m CSF-B. Siltstone velocity was on average higher than in sandstone and cuttings. Siltstone velocity decreased with depth. Coal from Unit III shows velocity values of ~2.2 km/s. Velocities of sandstone and shale range from 1.6 to 1.8 km/s, although several shale samples show velocity values similar to those of coal. Carbonate-cemented sedimentary rocks show high velocity (4.4–5.6 km/s). Velocity of sandstone and siltstone in Unit IV is scattered. Sandstone velocity ranges from 1.51 to 2.12 km/s, and siltstone velocity ranges from 1.57 to 2.38 km/s. On average, sandstone and siltstone velocities in Unit IV are relatively higher than in Unit III. Car-

bonate-cemented sandstone velocity ranges from 2.5 to 4 km/s, which is lower than in Unit III.

Electrical impedance

A frequency of 25 kHz was selected for the impedance measurements to minimize the imaginary part of the impedance, resulting in a phase angle of <3°. Resistivity of the paper filter on both the top and bottom sides of specimens is <1 Ωm, which has a smaller effect on the resistivity data. Electrical resistivity of cuttings ranges from 0.40 to 0.86 Ωm (Fig. F21A). On average, resistivity has values of ~0.64 Ωm and increases with depth. In Unit II, the resistivities of both sandstone and siltstone increase with depth in a similar trend. In Unit III, resistivity increased in the order of sandstone, siltstone, coal, and carbonate-cemented rocks. Several sandstones show lower resistivity than in Unit II, although several silt and shale samples have higher resistivity than in Unit II. Coal resistivity ranges from 9.5 to 30 Ωm, and carbonate-cemented rocks have values of ~60 Ωm, with the highest values reaching nearly 100 Ωm (i.e., more than two orders of magnitude larger than sandstone). Unit IV resistivity slightly increases with depth, and the resistivity at 2465 m CSF-B is ~3.3 Ωm in shale. Carbonate-cemented rock resistivity is higher than that of noncemented rocks, although the resistivity is one order of magnitude lower than that observed in Unit IV.

The relationship between formation factor and depth (Fig. F21B), estimated from the resistivity data, shows a similar trend with electrical resistivity. This is because the pore water temperature in cubic samples ranged only slightly from 23° to 25°C among samples. The resistivity shift between Units III and IV was observed to a small degree for siltstone, with a trend resembling the porosity shift (Fig. F16B).

MSCL versus core sample

Generally speaking, data from the MSCL show lower values than those data from discrete samples. GRA density by MSCL is lower than the bulk density measured with pycnometer for discrete samples (see Figs. F15, F17B for bulk density, Fig. F20 for *P*-wave velocity, and Fig. F21 for resistivity). The consistently lower values from the MSCL, despite the differences in measurement principles from discrete sample analysis, resulted from incomplete filling of core samples in core liner. The void space within core liner, and the smaller volume of sample material than assumed in the theory, would result in the smaller values in the measurement results. In particular, poor contacts of the core material with the core liner hampers accurate measurement of *P*-wave velocity. A secondary cause might be fractures and drilling-induced disturbances (filled with drilling mud) in the WRC material used for MSCL measurement, as discrete samples were selectively collected from intact parts of working halves.

On the other hand, general variations with depth matched with each other between MSCL and discrete sample analysis. We therefore use MSCL data only for physical properties interpretation on a broader scale.

Vitrinite reflectance analysis

Vitrinite reflectance (R_o) was measured in five samples from coal formations (in Sections 337-C0020A-15R-3, 19R-7, and 30R-2), small coal fragments from cuttings (Sample 337-C0020A-97-SMW), and a sandstone layer (Section 2R-2). Figure F22A shows the R_o variation with depth. R_o at 1211 m CSF-B had the lowest value of 0.24%, and the highest value of 0.35% was observed at a coal formation (Section 15R-3). The deepest coal in Hole C0020A was 0.29%. The depth trend for R_o is not clear.

R_o values are very low through the horizon, suggesting coal maturity is quite low at this site. The range of coal porosity in Hole C0020A is in good agreement with R_o values (Rodrigues and Lemos de Sousa, 2002). Low-grade maturation makes it difficult to measure the reflectance properly because the color of low-maturity vitrinite (in such case, huminite) is very heterogeneous and depends on the origin of the huminite. In addition, observable spots (1.6 µm) for R_o analysis are limited, and approximately half of the area measured for R_o almost approached the limitation of field of view. For this reason, R_o values in some samples are inaccurate (see the R_o histogram in Fig. F22B). Microstructures in coal fragments become more uniform with depth, which results in easier identification of vitrinite. Therefore, R_o values are more accurate for the deeper horizon. In low-maturity coal, it is necessary to separate pure vitrinite tips from other minerals for accurate vitrinite measurement. Collecting smaller fractions is one of the ways to address these problems, as we treated the fraction >150 µm for R_o measurement.

Anelastic strain recovery analysis

Diameter measurement results show that the average RCB core diameter ranged from 57.3 to 58.4 mm. In most of the samples, periodicity of the diameter was observed during core rotation at a constant rotation speed, and maximum (d_{max}) and minimum (d_{min}) diameter were identified (Fig. F23A). Deviation of the diameter between d_{max} and d_{min} normalized by d_{min} is

shown in Figure F23B. $S_{Hmax} - S_{Hmin}$ increased with depth. Even though the Young's modulus of each sample is not investigated, the trend does not change because the Young's modulus of sedimentary rocks can increase with depth via sediment consolidation. Therefore, the core diameter measurement results imply that tectonic horizontal stress is more effective at depth in Hole C0020A.

Inorganic geochemistry

Drilling mud

Drilling mud contamination presents a potential challenge when collecting, processing, and interpreting the composition of interstitial water from sediment cores obtained through riser drilling (Wenger et al., 2004). In order to address this problem, we first review the aspects of the drilling mud composition that provide a context for discussing variations in the interstitial water composition at depth. Throughout drilling of Hole C0020A, the formulation of the drilling mud was adjusted in response to changes in drilling procedures and hole conditions that occurred with depth. In order to provide a working depth reference of the drilling mud for comparison with the interstitial water of the sediment cores, we present the compositional changes in mud samples obtained from the active circulation tank in the context of the lithologic boundaries that were being drilled at the time of their collection. These units (see "Lithostratigraphy") are as follows: Unit I (647–1256.5 m MSF), Unit II (1256.5–1826.5 m MSF), Unit III (1826.5–2046.5 m MSF), and Unit IV (2046.5–2466.0 m MSF).

A total of eight drilling mud samples were sampled from the mud tank (LMT samples) in order to assess potential contamination during the course of drilling (Table T12). The first mud sample (337-C0020A-2-LMT) was collected 11 days before the commencement of drilling. Shortly after the initiation of the drilling in Unit I, a second sample was taken from the mud tank (Sample 23-LMT). Two mud water fluid samples were collected from core liner (LMW samples) for analysis from Unit II (Samples 337-C0020A-120-LMW and 189-LMW), one from Unit III (Sample 257-LMW), and two from Unit IV (Samples 280-LMW and 373-LMW). A final mud sample (392-LMT) was taken from the active mud tank immediately after termination of drilling operations and may be considered representative of the mud used in the final wiper trip of the borehole before logging and formation water sampling. The water was separated from the mud (see "Inorganic geochemistry" in the "Methods" chapter [Expedition 337 Scientists, 2013b]) and analyzed. A list of miscellaneous materials collected for analysis is found in MISC_MATERIAL_SAMPLE_LIST.XLS in GEOCHEM in "Supplementary material."

The shipboard pmH of the mud fluid was not recorded, as the samples had to be diluted 1:10 to carry out the mud water separation. The mud logger's report, however, indicates that during the course of drilling, the mud mix pmH values ranged from 9.3 to 11.9. The mud logs also reveal a number of significant modifications to the drilling mud that account for the recorded changes in mud water chemistry. Initially, and throughout the course of drilling in Unit I, KCl was combined with the mud, giving a mud density of 1.04–1.08 g/mL. During drilling in Unit II, NaCl was added to the mud along with NaOH, maintaining the mud density at 1.08 g/mL. In Unit III, ASTEX-S sulfonated asphalt sodium salt (SAS) was added to enhance hole stability as well as to enhance the lubrication characteristics of the drilling mud. The NaCl + KCl + SAS + NaOH mixture was continued throughout Units III and IV, and mud density was maintained at 1.10 g/mL until reaching the final depth of 2466 mbsf. Filtered mud water changed from colorless in Units I and II to a dark amber color in Units III and IV. Significant changes were made to the mud formulation when drilling through Unit III, and the change in coloration may be the result of the addition of ASTEX-S SAS to the mud or it could be the result of colloidal-sized particles that were released from the sediment during riser drilling of the coal-bearing intervals located in the lowermost portions of Unit II, as well as Units III and IV.

Total alkalinity of the mud water increased from 39.7 to 49.9 mM across Units I and II. Alkalinity then increased abruptly to 77.7 mM in Unit III, followed by a slight drop to 70.03 mM at the bottom of Unit IV. The abrupt change between Units II and III was a result of a change in the drilling mud formulation that involved the addition of NaOH. Chloride concentrations in the mud ranged from 970 to 1131 mM across Units I and II and then abruptly increased to 1548 mM in Unit III. Chloride values decreased somewhat in Unit IV, ranging from 1367 to 1394 mM, which is still roughly twice that of average seawater (559 mM). Potassium concentrations in the drilling mud were also significantly greater than seawater (10.5 mM) because of the initial addition of KCl to the drilling mud (Fig. F24A). A rough mass balance of the ions analyzed in the initial mud (Sample 2-LMT) shows that roughly ~600 mmol/L of KCl was added to seawater to bring the mud up to the

measured chloride values, and then an additional ~200 mmol/L of potassium as KOH was used to adjust the pmH. Potassium concentrations throughout the course of drilling ranged from 756 to 662 mM, with somewhat lower values in Unit IV, where the mud was reformulated to contain NaCl and NaOH in addition to KCl and KOH.

The sulfate concentration of Sample 2-LMT (27.95 mM) prior to drilling was similar to that of seawater (28.9 mM) (Fig. F24B). The sulfate content of mud water was adjusted to lower values during drilling in Units I and II (20.5–25.7 mM); however, a sharp increase in Unit III (56.0 mM) was followed by elevated values in the mud used throughout drilling in Unit IV (9.4–51.0 mM). These elevated values were a consequence of the addition of ASTEX-S SAS to the drilling fluid, which includes Na_2SO_4 as a major component. Sodium concentrations also paralleled those of chloride and sulfate, with sodium generally close to or exceeding seawater (480 mM). Sodium concentrations of the mud used in Units I and II ranged from 457 to 624 mM, increased to 1147 mM in Unit III, and decreased slightly to 1014 to 1020 mM in Unit IV. Salinity measurements showed similar trends ranging from 98‰ to 103‰ in Units I and II, increasing to 139‰ in Unit III, and decreasing again with values between 126‰ and 127‰ across Unit IV (Fig. F24C).

Because bromide was not included in the mud water additives, concentrations remained similar to those of the seawater (0.85 mM) that was mixed with the drilling mud. The measured bromide concentrations ranged from 0.68 to 0.94 mM across Units I–IV. A number of ions potentially present in deep interstitial water were notably below instrumental detection limits in the drilling mud samples, including NH_4^+, NO_3^-, and ΣPO_4^{3-}. Magnesium and calcium concentrations are consistently less than seawater values (54.0 and 10.6 mM, respectively). Prior to drilling, the recorded Mg^{2+} concentration was 28.2 mM and gradually decreased with depth to 2.23 mM at the bottom of Unit IV. Likewise, Ca^{2+} started at 5.96 mM before drilling and decreased to 4.05 mM at the bottom of Unit IV.

Dissolved silica increased significantly during drilling. The total dissolved silica content of the mud started at 0.12 mM and increased to only 0.23 mM in Unit I. However, concentrations increased to between 2.31 and 2.15 mM in Unit II, 4.42 mM in Unit III, and 5.28–7.20 mM in Unit IV. The increase may have occurred because of the addition of ASTEX-S SAS, which contains crystalline silica. It was also probably caused, in part, by the increased solubility of silica at high pH (Eikenberg, 1990; Southwick, 1985). Dissolved barium should be negligible in the mud because of the presence of sulfate from seawater (e.g., Torres et al., 1996) and from the added ASTEX-S SAS. Nonetheless, barium is found in the drilling mud samples in concentrations ranging from 5.1 to 42.6 µM across Units I–IV. The initial mud concentrations are the lowest, and most concentrations are between 9 and 15 µM.

Cuttings

Coring was not performed during drilling of Unit I; however, drilling cuttings were collected from the shale shaker, which separates sediments before returning the mud to the circulation tanks. Shipboard analyses of cuttings water samples continued through Unit II (Table T13) in order to provide a comparison between the cuttings water and interstitial water from sediment cores. A total of eight cuttings samples were processed and analyzed: three from Unit I (Samples 337-C0020A-56-SMW, 66-SMW, and 81-SMW) and five from Unit II (114-SMW, 128-SMW, 187-SMW, 197-SMW, and 213-SMW). The first sample (56-SMW) was done in replicate, and sediment fragments in the first portion were cleaned prior to further processing by manually wiping the adhering drilling fluid from individual cuttings pieces with KimWipes, whereas the other portion was processed in bulk without cleaning off drilling fluid. The second sample (66-SMW) was manually cleaned in a similar fashion, whereas all other samples were done in bulk because of the difficulty associated with cleaning small cuttings fragments. Within Unit II, the fluid from one sample (197-SMW) was collected using a Rhizon sampler (Seeberg-Elverfeldt et al., 2005) in order to determine whether there would be a significant difference between this procedure and that of the squeezed samples (see Fig. F24).

The results from the cuttings water bore many similarities to the drilling water, including elevated amounts of potassium ranging from 621 to 781 mM (Fig. F24A), high sulfate concentrations of 18.6–23.8 mM (Fig. F24B), increased salinity values of 70‰–103‰ (Fig. F24C), and high chloride concentrations of 1129–1515 mM, that are all indicative of drilling fluid contamination. Nonetheless, some significant differences were found between the water squeezed from the cuttings and that of the drilling mud water. In Unit I, ammonium and phosphate were present in the cuttings water but were below detection in the drilling mud fluid. Ammonium ranged from 11.0 to 3.7 mM in Unit I and decreased with depth, with concentrations generally <1 mM throughout Unit II. Phosphate ranged from 13.5 to 3.6 µM in Unit I and is mostly below detection in Unit II. The elevated ammonium concentrations were unusual and were

even greater than those observed in the interstitial water samples of the WRCs.

Calcium and magnesium concentrations decreased with depth in a fashion similar to the drilling mud. Magnesium concentrations (33.5–10.6 mM) are greater than those of the drilling mud, with the exception of one sample at the top of Unit II (0.15 mM). Calcium concentrations (2.44–0.76 mM) were lower than the drilling mud associated with Units I and II, with the exception at the top of Unit II (62.06 mM). As with the mud water samples, cuttings water samples presented significant amounts of dissolved barium (4.3–12.6 µM).

The differences between squeezing the deepest cuttings water samples (337-C0020A-187-SMW, 197-SMW, and 213-SMW) and those collected using a Rhizon sampler (197-SMW) were minimal. In this case, the Rhizon sampler was used with wet cuttings and no attempt was made to remove drilling mud from the cuttings before sampling, such that the fluid that was collected was in contact with the outside of the cuttings. The results with the Rhizon sampler for salinity, alkalinity, sodium, and potassium were bracketed by the values from the two adjacent squeezed cuttings, whereas results for chloride, bromide, and sulfate are similar to the values of one of the adjacent squeezed samples. These results suggest that the predominant source of water extracted by squeezing of the cuttings is actually the fluid on the exterior surfaces of the cuttings and not the fluid within. Dissolved ions of the alkaline earth elements Mg^{2+} (15.1 mM), Ca^{2+} (4.3 mM), Ba^{2+} (11.7 µM), and Sr^{2+} (54.2 µM) were all significantly greater than the adjacent squeezed counterparts. Although the cause is not clear, it may be that the samples taken with the Rhizon sampler were less prone to precipitation loss of carbonates and sulfates in the brief time that it took to extract the water.

Overall, the cuttings data provide limited information regarding the in situ interstitial water composition of Site C0020 because of the high degree of contamination from drilling fluid. They do, however, provide an end-member for any interactions that might occur between the drilling mud and extremely contaminated sediment. Enrichments in ammonium observed in the cuttings water samples of Unit I were greater than those observed in the interstitial water samples. The enrichment of ammonium is likely due to desorption of exchangeable ammonium caused by contact with the drilling mud, which is highly enriched in KCl (see above); a common analytical method to determine exchangeable ammonium in soils is to leach them with 1–2 M KCl solution such that K^+ saturates all of the NH_4^+ adsorption sites (Kowalenko and Yu, 1996).

Whole-round cores

A total of 48 whole-round samples were collected from 32 cores for interstitial water analyses in Hole C0020A, and the whole-round lengths ranged from 15 to 76 cm. Because of low porosity and permeability (see **"Physical properties"**), only 24 of the processed WRC samples yielded interstitial fluid through squeezing, with low volumes between 33.5 and 0.2 mL despite large subsamples (up to 70 cm per WRC for selected segments). Of the 24 cores that yielded interstitial water, 15 were from sediment in Unit II, 7 from Unit III, and 2 from Unit IV.

The interstitial water yield is shown in Figure **F25,** expressed as a volume of the fluid extracted per volume of sediment squeezed. The sediment volume was calculated based on the length of the whole-round section and the diameter of the section after peeling. The greatest yields (>30 mL/dm^3) were in poorly consolidated sandstone, including highly contaminated samples from the top of Unit II. Silty sandstone located in Units II and III had variable yields (0–32 mL/dm^3). In Units II and III, yields from siltstone were 0–12 mL/dm^3. No interstitial water was gained from coal and shale samples regardless of the location. In Unit IV, very little fluid (0.2–1 mL/dm^3) if any was extracted, regardless of lithology.

When cleaning off the cores for interstitial water squeezing, it was observed that after scraping off the potentially contaminated drilling mud fluid many of the clay-rich samples initially appeared dry underneath and then became wet again after a few seconds. This might have been due to capillary action or was possibly caused by gas separation from the fluids that pushed the interstitial water from the center toward the outside of the cores.

Salinity, total alkalinity, and pH

Downhole salinity information was derived based on the refractive index data collected for the 24 analyzed whole-round samples (Fig. **F26A;** Table **T14**). A large range in salinity values from 27‰ to 77‰ is observed throughout the sequence in Hole C0020A. The most saline fluids (68‰–77‰) were situated at the top of Unit II, where pore water was highly contaminated with saline drilling mud and should not be taken into consideration when describing downhole trends in pore water chemistry. Neglecting these highly contaminated samples, the salinity remained at ~40‰ in Units II and III and decreased at the bottom of Unit III, reaching 27‰ in Unit IV. Salinity values of ~40‰ were probably still significantly impacted by contamination. Nevertheless, the decreasing trend with depth is consistent with a gradual change in the paleosedimentary environ-

ment and may reflect the influence of a low-salinity end-member, suggesting an estuarine environment (see **"Lithostratigraphy"** and **"Paleontology"**). Alternatively, the presence of a deeper pure water source (e.g., clay dewatering, etc.) may have resulted in fluid migration, characterized by a lower salinity, in the overlying sediment column.

Interstitial water samples from 335 mbsf analyzed during the *Chikyu* shakedown cruise (Expedition CK06-06) revealed a maximum alkalinity of 127 mM at 299.6 mbsf, followed by a decrease in alkalinity to 77 mM at 360.8 mbsf (Tomaru et al., 2009; Higuchi et al., 2009). Excluding the highly contaminated samples from the upper part of Unit II (Fig. **F26B;** Table **T14**), the highest alkalinity was 14.2 mM found in Unit III. This indicates that pore water alkalinity decreases significantly with depth and most likely indicates that active contributions of dissolved inorganic carbon to the alkalinity through processes such as anaerobic oxidation of methane (AOM) (e.g., Borowski et al., 2000) are much less significant in Units II–IV than in the shallower sediments investigated in the shakedown cruise.

Given that the yields of interstitial water in the deeper analyzed parts of Hole C0020A were limited and leaving heavily contaminated samples out of consideration, only a few valid pmH measurements were carried out. At the top of Unit II, pmH values of 8.3–8.6 were found, followed by a pmH of 9.1 at the bottom of this unit. In Unit III, pmH values range between 7.5 and 8.2 (Fig. **F26C;** Table **T14**).

Chloride, bromide, and sulfate

Excluding the contaminated samples at the top of Unit II, chloride concentrations of interstitial water in Hole C0020A showed relatively little change with depth, with average values ~600 mM (Fig. **F27A;** Table **T14**). Positive deviations (as high as 715 mM) were likely a result of drilling mud contamination. In general, chloride concentrations were higher than those observed during the *Chikyu* shakedown cruise, which decreased very gradually in a linear fashion from 542 mM at 1.4 mbsf to 525 mM at 363.1 mbsf (Tomaru et al., 2009; Higuchi et al., 2009). The lowest values for Hole C0020A were 488 and 459 mM from Units III and IV, respectively. Whether these two values represent local freshening associated with the coalbeds or are part of the gradual decreasing trend, presumably due to clay alteration at depth (e.g., Tomaru et al., 2009), is uncertain.

Bromide exhibits a similar pattern, with concentrations fluctuating at ~800 µM throughout the analyzed sequence (Fig. **F27B;** Table **T14**). This value roughly coincides with the shallow pore fluid from the *Chikyu* shakedown cruise, which yielded a Br concentration of 824 µM at 1.4 mbsf, yet is significantly lower than Br^- concentrations that are in the deeper subsurface sediment (150–363 mbsf), which are generally 1000–1200 µM (Tomaru et al., 2009). As for the case of chloride, a decrease in bromide concentrations is observed at the bottom of Unit IV at 459 µM.

The dissolved sulfate concentrations across the analyzed sequence illustrate the extent of drilling mud water incorporation into the sediment cores (Fig. **F27C;** Table **T14**). In the case of highly contaminated samples, sulfate concentrations in the interstitial water samples were as high as 9.9 to 20.2 mM at the top of Unit II. Below these uppermost samples in Unit II, sulfate concentrations at range from 0.97 to 2.31 mM. This is somewhat greater than the majority of samples collected during the *Chikyu* shakedown cruise in 2006 from below the sulfate–methane transition, which exhibited sulfate concentrations either below detection or between 0.1 and 0.3 mM, with the exception of sampled sandy intervals that showed contamination by modern seawater and sulfate as high as 11 mM (Tomaru et al., 2009). The increase in sulfate in Units III and IV to values of 1.1 to l1.35 mM corresponds to an increase in sulfate in the drilling mud.

Phosphate and ammonium

The recorded phosphate and ammonium concentrations of the interstitial water samples can be assumed to represent values for in situ interstitial water concentrations diluted somewhat by drilling mud because there are only two exceptions where drilling mud has detectable amounts of these two species. Phosphate was not detectable throughout the major part of the sequence, with the exception of two interstitial water samples in the uppermost part of Unit II (Table **T14**). These samples were characterized by phosphate concentrations of 3.3–5.4 µM, which are close to the detection limit of ~2.7 µM.

Ammonium was detectable throughout Hole C0020A (Fig. **F28A;** Table **T14**). Ammonium concentrations were 3.3–7.8 mM in the upper, most contaminated samples of Unit II and decreased somewhat to between 2.0 and 2.89 mM in the lower part of the unit and 1.3–3.2 mM in Unit III. The data possibly suggest a downhole decrease in interstitial ammonium concentrations; however, there is no certainty regarding the actual source. The measured concentrations might represent (1) a diluted signal after incorporation of drilling mud water into the interstitial water sample, (2) natural variation in the interstitial water composition, or (3) variable desorption from clay minerals and organic matter exposed to the highly alkaline drilling mud.

Interstitial water samples were also analyzed for nitrate using ion chromatography. Reoccurring values of around a few hundred micromolar (maximum = 440 µM) were found in roughly half of the pore water samples; however, all of the values were below or close to the method's detection limit (350 µM). Accordingly, the nitrate results are considered to be unreliable and, therefore, these data were not included in the results table.

Alkali metals and alkaline earth elements

Sodium concentrations generally paralleled those of chloride, with relatively little change throughout the column (Fig. **F28B;** Table **T14**). The majority of the samples fell in the range of 515–620 mM. Several high values in Units III and IV (630 to 667 mM) correspond to high chloride values and probably are influenced by the addition of NaCl to the drilling mud over this interval. Low values of 466 and 413 mM in Units III and IV correspond to the lowest chloride values, which, as discussed, may represent either freshening through clay dewatering or the influence of an estuarine depositional environment.

Potassium was one of the major components of the drilling mud because of the addition of KCl and KOH. The admixture of even minor amounts of mud water with interstitial water has a serious impact on the overall K^+ concentrations (Fig. **F28C;** Table **T14**). For example, a 5% mixture of mud water (Ca^{2+} = 5.95 mM, K^+ = 847 mM) with seawater (Ca^{2+} = 10.55 mM, K^+ = 10.44 mM) yields a net composition of 10.3 mM Ca^{2+} and 52.3 mM K^+. High levels of contamination were clearly found at the top of Unit II, where potassium was as high as 448 mM. In cases where the contamination was not as high, values generally ranged from 10 to 50 mM, and in several instances within Units III and IV, potassium was actually below seawater values (2.34–3.31 mM).

Magnesium concentrations were generally greater in the interstitial water samples than in drilling mud at similar depths (Fig. **F29A;** Table **T14**). The uppermost four samples of Unit II show levels of magnesium (31.8–47.0 mM) that exceed those of the drilling mud water in the same unit (14.0–23.8 mM). The least contaminated samples in Units III and IV have concentrations of 12.4 and 7.3 mM, respectively, compared to 2.2–5.2 mM in the drilling mud across the same intervals. Although the interstitial water magnesium values are significantly greater than the mud water values, they are lower than concentrations measured during the *Chikyu* shakedown cruise for deep sediment interstitial water, which all exceed 70 mM at depths >200 mbsf (Higuchi et al., 2009). The loss of magnesium in the interstitial water is likely due to authigenic mineralization of dolomites between sand grains, which was observed in some of the deeper sediment layers associated with the coalbeds (see **"Lithostratigraphy"**).

Calcium concentrations in the interstitial water were high (14.7–39.2 mM) throughout the sediment column (Fig. **F29B;** Table **T14**) and were significantly greater than drilling mud concentrations (3.5–8.4 mM). They also exceed the interstitial water calcium concentrations of ~4 mM observed in most samples collected deeper than 300 mbsf during the *Chikyu* shakedown cruise (Higuchi et al., 2009). High calcium concentrations at Site C0020 may indicate that the low-alkalinity water in Units II–IV is undersaturated in calcite or aragonite but still saturated with regard to dolomite. This would suggest that progressive dolomitization is occurring in calcite as it is buried. Dolomites are often associated with microbial activity and AOM in organic-rich sediments along continental margins (e.g., Meister et al., 2007).

Strontium concentrations in the interstitial water (93.9–719.6 µM) also greatly exceed concentrations found in drilling mud (13.6–57.8 µM), and thus the influence by contamination on this element is probably low (Fig. **F29C;** Table **T14**). Strontium concentrations uniformly exceed seawater concentrations (~93 µM) as well as in the deeper cores from the *Chikyu* shakedown cruise (~90 µM at 200 mbsf to ~80 µM at 300 mbsf) (Higuchi et al., 2009). Because strontium is generally coprecipitated with calcium in authigenic calcites to a much greater degree than in authigenic dolomites (Snyder et al., 2007), the increase in strontium concentration may be another indicator of deep dolomitization.

Barium concentrations are low at the top of Unit II (12.8–31.1 µM), are greatest in Unit III (29.25–78.76 µM), drop in Unit IV (25.1–38.9 µM) (Fig. **F29D;** Table **T14**), and are, in general, greater than drilling mud values (5.7–14.43 µM, with the exception of one mud sample at 42.6 µM in Unit II). The elevated values in the drilling mud probably represent in situ dissolution of sedimentary barite in the pore water under anoxic conditions (e.g., Torres et al., 1996). Because of contamination by drilling mud and resulting sulfate enrichment, the sampled interstitial water is extremely supersaturated with respect to barite. However, precipitation is either inhibited by other components in the mud or the reaction kinetics are such that there is not enough time for a substantial portion of the dissolved barium to precipitate. In Unit IV, barium concentrations are roughly half those of Unit III, but given the presence of drilling mud sulfate, it is not possible to determine whether this is caused by a drop in the in situ pore water Ba concentrations or if more barium simply

precipitated from the pore water during sediment recovery and squeezing.

Transition metals and metalloids

Boron concentrations are generally somewhat lower than seawater (416 µM) in Units II–IV (Fig. F30A; Table T14). One sample was as low as 82 µM and four other samples were <150 µM, but generally the interstitial water samples presented concentrations comparable to or greater than the concentrations of boron in mud water samples (166–238 µM). Two samples in Unit II were greater than seawater at 465 and 691 µM, whereas one sample in Unit IV was significantly enriched at 1313 µM. The enrichments may be indicative of the diagenetic release of boron from sedimentary organic matter (e.g., Snyder et al., 2005; You et al., 1993). Desorption and adsorption on clay minerals in the alkaline drilling mud likely has an influence on the squeezed pore water, such that the variations in observed boron concentrations may not be representative of the actual in situ composition of interstitial pore water.

Lithium enrichments may be indicative of the dewatering reactions in deeply buried clay (Martin et al., 1991). Several cores from Unit III presented lithium concentrations >300 µM, which is higher than the drilling mud across the lower part of Unit II through Unit III (151.8–259.8 µM); however, the most contaminated interstitial water sample in the upper part of Unit II also contained lithium at 353.3 µM (Fig. F30B; Table T14). Although all of the samples showed significant enrichments relative to average seawater (26 µM), the overlap with drilling mud concentrations makes it difficult to derive more than a general observation that pore water does show some degree of enrichment in Unit III.

Dissolved silica concentrations generally decrease with depth from as high as 867 µM in Unit II to as low as 68.9 µM at the deepest sample recovered from Unit IV (Fig. F30C; Table T14). In contrast, dissolved silica concentrations in the mud samples increase with depth either because of the dissolution of silica-bearing fossils (see "Paleontology") or the dissolution of silica in the ASTEX-S SAS additive (Eikenberg, 1990; Southwick, 1985). The lower silica concentrations in deeper interstitial water samples may be due to lower contamination from drilling mud.

Interstitial water tends to have less iron than the drilling mud (Fig. F30D; Table T14), and thus, the water samples are highly sensitive to iron contamination. The highest iron concentrations (5.1–25.0 µM) are in the top of Unit II, which makes the actual interstitial water composition suspect. In contrast, manganese concentrations in interstitial water (Fig. F30E; Table T14) exceed those in the drilling mud, particularly in the coal-bearing Unit III, where the maximum dissolved manganese concentration is 41.3 µM. However, the long squeezing times of some samples under oxic conditions may have oxidized both iron and manganese to their higher, less soluble oxidation states (Stumm and Lee, 1961) so that actual concentrations may have been higher within the formation than the observed values of squeezed pore water. The increase in Mn across Unit III roughly parallels the enrichments observed in Li.

Formation water samples

This is the first IODP expedition in which a downhole Quicksilver In Situ Fluid Analyzer (IFA) was deployed to select and retrieve fluids directly from the walls of the borehole, collecting them in a single-phase multisample chamber (SPMC) and then transferring them shipboard into Single-Phase Sample Bottles (SSB) (see "Wireline logging" in the "Methods" chapter [Expedition 337 Scientists, 2013b]). In preparation for IFA sampling, a decision was made to seek out the sandy layers that were in close association with the coalbeds for sampling. The rationale behind this decision was that the high permeability of the sand would allow the fluid flowline of the IFA to more effectively draw fluids from deeper within the target sediment in a reasonable amount of time. During sampling, the guard flowline would allow any surficial fluids that are contaminated by drilling mud to be effectively drawn away from the point of contact between the sediment formation and the fluid flowline (Mullins, 2008).

Deployment of the IFA was successful in precisely identifying potential sampling sites down the borehole, and Downhole Fluid Analysis (DFA) provided a preliminary assessment of the permeability and flow of formation fluid into the probe. Six samples were collected in the SPMC from Units II and III (see "Wireline logging" in the "Methods" chapter [Expedition 337 Scientists, 2013b]) and transferred to SSBs for gas and water analysis. Unfortunately, the formation water samples all showed drilling mud contamination, including high salinity and high chloride (Table T15). Sulfate concentrations in the formation water ranged from 7.9 to 23.9 mM, which was less than drilling mud water across Units II and III (20.52–55.96 mM) but only slightly lower than highly contaminated drilling cuttings across these intervals (18.6–23.3 mM) and greater than the pore water of lower part of Unit II and all of Unit III (0.97–10.5 mM). Potassium in the SSBs also showed significant drilling mud contamination, with concentrations ranging from 76.5 to 375.5 mM, which is less than mud water samples across these units

(643.0–732.9 mM) and less than water extracted from drilling cuttings in Unit II (648.4–781.5 mM) but is comparable to the highly contaminated pore water samples at the top of Unit II (65.2–448.5 mM) and is significantly more contaminated than the samples from the lower part of Unit II and Unit III (3.3–57.1 mM).

Despite these results, a number of interesting conclusions can be made that will be of some use in the future design and deployment of in situ sampling devices. In some respects, formation water shows a change in composition between Units II and III. Sodium increases from 550–567 mM in Unit II to 641–861 mM in Unit III (Fig. **F31A**). Sulfate concentrations are between 5.1 and 7.9 mM in Unit II and more enriched in Unit III, with values from 11.4 to 23.8 mM (Fig. **F31B**). Chloride increases from 670–777 mM in Unit II to 769–1125 mM in Unit III (Fig. **F31C**). This change is likely due to the change in the formulation of the drilling mud between Units II and III to include ASTEX-S SAS as well an increase in both sodium chloride and potassium chloride. Despite the high sulfate concentrations, dissolved barium is present in the formation water (12.1–52.7 µM) in concentrations similar to the pore water over the lower parts of Unit II and Unit III (9.0–78.8 µM) and greater than the mud cuttings in Unit II (4.6–11.7 µM), suggesting that either the drilling mud contamination occurred at the time of sampling and the samples did not have time to precipitate barite, or barite precipitation was inhibited by other ions in solution.

Contamination assessment

The degree to which the sediment pore water has been contaminated by drilling mud may be determined quantitatively if a number of working assumptions are made. An estimate of the fraction of mud water contamination in the pore water may be determined by assuming binary mixing between mud fluid and interstitial water. In order to determine this fraction, a single ionic species whose composition is distinct between the mud end-member and a pore water end-member must be selected, where the change in composition in the uncontaminated pore water is assumed to be negligible with depth. Finally, it is assumed that the mixing process is essentially nonreactive. The degree to which these assumptions are considered valid or not is evaluated by using several different ionic species and comparing the calculated fraction of mud water contamination. In this particular case,

$$X_{DML} = ([A]_{meas} - [A]_{FW})/([A]_{DML} - [A]_{FW}),$$

where

X_{DML} = fraction of drilling mud liquid mixed into the sampled water,
$[A]_{meas}$ = measured concentration of species A,
$[A]_{FW}$ = assumed concentration of species A in the formation water, and
$[A]_{DML}$ = concentration of species A in the drilling mud.

In the case of interstitial water, drilling cuttings, and formation water, X_{DML} was determined using three different parameters: sulfate, potassium, and salinity because within the *Chikyu* shakedown cruise Hole C9001C (Tomaru et al., 2009; Higuchi et al., 2009) the formation water concentrations ($[A]_{FW}$) of these three parameters did not appear to change appreciably below 200 mbsf. The assumption is made that $[SO_4^{2-}]_{FW}$ is 0 mM because samples were collected well below the sulfate–methane transition (4.5 mbsf). Based on the deepest sample (363 mbsf) from this previous cruise, $[K^+]_{FW}$ is 12.2 mM and $[salinity]_{FW}$ is 38‰. Measured interstitial water concentrations ($[SO_4^{2-}]_{meas}$, $[K^+]_{meas}$, and $[salinity]_{meas}$) from Table **T14** were matched with the mud composition from the nearest depth within the same unit in order to select the appropriate values of $[SO_4^{2-}]_{DML}$, $[K^+]_{DML}$, and $[salinity]_{DML}$ from Table **T12.** Using this approach, the mud fraction was calculated and plotted with depth (Fig. **F32**). The average and standard deviation between the three derived mud fractions are also shown in the plot for the formation water.

The mud fraction in the interstitial water, based on sulfate in the most contaminated upper part of Unit II, ranged from 0.43 to 0.88 and then generally decreased to below 0.1. The mud fraction based on potassium was 0.32–0.69 in the contaminated samples in the upper part of Unit II and was generally <0.05 throughout the rest of Unit II and all of Units III and IV. Based on salinity, the contaminated upper samples had mud fractions between 0.50 and 0.65, whereas the deeper samples generally had mud fractions of 0.05 or less. When calculating the mud fraction from potassium and salinity, a few values were <0, suggesting actual shifts in the formation water potassium and salinity that make the estimated $[A]_{FW}$ value larger than it should be.

Using this approach for the cuttings water, showed even higher degrees of contamination based on sulfate concentrations, with mud fractions ranging from 0.76 to 0.90 in Unit II and 0.81 to 1.00 in Unit III. The mud fraction based on potassium could not be used because potassium concentrations in the cuttings were greater than both those in the pore water and those in the drilling mud, presumably caused by clay dissolution by the alkaline mud. The mud

fraction in the cuttings based on salinity was 0.690–0.75 in Unit II and 0.81–1.00 in Unit III.

The mud fraction in the formation water collected in the SSBs was 0.25–0.35 in Unit II and 0.20–0.43 in Unit III, based on the presence of sulfate. Based on potassium concentrations, the fraction of mud was 0.10–0.32 in Unit II and 0.17–0.51 in Unit III. Finally, the salinity of the formation water suggests a range of mud fractions of 0.03–0.24 in Unit II and 0.09–0.33 in Unit III. (Fig. F32). With the exception of the shallowest SSB in Unit I, all other samples show greater fractions of mud water contamination than are observed in the squeezed pore water samples. Using the mud fractions derived from sulfate, potassium, and salinity and the concentrations of the other dissolved species for each sample in Table T14, corrections in the pore water concentrations could be carried out using

$$[A]_{corr} = ([A]_{meas} - X_{DML}[A]_{DML})/X_{IW},$$

where

- $[A]_{corr}$ = corrected in situ concentration of the analyte,
- $[A]_{meas}$ = measured concentration of the analyte,
- $[A]_{DML}$ = element concentration in the drilling mud water,
- X_{DML} = molar fraction of drilling mud liquid introduced into the sample during drilling, and
- X_{IW} = fraction of in situ interstitial water in the sample, and where $X_{DML} + X_{IW} = 1$.

No attempt was made to carry out corrections where $X_{DML} > 0.2$.

The approach was taken of averaging the three corrections (sulfate, potassium, and salinity) and taking the error between the three to be 1 standard deviation from the mean. Results are shown in Figure F33 for alkalinity, Ca, Mg, and Sr. Note that error bars for alkalinity are much larger than for Ca, Mg, and Sr because the mud has an alkalinity similar to the interstitial water samples. In contrast, errors for the alkaline earth elements are relatively small because the mud concentrations for these elements are significantly lower than those of the interstitial water. The increase in alkalinity, Ca, Mg, and Sr in the corrected profiles of Figure F33 becomes much more discernible in the corrected profiles than in Figures F26 and F29.

Organic geochemistry

During Expedition 337, organic geochemists investigated gas and solid-phase samples on board the ship and took gas, solid-phase, and interstitial water samples for postcruise research. The shipboard gas program included continuous on-line monitoring of mud gas that was extracted from the drilling mud in a separator unit and transferred to a mud-gas monitoring laboratory unit next to the rig floor, as well as the analysis of gases in samples taken from cuttings, sediment cores, and formation fluid. The formation fluid samples were retrieved under in situ pressure by Downhole Fluid Analysis (DFA). Together with hydrocarbon gases and their stable carbon isotopic composition, hydrogen, carbon monoxide, and noble gases were the most important target compounds, and O_2 and Ar were monitored to account for the introduction of air and for corrosive processes during drilling operations. In addition, radon was recorded by a third-party tool provided by the Japan Agency for Marine-Earth Science and Technology (JAMSTEC) Institute for Research on Earth Evolution (IFREE).

For shipboard solid-phase analysis, samples were collected from cuttings and sediment cores and cuttings for elemental analysis (C in organic and inorganic form, N, and S) and characterization of the kerogen type via Rock-Eval pyrolysis. In addition, lipids (including fossil hydrocarbons, phospholipid fatty acids, and intact polar lipids) were extracted from cuttings and sediment cores by accelerated solvent extraction for both shipboard and shore-based analysis. The different types of biomarkers will help to characterize the deep coalbed biosphere and constrain the thermal history of the hole.

Fresh sediment samples were taken for shipboard and shore-based incubation experiments to study microbial life. On board the ship, a total of 43 experiments were started and will be continued postcruise: 34 WRCs from selected typical lithologies were processed in ^{14}C-radiotracer experiments to determine rates of microbial metabolic activities such as methanogenesis and acetogenesis. In addition, nine WRCs were used for a series of stable isotope probing (SIP) experiments in which compounds labeled with either ^{13}C or deuterium (D) will serve to track substrate utilization and uptake into cellular biomass. The analysis of gas, solid-phase, and fluid samples together with radiotracer and SIP experiments will allow us to track the carbon flow in the deep subseafloor biosphere within, above, and below the Shimokita coalbeds and will help us test the hypothesis that biogenic methane is formed in situ within coal seams.

Gases

On-line monitoring and sampling of mud gas

The goal of mud-gas monitoring was the real-time characterization of formation gases as they were re-

covered from the borehole and brought to the surface with the circulating drilling mud. On-line analyses were conducted using a methane carbon isotope analyzer (MCIA), a gas chromatograph (GC)–natural gas analyzer (NGA), and a process gas mass spectrometer (PGMS) while drilling operations were monitored and recorded via the SSX database. The on-line mud-gas analysis of hydrocarbon gases was complemented by dissolved hydrocarbon gas analysis in 48 samples of unwashed cuttings and 65 samples of sediment cores using the headspace technique.

During operations in Hole C0020A, gas monitoring data were recorded nonstop, including periods during which drilling was intermittent, such as when periodic "tripping" or emplacement of new pipe stopped progress, as well as periods of flushing to clean the hole. Because a round trip of drilling mud through the borehole took ~1–2 h (depending on hole depth and mud flow rate), interruptions in drilling operations affected the recovered mud gas after a lag time of 1–2 h. Figure **F34** shows the depth from which mud gas was recovered at a certain day and time (note that all activities were recorded in ship time [UTC + 8 h]). We observed that on-line data started to scatter widely when drilling paused and mud gas was recovered from the same depth for >5 min. Therefore, we strictly limited our data interpretation and sampling activities to mud gas that resulted from periods in which drilling advanced into the geological formation and mud flow allowed for sufficient mud-gas recovery. Furthermore, the drilling rate in combination with the mud circulation rate, mud weight, and mud to headspace ratio in the separator impacts the recovery of gas from the formation (Erzinger et al., 2006). Because the conversion of mud-gas contents into absolute gas concentrations in the drilled rock is not straightforward, we limit our presentation of results here to the discussion of the relative ratios of gas species in the mud gas.

For the deepening of Hole C0020A from 647 to 2466 mbsf, we identified 96 discrete time intervals in which drilling actively advanced into the formation (Table **T16**), totaling 68 h of drilling time during which more than a million discrete data points were recorded for the characterization of mud gas. Mud-gas monitoring yielded an almost continuous depth profile of the various target compounds from 647 to 2466 m MSF. A few data gaps exist, however. They correspond to periods in which no or not enough mud gas could be recovered, either because of low mud flow rates, or because of exceptional events like the complete loss of drilling mud at 1110 m MSF and the clogging of the mud-gas line when drilling mud was arriving from sediment horizons at ~750 and 960 m MSF.

Hydrocarbon gases

The primary and novel continuous monitoring instrument used to measure mud gas was the MCIA. It provides information on the content and carbon isotopic composition of methane in mud gas that is continuously flowing through the instrument without separation of compounds or further addition of carrier gas. In scientific ocean drilling, Expedition 337 provided the first opportunity to test the MCIA in the field, and the accuracy of the recorded data will be carefully evaluated on shore using selected mud-gas samples and isotope-ratio-monitoring gas chromatography/mass spectrometry as a well-established standard method for carbon isotopic analysis of hydrocarbon gases (e.g., Ertefai et al., 2010). By simultaneous monitoring of drilling parameters and MCIA data, we observed that operational changes strongly affected the methane content of the recovered mud gas but did not have an obvious effect on the $\delta^{13}C$ values of methane. Nevertheless, the potential effect of drilling on the carbon isotopic composition of methane recovered with mud gas deserves careful postcruise evaluation.

The MCIA was operated at a frequency of one measurement per second. During the 68 h active drilling period (Table **T16**), >186,000 data points were recorded for both the content and isotopic composition of methane in the mud gas continuously flowing through the MCIA. In general, 100–200 data points were obtained per drilled meter of sediment, depending on drilling parameters (i.e., ROP). Depth-based averages were compiled for these data to generate discrete data for corresponding depths (Table **T17**).

In the drilled depth interval between 647 and 2466 m MSF, methane is relatively depleted in ^{13}C, with $\delta^{13}C$ values ranging from –76.5‰ to –58.8‰ (versus Vienna Peedee belemnite [VPDB]) and averaging around –65.6‰ vs. VPDB. According to the well-established carbon isotopic systematics of methane (e.g., Whiticar, 1999), the carbon isotopic composition of mud-gas methane suggests biogenic methane sources to a depth of 2466 m MSF. Figure **F35** illustrates that the carbon isotopic composition of methane varies distinctly with sediment depth. At the shallowest drilled depth of ~640 m MSF, $\delta^{13}C$ values are around –65‰ vs. VPDB and closely match $\delta^{13}C$ values of methane that were observed at this site in sediment cores recovered from ~358 mbsf during the *Chikyu* shakedown cruise (Expedition CK06-06) (F. Inagaki et al., unpubl. data). Below ~1100 m MSF,

$\delta^{13}C$ values decrease with respect to depth and reach a local minimum of around –75‰ vs. VPDB at ~1400 m MSF. With further increasing depth, $\delta^{13}C$ values first increase to about –62‰ vs. VPDB at 1800 m MSF, remain more or less constant between 1800 and 2050 m MSF, and finally show a slight trend toward more negative values between 2050 m MSF and the bottom of the hole at 2466 m MSF. The correspondence of these isotopic variations with depth to microbial communities and availability of substrates will be further investigated in postcruise studies.

On-line monitoring of methane by the MCIA was supplemented by on-line GC-NGA analysis of methane and higher hydrocarbon gases with a frequency of roughly three analytical runs per hour, which yielded a total of 189 analyses (Table **T18**) during active drilling times (Table **T16**). Although the interpretation of methane content alone is not straightforward, as it cannot be directly related to methane concentration in the formation (see above), simultaneous analysis of methane and higher hydrocarbon gases allows calculation of C_1/C_{2+} ratios. The C_1/C_{2+} ratio is a valuable parameter to distinguish between hydrocarbon gases from biogenic and thermogenic sources (e.g., Whiticar, 1999). C_1/C_2 ratios were obtained not only during on-line mud-gas monitoring (Table **T18**) but also for dissolved gases in cuttings (Table **T19**) and sediment cores (Table **T20**) using headspace analysis. The results of the three different methods are depicted together in Figure **F36.**

Overall, on-line mud-gas monitoring resulted in systematically higher C_1/C_2 ratios than headspace analysis of cuttings, and C_1/C_2 ratios in core samples plot intermediate between the two (Fig. **F36A**). Methane degasses more easily than ethane, and the distinctly lower C_1/C_2 ratios in cuttings compared to mud gas might result from preferential degassing of methane during sample retrieval. Nevertheless, gas analyses from cuttings, cores, and mud gas altogether point to a biogenic source of the methane observed in Hole C0020A.

Because the occurrence of major amounts of C_2 (to C_5) is associated with thermogenic hydrocarbon generation, high C_1/C_2 ratios indicate biogenic methane formation when methane concentration exceeds 10,000 parts per million (ppm). However, for the interpretation of C_1/C_2 ratios one has to consider that minor amounts of C_2 (and C_3, C_4, and C_5) can also be generated in situ during early diagenesis of organic matter. The importance of this process increases with increasing burial depth, resulting in a consistent ("normal") decrease in C_1/C_2 with increasing temperature (Pimmel and Claypool, 2001; Ocean Drilling Program, 1992). The plot of C_1/C_2 ratios obtained from on-line mud-gas monitoring versus in situ temperature (assuming a geothermal gradient of 24°C/km and a bottom water temperature of 6°C) shows a normal increase with depth and suggests that the gases formed in situ, rather than having been transported from greater depth (Fig. **F36B**).

Although C_1/C_2 ratios of mud gas generally decrease with increasing depth as expected, they show a distinct excursion toward higher values between 1840 and 2054 m MSF (i.e., the depth interval in which 12 coal layers were observed in sediment cores and during downhole logging). At greater depth, C_1/C_2 ratios decrease again. The excursion of the C_1/C_2 ratio points to the enhanced activity of biogenic methanogenesis in or between the coal layers relative to under- and overlying sediments.

In contrast to on-line mud-gas monitoring, analysis of dissolved gases in cuttings and cores by headspace sampling provides some clues on the concentration of hydrocarbon gases, though most of the gas dissolved in pore fluid may have escaped prior to sampling because of depressurization of the core during recovery. We collected 48 cuttings samples as well as 65 headspace samples from sediment cores, including four that we took directly from the coal layers. For better comparability, all concentrations are reported in moles hydrocarbon per liter interstitial water, based on concentration measurements in vials and the mass and porosity of sediment sampled. In several samples, the hydrocarbon concentration was greater than the calculated values for in situ saturation of interstitial water despite some degassing during core recovery. This suggests that substantial free or sorbed gas existed in the sediments at depth. In cuttings, methane was still present in concentrations ranging from 3 µM to ~1.4 mM. Methane concentrations reached particularly high values at ~1820 and 1920 m MSF (Table **T19**), suggesting a methane source in the coal layers found at this depth. This trend is even more obvious in headspace samples taken from cores. For samples taken from the sediment cores without coal layers, methane concentrations were usually <5 mM (Table **T20**), but in samples taken from coal layers or adjacent sediments, methane concentrations were distinctly elevated, exceeded 50 mM in several cases, and reached a maximum of ~270 mM at 1920 m CSF-B. The latter concentration exceeds the in situ solubility of methane and points to the presence of coalbed methane, which is typically sorbed in micropores of organic matter. We noted bubbling of free gas from adjacent sediments in the coal-bearing cores and took four void gas samples from Core 337-C0020A-22R, in which the methane content exceeded 80%.

In the process of riser drilling, drilling mud is recycled (the mud is pumped through the hole, returned to the ship, and used again). In order to ensure that the gases measured during mud-gas logging were derived from the formation, it was necessary to determine if carryover of gases existed in the mud gas that was to be reused. Over the course of 10 days, 14 samples were taken from the drilling mud tank. Over this period, the drilling mud had an average concentration of 25 ppm methane and traces of higher hydrocarbons (<12 ppm; Table **T21**) in the gas phase of headspace vials. These levels are insufficient to strongly impact concentration measurements in formation-derived samples, which sometimes released several thousand parts per million methane in the headspace of vials using the same sample/headspace ratio.

Oxygen, argon, and nitrogen

A major impetus for the use of a PGMS for on-line mud-gas monitoring was the determination of ratios of oxygen/argon and nitrogen/argon to detect the presence of corrosive processes occurring at the drill bit. Atmospheric concentrations of nitrogen, oxygen, argon, and hydrogen are 78%, 20%, 0.93%, and 550 ppb (v/v), respectively. These concentrations yield an atmospheric signature of nitrogen/argon and oxygen/argon ratios of 83 and 21, respectively. The nitrogen/argon and oxygen/argon ratios throughout the drilling procedure averaged 84 and 22, respectively, and point to the absence of oxidative processes (Table **T22**). Nitrogen, oxygen, and argon concentrations were 78.2% ± 3.7%, 20.7% ± 0.6%, and 0.9% ± 0.03%, respectively, and showed little variation with depth throughout Hole C0020A (Fig. **F37**). These concentrations are similar to those in air and indicate that a major portion of the mud gas was air originally contained in drilling mud or intruding from the degasser system. Concentrations of xenon and helium were below the detection limit of the PGMS. Note that on-line mud-gas monitoring by the PGMS only started at 1005 m MSF because of insufficient gas flow to the instrument during the first day of mud-gas monitoring (15 August 2012).

Continuous on-line monitoring of oxygen, argon, and nitrogen by the PGMS was complemented by sporadic mud-gas analysis using the GC-NGA (with a thermal conductivity detector [TCD]) (Table **T23**). In general, oxygen, argon, and nitrogen concentrations were typical of atmospheric concentrations.

Hydrogen and carbon monoxide

During mud-gas monitoring, volumetric hydrogen concentrations as determined by the PGMS were typically 2 orders of magnitude higher in the mud gas than in ambient air (Fig. **F37**). The average hydrogen concentration in the mud gas was 2.4% (Table **T22**). Although oxygen concentrations were not suggestive of corrosion, elevated hydrogen concentrations in the mud gas point to the formation or release of hydrogen during the drilling process. Sporadic analysis of the mud gas by the GC-NGA (using a TCD) showed carbon monoxide concentrations exceeding atmospheric levels (Table **T23**).

For determining the concentrations of dissolved hydrogen and carbon monoxide, the investigation of dedicated samples taken from sediment cores is more informative than continuous on-line mud-gas analysis by the PGMS and GC-NGA. A combination of two methods was used for this purpose (i.e., the extraction and incubation methods). The extraction method is based on the direct extraction of dissolved hydrogen and carbon monoxide into the helium headspace of a sample vial and is conducted immediately after sample recovery. This method was used not only to analyze samples taken from sediment cores, but also to check the hydrogen and carbon monoxide background in drilling mud that was caught between the sediment and the core liner. We collected a total of 63 samples for hydrogen and carbon monoxide analysis from the sediment cores (~2 samples per core) and 25 corresponding samples of drilling mud from the core liners (Table **T24**).

The depth profile of hydrogen concentration displays no systematic trends, and within one single core, hydrogen concentration often varies substantially (Fig. **F38**). The dissolved hydrogen concentrations span a range of 0.398–562 µM and average ~48 µM. Carbon monoxide concentrations vary throughout the drilled sediment interval. Carbon monoxide concentrations in sediment samples and drilling fluid recovered from above 1821 m CSF-B were <400 nM, but below 1920 m CSF-B, concentrations were higher than in the shallower sediment and drilling fluid and reached a maximum of ~100 µM within the coal layer at 1920 m CSF-B. The depths of the carbon monoxide pulses seem to correspond to coalbeds.

Drilling mud contained high hydrogen concentrations (333 nM to 74 µM) but carbon monoxide contents were low (<0.5 µM), except for a few cases in the coalbeds, in which shreds of coaly sediment had been blended into the drilling mud (1–1.4 mM) (Table **T25**). Overall, there was no obvious relationship between hydrogen concentrations in sediment samples and associated drilling mud. Although it seems likely that high hydrogen concentrations in the drilling mud would lead to the contamination of the sediment cores, hydrogen concentrations in sediment samples were, in some cases, orders of magnitude

higher than in the corresponding drilling mud (e.g., Cores 337-C0020A-6R and 11R). In particular within the coal-containing intervals, hydrogen concentration in sediment was distinctly higher than in drilling mud. This suggests the release of hydrogen from the coaly sediment.

The observation of high hydrogen concentrations in the drilling mud is in agreement with the observation of hydrogen contents above atmospheric levels during PGMS analysis of mud gas and underlines that the analysis of hydrogen in interstitial water with the extraction method might be impacted by hydrogen formation during the drilling process.

In contrast to the extraction method, the determination of hydrogen concentrations with the incubation method is likely to be less impacted by the presence of hydrogen in the drilling fluid. This is because hydrogen that might initially be present in the sample is flushed out before experiments are initiated to monitor the evolution of hydrogen in the incubated samples over time. The observation of hydrogen concentrations over time aims to identify the establishment point at which a steady state is reached between biogenic processes that produce and consume hydrogen. We collected 64 sediment samples, approximately two per core, for determining the hydrogen concentration by the hydrogen incubation method (Table **T26**). We analyzed a total of three time points from all vials between sampling and the end of the expedition, including the initial time zero measurement. Time Point 1 was sampled after ~1 week of incubation, followed by a second time point 1 week later. The blank or initial hydrogen values were typically 1.5 ppm or less. Within 1 week of incubation, hydrogen contents increased on average by 54 ppm (n = 64) but varied largely from 1.5 to >2500 ppm in the individual samples. To test the exceedingly high increase in hydrogen concentrations observed in some samples, we performed a test of hydrogen increases in paired samples with one control sample killed by three cycles of deep freezing at –80°C (samples from Sections 337-C0020A-32R-1 and 32R-6). Control samples had similar or higher hydrogen concentrations after a 4 day incubation with 2199 and 70 ppm in live samples versus 1517 and 259 ppm in killed samples, respectively. This result is consistent with hydrogen being released abiotically from the sediments rather than being produced by biological processes. Hydrogen concentrations did not systematically vary over depth.

Carbon monoxide analysis was completed concurrently with hydrogen analysis on the reduced gas analyzer provided as a third-party tool by JAMSTEC Institute of Kochi Core Sample Research. Though vials were purged, a substantial accumulation of carbon monoxide (95 ppm) was observed in coal-associated lithologies at ~2001 m CSF-B. These data suggest that carbon monoxide might play an important role in carbon cycling in coalbeds.

On-line analysis of radon

Radon (Rn) is an inert radioactive gas of the daughter nuclei of uranium and thorium with rather short half-lives. Among Rn isotopes, ^{222}Rn has the longest half-life of 3.82 days, followed by ^{220}Rn with a half-life of only 55.3 s. Rn has widely been monitored to detect microcracking prior to seismic activities (e.g., Igarashi et al., 1995). In scientific drilling, concentrations of Rn dissolved into the circulation mud are anticipated to reflect the lithologic units of the formation; its parental elements, uranium and thorium, are generally rich in the terrigenous sediments and felsic rocks. In addition, some coalbeds contain abundant uranium up to 200 ppm (Takeda, 1981). The typical environmental background of Rn on the *Chikyu* was on an order of several Bq/m^3. During on-line mud-gas monitoring, Rn concentrations were distinctly higher than this background and reached as high as 120 Bq/m^3. Data are reported in Table **T27.**

Gases in fluids retrieved by DFA

A total of six formation water samples were sampled from 1279 to 1978 m WMSF by DFA and analyzed for methane, ethane, propane, and n-butane as well as molecular hydrogen and carbon monoxide (Table **T28**). Because samples were recovered under in situ pressure and did not suffer loss of gases during retrieval, the resulting concentration data are likely to be the most representative data for in situ concentrations obtained during Expedition 337. Methane concentrations ranged from 17.3 to 39.6 mM. The concentrations were significantly higher than those in headspace samples from sediment cores (<5 mM) but lower than the in situ solubility of methane and indicate the absence of free gas in the sampling intervals. Methane was the dominant hydrocarbon gas. Ethane concentrations were 1 order of magnitude lower and ranged from 1.3 to 4.1 µM, whereas concentrations of ethane and n-butane were in the nanomolar range. The corresponding C_1/C_{2+} ratios ranged from 1629 to 2995 and point clearly to biogenic methane sources (Whiticar, 1999). Although the ratios in DFA samples from 1808 to 1978 m WMSF were higher than those from on-line mud-gas monitoring, the depth profile of DFA samples is consistent with those from mud-gas monitoring, showing a distinct excursion toward higher values between 1840 and 2045 m WMSF.

Hydrogen concentrations ranged from 10.7 to 492 µM (Table T28). Hydrogen concentrations from 1279.5 to 1844 m WMSF were higher than those from the sediment core samples retrieved from roughly corresponding m WMSF. Hydrogen concentrations from 1901.5 to 1978 mbsf were similar to those from the sediment core samples. The high hydrogen concentrations compared to the sediment samples suggest that concentrations in the DFA sample are in situ concentrations. We cannot, however, eliminate the possibility of contamination from drilling mud because the drilling mud inside the borehole was not sampled by DFA. Therefore, the in situ hydrogen background in drilling mud remains unknown.

Carbon monoxide concentrations ranged from 0.857 to 6.70 µM (Table T28). Carbon monoxide concentrations from 1279.5 to 1844 m WMSF were 1 order of magnitude higher than those from sediment samples. Carbon monoxide concentrations from 1901.5 to 1978 m WMSF were similar to those from the sediment samples.

Solid phase

Total carbon, nitrogen, and sulfur contents, inorganic carbon, organic carbon, and carbonate content of the solid phase

Carbonate and elemental analyses have been carried out on 51 core samples from Units II to IV (Table T29), and 34 selected cuttings samples from the four stratigraphic units (Table T30) and are summarized in Figure F39. Inorganic carbon contents were relatively uniform and generally <0.5 wt% for both core and cuttings samples throughout the hole. Several relatively high inorganic carbon values (1.6–6.3 wt%) were observed for the core samples, two of which were cemented sandstones from Unit III. Inorganic carbon values from the cuttings samples were higher than those from the corresponding core samples by factors of 1.1–74. Total organic carbon (TOC) contents of the core samples showed strong lithologic control: coal had the highest average TOC contents (40.9 ± 9.9 wt%), followed by mudrocks (clay-rich lithologies and shales) (1.4 ± 1.0 wt%), silty (0.43 ± 0.29 wt%), and sandy (0.26 ± 0.18 wt%) lithologies. Therefore, Unit III, with its heterogeneous lithologic composition, showed a large downcore variation in TOC contents. Most of the cuttings samples from Units II to IV, except for those taken near the coal layers, had TOC contents higher than the corresponding core samples. These high values are the combined effects of depth averaging of low-TOC strata with organic-rich strata (such as clasts of coal) and input from the drilling mud, which contains organic additives. Accordingly, TOC values in Unit I, represented only by cuttings samples, might be overestimates of the actual values in individual strata. Total nitrogen (TN) contents of core samples of different lithologies followed a similar pattern to that of TOC: coal = 0.84 ± 0.26 wt%, shale = 0.07 ± 0.02 wt%, siltstone = 0.04 ± 0.02 wt%, and sandy lithologies = 0.03 ± 0.02 wt%. However, unlike the TOC record, 70% of the cuttings samples from Units II to IV had TN values lower than the corresponding core samples. TN contents of cuttings from Unit I had an average value (0.07 ± 0.02 wt%) close to that of shale. Both depth averaging and the drilling mud may have affected the TN record of cuttings. The molar TOC/TN ratios of the core samples ranged from 3 to 65 (Fig. F39). The samples with low TOC/TN values (<5) usually had a TOC content <0.1 wt%; accordingly, the values are more strongly impacted by imprecise analysis as well as inorganic N contributions. For samples with TOC content >0.1 wt%, both the sandy and silty lithologies had an average TOC/TN ratio of ~13, whereas for the clayey sediment and coal, the average went up to 22 and 58, respectively. However, the clastic sediment had a large within-group variation in the TOC/TN ratio (1σ = 7–10), making it difficult to link the origin of organic matter (terrestrial or marine) to lithologic compositions. The TOC/TN ratios from cuttings samples in Units II–IV were generally higher than the corresponding core samples because of the overestimation of TOC and underestimation of TN. Total sulfur (TS) values in the hole were generally low (from below detection to 1.4 wt%) and showed no clear association with lithology or specific trends with depth. The cluster of samples with low TS contents in Unit III were from a variety of different lithologies, including coal.

Characterization of the type and maturity of organic matter by Rock-Eval pyrolysis

Rock-Eval pyrolysis was carried out on cuttings samples from Unit I (Table T31) and core samples from Units II–IV (Table T32). The data are displayed in Figure F40. Compared to the core samples, the cuttings samples yielded lower peak temperature maxima (T_{max}) values (319° ± 47°C), larger amounts of free hydrocarbons (S1: 0.86 ± 0.40 mg hydrocarbon [HC]/g sediment), and higher hydrogen index (HI) values (227 ± 83 mg HC/g TOC). T_{max} values from the cuttings samples were lower than those reported for shallower, young shelf sediment (e.g., D'Hondt, Jørgensen, Miller, et al., 2003) and were regarded as signals of incompletely removed organic contaminants from the drilling mud. Four of the 51 core samples yielded poorly resolved S2 peaks with T_{max} values between 496° and 604°C and were excluded from the

data set presented in this report. In Units II–IV, most of the core samples yielded T_{max} values in the range of 400°–440°C, indicating organic matter in a thermally immature to early mature state. Some of the sandy samples had lower T_{max} values, probably as a consequence of contamination from drilling mud.

Most of the core samples had no detectable S1 peak. The four samples in Units II and III with S1 yields of 0.1–0.6 mg HC/g sediment had low T_{max} values (<400°C) and were considered contaminated. There is a large variation in the S1 yield among different coal samples: although the shallower coal had barely detectable S1 peaks consistent with a relatively low coal rank (e.g., less than that of bituminous coal), the deepest coal bore a S1 content of 2.2 mg HC/g sediment. The very high production index (PI) values (and relatively high S1 values) observed within drilling cuttings (Table **T31**) could reasonably represent (1) the presence of low molecular weight humic and fulvic acids, (2) instances of drilling mud infiltration, or (3) nonindigenous bituminous organic matter (Peters, 1986). For data acquired from core samples (Table **T32**), except for a few samples, the PI values >0.001 all correspond to sandstones—a permeable lithology that when poorly cemented is easily contaminated. Thus, as for drill cuttings, these high values do not represent thermally driven conversion of kerogen to bitumen but either thermally immature organic matter or infiltration of drilling fluid.

For the other Rock-Eval parameters presented in Figure **F40**, a link to lithology was observed. The average values of S2, S3, and HI decreased in the order of coal > mudrocks (shales and other clayey lithologies) > silty or sandy lithologies, suggesting higher contents of hydrogen-rich organic matter in fine-grained sediment and coal. The high yields of S3 components (15.2 ± 2.8 mg CO_2/g sediment) in coal are consistent with the expectation of abundant lignocellulosic materials, which are found to contribute substantially to S3 signals (Carrie et al., 2012). The opposite order applies to the average oxygen index (OI) values, with 85% of the sandy and silty lithologies having OI values >100. Because of the high values contributed by the coal samples, the downcore profiles of S2 and S3 appeared rather uniform except for the few excursions from coal, whereas the distributions of HI and OI values were highly scattered as a reflection of the lithologic changes. The summed values of pyrolyzable carbon and residual organic carbon generally correlate well with TOC values, with the high proportion of residual organic carbon found in many samples indicating the presence of recalcitrant organic materials, not readily amenable to pyrolysis or even combustion, which can be particularly abundant in coals.

Lipid analysis

Shipboard lipid analysis focused on fossil hydrocarbon markers to characterize the sources of sedimentary organic matter and to construct a thermal history of Site C0020. Shipboard work included measurement and limited exploratory investigation of data. From this, it can be seen that in many cases biomarker characteristics vary more by lithology than by the depth interval. Data are presented by compound type for coal, siltstone, and mudstone lithologies; rock types that are typically associated with high concentrations of organic matter and considered the most resistant to contamination by drilling fluid infiltration (Peters et al., 2005). Biomarker data derived from cuttings have been included in a preliminary exploration of data but are presented separately.

n-Alkanes

n-Alkanes were detected in all lithotypes with samples of coal, mudstone, and siltstone always exhibiting an odd-over-even predominance (Fig. **F41**). In all cases, except where petroleum biomarkers (biomarkers associated with processes or conditions that generate petroleum) are present, carbon number distributions show a strong odd-over-even preference and were skewed toward high carbon numbers (e.g., $>C_{25}$). This distribution preference is consistent with the sedimentary organic matter being derived from higher plants (Meyers and Ishiwatari, 1993). However, land plant–derived organic matter is not the only source of high carbon number *n*-alkanes, and the solvent extracts of many phytoplankton species also yield *n*-alkanes in the higher carbon number range (Volkman et al., 1998). Additionally, the rapid solvent evaporation procedure used to facilitate shipboard work also has the potential to remove low carbon numbered compounds of relatively high volatility and may have enhanced any skew toward higher carbon numbers.

The carbon preference index (CPI) for *n*-alkanes (Table **T33**) varies downhole, with slightly lower values measured in samples for the deepest cores. This is consistent with a higher thermal maturity for these deeper samples but still indicates a very low level of thermal maturation. Where pristane/phytane ratios can be reliably measured, pristane typically predominates in siltstone and coal, indicating greater inputs of tocopherol precursors that contain C_{19} isoprenoids (these compounds are abundant in woody organic matter and lignocelluosic organic matter) and/

or higher oxidation rates of potential phytane precursors (Peters et al., 2005). Slightly lower values in mudstone may represent reduced inputs of woody organic matter and less oxidizing conditions in the depositional environment.

Polycyclic aromatic hydrocarbons

Shipboard biomarker work focused on three- and four-ring polycyclic aromatic hydrocarbons (PAHs). These compounds are common in most coals at even low thermal maturities (Radke et al., 1980), although when present at very low thermal maturities (e.g., R_o values of 0.25% or less), their interpretation as indicators of thermal maturity is not possible. Within all samples PAH abundance varies, with phenanthrene being variably prominent in mass chromatograms of diagnostic ions (Fig. **F42**). Unlike in cuttings, the anthracene isomer is not seen in core samples and neither is the 4-methylphenanthrene (MP) isomer observed. This indicates that these compounds may have been introduced into cuttings samples during drilling operations. The variable prominence of phenanthrene makes it difficult to apply for geochemical purposes, and, as was the case for low carbon number *n*-alkanes, this may result from the solvent concentrating procedure used to facilitate shipboard work that has the potential to remove relatively volatile compounds.

The tetracyclic PAHs are more abundant, and summed ion chromatograms are provided in Figure **F43.** Pyrene and fluoranthenes (a nonalternant PAH associated with low-temperature combustion) (Killops and Killops, 2005) are present in all lithologies and noticeably more abundant in coal. Within some sections, a trend to higher proportions of fluoranthene relative to pyrene with higher HI values is observed, likely reflecting increased proportions of oxidized (Type IV) organic matter in these sections.

n-Alkanoic acids and n-alkanols

Given the strong odd-over-even predominance seen for *n*-alkanes and the presence of wood fragments in many samples, the even-over-odd predominance for high carbon number *n*-alkanoic acids ($>C_{24}$) evidenced in mass chromatograms in Figure **F44** is to be expected (Meyers and Ishiwatari, 1993; Killops and Killops, 2005) (Table **T34**). As for *n*-alkanes, there is a skew toward higher carbon numbered *n*-alkanoic acids in many but not all coal, mudstone, and siltstone samples. Variation in the even-over-odd predominance of *n*-alkanoic acids with depth may represent both variation in the source of organic matter (reduced inputs of terrestrial organic matter) and increased levels of thermal maturation. However, the sudden drop toward the bottom of Unit III (~2000 m CSF-B) is unlikely to be solely the result of thermal maturity (Fig. **F45**).

n-Alkanols are visible but less prominent on ion chromatograms, with the C_{18} homolog being the most abundant, except in a clast of coal taken from coal-bearing breccias in Unit II (interval 337-C0020A-2R-2, 0–15 cm). Of the higher carbon *n*-alkanols with the C_{24}, C_{26}, and C_{28} alkanols are typically the most abundant, making their carbon number distribution similar to that of the *n*-alkanoic acids.

Alkenoic acids were detected in some samples at very low concentrations, but are likely to have been introduced during drilling operations (e.g., they were not common in laboratory blanks). Thus, as laboratory contamination can be ruled out, the two remaining possible origins are infiltrated drilling fluid or a sedimentary origin (e.g., they could be indigenous to the formation).

Some siltstone samples evidence a series of broad peaks (marked by an asterisk in Fig. **F44**) that are also seen in control samples that contain drilling mud (see **"Cuttings"** below). These compounds dominate the chromatograms of loosely consolidated sandstones and the solvent-soluble components of drilling mud washed from the surface of cuttings samples. This indicates that some siltstone samples have been contaminated, albeit to a far lesser degree than sandy lithologies.

High relative abundances of C_{15} and C_{16} *iso*- and *anteiso*-alkenoic acids and also C_{16} and C_{18} *n*-alkenoic acids are found at ~2000 m CSF-B (Fig. **F46**). *Iso*- and *anteiso*-fatty acids were not found or are not as abundant in coal and samples from the deepest sections of Core 337-C0020A-25R, nor are they as abundant in overlying mudstone units or clasts of coal from coal-bearing breccias in Unit II. Methyl-branched fatty acids are common biosynthetic products produced by bacteria (Kaneda, 1991), and their presence presumably indicates a bacterial contribution to the fatty acid pool in this interval. Because only free fatty acids were considered, it is not possible to directly infer the presence of an active deep biosphere from this observation alone, but this observation indicates a localized input of bacterial organic matter to these intervals that is not as prominent in other samples.

Steroids

Steroidal biomarkers are known to undergo significant changes in the subsurface in the 40°–60°C temperature range (Mackenzie et al., 1982) and have recently been applied to elucidating subsurface thermal regimes in Northern Hokkaido (Amo et al.,

2007) (Table T35). The C_{27} to C_{29} homologs of the Δ^4 and Δ^5 sterenes and $\Delta^{4,22}$ and $\Delta^{5,22}$ steradienes are identified in Figure F47 (tabulated parameters and abundances are in Table T36). Although steradienes are encountered throughout Hole C0020A, they are hard to interpret because of coelution of other compounds and were not interpreted further during shipboard work. Neither stenols nor stanols were detected in core samples, a finding that is similar to that from previous studies in Hokkaido (Amo et al., 2007) that investigated organic matter of similar thermal maturity.

The abundance of a given sterene homolog varies considerably with lithology and also with depth at Site C0020. Coals contain the greatest proportion of C_{29} sterene homologs, representing a higher proportion of terrestrially derived plant material in sedimentary organic matter (C_{29} sterols such as β-sitosterol and stigmasterol are proportionally more abundant in plants). By comparison, some of the mudstone samples (Fig. F48) contain greater proportions of sterenes that derive from C_{27} and C_{28} sterol homologs, probably representing a greater input from aquatic organisms, particularly algae (Volkman, 1986).

Steranes, by comparison, are far less abundant than sterenes but show similar preferences with regard to carbon number at Site C0020. The thermally immature 5β,14α,17α(H) and 5α,14α,17α(H)20(R) isomers generally predominate. In some instances, sterane isomers that are characteristic of higher thermal maturities are present and are found with triaromatic steroids and thermally mature hopanes—biomarkers found in oils (see Fig. F49). These oil-window biomarkers could indicate migrated petroleum or the erosion and redeposition of an older geological formation that contained thermally mature organic matter including hydrocarbon biomarkers (e.g., Parnell et al., 2007). Drilling during Expedition 337 did not encounter source rocks sufficiently thermally mature to have generated oil; thus, a sedimentary origin seems more feasible until evidence of oil-prone source rocks can be proven.

The conversion of sterenes to steranes is thermally driven and occurs at geologically mild temperatures (40°–60°C) and completes prior to the onset of catagenesis and petroleum formation (Mackenzie et al., 1982). Pathways for the thermal evolution of the sterane/sterene parameter shown in Figure F50 were calculated for Hole C0020A using geothermal gradients of 22°C/km, 24°C/km, and 26°C/km and validate other studies on temperature controls in Amo et al. (2007). It is important to note the considerable scatter evident in sterene data is because of the comparison of data from different lithologies and because this situation did not apply for the data acquired at Hokkaido, shown in the inset of Figure F50. Different mineral surfaces are known to variably catalyze and promote the conversion of sterenes to steranes, and the coal-rich lithologies seem to differ considerably from other lithotypes in both the rate of sterane formation and the relative proportion of the Δ^4 and Δ^5 isomers. Despite this, the point at which pre-oil-window biomarkers begin to form is denoted by a pronounced increase in the parameter between 1800 and 2000 m MSF.

The proportion of the C_{29} sterene homolog is plotted in Figure F51 and compared to the proportion of sediment (sand, mud, and silt) lithologies logged from cuttings samples, which yielded a continuous record over the drilled interval. The highest proportion of mudstone corresponds to a minimum in the proportion of C_{29} sterenes. Key decreases in the parameter occur at ~1200, 1600, and 2000 m CSF-B, where the proportion of mud also drops. Presumably this is consistent with decreased proportions of terrestrially derived sedimentary organic matter that contains C_{29} sterols, which are the chemical precursors of the C_{29} sterenes (Volkman, 1986).

Hopanoids

Time did not permit the satisfactory elucidation of all major peaks in the time range over which hopanes and other pentacyclic terpanoids and terpenoids elute on a *m/z* 191 ion chromatogram (Fig. F49). Diploptene was only detected in cuttings samples from the shallowest interval. The C_{30} and C_{31} homologs of the Δ^{13} and Δ^{17} hopenes are generally the most abundant hydrocarbon terpenoids in deeper intervals. The 14β,17β(H) isomer configuration dominates in most intervals, except where there is evidence of a fossil fuel contribution to samples. This is the case for Sample 337-C0020A-1R-2, 65–81 cm, in which the 14α,17β(H) hopane isomers are dominant. Sample 337-C0020A-1R-2, 65–81 cm, also has a high proportion of lower carbon *n*-alkanes, as does Sample 2R-3, 60–81 cm, for example, which also possesses an unresolved complex mixture and is dominated by 14α,17β(H) hopane isomers. Note that the distribution of hopane carbon numbers in these samples is different to that seen in drilling mud components; ASTEX-S SAS had not been added to drilling mud at this stage and in any case has higher proportions of the C_{35} 14α,17β(H) 22 S and R homologs (see Fig. F52). Visual core description did not note the presence of oil in this interval, but headspace gas monitoring detected notably high proportions of butane in Core 2R. These latter observations, in combination with the high proportions of lower carbon *n*-alkanes, may suggest a lighter oil. A light oil would

be difficult to identify during visual core description without recourse to an ultraviolet (UV) light source to induce fluorescence.

Cuttings

Chromatograms for extracts obtained from cuttings are presented together with core samples in Figures **F51** and **F53.** The distribution of C_{27} to C_{29} Δ^4 and Δ^5 sterenes for Samples 337-C0020A-25-SMW (646.5–656.5 m MSF) and 81-SMW (1096.5–1106.5 m MSF) and a total ion chromatogram for Sample 25-SMW (646.5–656.5 m MSF) are given in Figure **F53.** Data for parameters derived from cuttings are presented in Table **T36.** Extract yields for *n*-alkanes and sterenes are equitable to those reported for mudstone and siltstone sampled from core, indicating that data for these compounds are reliable. An additional level of quality control is outlined in the following paragraph.

Assessment of the effect of drilling operations on hydrocarbon biomarkers

To gauge the impact of the immersion of cuttings within drilling mud, cuttings samples were subjected to sequential extraction. The solvent-soluble products obtained by sonicating samples in solvents were stored and subjected to analysis. The surface of the samples was then rinsed by sonicating samples prior to collecting the solvent to obtain a second extract. Cuttings samples thus cleaned were then crushed and solvent extracted, yielding a third extract. Chromatograms of the products from each stage are displayed in Figure **F53.** The first extraction stage yielded broad, late-eluting peaks that interfere with both chromatography and mass spectrometry. The second stage products are far cleaner, indicating that the cuttings surfaces have been cleaned. The final extraction stage yields thermally immature biomarkers similar to those found in coal and mudstone samples, suggesting that relatively uncontaminated signals can be produced from cuttings that have been aggressively cleaned. Such an approach, where samples are aggressively preextracted, although possibly losing some analyte, has undoubtedly been used before but differs from that presented in literature for petroleum exploration and production, which places an emphasis on either not losing analyte or disrupting samples by cleaning with solvent (Peters et al., 2005). This latter approach is no doubt intended to preserve analyte in porous samples (e.g., reservoir rock), but for scientific, riser-equipped drilling, the loss of analyte for an increase in sample fidelity by the removal of contamination is perhaps preferable.

SAS is a commercially traded drilling additive used to reduce instances of downhole sticking. It comprises a mixture of asphalt (Gilsonite) and mineral phases. GC-mass spectrometer analysis of its content revealed a series of thermally mature components such as hopanes with an 14α,17β(H) configuration. Distinctive features of this hopane fingerprint include high proportions of the C_{35} homologs (Fig. **F52**) and an absence of bisnorhopane (a norhopane that is enriched in many biodegraded petroleum residues). This hopane fingerprint is distinct from both the oil shown in interval 337-C0020A-2R-3, 60–81 cm, and typical samples encountered during Expedition 337 (Fig. **F49**) and made co-mingling of SAS with hopanes indigenous to the hole relatively simple to spot during Expedition 337. An example of a sandstone sample infiltrated by SAS is shown in Figure **F52.**

Procedural blanks

Analysis of procedural blanks indicated that little hydrocarbon biomarker contamination was introduced to samples during laboratory handling. Some peaks occur prior to 25 min, but they were present at too low a concentration to identify by analysis in scan mode (Fig. **F54**).

Microbiology

Expedition 337 was the first riser drilling IODP expedition to incorporate extensive shipboard microbiological and molecular biological analyses. Microbiological samples obtained provided a unique and unprecedented opportunity to not only expand the known depth limits of microbial life in the subseafloor, but also—using chemical and molecular tracers—to assess the degree to which contamination introduced by riser drilling operations affects sample quality. In the designated microbiology laboratory on the *Chikyu*, cell separation and enumeration, DNA extraction, PCR assays on key phylogenetic and metabolic marker genes, molecular fingerprinting analyses, and microscopic observations were all accomplished during the expedition. A wide range of incubations with stable isotope-labeled substrates was initiated to study stable isotope incorporation into nucleic acids and whole cells (for incorporation into lipids and metabolic compounds, see **"Organic geochemistry"**). Radioactive tracer experiments, which involved ^{35}S-labeled sulfate for determination of potential sulfate reduction rates (pSRRs) and a broad set of ^{14}C-labeled substrates to study potential rates of microbial C-cycling reactions (see **"Organic geochemistry"** for ^{14}C-experiments), were carried out in a designated radioisotope van. A large number of samples were, moreover, inoculated with media selecting for a wide range of microbial metabolisms,

including iron reduction, methanogenesis, and acetogenesis.

The sampling scheme for WRCs and experimental procedures for shipboard and shore-based analyses are illustrated in Figure **F55.** In total, nearly 300 WRCs out of 32 drill cores were sampled for microbiological investigations (for details, see MBIO_SAMPLE_LIST.XLSX in MBIO in **"Supplementary material"**). Contaminated outer core layers containing potential drilling mud contamination were removed from all WRCs by sterile spatulas or ceramic knives prior to sampling.

Contamination tests

Chemical tracer

Measured perfluorocarbon (PFC) tracer concentrations fluctuated greatly over time and remained under the target concentration of 1 mg/L for most of the expedition (Fig. **F56**). During the initial days of the expedition, PFC concentrations in mud tank samples remained remarkably low, despite daily additions of 100 mL of PFC tracer (Table **T37**), which were, in principle, sufficient to produce PFC tracer saturation (~2 mg/L) (Colwell et al., 1992). The low initial concentration turned out to be, in part, a problem of the extraction method used. Without further PFC tracer addition, measured PFC values increased drastically when a 1 h preincubation step at 80°C with active sample mixing was included prior to the 30 min preincubation without mixing in the autosampler (also see **"Microbiology"** in the "Methods" chapter [Expedition 337 Scientists, 2013b]). Before coring began, this new preincubation period was increased to 2 h (starting 17 September) to ensure maximum PFC tracer recovery and thus as accurate as possible quantification of drilling mud contamination.

Despite daily PFC additions to active tanks and methodological improvements, PFC concentrations in drilling mud were found to fluctuate considerably on a day-to-day basis. The good agreement between measurements in the physically separated active Tanks 4 and 5, from which we obtained drilling mud samples at the same time of day, indicates that this was not a matter of insufficient homogenization. Instead, these fluctuations are probably to a large extent explained by day-to-day variations in drilling mud production and hence PFC dilution. Because of these fluctuations and the limited sampling frequency of one time per day, the exact PFC concentration in drilling mud at the time of coring was unknown. Fortunately, PFC concentration in active tanks, core liner fluid, and upon recovery in the mud ditch typically exceeded 100 µg/L, allowing calculations of drilling mud intrusion using an assumed constant PFC concentration of 100 µg/L. Because this concentration is lower than most of the measured PFC concentrations, contamination estimates based on this value should be considered conservative.

On average, PFC concentrations in mud fluid from the active tanks, core liner, and upon recovery from the mud ditch show good agreement (typically within a factor of 2), indicating that PFC losses (e.g., because of volatilization during core processing and mud recovery) are minor. The on average slightly lower measured values in the core liner and mud ditch compared to the active tanks might at least in part be due to dilution with core samples during drilling operations.

Using the same preincubation method as for drilling mud, PFC concentrations were determined in cuttings and cores. Volumes of drilling mud intrusion and numbers of contaminant cells introduced were subsequently calculated using an assumed PFC concentration of 100 µg/L (0.1 µg PFC/mL) drilling mud and cell concentration of 2.66×10^8 cells/mL drilling mud (mean value of microscopic direct counts) (Table **T38,** also see **"Cell counts,"** as well as Smith et al., 2000, for details on calculation method). Cuttings were highly contaminated with drilling mud, with all values except one (Sample 337-C0020A-267-SMW) exceeding 1% (v/v) contamination of pore fluid, and contamination in many samples exceeding 100 µL/g sample (Table **T39**). Although the outside and exterior of cores typically showed high levels of contamination, the inner portions in most cases showed much lower contamination (Table **T40**). In many samples obtained from the innermost portions of cores, PFC tracers were even below detection. To estimate the maximum drilling mud contamination and number of contaminant cells that could still be present in samples where PFC was below detection, we inferred the PFC detection limit based on the data distribution of PFC values measured on cores (Fig. **F57**). Drilling mud contamination of samples, in which PFC was below detection, was conservatively calculated substituting the detection limit value of 8 pg. We then calculated the maximal amount of drilling mud, and hence contaminant cells, within core samples where PFC was below detection (bracketed values in Table **T40**) based on

- A detection limit of 8 pg,
- An assumed concentration of 100 µg PFC/mL drilling mud,
- The volume of headspace injected into the gas chromatograph with electron capture detector (GC-ECD; 0.5 cm^3),
- The total sample amount (g),

- The total sample volume (g sample × sample bulk density),
- The total headspace volume (20 cm^3 – total volume of sample), and
- An average cell concentration of 2.66×10^8 cells/mL drilling mud.

To examine the relationship between drilling mud contamination and environmental variables, we plotted drilling mud contamination versus depth (Fig. F58). Apart from the expected trend of higher contamination in exterior compared to interior parts of cores, the critical importance of vertically resolved contamination measurements was underscored; several cores, from depths spanning almost the entire interval cored, harbored very high drilling mud contamination all the way to the core center. We also examined the relationship between contamination within core interiors and lithology (Fig. F59). Perhaps surprisingly, no clear contamination trends could be attributed to lithology. PFC results for core, drilling mud, and cuttings are summarized in PFC-CORE.XLSX, PFC-CUTTINGS.XLSX, and PFC-DRILLING MUD.XLSX in MBIO in "Supplementary material."

Cell counts

Cell counts in drilling mud and cuttings

Cell concentrations in drilling mud were enumerated daily. Cell counts ranged from 1.10×10^8 to ~8.37×10^8 microbial cells/mL drilling mud before drilling started and did not change markedly throughout drilling operations. We also observed 1.6×10^7 to 9.8×10^7 cells/mL in cuttings samples from 646 to 1046 m MSF (Table T39). These cell counts are close to or higher than the cell counts observed in the shallower (100~346 mbsf) part of this site obtained during the *Chikyu* shakedown cruise (Expedition CK06-06). Simple extrapolation from the cell abundance curve from shallower depths predicts that the number of the cells in the formation is $<10^6$ cells/cm^3. Combined with the fact that high PFC concentrations were detected in cuttings, we attribute these high cell numbers predominantly to contamination with drilling mud. Calculations based on cell numbers in drilling mud samples indicate that roughly 6%–38% of the volume of cuttings consists of drilling mud.

Cell counts in core samples

From the microbiology community WRCs, 2 cm^3 was aseptically taken from the innermost parts, immediately fixed, and processed using the cell separation method described in "Microbiology" in the "Methods" chapter (Expedition 337 Scientists, 2013b). In total, 94 samples were taken for cell enumeration (Fig. F55; also see MBIO_SAMPLE_LIST.XLSX in MBIO in "Supplementary material"). Cell separation was done under a clean air-flow safety cabinet with daily intensive cleaning prior to separation. To minimize the contamination risk from stock solutions, small aliquots of these solutions were stored after filtration and underwent cell separation. After cell separation, these solutions were again passed through a 0.22 µm pore cartridge filter and poured directly into sample tubes. The initial attempts to determine cell abundance in core samples during Expedition 337 were performed using an image-based automatic cell enumeration system (Morono et al., 2009; Morono and Inagaki, 2010). However, because of very low cell abundances, entire filter membranes had to be counted, resulting in long processing periods. Therefore, we decided to count microbial cells from core samples using visual direct counts and flow cytometry (FCM). For direct counts, we selectively counted green fluorescent cells under the microscope. Particles that emitted other colors were not counted.

Although cell abundance was generally low (Fig. F60), cell numbers were above the minimum quantification limit (MQL) even in deeper layers. The cell counts as well as the MQL obtained by FCM are generally higher than the microscopic counts. This is mainly due to the existence of noncellular particles that fluoresce in green color. There was no problem avoiding these particles during counting under a microscope. However, these unspecific signals were difficult to eliminate from the FCM data. In addition, we saw these noncellular particles in blank samples, suggesting that these particles might be generated through the sample preparation protocol. Although we could not solve this problem on board the ship, we will try to eliminate it in shore-based work. Seven and five blanks were counted by microscope and FCM, respectively, and resulted in MQLs of 115 and 6350 cells/cm^3, respectively.

In core samples from intervals 337-C0020A-25R-3, 140–141 cm (1999 m CSF-B); 32R-1, 144–145 cm (2457 m CSF-B); and 32R-2, 43–65 cm (2458 m CSF-B), we found microbial cells attached to surfaces of mineral particles (Fig. F61). By comparison, we did not see any particles with attached cells in blank samples. Considering the size of these particles (i.e., 10~20 µm in diameter), it seems unlikely that they were introduced via drilling mud intrusion. Instead, because these samples were all from sandy silt or sandstone, they could be evidence of indigenous microbes residing on mineral surfaces.

DNA extraction

Hot alkaline lysis protocol

Thirty-eight out of 47 microbiology community WRCs (MBIO, Fig. F55) were used for DNA extraction using the hot alkaline lysis protocol. For each extraction, 2–5 cm^3 of sample was used. Apart from the extract from the coal layer at Section 337-C0020A-24R-5, which had a black color, crude extracts generally had a brown color. To prevent PCR inhibition, we purified all extracted DNA with an Aurora system (Boreal genomics, Vancouver, Canada). For this purpose, the Aurora low molecular weight soil protocol (without the wash block) was used according to the manufacturer's instructions. For samples with dense black color, the Aurora 0.7-53kb DNA from soil with enhanced contaminant rejection protocol was used. The final volume of purified DNA solution was ~60 µL and was used for subsequent quantitative polymerase chain reaction (qPCR) and terminal restriction fragment length polymorphism (T-RFLP) analyses.

Chemical lysis protocol

DNA extractions using the chemical lysis protocol were performed on 13 drilling mud samples from active Tank 4, 12 unwashed cuttings samples, 4 washed cuttings samples, and 11 of the 47 microbiology community WRCs (MBIO, Fig. F55). Drilling mud samples were chosen at time points spanning the entire expedition to monitor changes in microbial communities and DNA signatures within drilling mud as background controls for DNA detected in cores. DNA was also extracted from unwashed cuttings obtained throughout the expedition, both as additional background controls for DNA contamination in cores and to examine the potential for cuttings to provide information on indigenous deep subseafloor microorganisms. It was anticipated that DNA of strictly anaerobic microorganisms, which might be below detection in drilling mud, could perhaps be detected in cuttings. Under this scenario, useful phylogenetic and/or metabolic information on in situ communities could be obtained from cuttings originating from drilling intervals without WRC sampling, such as the depth interval from 646 to 1046 m MSF (i.e., Unit I). For comparison to unwashed cuttings, DNA was also extracted from four samples of washed cuttings obtained during the early stage of the expedition.

DNA extractions were performed in parallel on the contaminated exterior and the typically cleaner inner core portions, resulting in a total of 22 DNA extractions from cores. Samples were chosen based on depth, lithology, and contamination of the core interior, with the aim of extracting DNA from samples spanning the entire depth interval sampled, from all main lithologies, and from samples with minimal drilling mud intrusion. Two cores were dominated by fine to medium sandstone (Sections 337-C0020A-10R-2 and 16R-2), two by fine sandstone (Sections 28R-6 and 30R-4), two by siltstone (Sections 3R-3 and, 20R-3), two by coal (Sections 15R-2 and 24R-3), and three by shale (Sections 7R-1, 15R-5, and 26R-7). Drilling mud contamination was below detection in the inner portion of seven of these samples (Sections 7R-1, 10R-2, 15R-5, 20R-3, 26R-7, 28R-6, and 30R-4) but was always detectable in the exterior portion (Tables T40, T41), with estimated contaminant cells in the exterior exceeding 10^5 cells in all except Section 28R-6, with 5.6×10^3 cells/cm^3.

Extracellular DNA extraction

Samples for shipboard extracellular DNA extraction (MLWR, Fig. F55) were obtained from 22 WRCs. Of these, all but one highly contaminated sample from Section 32R-2 were processed, typically within 24 h of sampling. Several core samples consisting of unconsolidated sand, fine sandstone, and shale were observed to contain intact snail and clam shells, infilled fossilized worm burrows, and terrestrial plant debris, making them promising samples for the planned exploration of extracellular DNA pools as genetic archives of ancient biological communities.

PCR

Sources of DNA in drilling mud

Most probable number PCR assays were performed on DNA extracts from drilling mud, cuttings, and cores using PCR primer pairs targeting phylogenetic clusters ubiquitously detected in surface seawater (SAR11 and Marine Group I [MGI] Archaea), viscosifiers used during riser drilling (*Xanthomonas* and *Halomonas*), and anthropogenic wastewater (*Bifidobacterium, Blautia*, and *Methanobrevibacter*) (Table T41). All three indicator organism groups yielded successful PCR amplification; however, the frequency of detection and abundance varied tremendously. *Xanthomonas* and *Halomonas* were detected in the vast majority of drilling mud and cuttings samples, two of 11 core interiors, and six of 11 core exteriors. SAR11 was found in all the initial samples but not later on during the expedition. The MGI Archaea, *Bifidobacterium, Blautia*, and *Methanobrevibacter* were only detected a few isolated times and at low abundances. These results clearly suggest that the biggest risk of core DNA contamination obtained by riser drilling during Expedition 337 was from microbes that have been linked to mud viscosifiers used

to prepare drilling mud (Masui et al., 2008). Microbes from surface seawater represented a significant source of contamination in the initial phase but less so later on, whereas the risk of contamination with human sewage–derived DNA was low.

Open questions remain regarding the variables explaining the observed DNA contamination trends. Considering the chemically harsh environment of drilling mud, with highly alkaline pH (9–11.5) and hypersaline (578–847 mM K^+ to 1150 mM Na^+) conditions, one might expect seawater- and human sewage–derived microorganisms to die and their DNA to disappear (e.g., due to hydrolysis by DNAses or uptake by surviving organisms) within a short time after drilling mud preparation. The observed disappearance of DNA indicative of these organisms within the initial drilling period is consistent with this interpretation. Yet, fresh drilling mud was also prepared later during the expedition and hence one would expect a reemergence of DNA indicative of seawater microbes during this later stage of the expedition. Since the mud in the initial drilling period of operations was prepared prior to Expedition 337, the seawater in the tank was taken from a different geographic location, possibly influencing the variability of contaminant cell abundance in the mud over the course of drilling operations.

Whether the observed high abundances of *Xanthomonas* and *Halomonas* DNA can be attributed to living organisms or high inputs of DNA included in viscosifiers is also not clear. Xanthomonads are used industrially in the synthesis of xanthan gum, a component of the drilling mud gelling agent bentonite, and could potentially grow within drilling mud using organic compounds supplied as gelling agents as an energy source. However, past efforts to grow Xanthomonads from drilling mud using standard *Xanthomonas* enrichment assays have failed (Masui et al., 2008), suggesting that alive xanthomonads are absent and that *Xanthomonas* DNA detected may be left over from the production process of bentonite. The presence of *Halomonas* is perhaps easier to explain: members of this versatile group are widely distributed in seawater, can tolerate high salinities and pH, grow aerobically and anaerobically, and utilize a wide range of organic carbon compounds as energy sources. Thus, though it remains to be shown, it is possible that the broadly adapted and opportunistic *Halomonas* can grow within drilling mud and account for a significant fraction of the high cell densities observed there.

qPCR

Quantifications of bacterial and archaeal 16S rRNA genes were performed on DNA extracts obtained from cores using the alkaline lysis and chemical lysis methods (Fig. **F62**). Negative controls, in which molecular-grade water had been substituted for sample material during extractions, were also examined.

Because of background bacterial contamination from extraction and PCR reagents, amplification of bacterial DNA was also observed in negative controls for the DNA extraction. Therefore, we set the detection limit for bacterial gene detection in DNA extracted from cores to 2× the copy number obtained in negative controls (1.5×10^4 copies/cm^3). Archaeal qPCR did not show any amplification from negative controls and could thus detect as few as 1 copy of rRNA genes per reaction.

For both extraction methods, we observed that bacterial DNA from cores amplified at a lower PCR amplification rate than bacterial DNA from extraction negative controls or PCR negative controls, indicating PCR inhibition by co-extracted substances for both the hot alkaline lysis and chemical lysis methods—despite purification by the Aurora system and Norgen Cleanup kit, respectively. Thus, estimated copy numbers most likely underestimate actual copy numbers in cores. More accurate quantifications will be attempted on shore by further improvements to the DNA extraction and purification methods, as well as a newly developed digital PCR technique that is less affected by PCR inhibitors, such as humic acids (Hoshino and Inagaki, 2012).

Overall, our qPCR data confirm the very low in situ cell abundances of microorganisms determined by cell counts (Fig. **F62**). Highly elevated bacterial gene copy numbers of $>10^6$ cm^{-3} were only found in Sections 337-C0020A-1R-2, 2R-3, and 5R-3 (Table **T41**), which were highly contaminated with drilling mud all the way to the innermost parts according to PFC analyses (Table **T40**). All other cores harbored estimated bacterial gene copy numbers between 10^3–10^6 cm^{-3} of sample. Archaeal 16S rRNA gene copy numbers were consistently lower than bacterial copy numbers by two or more orders of magnitude. Several of the core samples with bacterial 16S rRNA genes detected by general bacterial primers also tested positive for 16S rRNA genes of *Xanthomonas* and *Halomonas*, indicating drilling mud contamination. The degree of contamination (i.e., whether contaminant DNA dominates or is only a minor fraction of total DNA in these samples) will be evaluated by next-generation DNA sequencing on shore.

Bacterial and archaeal gene copy numbers were converted to cell numbers using standard conversion factors, in which 4.07 and 1.76 copies of 16S rRNA genes were assumed per bacterial and archaeal cell, respectively (values from Ribosomal Database Proj-

ect, rdp.cme.msu.edu/; Fig. F62). Both DNA extraction methods showed good agreement in estimates of bacterial and archaeal cell numbers, in spite of using different primer pairs. Interestingly, our data suggest that archaeal abundance showed no clear depth-related trend, whereas an overall decrease in bacterial abundance occurred with depth. The fact that Archaea were detectable to greater depths than Bacteria is attributable to the much higher detection limit of Bacteria that resulted from the higher level of bacterial background DNA in both PCR reaction and DNA extraction negative controls. In addition to digital PCR quantification, the use of larger core volumes for DNA extractions and improvements to the DNA purification procedure in shore-based investigations will hopefully enable us to reliably quantify Bacteria to greater depths than during the expedition.

DNA fingerprinting techniques

T-RFLP, which is a molecular fingerprinting technique to monitor differences in microbial community structures across different habitats, was performed on 37 microbiology community samples, 10 drilling mud samples, and 3 extraction negative controls. Full 16S rRNA gene amplification was tested by PCR using bacterial and archaeal domain-specific primers. Full archaeal 16S rRNA genes were not amplifiable from any of the samples, but we were able to amplify bacterial 16S rRNA genes. Yet, checks with gel electrophoresis revealed only faint bands of amplified DNA in DNA extracts from below Core 337-C0020A-20R (1962 m CSF-B).

The bacterial community structure of drilling mud samples showed consistent peak locations, suggesting that the microbial community composition of drilling mud was stable throughout the entire drilling period. Terminal restriction fragments (T-RFs) of 181, 553, and 572 base pairs (bp) were observed in all drilling mud samples (Fig. F63) and could thus be used to assess drilling mud contamination in cores. We also obtained bacterial PCR products from negative controls of the DNA extraction. These negative controls provided 200, 666, and 780 bp T-RFs in T-RFLP profiles. Moreover, a T-RF of 233 bp was detected within PCR negative controls, though this amplicon was not detected by agarose gel electrophoresis.

T-RFLP results from cores show only a few peaks, indicating low diversity of indigenous bacterial communities and/or very low copy numbers of amplifiable template DNA in the initial PCR (Fig. F64). T-RFLP profiles also indicate that contamination during drilling, DNA extraction, and from PCR reagents was significant because T-RFs characteristic of drilling mud and DNA extraction negative controls were observed in most core samples. Certain samples contained T-RFs that could not be attributed to contamination, however; for example, a T-RF of 566 bp was unique to DNA extracts from Samples 13R-2, 105–120 cm, to 32R-2, 43–65 cm. Additional T-RFs of 99 and 763 bp appeared only from Samples 19R-8, 60–77 cm, 20R-3, 13–23 cm, and 20R-7, 62–76 cm. Our results from T-RFLP thus demonstrate that, despite low yields, DNA of indigenous bacterial cells was obtained by the shipboard molecular biology program.

Functional genes

We performed PCR assays targeting functional marker genes of methanogenesis and anaerobic methanotrophy (methyl coenzyme M reductase [*mcrA*]), dissimilatory sulfate reduction (dissimilatory sulfate reductase [*dsrB*]), and acetogenesis (formyl tetrahydrofolate synthetase [*fhs*]) on DNA extracts from drilling mud, cuttings, and, in the case of *mcrA*, cores (Table T41). Because of time constraints, we were unable to check for *dsrB* and *fhs* presence in cores during the expedition, but we plan to do this soon after returning to our home laboratories.

Although *mcrA* was consistently below detection in DNA extracts from drilling mud, we were able to amplify PCR product of the right amplicon size for *mcrA* in two cuttings samples (Samples 337-C0020A-30-SMW and 61-SMW) and the interiors of two cores (Sections 16R-2 and 20R-3; Table T41). *dsrB* was not detectable in any drilling mud or cutting samples. *fhs* was detectable in most cuttings but below detection in drilling mud after 50 cycles of PCR amplification. After an additional 50 PCR cycles, however, amplicons of the right fragment size were also found in DNA extracts from drilling mud.

Our shipboard results from PCR assays on metabolic marker genes are further evidence that DNA belonging to indigenous microorganisms was extracted on board the ship. *mcrA* genes of probably methanogenic microorganisms were solely detected in core samples and cuttings—not in drilling mud. *fhs* genes were found to be in vastly higher abundance in cuttings compared to drilling mud. These results also suggest that, despite being highly contaminated with drilling mud, cuttings can provide potentially useful genetic information on anaerobic microorganisms inhabiting the deep subseafloor in Hole C0020A.

Potential sulfate reduction rates

A total of 28 WRCs were sampled for pSRR measurements, covering the entire drilling interval at Site C0020 (Table T42). For each sample depth, two sets

of duplicate samples (A, B and C, D) were obtained. Additionally, a set of samples (A–D) was obtained from the pooled master sample (1950–2000 msbf). Sample volumes were ~5 cm^3 and measured sample weights ranged from 4.4 to 9.8 g depending on density and moisture. A and B samples were incubated with N_2 headspace, whereas 15 mL of CH_4 (99.9%) were added via syringe to the N_2 headspace of C and D samples, resulting in an increased pressure of ~2 bar. An additional set of samples (A, B, C, and D), obtained from mud tanks that were actively circulating drilling mud before sampling, were incubated as contamination controls.

To each sample, 3.7 MBq of ^{35}S Na_2SO_4 (30 µL of aqueous solution) was added, except for Sample 337-C0020A-30R-3, 72–77 cm, where 7.4 MBq was added. For drilling mud samples, 2.1 MBq was added. The incubation time for all samples incubated before 11 September 2012 was 10 days. Sample 30R-2, 72–77 cm, and the drilling mud samples were incubated for 9 and 6 days, respectively. Samples obtained from the pooled master sample (1950–2000 m CSF-B) were incubated for 5 days. Three incubation temperatures were chosen to account for increasing in situ temperature with depth. Temperature I (~25°C, room temperature) was used for samples from Cores 1R through 6R (1276.70–1495.00 m CSF-B), Temperature II (35°C, Incubator I) was used for samples from Cores 8L and 9R through 22R (1607.16–1977.84 m CSF-B), and Temperature III (45°C, Incubator II) was used for samples from Cores 23R through 32R (1984.13–2456.63 m CSF-B) (Table T42) and for the pooled master sample. Drilling mud samples were incubated at room temperature.

Incubation for shore-based cultivation of deep subseafloor microbes

Six unwashed samples of cuttings from 696.5 to 1206.5 m MSF and formation fluid obtained from the Quicksilver probe at 1279.5, 1844.0, and 1978.0 m WMSF were used as inoculum to enrich for anaerobically respiring microbes such as methanogens, homoacetogens, and ferric iron reducers. Formation fluid from 1489.3, 1808.0, and 1901.2 m WMSF and all WRCs obtained during the expedition, were stored under anaerobic conditions at 4°C for shore-based cultivation. After the shipboard incubation of unwashed cuttings, growing cells were confirmed based on culture turbidity and microscopic observations of enriched cells. We observed particularly high turbidity and many cells in media targeting iron reducers (i.e., media of ferric citrate, lepidocrocite, goethite, hematite, and magnetite) and homoacetogens (i.e., medium of H_2/CO_2 plus bromoethanesulfonic acid [BES]) (Fig. F65). In addition, there seemed to be cell growth with media targeting hydrogenotrophic and methylotrophic methanogens (i.e., media with H_2/CO_2 and methanol, respectively). Because these first-generation enrichment cultures likely contain carbon and energy sources originally present in unwashed cuttings, it is uncertain whether the targeted microbes grew on the substrates supplied in the media or substrates present in drilling mud. Continuous subculturing will be conducted on shore in order to remove the effects of substrates other than the ones supplied through media.

Using light microscopy, fungal sporelike structures were identified in incubated core samples (Sections 337-C0020A-8L-5, 10R-2, 13R-1, 14R-2, 15R-3, 15R-5, 20R-7, and 28R-3) and seawater (Table T43). Furthermore, based on size, morphology, and motility, several types of microorganisms were discriminated. Motile filaments were observed in high abundance in drilling mud (Sample 337-C0020A-245-LMW) and core Sections 7R-1, 15R-7, and 25R-2 and in low abundance in seawater and core Sections 13R-1, 15R-3, and 20R-7, suggesting origin from drilling mud. We will conduct shore-based PCR assays to target fungal DNA and discriminate between indigenous and contaminant communities.

Additional sampling for shore-based microbiological investigations

Single-cell analyses of carbon and nitrogen assimilation rates of subseafloor autotrophic and heterotrophic microbial communities

Six WRC samples and the pooled master sample were used for detecting incorporation of stable isotope-labeled substrates into whole cells by nanoscale secondary-ion mass spectrometry (NanoSIMS): intervals 337-C0020A-4R-1, 100–141.5 cm; 4R-2, 0–47 cm (1376 m CSF-B); 8L-4, 50–100 cm (1606 m CSF-B); 14R-1, 40–80 cm (1820 m CSF-B); 15R-3, 20–48 cm (1921 m CSF-B); 18R-1, 71–114 cm (1946 m CSF-B); 25R-2, 50–60 cm; 26R-4, 40–140 cm (2114 m CSF-B); and 32R-4, 70–141 cm (2461 m CSF-B). After whole-round cutting, samples were flushed with N_2, vacuum-sealed, and stored at 4°C. Utilizing aseptic techniques and within 24–48 h after retrieval, core surfaces were removed three successive times to remove contaminated outer parts—either within an aerobic clean bench or nitrogen glove bag, Sections were freshly packaged, reflushed with N_2, vacuum-sealed, and stored at 4°C until inoculation.

Samples were obtained in an anaerobic glove box using a wide spatula and hammer to break cores into centimeter-sized pieces. Pieces were then divided evenly among 120 50 mL glass vials and sealed with

butyl rubber stoppers. Within 24 h, samples were flushed with filtered Ar to remove H_2 and N_2 from headspace and stored at 4°C until substrate addition.

Vials were filled to achieve an estimated sample volume of 5–10 cm^3 per incubation (depending on total sample volume). Substrates were added to establish concentrations of ^{13}C (mixture of 15 µM each of ^{13}C and natural-abundance isotope-ratio C-bearing substrates), ^{15}N (mixture of 1.5 µM of ^{15}N and natural-abundance isotope-ratio N-bearing substrates), and 20 vol% deuterium in water. Killed controls were autoclaved before any seawater or substrate was added. Samples were stored at 4°C on board the ship and during shipping to home institutions, where they were then incubated at near in situ temperatures.

Sandwich experiment

The coal WRC from Section 337-C0020A-18R-1 was prepared for shipboard stable isotope incubation. The section was dabbed with KimWipes soaked in anaerobic Milli-Q water in a glove box, and then gently broken into 1–2 cm thick sections to create artificial fracture surfaces. UV-sterilized 47 mm polycarbonate and cellulose acetate membranes were soaked with substrate and placed between core breaking points, and then "sandwiched" back together by wrapping them with Parafilm. Labeled substrates were added with 1 µM carbon and/or 0.1 µM nitrogen according to Table **T10** in the "Methods" chapter (Expedition 337 Scientists, 2013b), with the exception of cellulose, of which a suspension containing 176 mg was placed on the polycarbonate membrane. "Sandwiches" were anaerobically incubated in the dark at 42°C without shaking.

Hydrogenase activity measurements

Samples for hydrogenase activity measurements were sampled from WRCs also used for pSRR incubations. The potentially contaminated outer 1 cm of 28 WRCs was carefully removed in an anaerobic glove box using sterilized spatulas and knifes. Approximately 50 cm^3 was packed in ESCAL bags, flushed with nitrogen, vacuum-sealed, and stored at –80°C for shore-based tritium incubation experiments.

Conclusions

Data obtained during Expedition 337 demonstrate the suitability of PFC tracers to monitor contamination during riser drilling operations and indicate that the majority of core samples obtained have low levels of contamination at the core center. The successful extraction of cells and DNA demonstrates that the monitoring of microbial populations in cores obtained by riser drilling is possible on board the ship. Community fingerprinting analyses suggest that a substantial fraction of the DNA detected within cores belongs to indigenous communities of microorganisms. Although high cell numbers found in sandy and less consolidated layers were almost certainly the result of sample contamination by drilling mud, cell numbers only slightly above the detection limit in other cores—all the way to Core 337-C0020A-32R at 2460 m CSF-B—are less likely to result from drilling mud contamination. Shore-based molecular analyses will reveal the extent to which cells and DNA detected indeed belong to in situ microbial communities, and, if so, what their metabolic potential is based on functional gene and metagenomic analyses.

A broad range of experiments investigating microbial community zonation and activity in Expedition 337 core samples was initiated on board the ship. In the upcoming months and years, these experiments will produce novel insights to the life histories of subseafloor microbes in the deep core samples and coalbeds at Site C0020. The focus on combined nanoSIMS and single-cell approaches is likely to provide altogether novel insights to the modes of biomass assimilation and energy production in these fascinating, deeply buried microbial communities from the deepest borehole sampled by scientific drilling to this date.

References

Amo, M., Suzuki, N., Shinoda, T., Ratnayake, N.P., and Takahashi, K., 2007. Diagenesis and distribution of sterenes in late Miocene to Pliocene marine siliceous rocks from Horonobe (Hokkaido, Japan). *Org. Geochem.,* 38(7):1132–1145. **doi:10.1016/j.orggeochem.2007.02.010**

Beardsmore, G.R., and Cull, J.P., 2001. *Crustal Heat Flow: A Guide to Measurement and Modelling:* Cambridge (Cambridge Univ. Press).

Boggs, S., Jr., 2006. *Principles of Sedimentology and Stratigraphy* (4th ed.): New York (Prentice-Hall).

Borowski, W.S., Alperin, M.J., Rodriguez, N.M., and Paull, C.K., 2000. Significance of anaerobic methane oxidation in methane-rich sediments overlying the Blake Ridge gas hydrates. *In* Paull, C.K., Matsumoto, R., Wallace, P.J., and Dillon, W.P. (Eds.), *Proc. ODP, Sci. Results,* 164: College Station, TX (Ocean Drilling Program), 87–99. **doi:10.2973/odp.proc.sr.164.214.2000**

Bujak, J.P., 1984. Cenozoic dinoflagellate cysts and acritarchs from the Bering Sea and northern North Pacific, DSDP Leg 19. *Micropaleontology,* 30(2):180–212. **doi:10.2307/1485717**

Bujak, J.P., and Matsuoka, K., 1986. Late Cenozoic dinoflagellate cyst zonation in the western and northern Pacific. *In* Wrenn, J.H., Duffield, S.L., and Stein, J.A. (Eds.), *Papers from the First Symposium on Neogene Dinoflagellate Cyst Biostratigraphy.* AASP Contrib. Ser., 17:7–26.

Carrie, J., Sanei, H., and Stern, G., 2012. Standardisation of Rock-Eval pyrolysis for the analysis of recent sediments and soils. *Org. Geochem.,* 46:38–53. **doi:10.1016/j.orggeochem.2012.01.011**

Cloud, P.E., 1955. Physical limits of glauconite formation. *AAPG Bull.,* 39(4):484–492. **http://aapgbull.geoscienceworld.org/content/39/9/1878.abstract**

Colwell, F.S., Stormberg, G.J., Phelps, T.J., Birnbaum, S.A., McKinley, J., Rawson, S.A., Veverka, C., Goodwin, S., Long, P.E., Russell, B.F., Garland, T., Thompson, D., Skinner, P., and Grover, S., 1992. Innovative techniques for collection of saturated and unsaturated subsurface basalts and sediments for microbiological characterization. *J. Microbiol. Methods,* 15(4):279–292. **doi:10.1016/0167-7012(92)90047-8**

Derry, L.A., and France-Lanord, C., 1996. Neogene Himalayan weathering history and river $^{87}Sr/^{86}Sr$: impact on the marine Sr record. *Earth Planet. Sci. Lett.,* 142(1–2):59–74. **doi:10.1016/0012-821X(96)00091-X**

D'Hondt, S.L., Jørgensen, B.B., Miller, D.J., et al., 2003. *Proc. ODP, Init. Repts.,* 201: College Station, TX (Ocean Drilling Program). **doi:10.2973/odp.proc.ir.201.2003**

Dowdle, W.L., and Cobb, W.M., 1975. Static formation temperature from well logs—an empirical method. *J. Pet. Technol.,* 27(11):1326–1330. **doi:10.2118/5036-PA**

Duzgoren-Aydin, N.S., Aydin, A., and Malpas, J., 2002. Re-assessment of chemical weathering indices: case study on pyroclastic rocks of Hong Kong. *Eng. Geol.,* 63(1–2):99–119. **doi:10.1016/S0013-7952(01)00073-4**

Eikenberg, J., 1990. *On the Problem of Silica Solubility at High pH:* Villigen, Switzerland (Paul Scherrer Inst.).

Espinosa-Paredes, G., Morales-Díaz, A., Olea-Gonzáles, U., and Ambriz-Garcia, J.J., 2009. Application of a proportional-integral control for the estimation of static formation temperatures in oil wells. *Mar. Pet. Geol.,* 26(2):259–268. **doi:10.1016/j.marpetgeo.2007.11.002**

Ertefai, T.F., Heuer, V.B., Prieto-Mollar, X., Vogt, C., Sylva, S.P., Seewald, J., and Hinrichs, K.-U., 2010. The biogeochemistry of sorbed methane in marine sediments. *Geochem. Cosmochim. Acta,* 74(1):6033–6048. **doi:10.1016/j.gca.2010.08.006**

Erzinger, J., Wiersberg, T., and Zimmer, M., 2006. Real-time mud gas logging and sampling during drilling. *Geofluids,* 6(3):225–233. **doi:10.1111/j.1468-8123.2006.00152.x**

Expedition 337 Scientists, 2013a. Expedition 337 summary. *In* Inagaki, F., Hinrichs, K.-U., Kubo, Y., and the Expedition 337 Scientists, *Proc. IODP,* 337: Tokyo (Integrated Ocean Drilling Program Management International, Inc.). **doi:10.2204/iodp.proc.337.101.2013**

Expedition 337 Scientists, 2013b. Methods. *In* Inagaki, F., Hinrichs, K.-U., Kubo, Y., and the Expedition 337 Scientists, *Proc. IODP,* 337: Tokyo (Integrated Ocean Drilling Program Management International, Inc.). **doi:10.2204/iodp.proc.337.102.2013**

Higuchi, K., Ishii, Y., Kaminishi, T., Ibusuki, A., Aoike, K., and Kobayashi, S., 2009. *CDEX Technical Report* (Vol. 6): *Drilling Completion Report Shimokita-West:* Yokohama (CDEX-JAMSTEC).

Hoshino, T., and Inagaki, F., 2012. Molecular quantification of environmental DNA using microfluidics and digital PCR. *Syst. Appl. Microbiol.,* 35(6):390–395. **doi:10.1016/j.syapm.2012.06.006**

Igarashi, G., Saeki, S., Takahata, N., Sumikawa, K., Tasaka, S., Sasaki, Y., Takahashi, M., and Sano, Y., 1995. Ground-water radon anomaly before the Kobe earthquake in Japan. *Science,* 269(5220):60–61. **doi:10.1126/science.269.5220.60**

Ijiri, A., Sakamoto, T., Tsunogai, U., Gamo, T., Saito, S., and Suyehiro, K., 2003. Data report: authigenic carbonates at Sites 1150 and 1151. *In* Suyehiro, K., Sacks, I.S., Acton, G.D., and Oda, M. (Eds.), *Proc. ODP, Sci. Results,* 186: College Station, TX (Ocean Drilling Program), 1–6. **doi:10.2973/odp.proc.sr.186.109.2003**

Kaneda, T., 1991. *Iso-* and *anteiso*-fatty acids in bacteria: biosynthesis, function, and taxonomic significance. *Microbiol. Rev.,* 55(2):288–302. **http://www.ncbi.nlm.nih.gov/pmc/articles/PMC372815/pdf/microrev00033-0106.pdf**

Killops, S.D., and Killops, V.J., 2005. *Introduction to Organic Geochemistry* (2nd ed.): Oxford (Blackwell Science Ltd.).

Kowalenko, C.G., and Yu, S., 1996. Solution, exchangeable and clay-fixed ammonium in south coast British Columbia soils. *Can. J. Soil Sci.,* 76(4):473–483. **doi:10.4141/cjss96-059**

Kurita, H., 2004. Paleogene dinoflagellate cyst biostratigraphy of northern Japan. *Micropaleontology,* 50(Suppl. 2):3–50. **doi:10.2113/50.Suppl_2.3**

Kurita, H., and Matsuoka, K., 1994. *Trinovantedinium boreale* Bujak–dominated dinoflagellate assemblages in Eocene–Oligocene stratified water in northern Japan. *Rev. Palaeobot. Palynol.,* 84(1–2):129–153. **doi:10.1016/0034-6667(94)90047-7**

Kurita, H., and Obuse, A., 1994. Paleogene dinoflagellate cysts and pollen from Haboro Formation, northern central Hokkaido, Japan, and their chronostratigraphic and paleoenvironmental implications. *Chishitsugaku Zasshi,* 100(4):292–301. **doi:10.5575/geosoc.100.292**

Kurita, H., and Obuse, A., 2003. Middle Miocene–uppermost lower Pliocene dinoflagellate cyst biostratigraphy, ODP Leg 186 Hole 1151A, off Sanriku Coast of northern Japan, northwestern Pacific. *In* Suyehiro, K., Sacks, I.S., Acton, G.D., and Oda, M. (Eds.), *Proc. ODP, Sci. Results,* 186: College Station, TX (Ocean Drilling Program), 1–19. **doi:10.2973/odp.proc.sr.186.105.2003**

Kurita, H., Obuse, A., and Akiba, F., 1998. Upper Oligocene–lower Miocene palynostratigraphy (dinoflagellate cysts and pollen) in eastern Hokkaido with calibration against diatom biostratigraphy. *Res. Rep.—JAPEX Res. Cent.,* 13:11–31.

Kurnosov, V., Tseitlin, N., and Narnov, G., 1980. Clay minerals: paleogeographic and diagenetic aspects. *In* Scientific Party, *Init. Repts. DSDP,* 56/57: Washington, DC (U.S. Govt. Printing Office), 979–1003. **doi:10.2973/dsdp.proc.5657.134.1980**

Limmer, D.R., Böning, P., Giosan, L., Ponton, C., Köhler, C.M., Cooper, M.J., Tabrez, A.R., and Clift, P.D., 2012. Geochemical record of Holocene to recent sedimentation on the western Indus continental shelf, Arabian Sea. *Geochem., Geophys., Geosyst.,* 13(1):Q01008. **doi:10.1029/2011GC003845**

Mackenzie, A.S., Brassell, S.C., Eglinton, G., and Maxwell, J.R., 1982. Chemical fossils: the geological fate of steroids. *Science,* 217(4559):491–504. **doi:10.1126/science.217.4559.491**

Mann, U., and Müller, G., 1980. Composition of sediments of the Japan Trench transect, Legs 56 and 57, Deep Sea Drilling Project. *In* Scientific Party, *Init. Repts. DSDP,* 56/57: Washington, DC (U.S. Govt. Printing Office), 939–977. **doi:10.2973/dsdp.proc.5657.133.1980**

Martin, J.B., Kastner, M., and Elderfield, H., 1991. Lithium: sources in pore fluids of Peru slope sediments and implications for oceanic fluxes. *Mar. Geol.,* 102(1–4):281–292. **doi:10.1016/0025-3227(91)90012-S**

Masui, N., Morono, Y., and Inagaki, F., 2008. Microbiological assessment of circulation mud fluids during the first operation of riser drilling by the deep-earth research vessel *Chikyu. Geomicrobiol. J.,* 25(6):274–282. **doi:10.1080/01490450802258154**

Matsuoka, K., Bujak, J.P., and Shimazaki, T., 1987. Late Cenozoic dinoflagellate cyst biostratigraphy from the west coast of northern Japan. *Micropaleontology,* 33(3):214–229. **doi:10.2307/1485638**

McRae, S.G., 1972. Glauconite. *Earth-Sci. Rev.,* 8(4):397–440. **doi:10.1016/0012-8252(72)90063-3**

Meister, P., McKenzie, J.A., Vasconcelos, C., Bernasconi, S., Frank, M., Gutjahr, M., and Schrag, D.P., 2007. Dolomite formation in the dynamic deep biosphere: results from the Peru margin. *Sedimentology,* 54(5):1007–1032. **doi:10.1111/j.1365-3091.2007.00870.x**

Meyers, P.A., and Ishiwatari, R., 1993. Lacustrine organic geochemistry—an overview of indicators of organic matter sources and diagenesis in lake sediments. *Org. Geochem.,* 20(7):867–900. **doi:10.1016/0146-6380(93)90100-P**

Morono, Y., and Inagaki, F., 2010. Automatic slide-loader fluorescent microscope for discriminative enumeration of subseafloor life. *Sci. Drill.,* 9:32–36. **doi:10.2204/iodp.sd.9.06.2010**

Morono, Y., Terada, T., Masui, N., and Inagaki, F., 2009. Discriminative detection and enumeration of microbial life in marine subsurface sediments. *ISME J.,* 3(5):503–511. **doi:10.1038/ismej.2009.1**

Mullins, O.C., 2008. *The Physics of Reservoir Fluids: Discovery Through Downhole Fluid Analysis:* Houston (Schlumberger).

Nesbitt, H.W., Markovics, G., and Price, R.C., 1980. Chemical processes affecting alkalis and alkaline earths during continental weathering. *Geochim. Cosmochim. Acta,* 44(11):1659–1666. **doi:10.1016/0016-7037(80)90218-5**

Nesbitt, H.W., and Young, G.M., 1982. Early Proterozoic climates and plate motions inferred from major element chemistry of lutites. *Nature (London, U. K.),* 299(5885):715–717. **doi:10.1038/299715a0**

Ocean Drilling Program, 1992. Guidelines for pollution prevention and safety. *JOIDES J.,* 18 (Spec. Iss. 7). **http://odplegacy.org/PDF/Admin/JOIDES_Journal/JJ_1992_V18_No7.pdf**

Okada, H., 1980. Pebbles and carbonate nodules from Deep Sea Drilling Project Leg 56 cores. *In* Scientific Party, *Init. Repts. DSDP,* 56/57: Washington, DC (U.S. Govt. Printing Office), 1089–1105. **doi:10.2973/dsdp.proc.5657.144.1980**

Osborne, M.J., and Swarbrick, R.E., 1997. Mechanisms for generating overpressure in sedimentary basins: a reevaluation. *AAPG Bull.,* 81(6):1023–1041. **http://aapgbull.geoscienceworld.org/content/81/6/1023.abstract**

Parnell, J., Bowden, S., Andrews, J.T., and Taylor, C., 2007. Biomarker determination as a provenance tool for detrital carbonate events (Heinrich events?): fingerprinting Quaternary glacial sources into Baffin Bay. *Earth Planet. Sci. Lett.,* 257(1–2):71–82. **doi:10.1016/j.epsl.2007.02.021**

Peters, K.E., 1986. Guidelines for evaluating petroleum source rock using programmed pyrolysis. *AAPG Bull.,* 70(3):318–329. **http://archives.datapages.com/data/bulletns/1986-87/data/pg/0070/0003/0300/0318.htm**

Peters, K.E., Walters, C.C., and Moldowan, J.M., 2005. Geochemical screening. *In* Peters, K.E., Walters, C.C., and Moldowan, J.M. (Eds.), *The Biomarker Guide* (Vol. 1): *Biomarkers and Isotopes in the Environment and Human History* (2nd ed.): Cambridge (Cambridge Univ. Press), 72–118. **doi:10.1017/CBO9780511524868.006**

Pimmel, A., and Claypool, G., 2001. Introduction to shipboard organic geochemistry on the *JOIDES Resolution. ODP Tech. Note,* 30. **doi:10.2973/odp.tn.30.2001**

Radke, M., Schaefer, R.G., Leythaeuser, D., and Teichmüller, M., 1980. Composition of soluble organic matter in coals: relation to rank and liptinite fluorescence. *Geochim. Cosmochim. Acta,* 44(11):1787–1800. **doi:10.1016/0016-7037(80)90228-8**

Rateev, M.A., Gorbunova, Z.N., Lisitzyn, A.P., and Nosov, G.L., 1969. The distribution of clay minerals in the oceans. *Sedimentology,* 13(1–2):21–43. **doi:10.1111/j.1365-3091.1969.tb01119.x**

Rodrigues, C.F., and Lemos de Sousa, M.J., 2002. The measurement of coal porosity with different gases. *Int. J. Coal Geol.,* 48(3–4):245– 251. **doi:10.1016/S0166-5162(01)00061-1**

Sato, S., 1994. On the palynoflora in the Paleogene in the Ishikari coal field, Hokkaido, Japan. *J. Fac. Sci., Hokkaido Univ., Ser. 4,* 23(3):555–559. **http://eprints.lib.hokudai.ac.jp/dspace/handle/2115/36789**

Schiøler, P., 2005. Dinoflagellate cysts and acritarchs from the Oligocene–lower Miocene interval of the Alma-1X well, Danish North Sea. *J. Micropalaeontol.,* 24(1):1–37. **doi:10.1144/jm.24.1.1**

Seeberg-Elverfeldt, J., Schlüter, M., Feseker, T., and Kölling, M., 2005. Rhizon sampling of porewaters near the sediment-water interface of aquatic systems. *Limnol. Oceanogr.: Methods,* 3(8):361–371. **http://aslo.org/lomethods/free/2005/0361.pdf**

Shimada, M., 1967. The pollen flora from the Tertiary and Cretaceous of Japan in correlation with the palaeobotanical records. *Rev. Palaeobot. Palynol.,* 5(1–4):235–241. **doi:10.1016/0034-6667(67)90227-8**

Shipboard Scientific Party, 2000. Site 1150. *In* Sacks, I.S., Suyehiro, K., Acton, G.D., et al., *Proc. ODP, Init. Repts.,* 186: College Station, TX (Ocean Drilling Program), 1–53. **doi:10.2973/odp.proc.ir.186.104.2000**

Singh, M., Sharma, M., and Tobschall, H.J., 2005. Weathering of the Ganga alluvial plain, northern India: implications from fluvial geochemistry of the Gomati River. *Appl. Geochem.,* 20(1):1–21. **doi:10.1016/j.apgeochem.2004.07.005**

Smith, D.C., Spivack, A.J., Fisk, M.R., Haveman, S.A., Staudigel, H., and the Leg 185 Shipboard Scientific Party, 2000. Methods for quantifying potential microbial contamination during deep ocean coring. *ODP Tech. Note,* 28. **doi:10.2973/odp.tn.28.2000**

Snyder, G.T., Hiruta, A., Matsumoto, R., Dickens, G.R., Tomaru, H., Takeuchi, R., Komatsubara, J., Ishida, Y., and Yu, H., 2007. Pore water profiles and authigenic mineralization in shallow marine sediments above the methane-charged system on Umitaka Spur, Japan Sea. *Deep Sea Res., Part II,* 54(11–13):1216–1239. **doi:10.1016/j.dsr2.2007.04.001**

Snyder, G.T., Savov, I.P., and Muramatsu, Y., 2005. Iodine and boron in Mariana serpentinite mud volcanoes (ODP Legs 125 and 195): implications for forearc processes and subduction recycling. *In* Shinohara, M., Salisbury, M.H., and Richter, C. (Eds.), *Proc. ODP, Sci. Results,* 195: College Station, TX (Ocean Drilling Program), 1–18. **doi:10.2973/odp.proc.sr.195.102.2005**

Southwick, J.G., 1985. Solubility of silica in alkaline solutions: implications for alkaline flooding. *SPE J. (Soc. Pet. Eng.),* 25(6):857–864. **doi:10.2118/12771-PA**

Stumm, W., and Lee, G.F., 1961. Oxygenation of ferrous iron. *Ind. Eng. Chem.,* 53(2):143–146. **doi:10.1021/ie50614a030**

Taira, A., and Curewitz, D. (Eds.), 2005. *CDEX Technical Report* (Vol. 2): *Shimokita Area Site Survey: Northern Japan Trench Seismic Survey, Northern Honshu, Japan:* Yokohama (CDEX-JAMSTEC)

Takeda, E., 1981. Minor elements in Japanese coal. *Chishitsu Chosasho Geppo,* 32(11):583–682. (in Japanese)

Tomaru, H., Fehn, U., Lu, Z., Takeuchi, R., Inagaki, F., Imachi, H., Kotani, R., Matsumoto, R., and Aoike, K., 2009. Dating of dissolved iodine in pore waters from the gas hydrate occurrence offshore Shimokita Peninsula, Japan: ^{129}I results from D/V *Chikyu* shakedown cruise. *Resour. Geol.,* 59(4):359–373. **doi:10.1111/j.1751-3928.2009.00103.x**

Torres, M.E., Bohrmann, G., and Suess, E., 1996. Authigenic barites and fluxes of barium associated with fluid seeps in the Peru subduction zone. *Earth Planet. Sci. Lett.,* 144(3–4):469–481. **doi:10.1016/S0012-821X(96)00163-X**

Underwood, M.B., Basu, N., Steurer, J., and Udas, S., 2003. Data report: normalization factors for semiquantitative X-ray diffraction analysis, with application to DSDP Site 297, Shikoku Basin. *In* Mikada, H., Moore, G.F., Taira, A., Becker, K., Moore, J.C., and Klaus, A. (Eds.), *Proc. ODP, Sci. Results,* 190/196: College Station, TX (Ocean Drilling Program), 1–28. **doi:10.2973/odp.proc.sr.190196.203.2003**

Underwood, M.B., Saito, S., Kubo, Y., and the Expedition 322 Scientists, 2009. NanTroSEIZE Stage 2: subduction inputs. *IODP Prel. Rept.,* 322. **doi:10.2204/iodp.pr.322.2009**

Volkman, J.K., 1986. A review of sterol markers for marine and terrigenous organic matter. *Org. Geochem.,* 9(2):83–99. **doi:10.1016/0146-6380(86)90089-6**

Volkman, J.K., Barrett, S.M., Blackburn, S.I., Mansour, M.P., Sikes, E.L., and Gelin, F., 1998. Microalgal biomarkers: a review of recent research developments. *Org. Geochem.,* 29(5–7):1163–1179. **doi:10.1016/S0146-6380(98)00062-X**

Wang, W.-M., 2006. Correlation of pollen sequences in the Neogene palynofloristic regions of China. *Palaeoworld,* 15(1):77–99. **doi:10.1016/j.palwor.2006.03.002**

Wang, W.-M., Saito, T., and Nakagawa, T., 2001. Palynostratigraphy and climatic implications of Neogene deposits in the Himi area of Toyama Prefecture, Central Japan. *Rev. Palaeobot. Palynol.,* 117(4):281–295. **doi:10.1016/S0034-6667(01)00097-5**

Wei, G., Li, X.-H., Liu, Y., Shao, L., and Liang, X., 2006. Geochemical record of chemical weathering and monsoon climate change since the early Miocene in the South China Sea. *Paleoceanography,* 21(4):PA4214. **doi:10.1029/2006PA001300**

Wenger, L.M., Davis, C.L., Evensen, J.M., Gormly, J.R., and Mankiewicz, P.J., 2004. Impact of modern deepwater drilling and testing fluids on geochemical evaluations. *Org. Geochem.,* 35(11–12):1527–1536. **doi:10.1016/j.orggeochem.2004.07.001**

Whiticar, M.J., 1999. Carbon and hydrogen isotope systematics of bacterial formation and oxidation of methane. *Chem. Geol.,* 161(1–3):291–314. **doi:10.1016/S0009-2541(99)00092-3**

Yagishita, K., Obuse, A., and Kurita, H., 2003. Lithology and palynology of Neogene sediments on the narrow edge of the Kitakami Massif (basement rocks), northeast Japan: significant change for depositional environments as a result of plate tectonics. *Isl. Arc,* 12(3):268–280. **doi:10.1046/j.1440-1738.2003.00399.x**

Yamanoi, T., 1978. Neogene pollen stratigraphy of the Oga Peninsula, Northeast Honshu, Japan. *Chishitsugaku Zasshi,* 84:69–86.

Yamanoi, T., 1992. Miocene pollen stratigraphy of Leg 127 in the Japan Sea and comparison with the standard Neogene pollen floras of northeast Japan. *In* Pisciotto, K.A., Ingle, J.C., Jr., von Breymann, M.T., Barron, J., et al., *Proc. ODP, Sci. Results,* 127/128 (Pt. 1): College Station, TX (Ocean Drilling Program), 471–491. **doi:10.2973/odp.proc.sr.127128-1.150.1992**

Yanagisawa, Y., and Akiba, F., 1998. Refined Neogene diatom biostratigraphy for the northwest Pacific around Japan, with an introduction of code numbers for selected diatom biohorizons. *Chishitsugaku Zasshi,* 104:395–414.

You, C.-F., Spivack, A.J., Smith, J.H., and Gieskes, J.M., 1993. Mobilization of boron in convergent margins: implications for boron geochemical cycle. *Geology,* 21(3):207–210. **doi:10.1130/0091-7613(1993)021<0207:MOBICM>2.3.CO;2**

Publication: 30 September 2013
MS 337-103

Figure F1. Profile derived from macroscopic observation of cuttings with boundary units (black lines) and the relative abundance of wood/lignite, glauconite, diatoms, and sponge spicules, Hole C0020A.

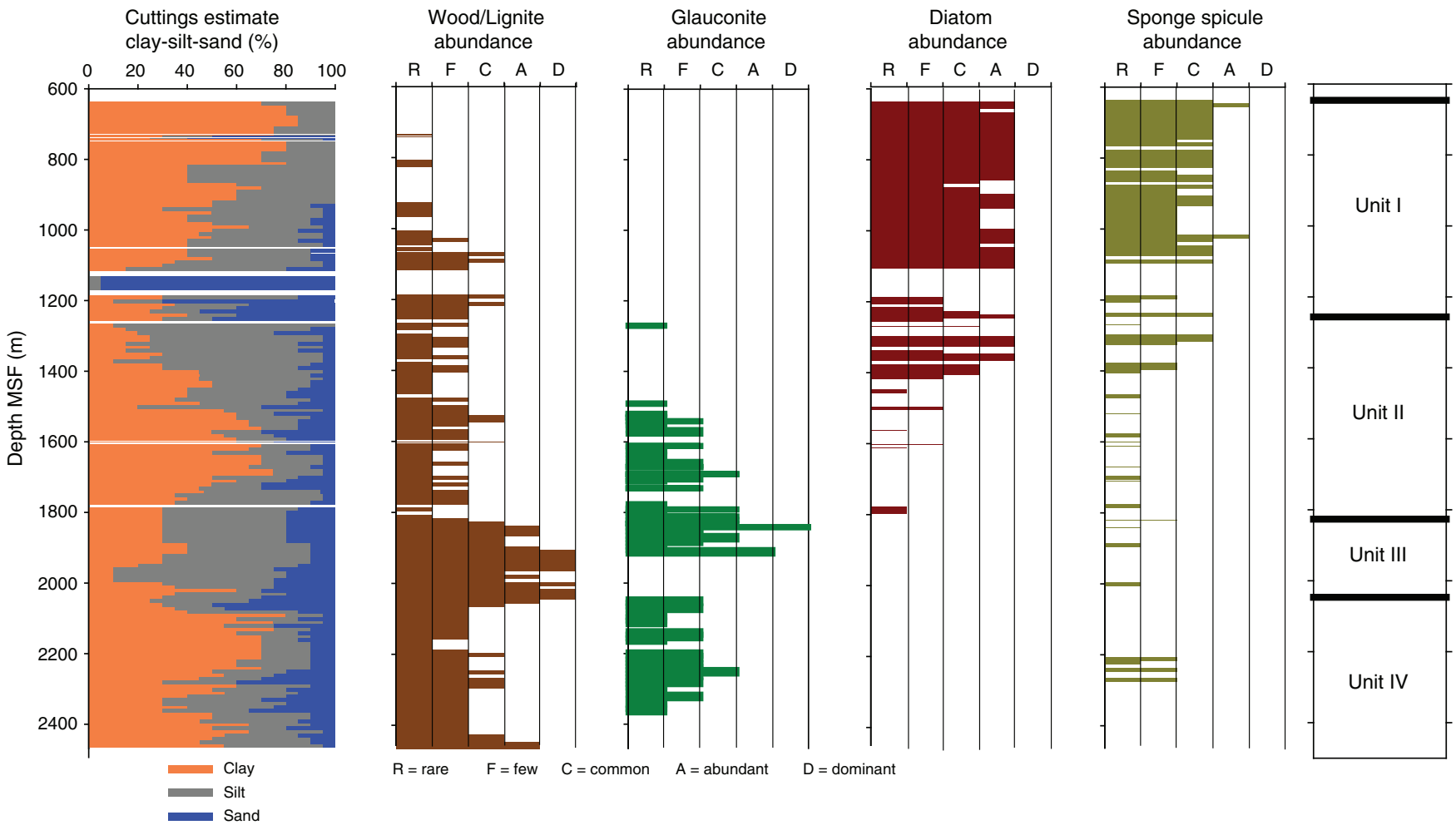

Figure F2. Smear slide photomicrographs. **A.** Cuttings containing diatom-bearing silty clay, typical lithology of Unit I. **B.** Fragmented diatoms in a volcanic glass and clay-rich matrix. **C.** Silty sandstone and volcanic glass. **D.** Glauconite. **E.** Abundant woody fragments within weathered volcanic material beneath the first coalbeds. **F.** Well-preserved wood fragment. **G.** Bright green circular grains of siderite within organic-rich sediment. **H.** Siderite within coal layers. **I.** Glauconite in sandstone.

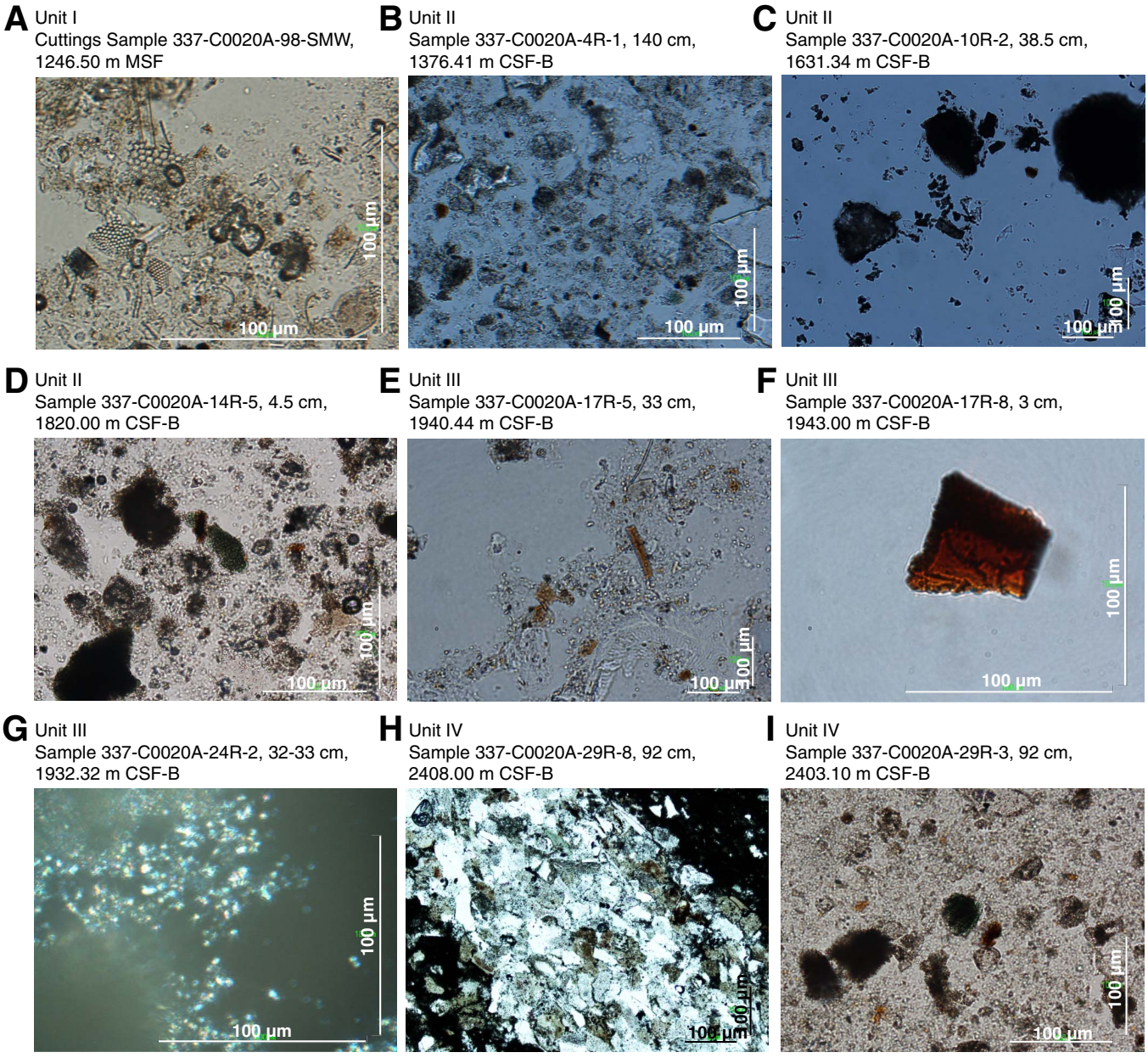

Figure F3. Section photographs. **A.** Fine to medium sandstone intercalated with thin siltstone layers (2–3 mm) with dolomitic bands. **B.** Sandstone with pebbles of igneous rocks, few cherts, and rare pumice. **C.** Grain-supported conglomerate at the bottom. A small coarsening-upward interval with a fine conglomerate at the top (43 cm). The clayey fine sandstone visible above is typical for Subunit IIa. **D.** Organic-rich layer in medium sandstone (87 cm, Subunit IIb). Slightly dipping beds, parallel lamination, and horizontal burrows (88 cm) filled with siltstone are also visible. **E.** Vertical burrows filled with medium sandstone in a silty shale (Subunit IIb). Shell fragments appear in the lower part. (Continued on next page.)

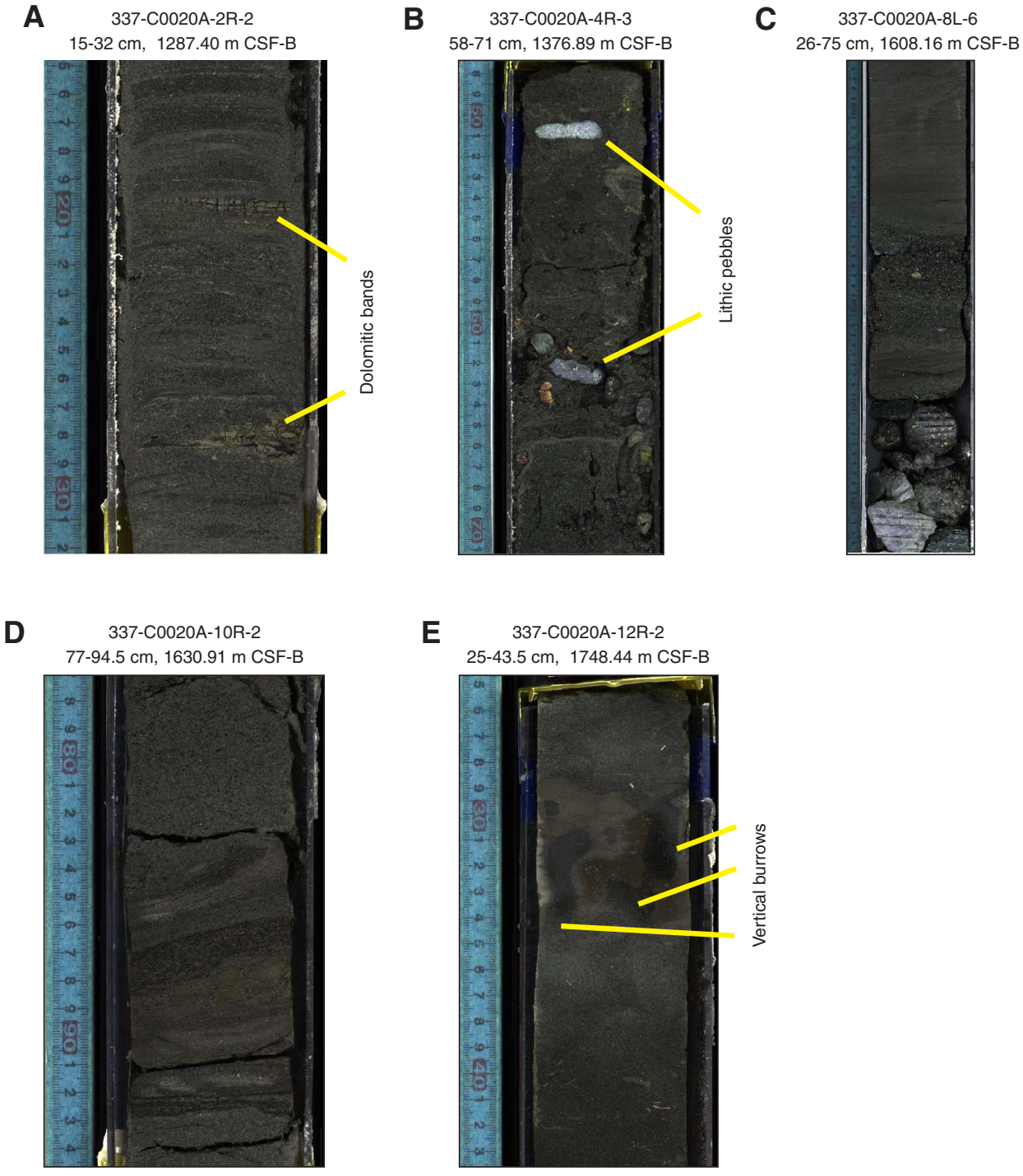

Figure F3 (continued). F. Abundant shell fragments in medium sandstone (Subunit IIb). **G.** Coaly shale with pyrite (upper part) in contact with coal interval (lower part) from Unit III. **H.** Light brown cemented (sideritic) mudstone and concretions (Unit III). In the middle of this brown horizon, a thin coaly layer appears. **I.** Sandstone with siderite bands (brownish color; Unit IV). **J.** Siltstone with siderite concretion in silty shale (Unit IV). Lenticular bedding is visible in this section.

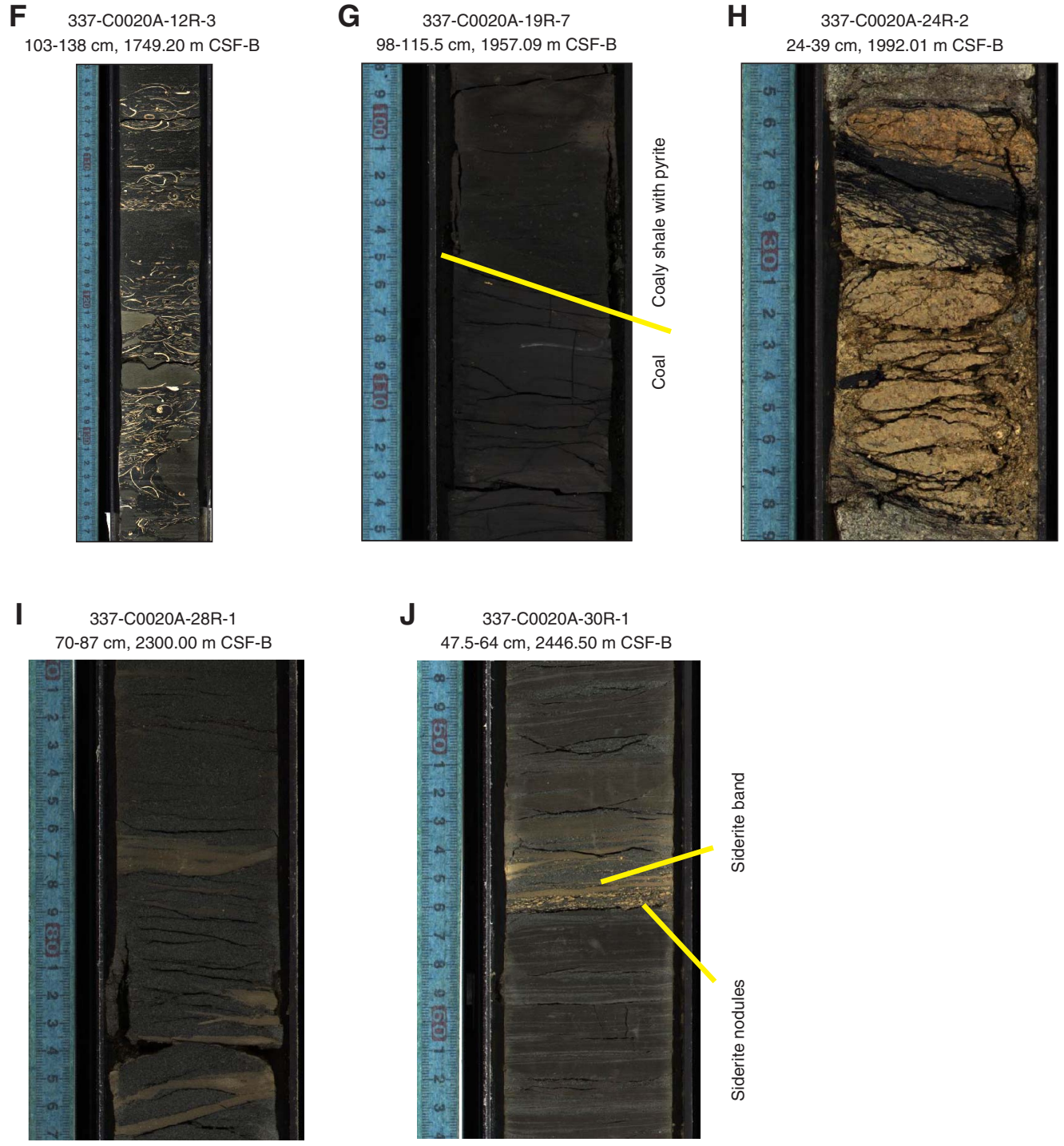

Figure F4. Scanning electron micrograph images. **A.** Pyrite grain. **B.** Naturally occurring barite in coal from section shown in A. **C.** Coal. **D.** Coal.

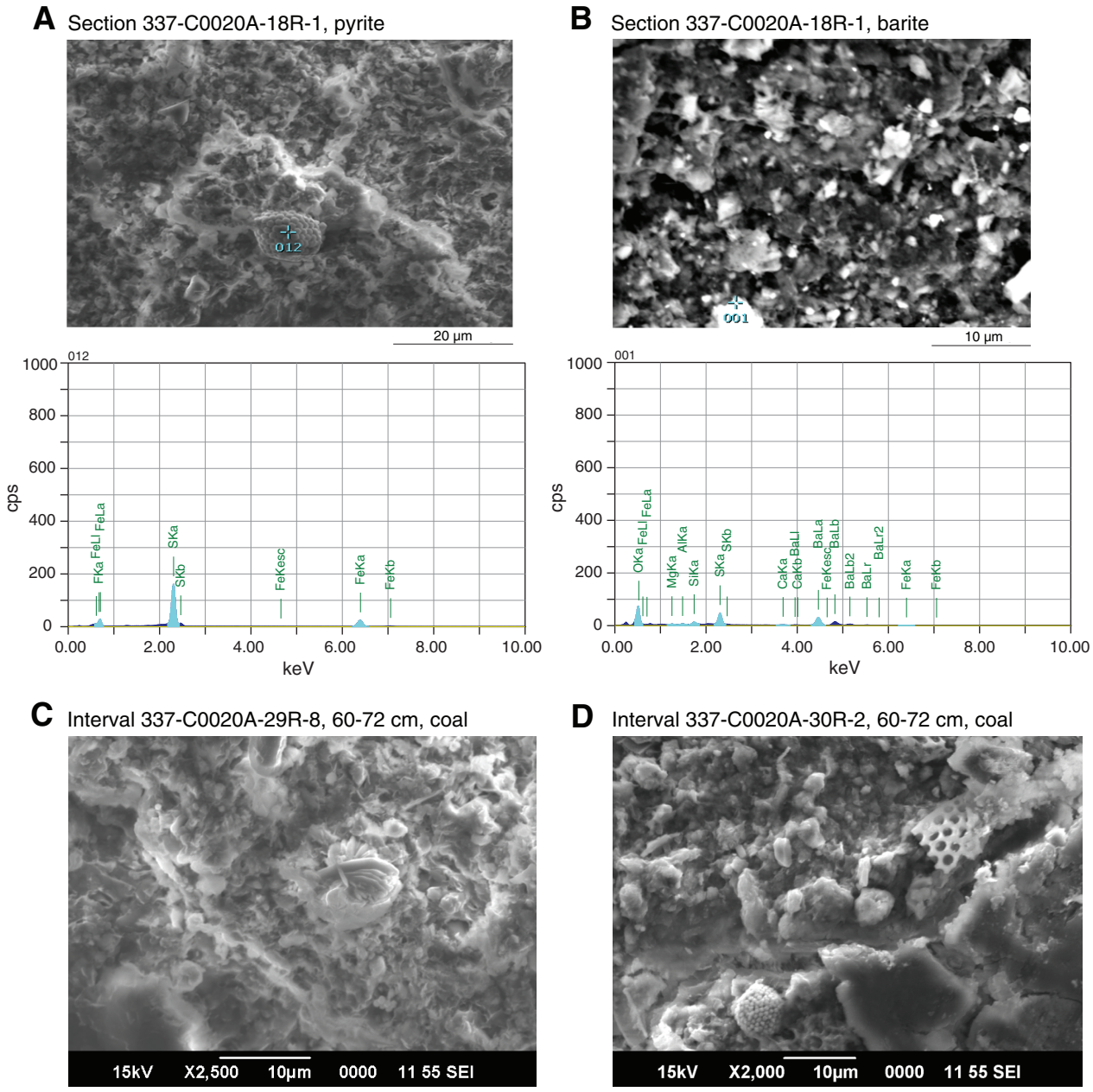

Figure F5. Plot of downhole changes in the relative abundance of quartz, feldspar, clay, and calcite derived from X-ray diffraction (XRD) measurements, Hole C0020A.

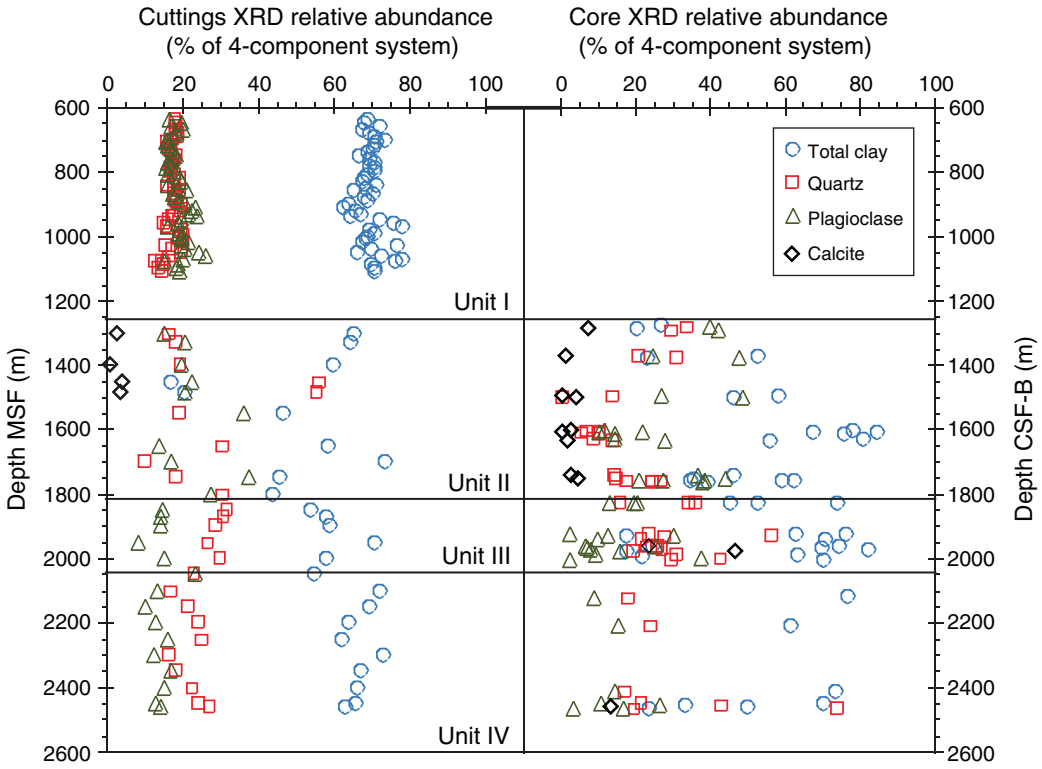

Figure F6. Plots for selected geochemical ratios used as properties for various physical or mineralogical phenomena against depth, Hole C0020A. CIA = chemical index of alteration.

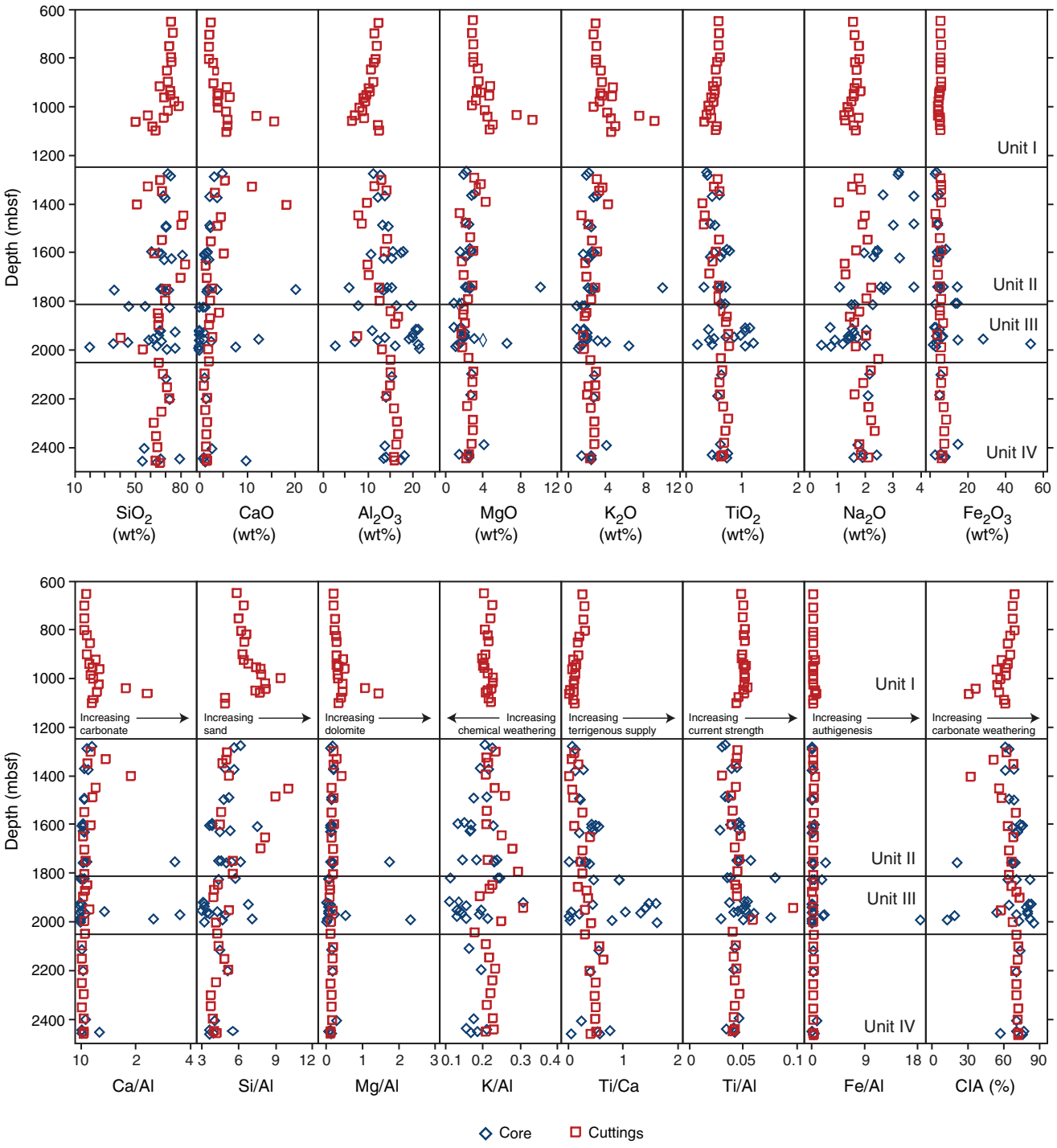

Figure F7. Cross-plots for various geochemical element ratios and plots of ratios against CaO and quartz from XRD measurements, Hole C0020A. CIA = chemical index of alteration.

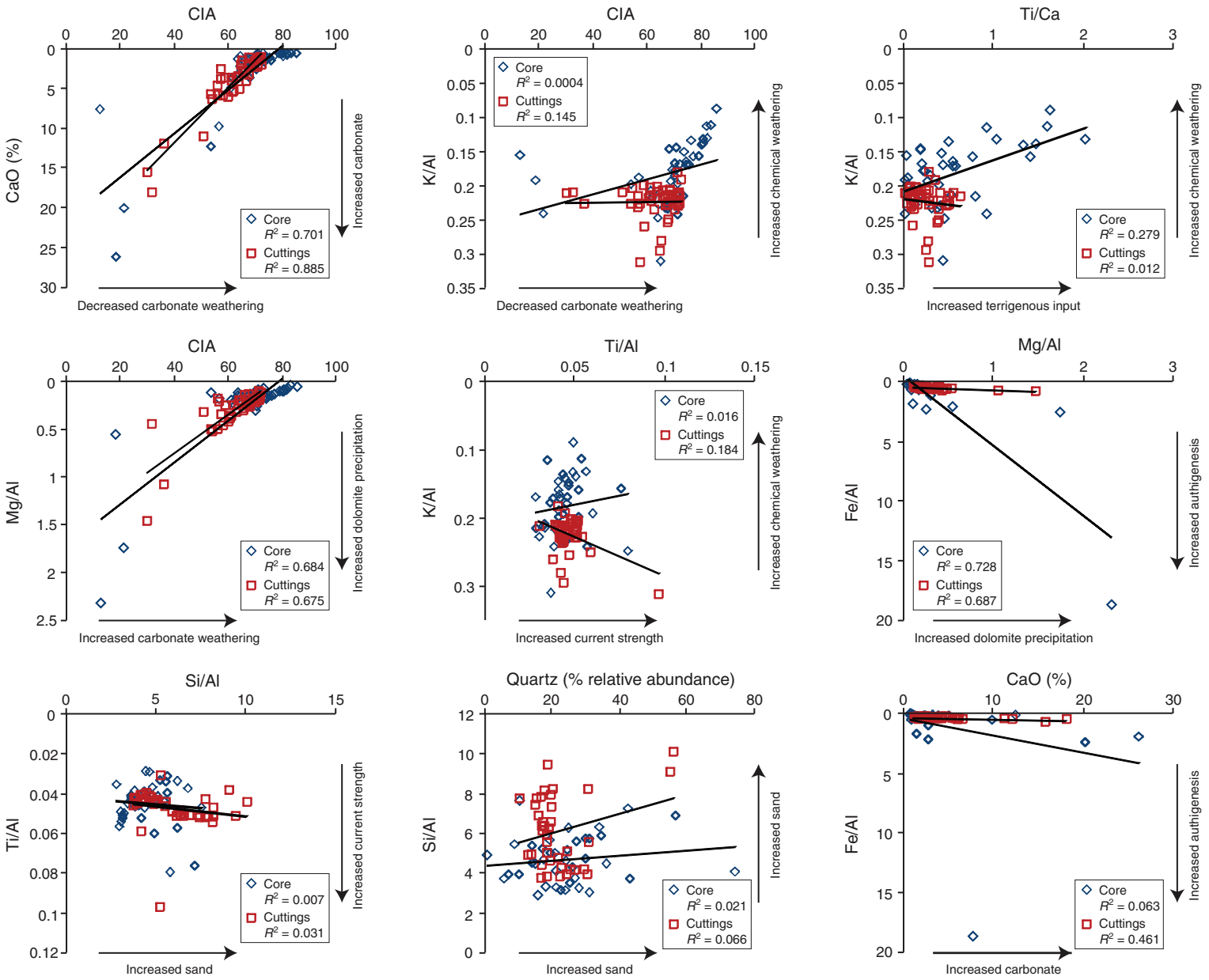

Figure F8. Profile derived from macroscopic observation of cuttings and core with the age; relative abundance of wood/lignite, glauconite, diatoms, and sponge spicules; and the interpretation of the depositional environment, Hole C0020A.

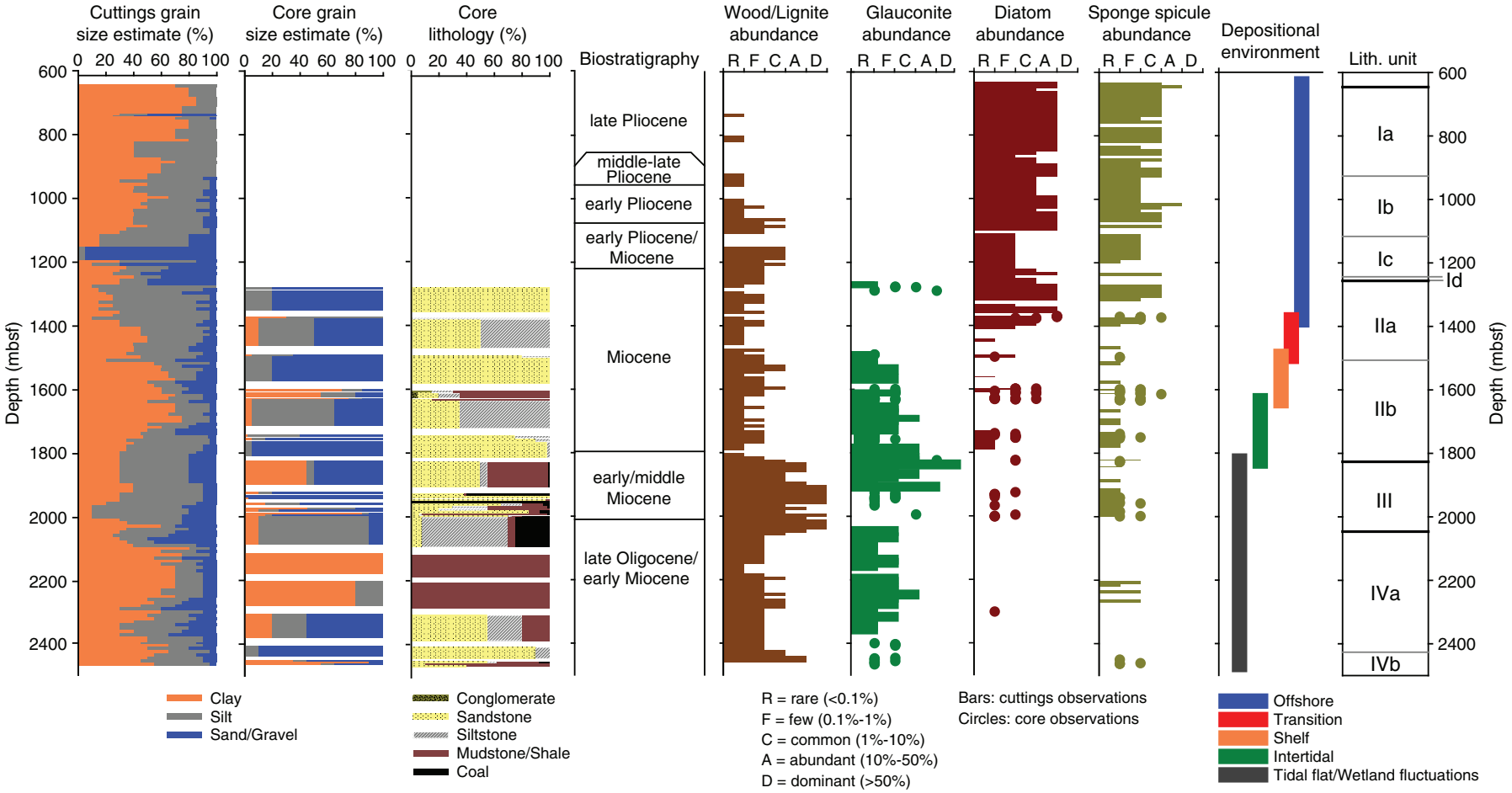

Figure F9. Section photographs of drilling disturbances in cores. **A.** Mud drilling injection causing some lamination in semiconsolidated sandstone. **B.** Laminations of drilling mud in silty sandstone, which at a glance looks "natural" and may lead to false interpretation of sedimentary structure originally present in core samples. **C.** Laminations caused by mud injections. In this core, mud laminations present with some offset. It was quite hard to differentiate between natural and injection laminations. **D.** Fine laminations caused by mud injections which again look natural. **E.** "Nugget structure" in the core caused by injections of drilling mud.

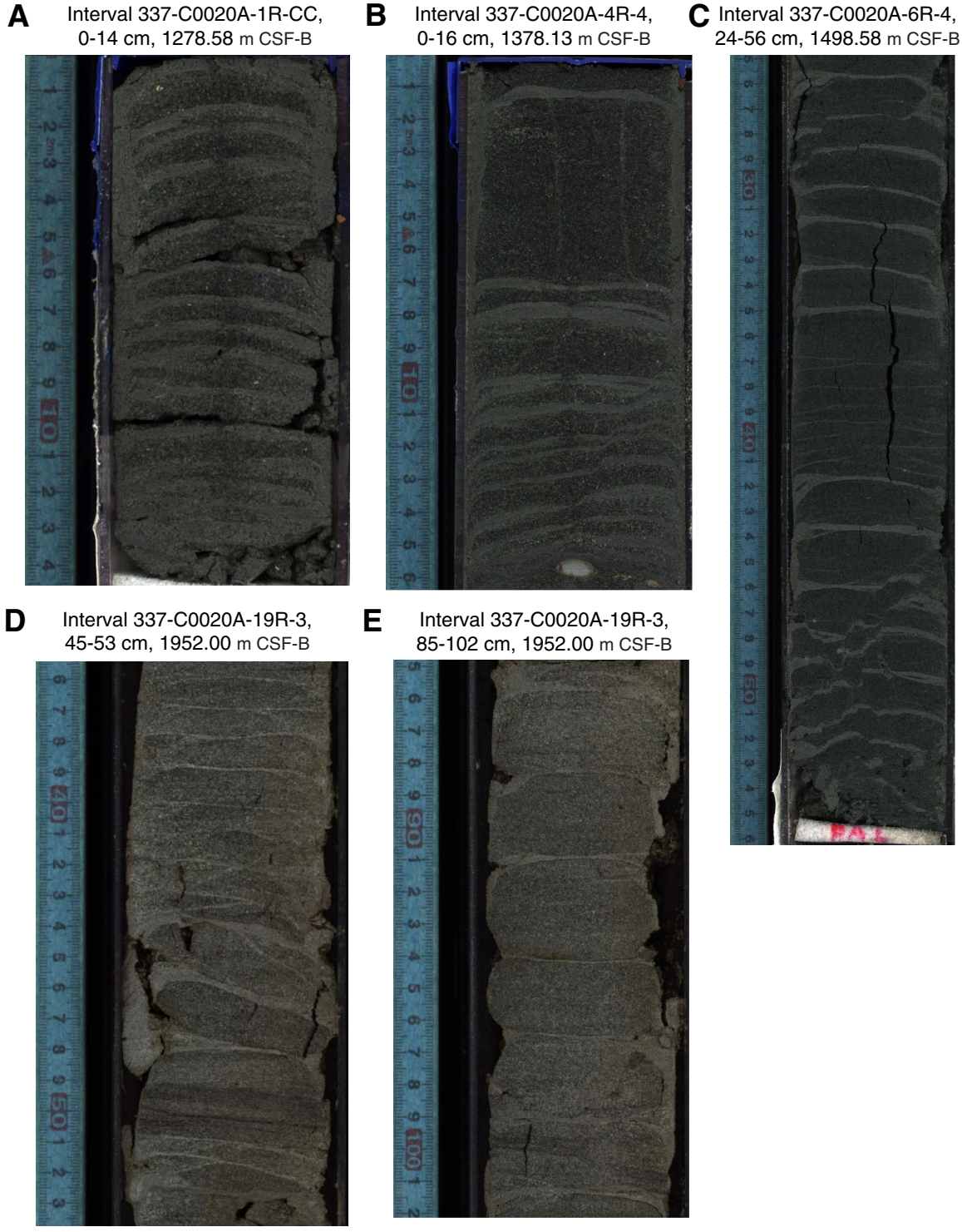

Figure F10. Site summary diagram of downhole logging for Site C0020 from 1200 to 2466 m WMSF, showing caliper (hole diameter), natural gamma ray, spontaneous potential, laterolog resistivity (RLA) of five different depths of investigation (RLA5 = deepest), neutron porosity, photoelectric factor, density, *P*- and *S*-wave velocities and Poisson's ratio calculated from these velocities, natural gamma ray from three different radioactive materials, a series of permeability and porosity measurements by NMR method together with their original data (NMR T2 distribution), and the borehole resistivity image. SDR = Schlumberger-Doll Research, T/C = Timur-Coates, CMR = combinable magnetic resonance.

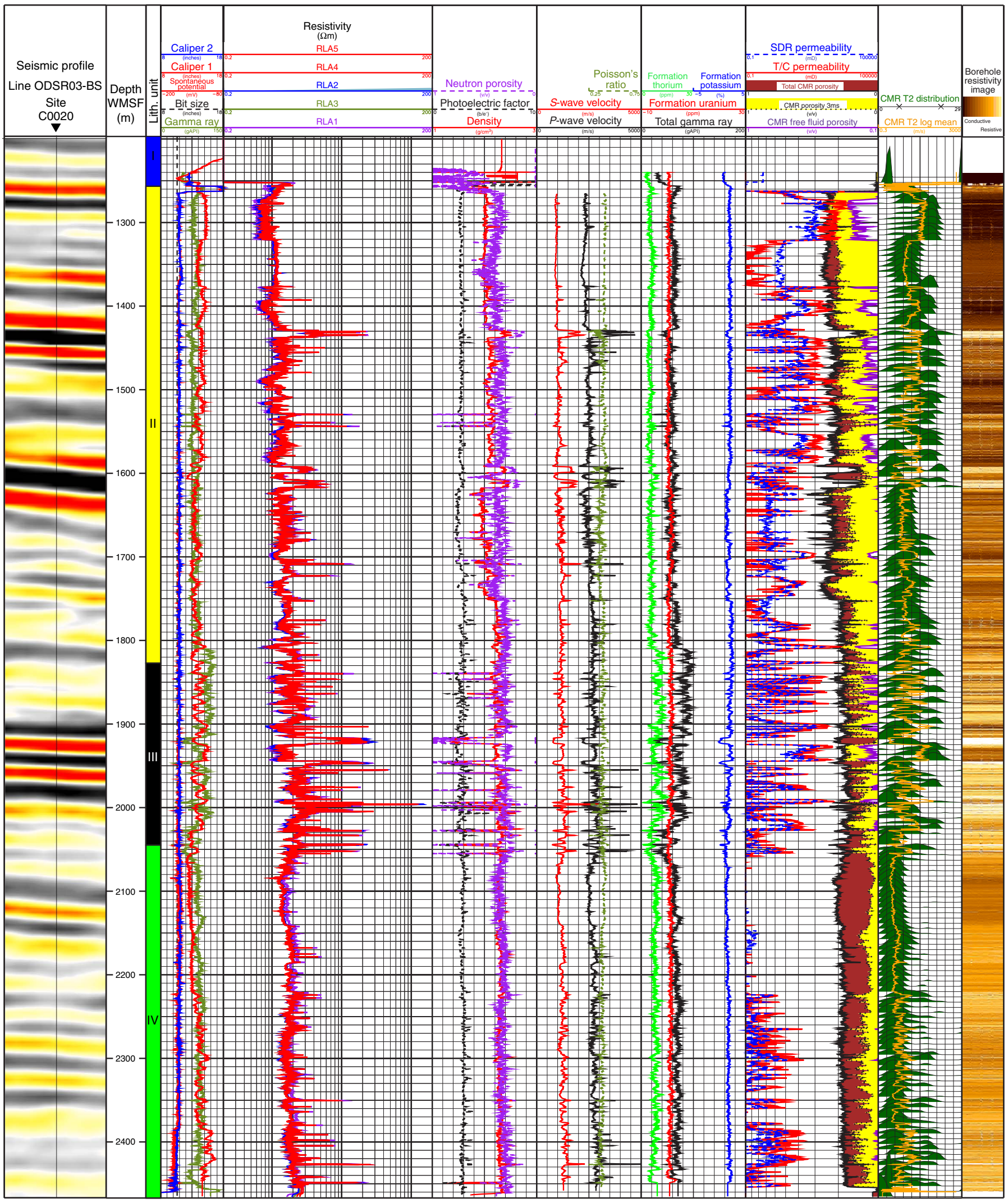

Figure F11. Summary of temperature measurements, Site C0020. Two types of logging tools, the Environmental Measurement Sonde (EMS) and the Modular Formation Dynamics Tester (MDT), measured borehole temperature in situ. The MDT recorded the temperature, during pretests (single probe [SP]) and fluid sampling (Quicksilver [QS] probe). The maximum temperature at the bottom of the hole was estimated by temperature build-up pattern during logging operations (Horner plot method) that shows the maximum temperature gradient of 24.0°C/km.

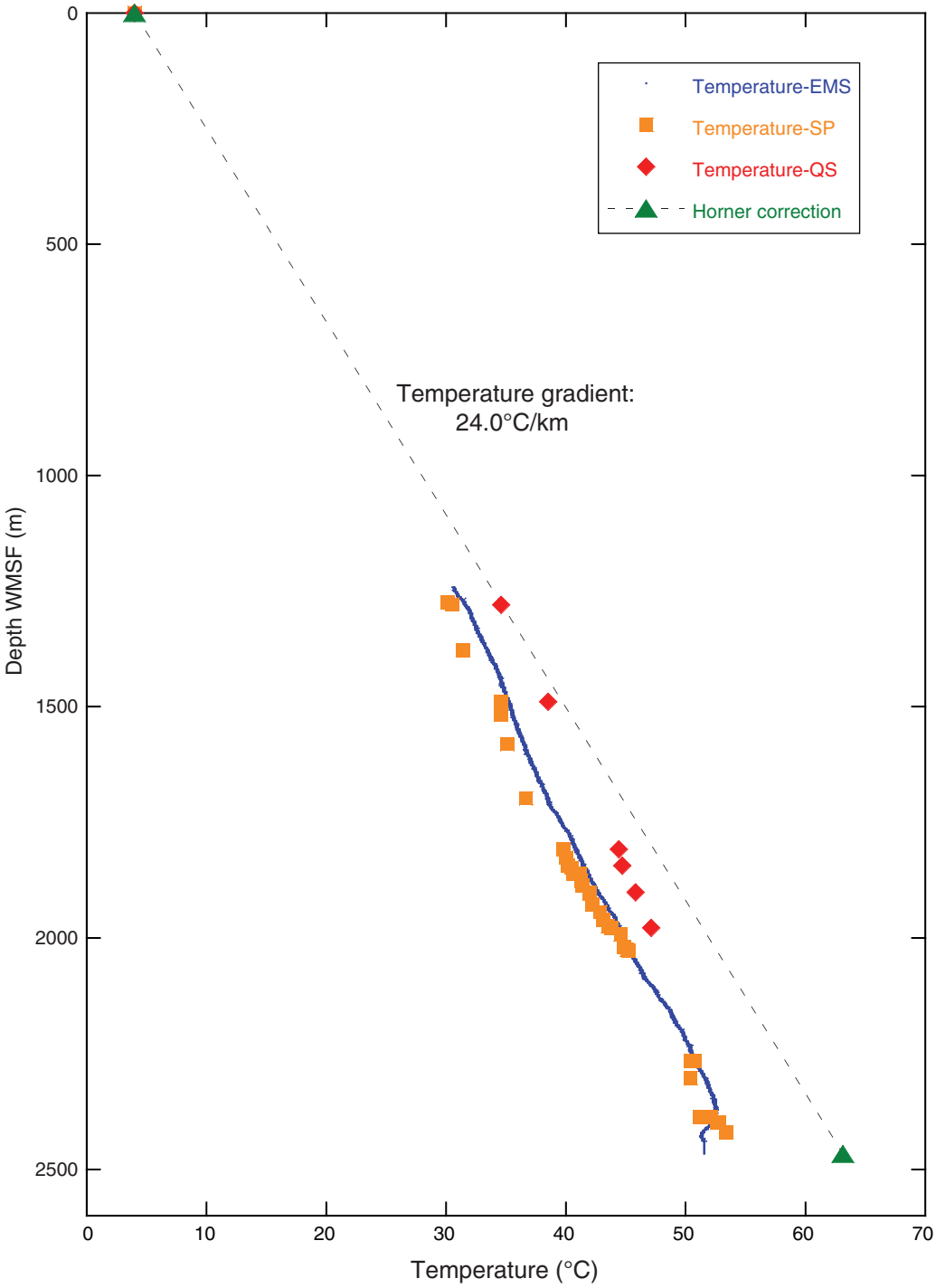

Figure F12. Synthetic seismogram and its correlation to the seismic profile, Site C0020. The synthetic seismogram generated from velocity log and density log data show a very good correlation to seismic profile Line ODSR03-BS. TWT = two-way traveltime.

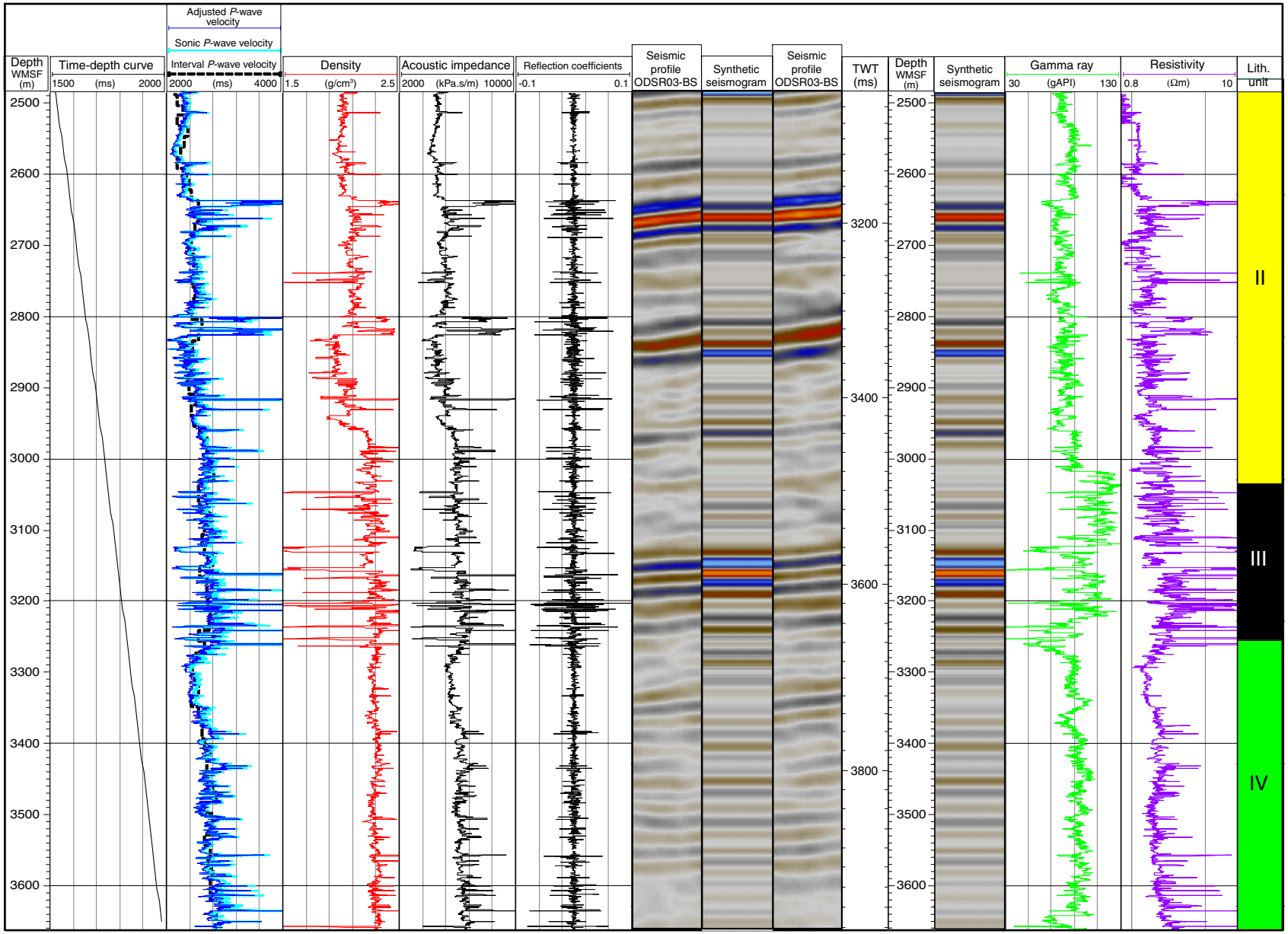

Figure F13. Correlation of seismic profile and logging data, Site C0020. Gamma ray and resistivity log data are displayed along the well. The layers of high resistivity correspond to the top horizon of the strong reflection zones on the profile. CMP = common midpoint.

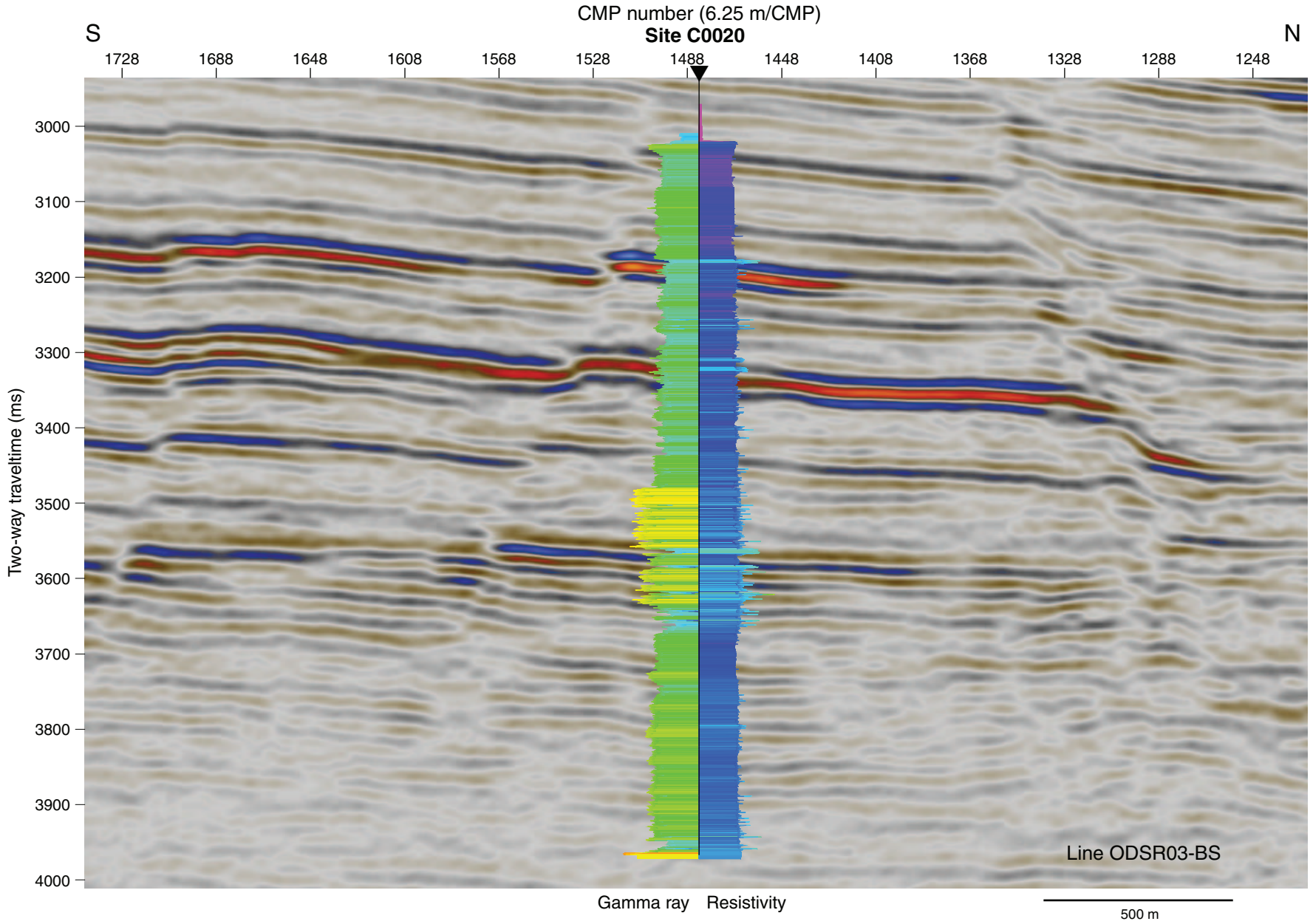

Figure F14. Correlation of seismic profile and lithologic units, Site C0020. It is clear that several strong reflections are in Unit II and a series of moderate reflections correspond to the coal layers of Unit III. The weak reflections within the Unit IV may be due to the massive mudstone sequence of this unit. CMP = common midpoint.

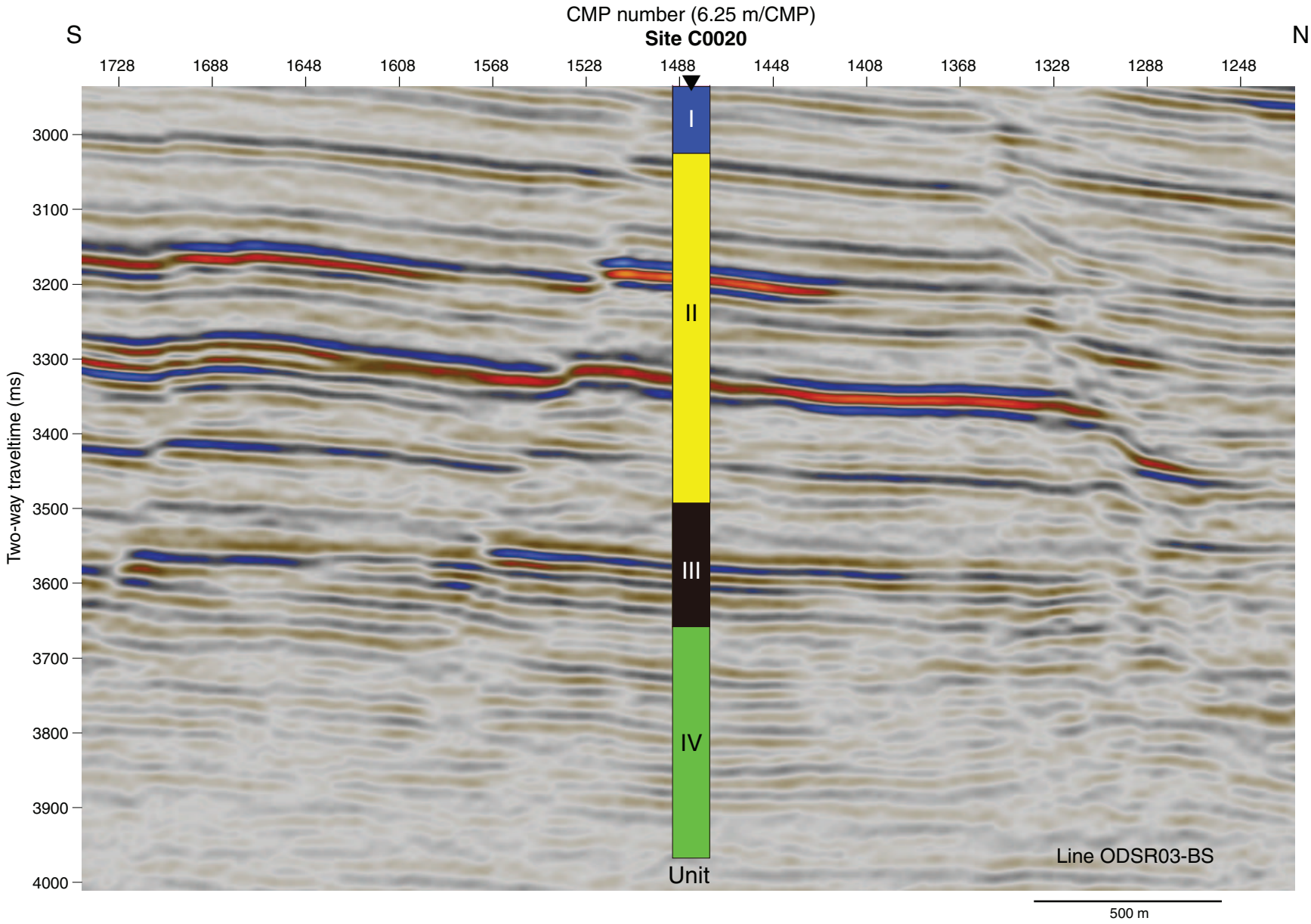

Figure F15. Plots of MSCL-W data for rotary core barrel (RCB) and MSCL-S data for large-diameter coring (LDC) systems, Site C0020. GRA = gamma ray attenuation.

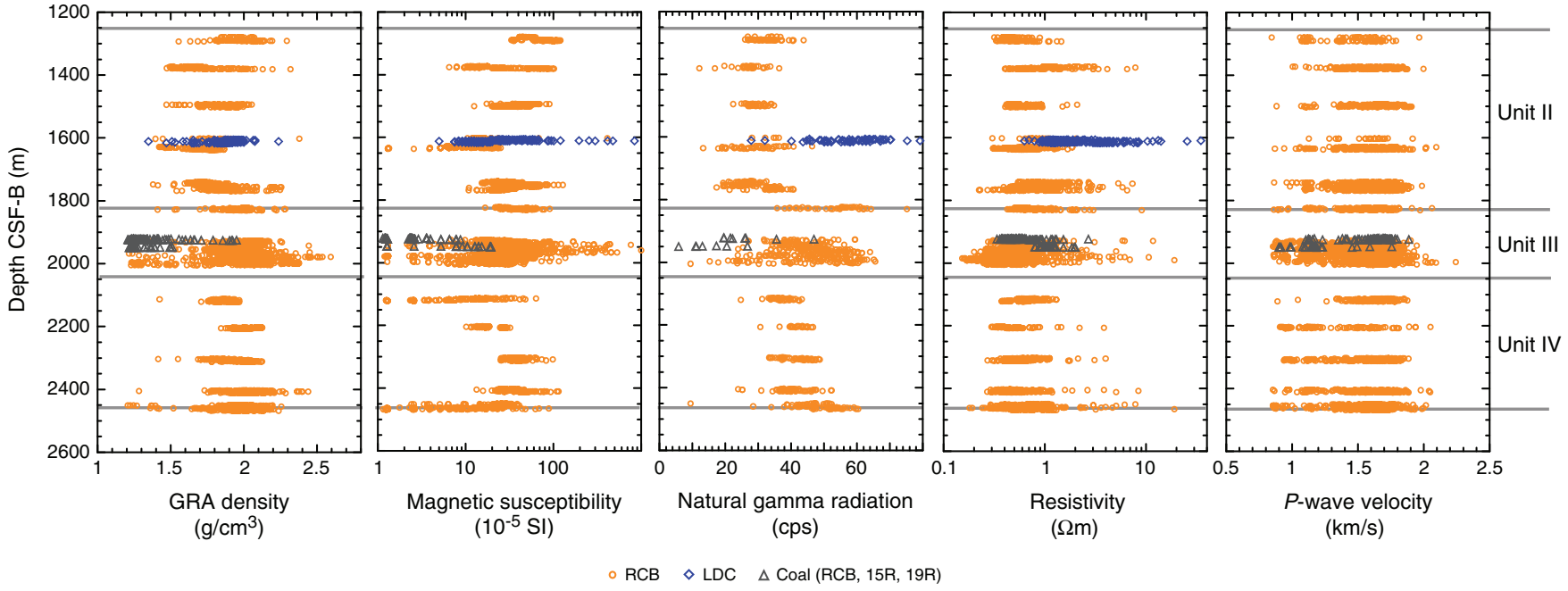

Figure F16. A. Distribution of porosity and its dependence on fragment size in cuttings samples and comparison with discrete core samples, Site C0020. In general, porosity decreases with an increase in cuttings fragment size at the same depth. Notice that discrete core samples measured for physical properties are 20 mm length cubic shape. **B.** Distribution and lithologic variation of porosity in discrete core samples and comparison with cuttings. Sandstone and siltstone porosity gradually decreased with depth, though carbonate-cemented rocks deviate from the consolidation curve with remarkably low porosity. Coal porosity does not deviate from that of sedimentary rocks. Higher porosity and slower reduction in porosity with depth is observed in cuttings samples. Discrete core samples can be more representative of in situ porosity than the porosity of cuttings. Note that cuttings data plotted on B is the >4 mm fraction.

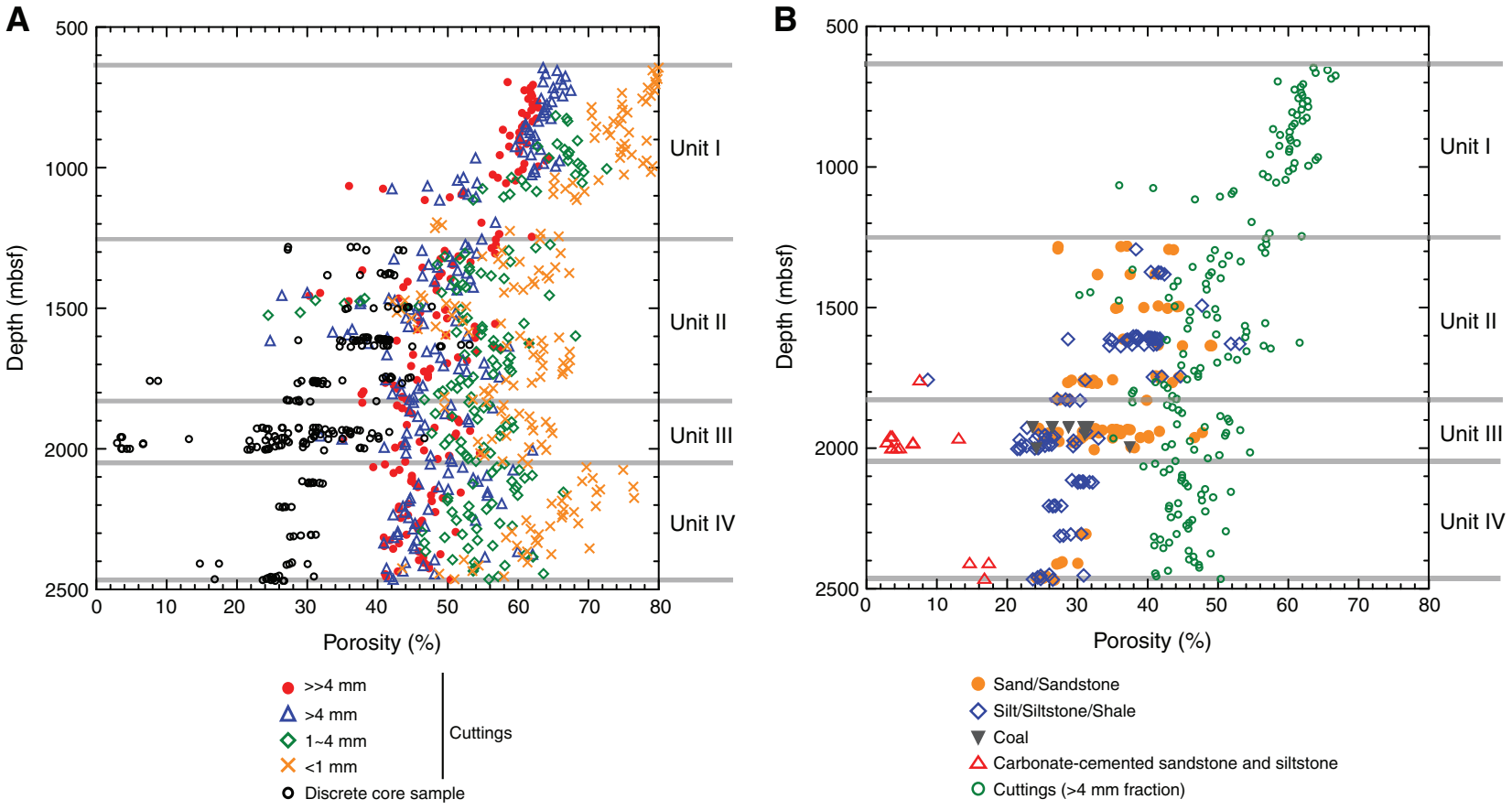

Figure F17. A. Distribution of bulk density and its dependence on fragment size in cuttings samples and comparison with discrete core samples, Site C0020. **B.** Distribution and lithologic variation of bulk density in discrete core samples and comparison with cuttings.

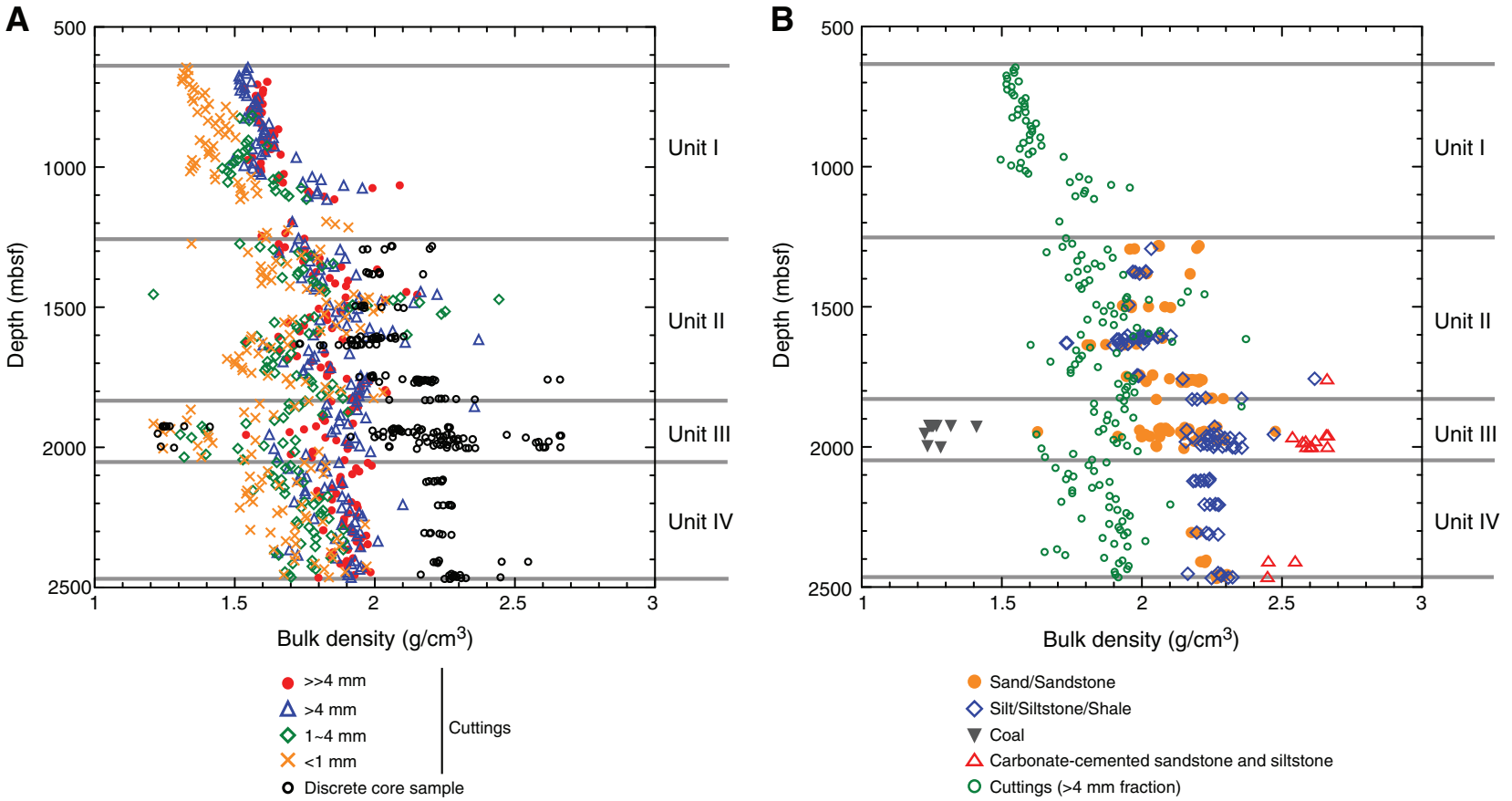

Figure F18. A. Distribution of grain density and its dependence on fragment size in cuttings samples and comparison with discrete core samples, Site C0020. **B.** Distribution and lithologic variation of grain density in discrete core samples and comparison with cuttings.

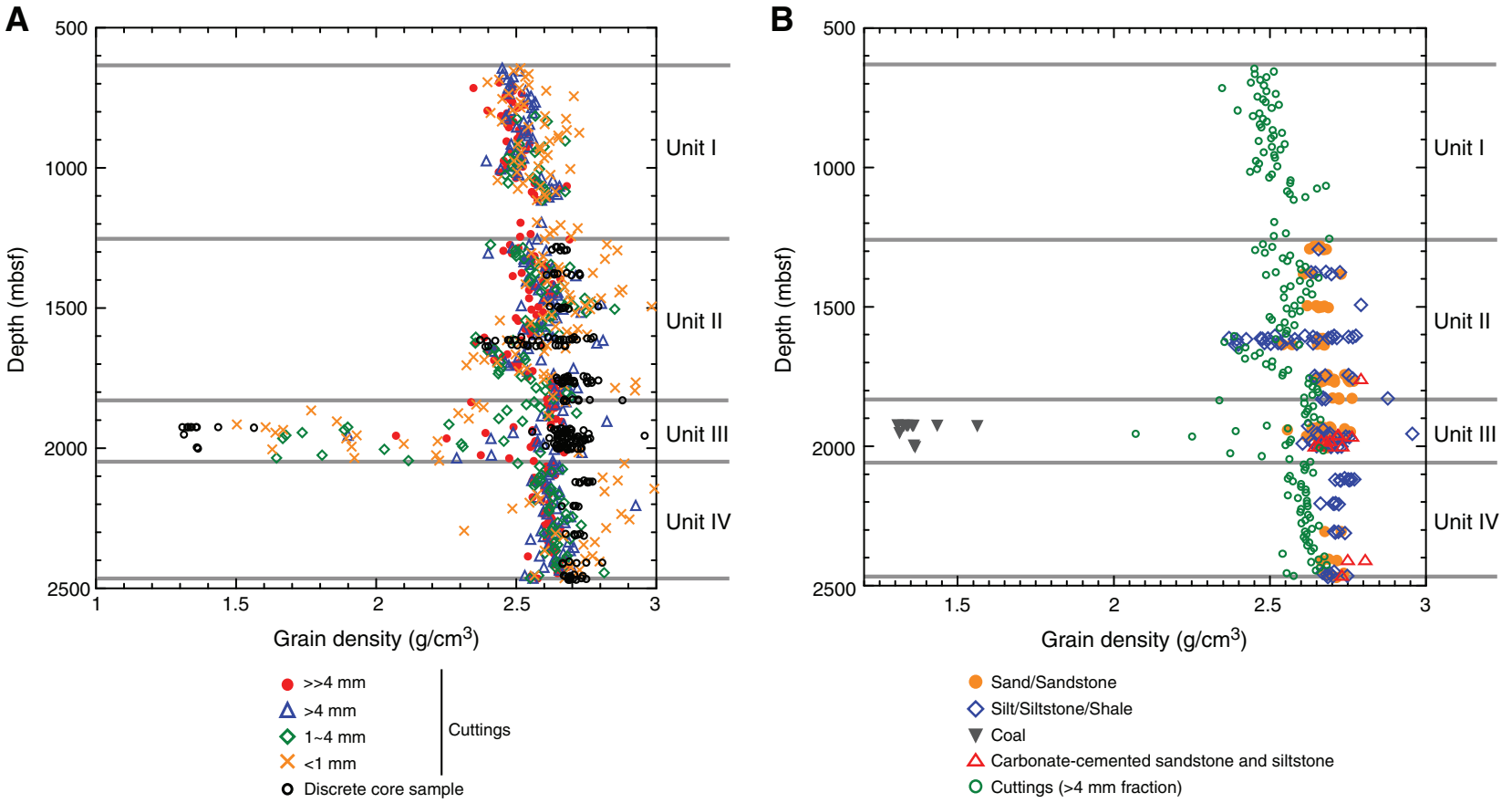

Figure F19. Distribution and lithologic variation of thermal conductivity in discrete core samples, Site C0020. Thermal conductivity of sandstone apparently linearly decreases with depth. Coal samples show lower thermal conductivity and higher values are observed in carbonate-cemented rock samples.

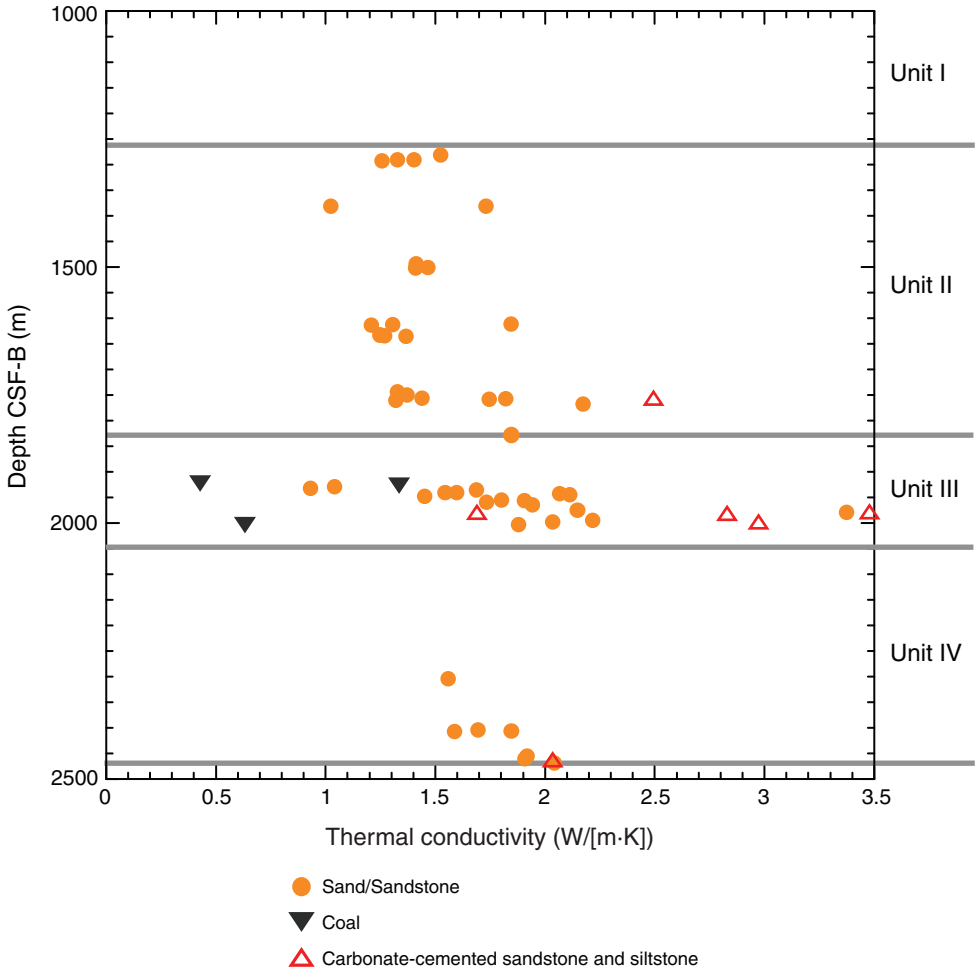

Figure F20. Distribution and lithologic variation of *P*-wave velocity in discrete core samples and cuttings samples, Site C0020.

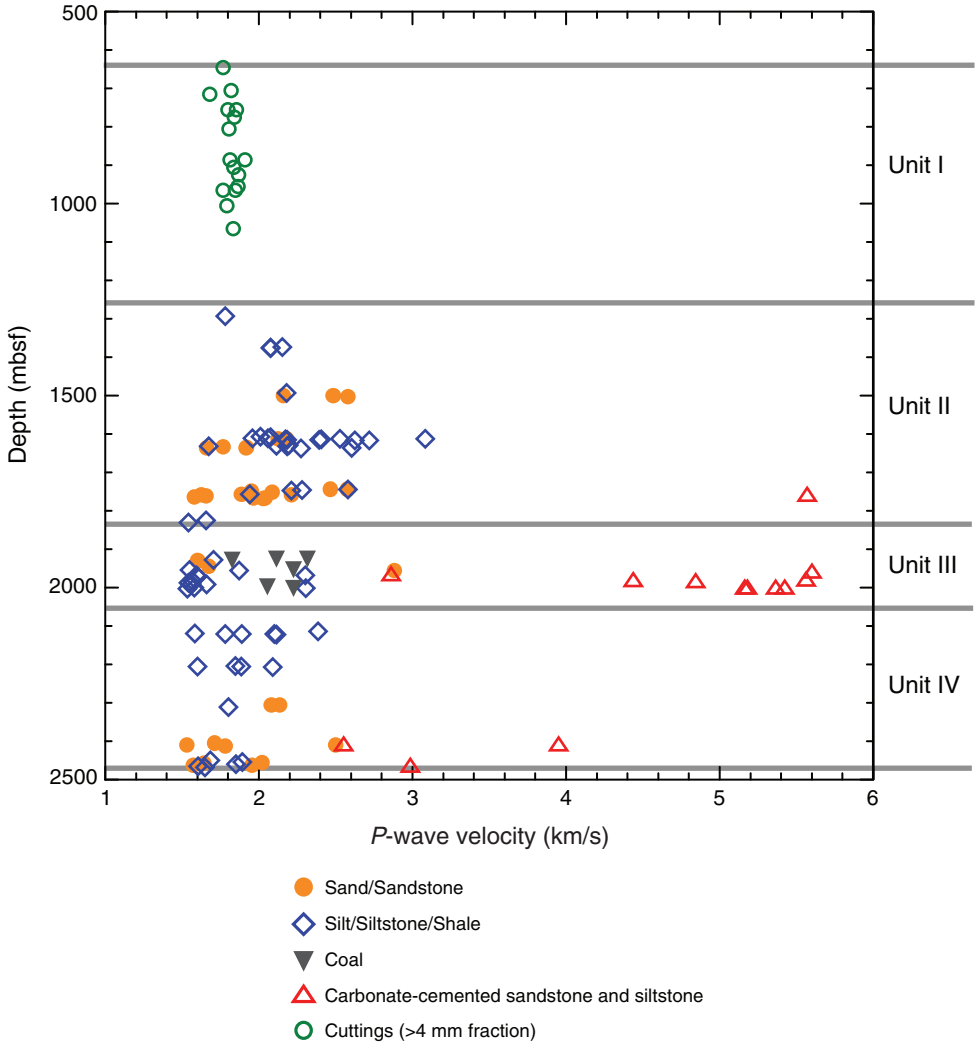

Figure F21. Distribution and lithologic variation of (**A**) electrical resistivity and (**B**) formation factor in discrete core samples and cuttings samples, Site C0020.

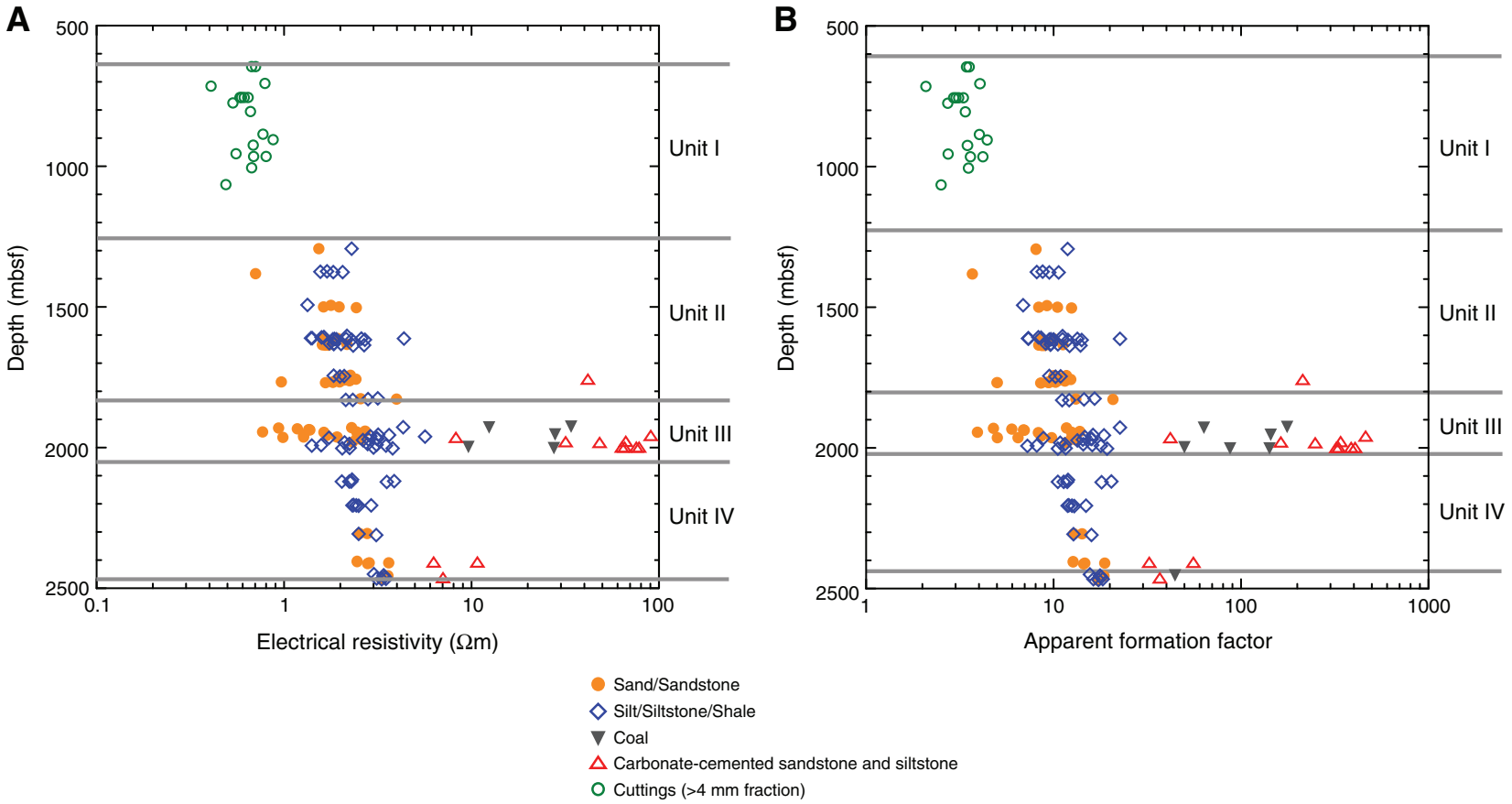

Figure F22. A. Distribution of vitrinite reflectance (R_o). Blue bar = standard deviation of R_o. **B.** Two examples of histograms for measured vitrinite reflectance from Sections 337-C0020A-15R-3 and 30R-2.

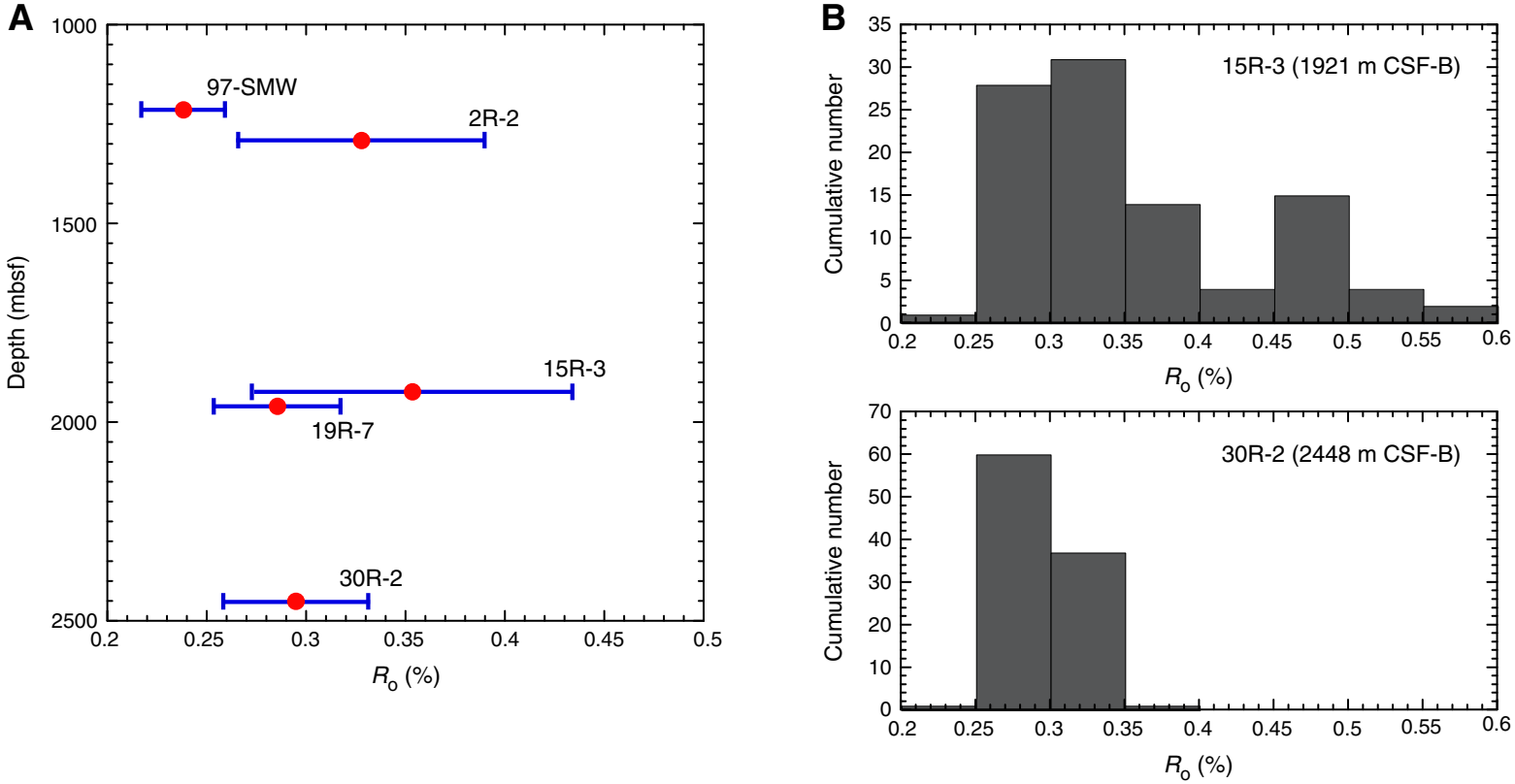

Figure F23. A. Example of 2-D core diameter measurement in whole-round core samples used for ASR measurement. **B.** Deviation between the major axis and the minor axis of core diameter used for ASR measurement. Mean, maximum, and minimum core diameters are plotted in the same figure.

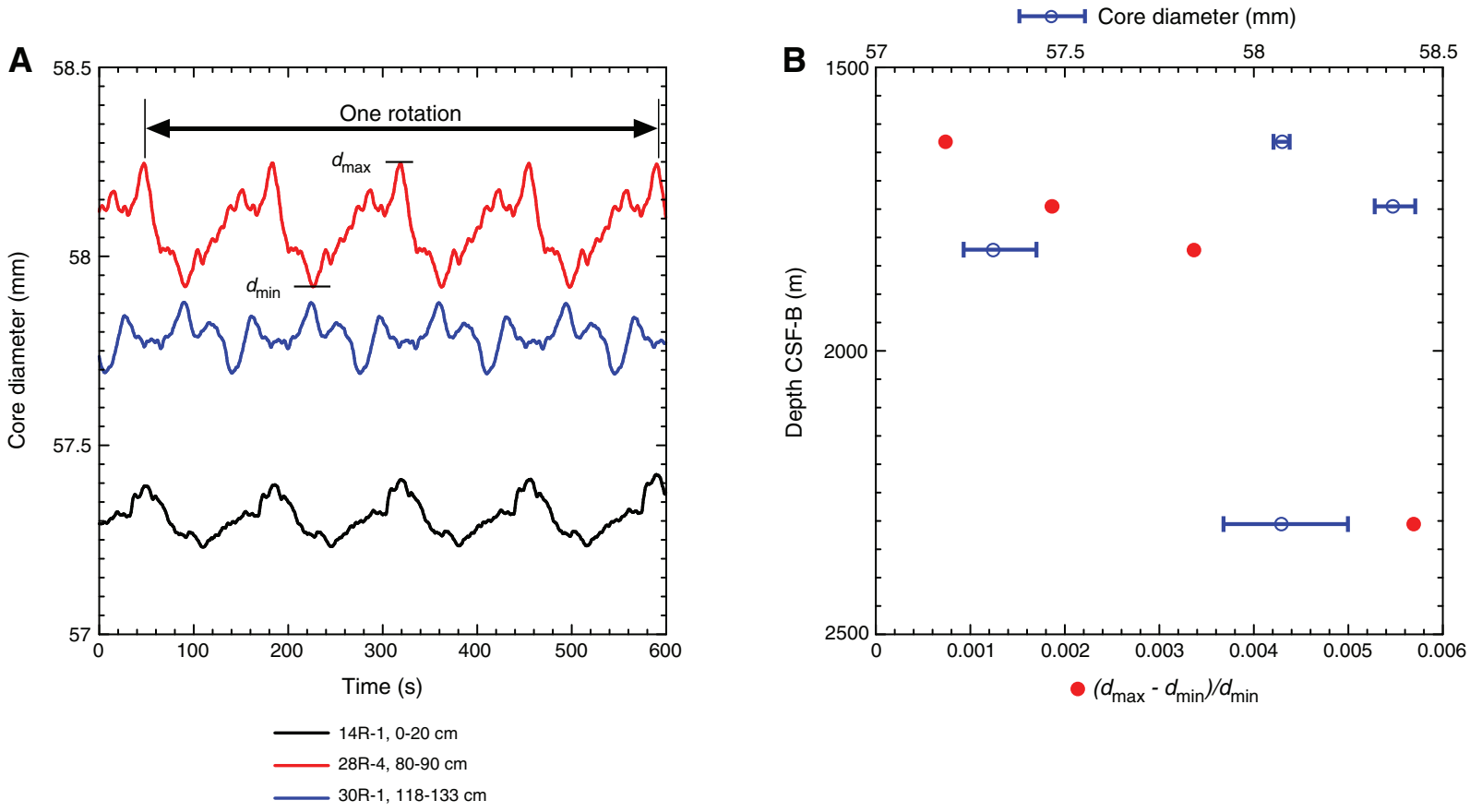

Figure F24. Plots of (**A**) potassium and (**B**) sulfate concentrations as well as (**C**) salinity for cuttings samples collected at Site C0020 and drilling mud samples collected prior to, during, and after drilling operations. R = cuttings sample measured with the Rhizon sampler.

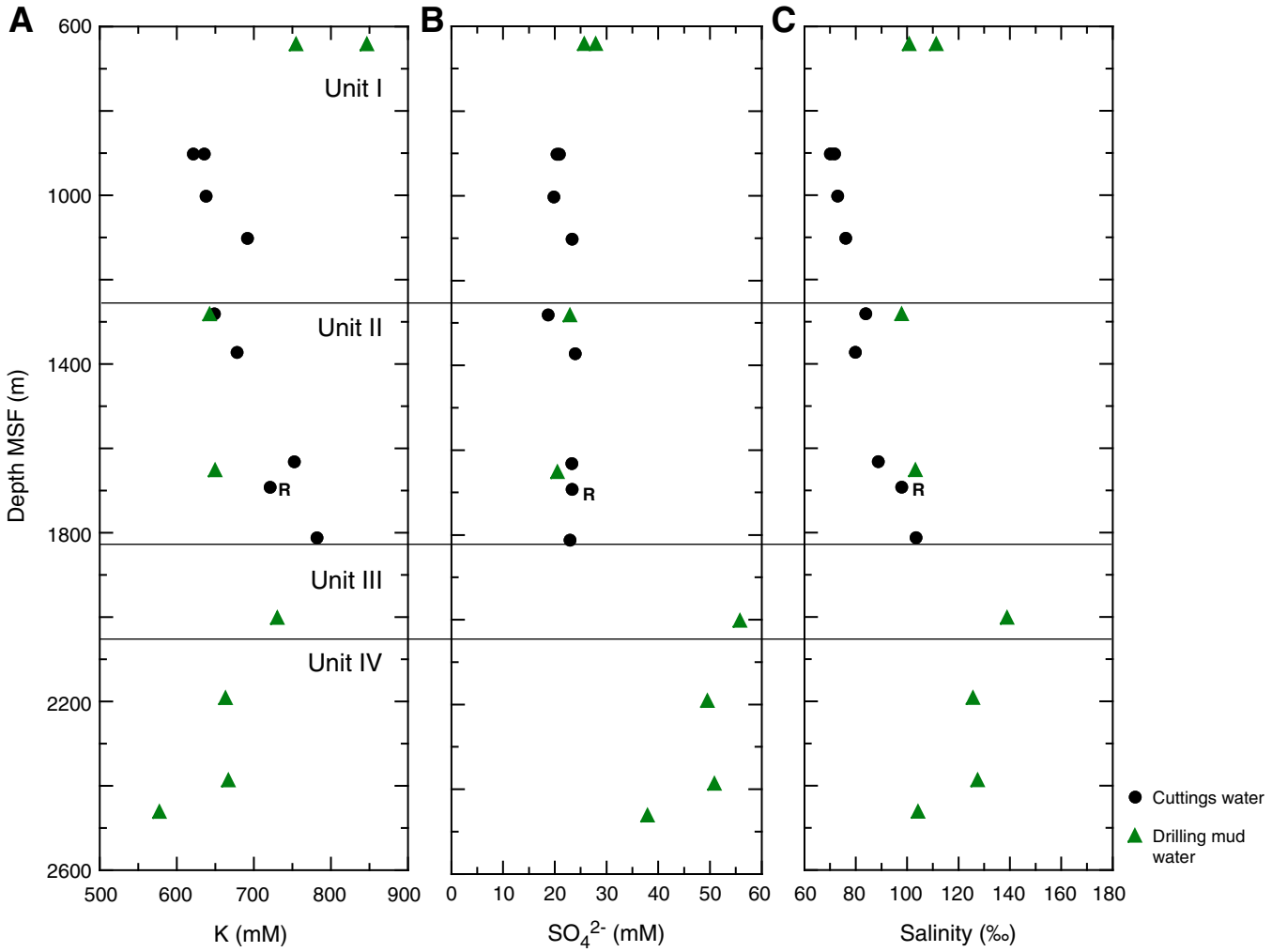

Figure F25. Volumetric interstitial water yield, Site C0020.

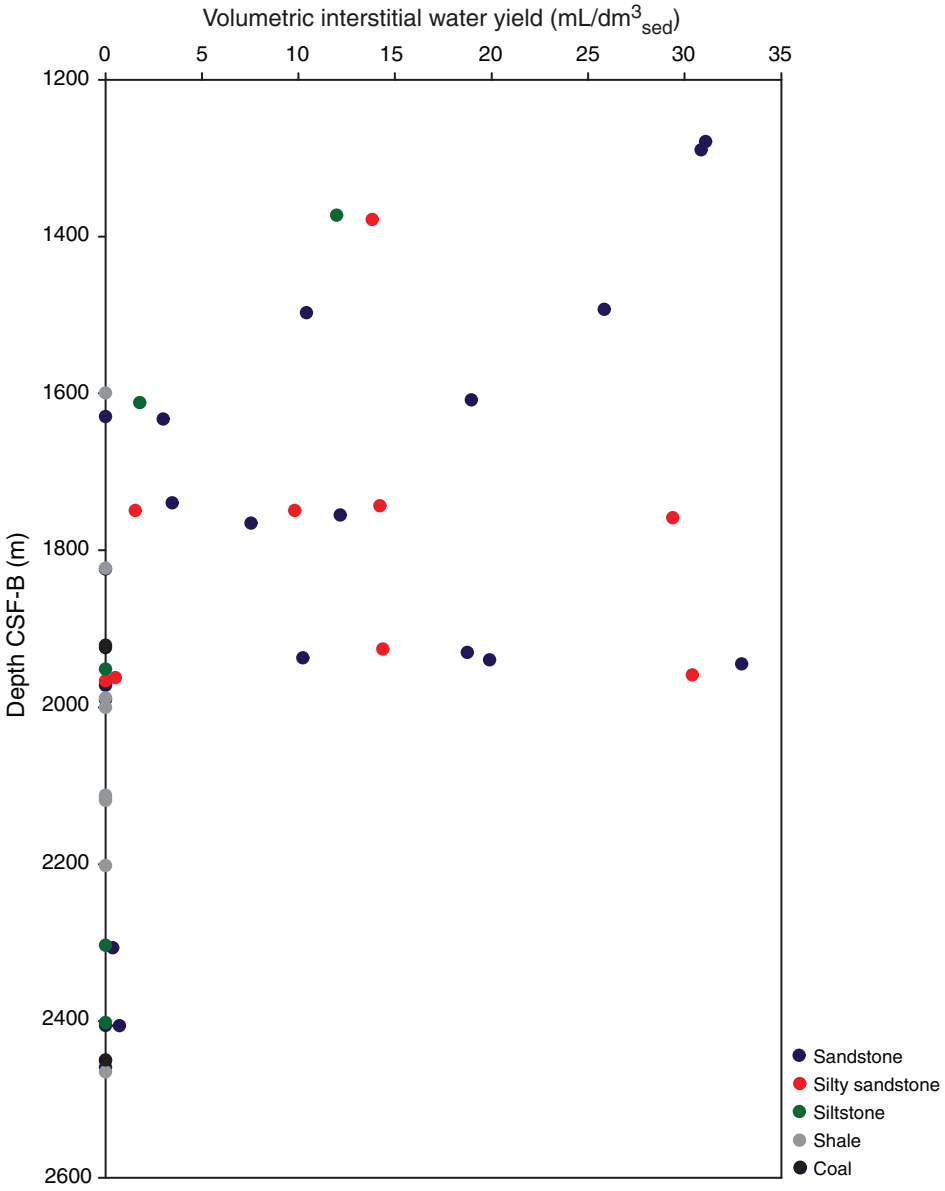

Figure F26. Plots of (**A**) salinity, (**B**) total alkalinity, and (**C**) pmH for interstitial water, Site C0020.

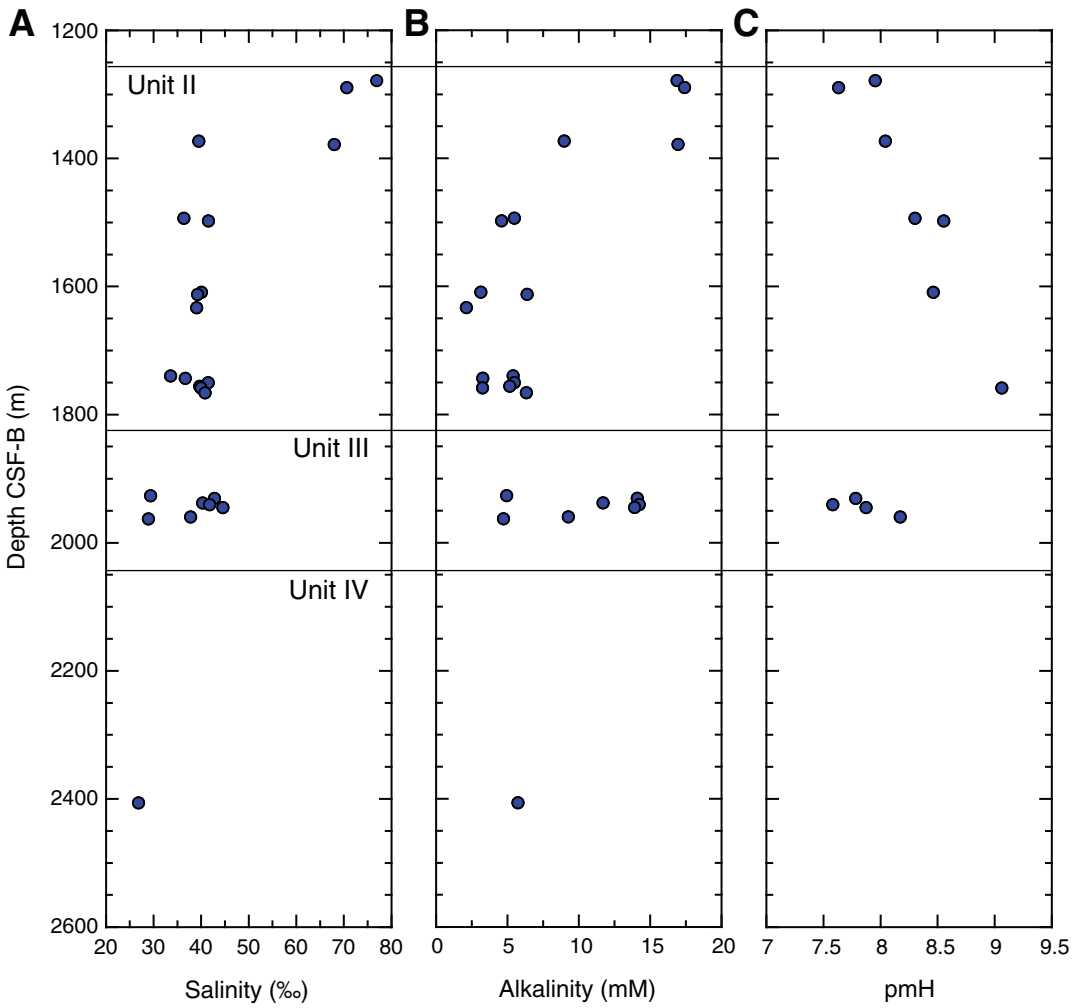

Figure F27. Plots of major anion concentrations for interstitial water, Site C0020. **A.** Chloride. **B.** Bromide. **C.** Sulfate.

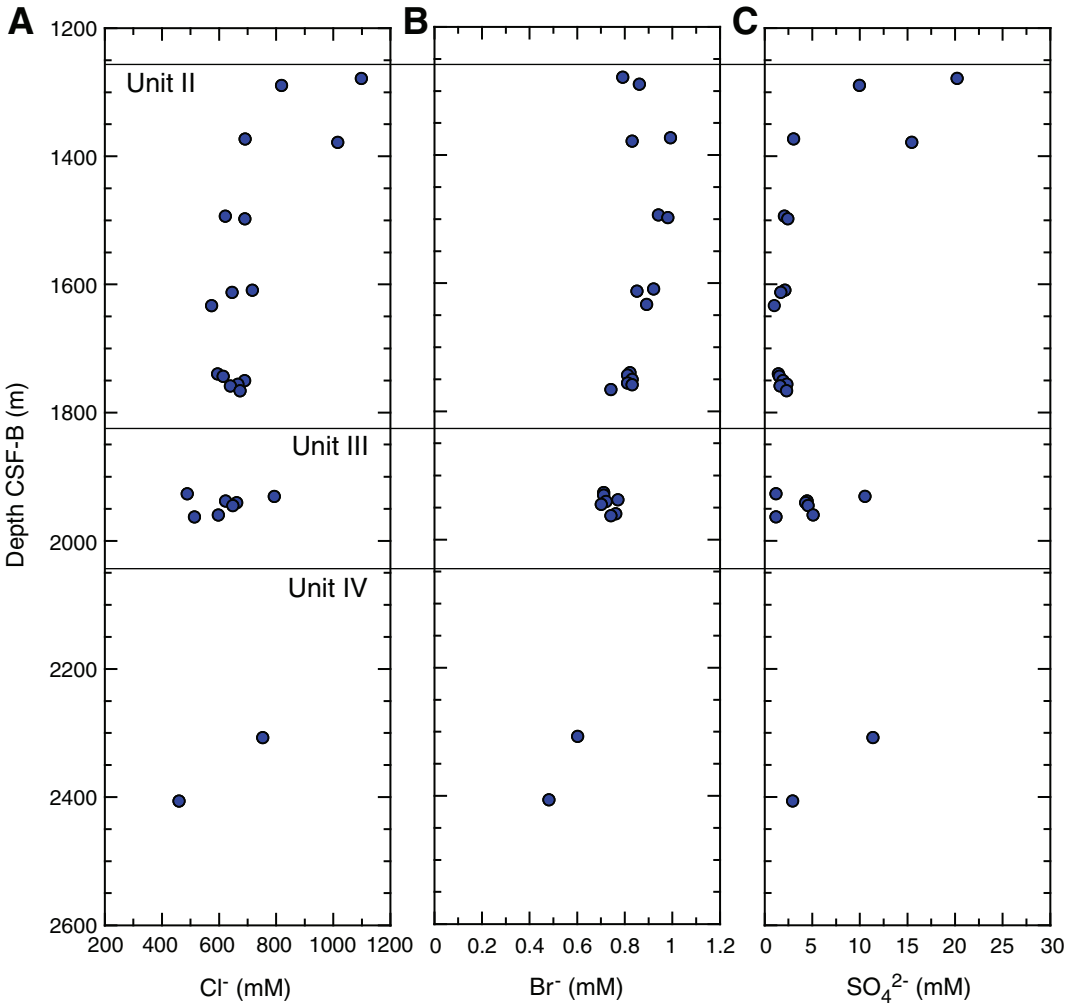

Figure F28. Plots of (**A**) ammonium, (**B**) sodium, and (**C**) potassium concentrations for interstitial water, Site C0020.

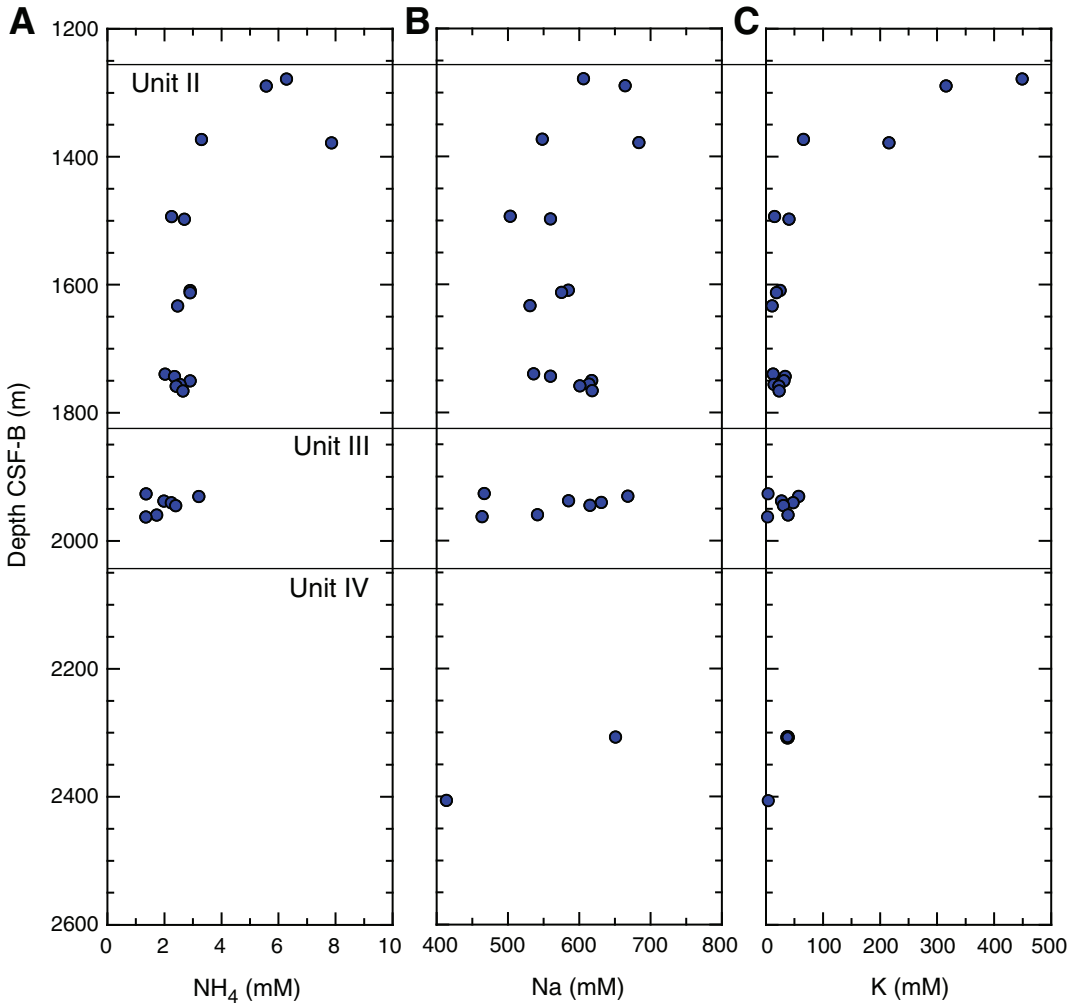

Figure F29. Plots of (**A**) magnesium, (**B**) calcium, (**C**) strontium, and (**D**) barium concentrations for interstitial water, Site C0020.

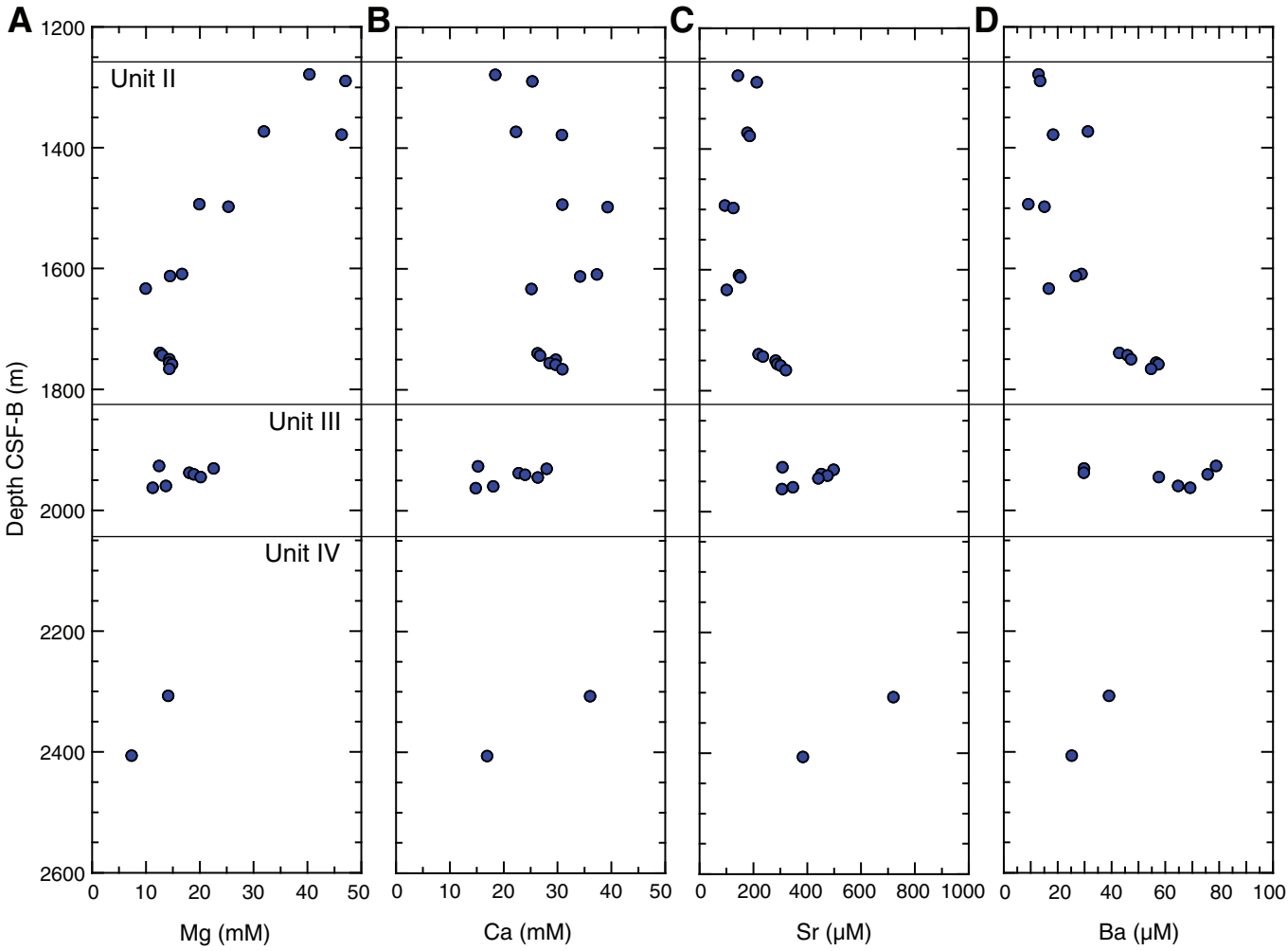

Figure F30. (A) Boron, (B) lithium, (C) silica, (D) iron, and (E) manganese concentrations for interstitial water, Site C0020.

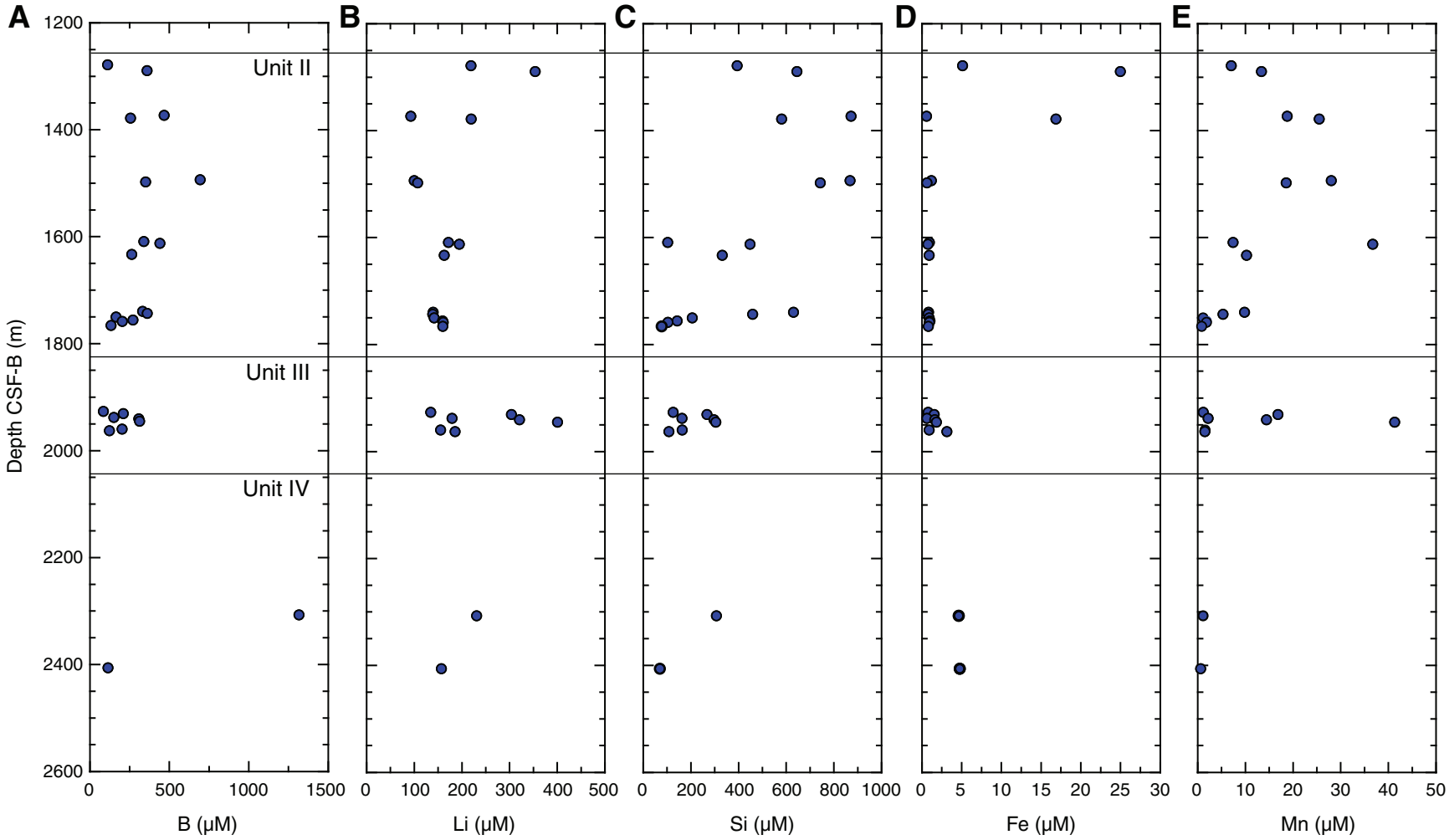

Figure F31. Depth profiles of formation water and drilling mud water, Site C0020. **A.** Sodium. **B.** Sulfate. **C.** Chloride.

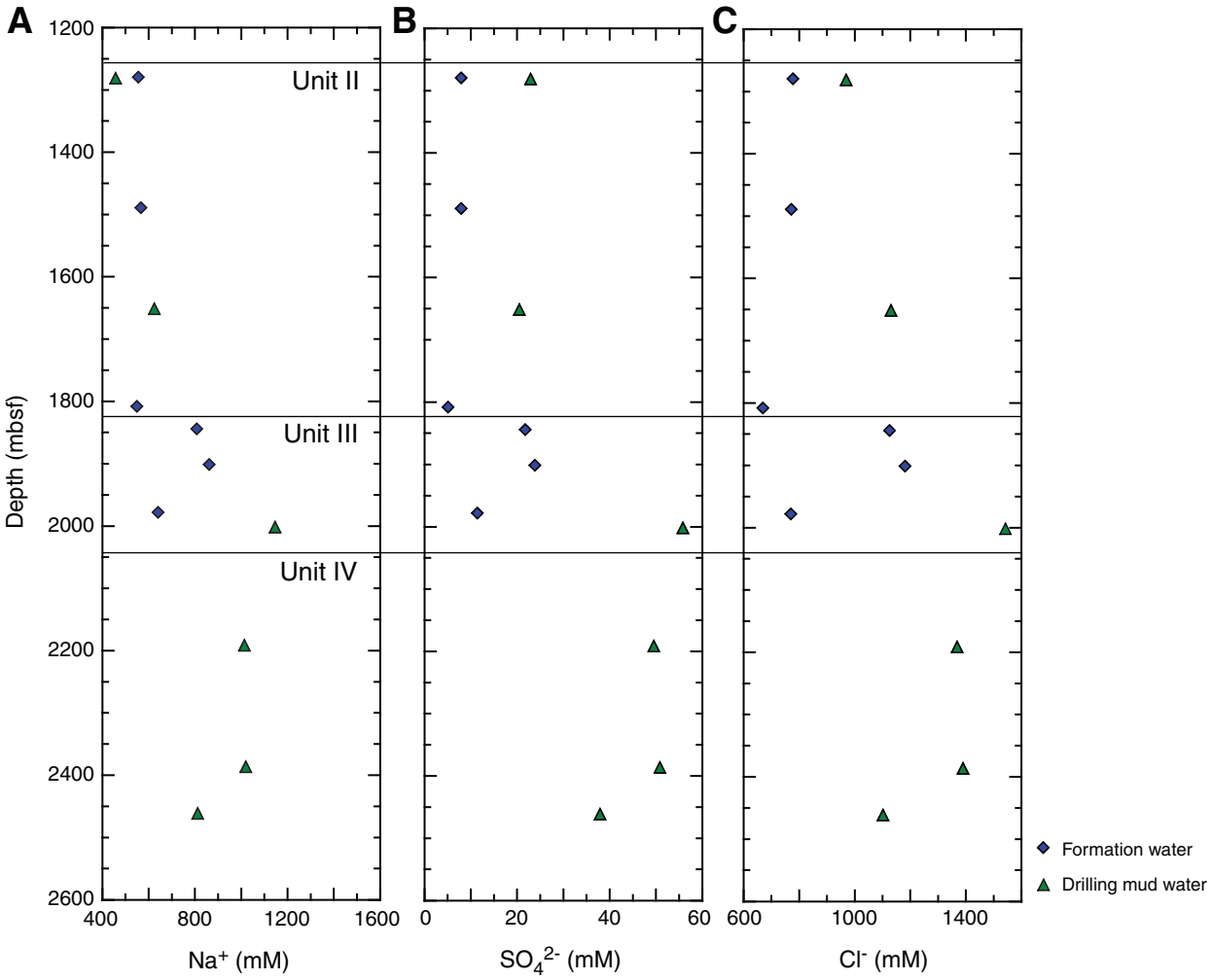

Figure F32. Estimates of drilling mud (X_{DML}) incorporated into interstitial water samples from Site C0020. X_{DML} was estimated based on concentrations of sulfate, potassium, and salinity. Shaded field = ±1σ region of the average X_{DML} values (not shown) calculated for the pore water. Open symbols are for X_{DML} in the formation waters collected in SSBs. The color is the same as the corresponding mud fractions based on sulfate, potassium, and salinity that were applied to the pore water. With the exception of the first SSB sample in Unit II, all of the other samples showed mud fractions that exceeded those of the pore water.

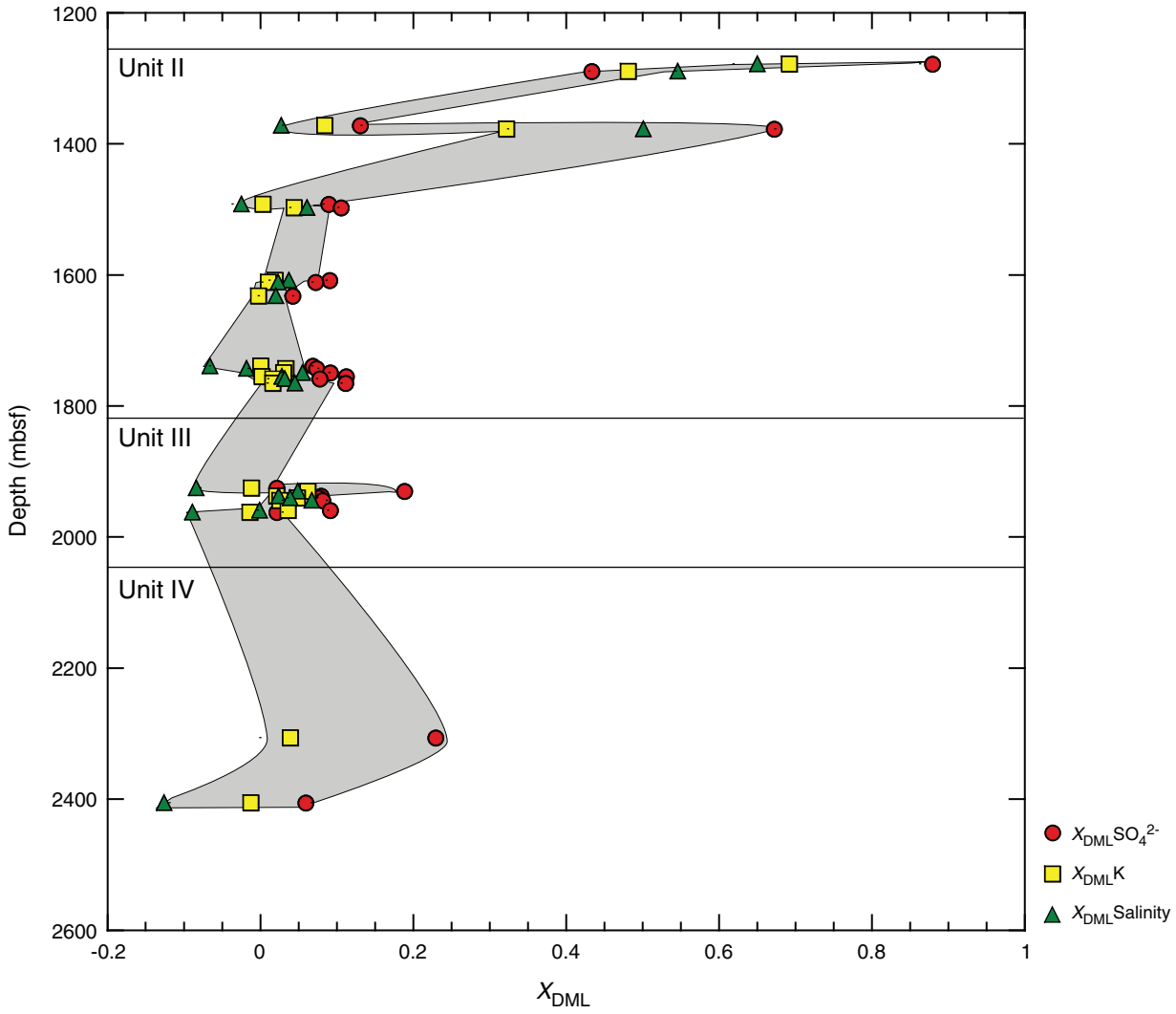

Figure F33. Depth profiles of corrected (**A**) total alkalinity, (**B**) calcium, (**C**) magnesium, and (**D**) strontium concentrations of interstitial water at Site C0020 based on the averaged X_{DML}. Error bars in A delineate the ±1σ uncertainty.

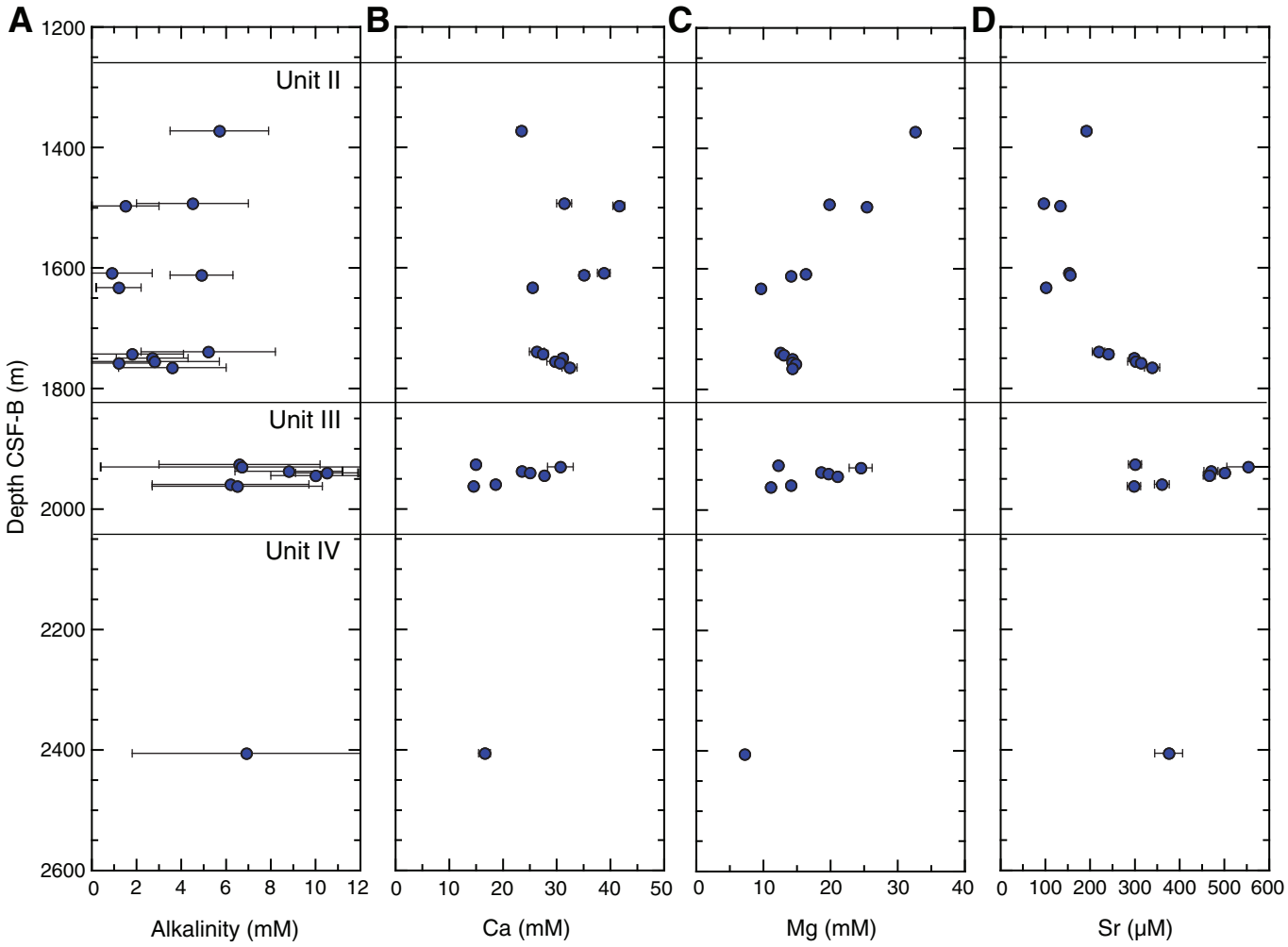

Figure F34. Diagram of depth of the incoming mud gas below the seafloor versus date and time of its arrival in the mud-gas monitoring van, Hole C0020A. The progression of drilling into the formation allows all days to be displayed on a 24 h scale in one panel. During mud-gas monitoring, all data were recorded in ship local time (UTC + 8 h).

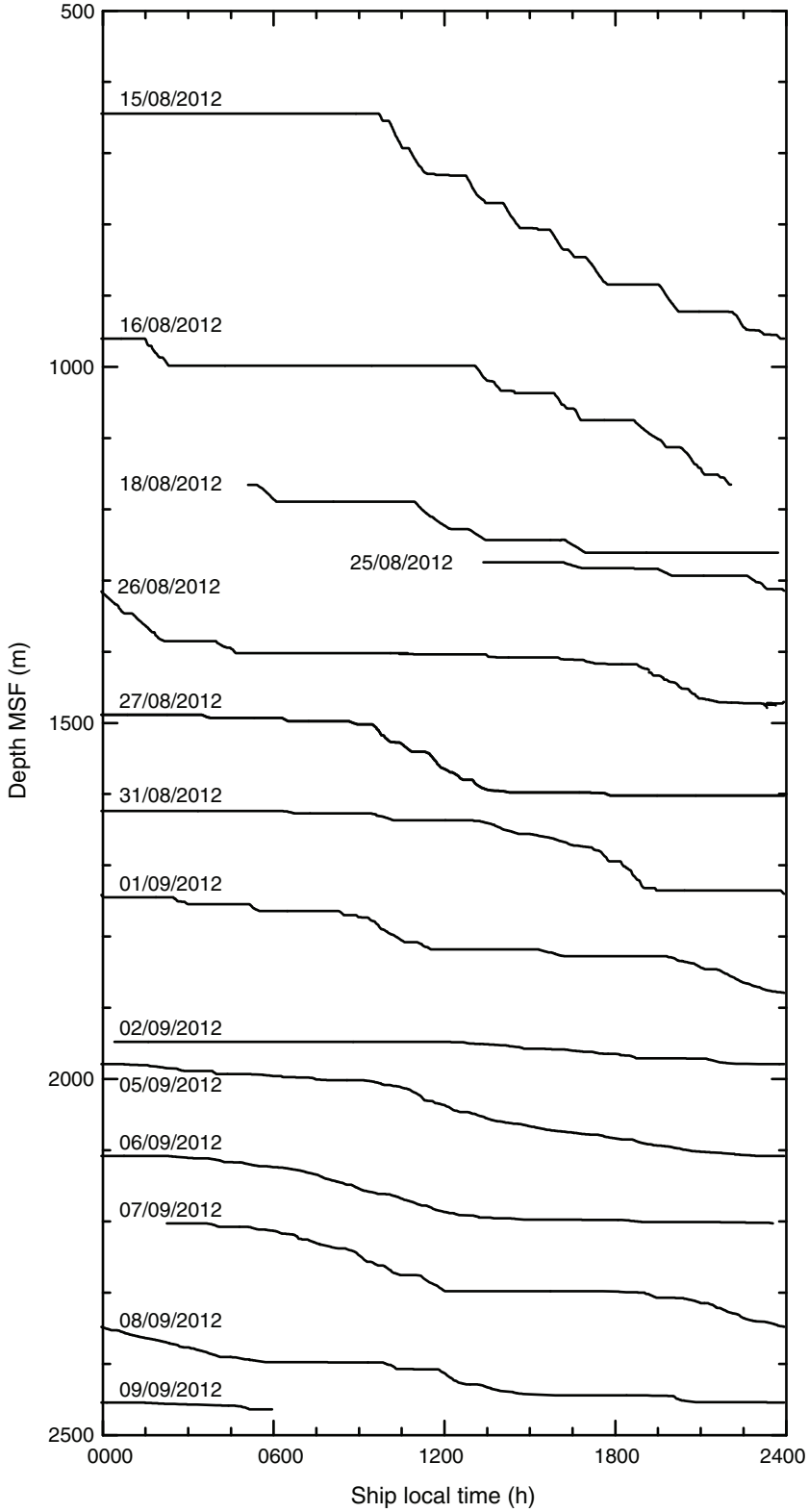

Figure F35. $\delta^{13}C$ values of methane at Site C0020, measured on samples retrieved from Holes C0020A and C9001D. MCIA on-line mud-gas monitoring in Hole C0020A recorded $\delta^{13}C$ values of methane with a frequency of 1 measurement/s, yielding a total of ~186,000 data points for the time intervals with mud-gas recovery (see Table T16). In general, 100–200 data points were recorded per meter of drilled sediment in Hole C0020A and the average values are plotted against depth. For comparison, $\delta^{13}C$-CH_4 data are shown for the upper 358 mbsf of Site C0020 that result from headspace analysis of core samples taken from Hole C9001D during the *Chikyu* shakedown cruise (Expedition CK06-06) in 2006 (F. Inagaki et al., unpubl. data). VPDB = Vienna Peedee belemnite.

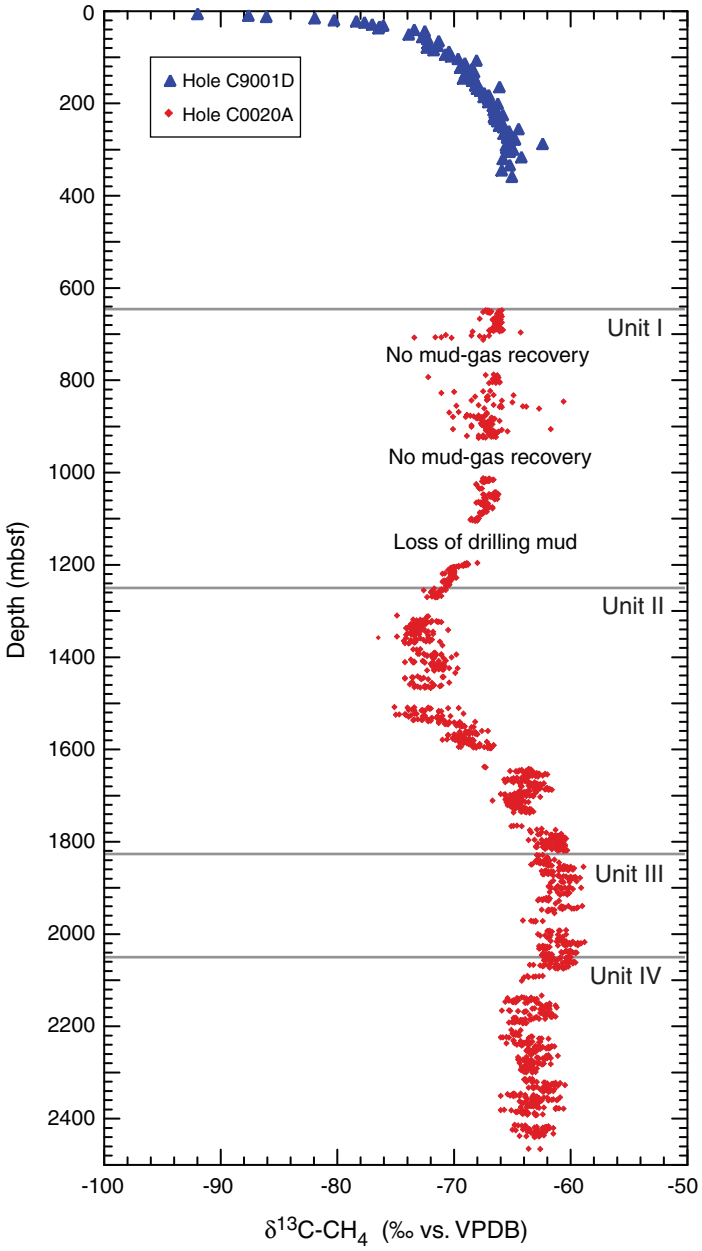

Figure F36. A. C_1/C_2 ratios in mud gas analyzed by on-line mud-gas monitoring and in cuttings and cores by headspace technique, Site C0020. **B.** Mud-gas C_1/C_2 ratios versus in situ temperature (based on a geothermal gradient of 24°C/km and a bottom water temperature of 6°C). High C_1/C_2 ratios are characteristic of biogenic methane formation; low ratios indicate enhanced thermogenic sources. At Site C0020, C_1/C_2 ratios point to biogenic methane sources. C_1/C_2 ratios generally decrease with increasing depth as expected, but they show a distinct excursion toward higher values between 1840 and 2054 m MSF (i.e., the depth interval containing 12 coal layers). The excursion of the C_1/C_2 ratio points to enhanced activity of biological methanogenesis in or between the coal layers. TOC = total organic carbon.

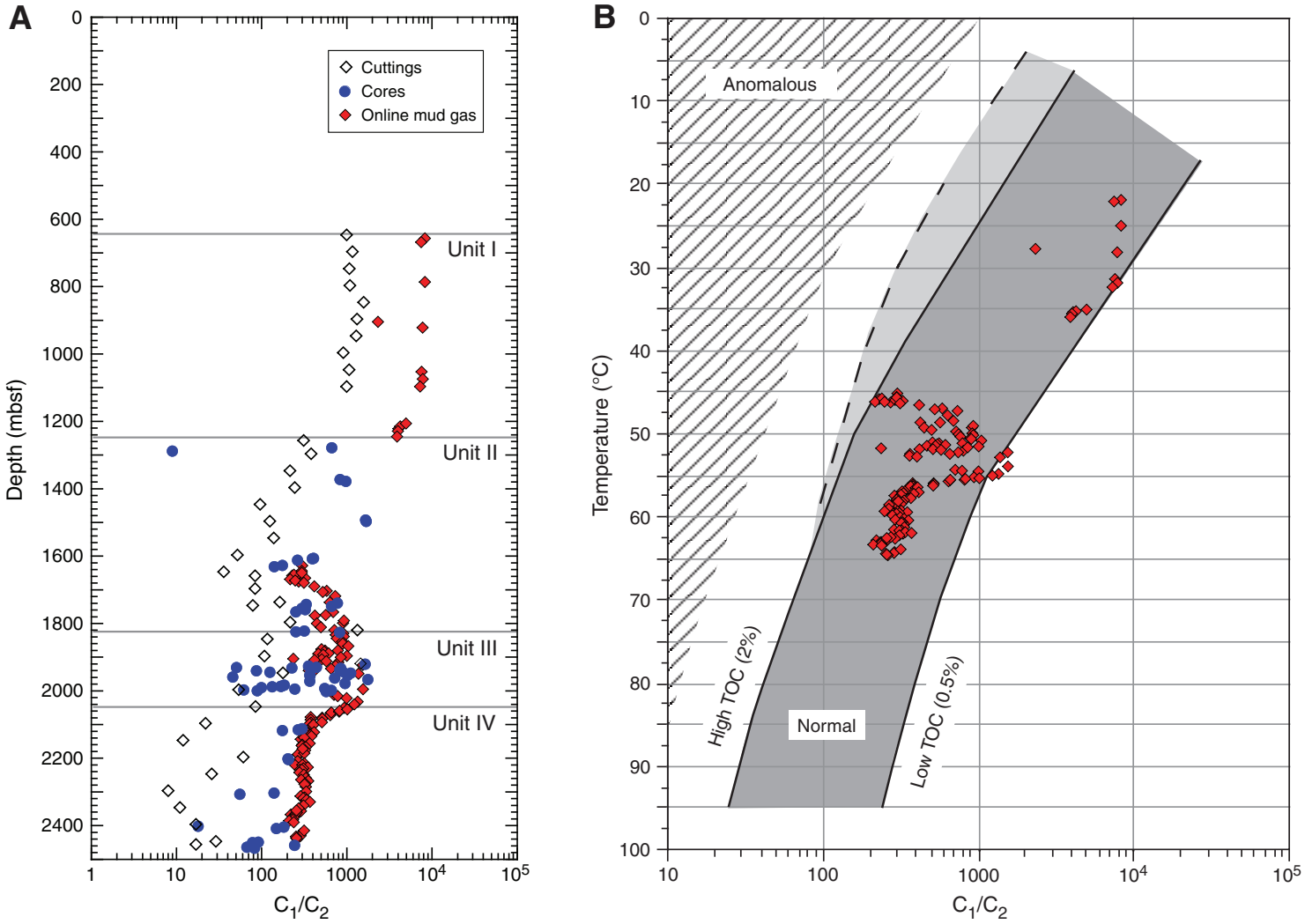

Figure F37. Ratios of hydrogen, oxygen, and nitrogen to argon in mud gas at Site C0020, analyzed during on-line mud-gas monitoring using PGMS. On-line mud-gas monitoring by PGMS only started at 1005.5 m MSF because of insufficient gas flow to the instrument during the first day of mud-gas monitoring (15 August 2012).

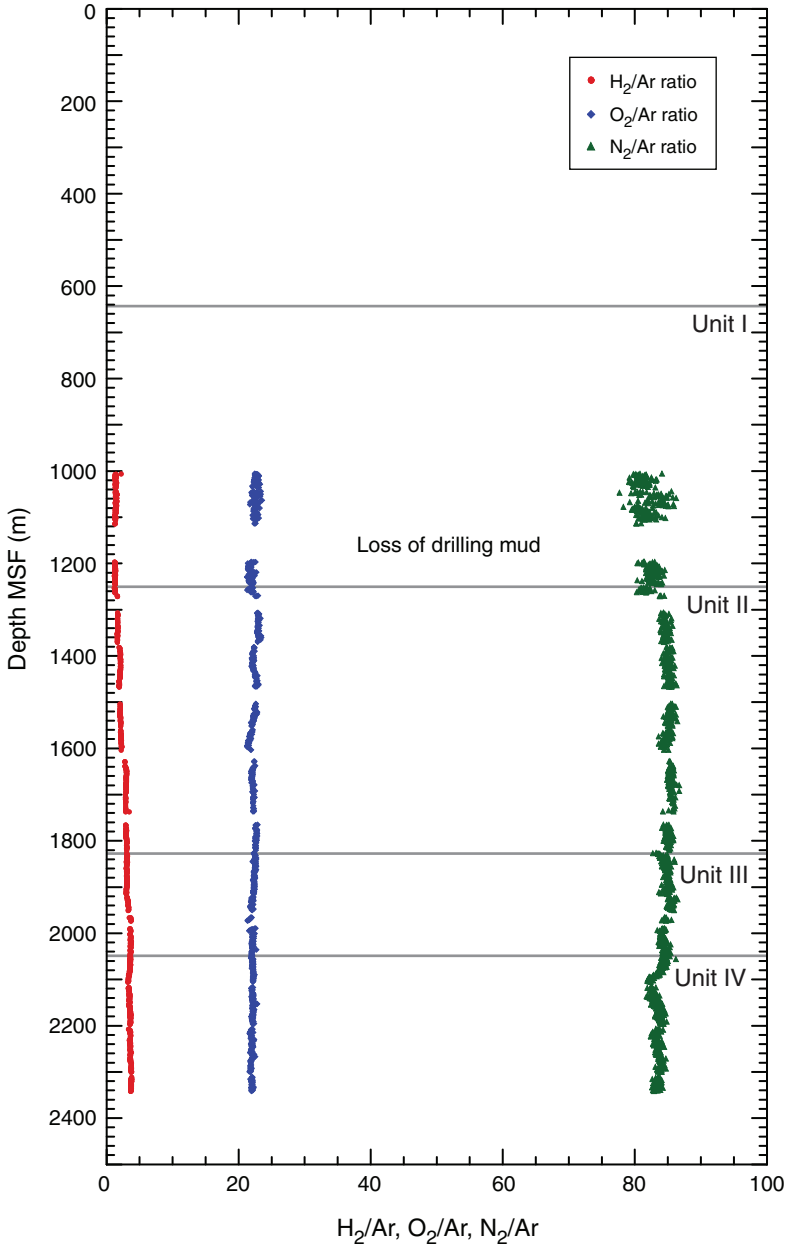

Figure F38. Downhole profile of (**A**) H_2 and (**B**) CO concentrations from the extraction method, Site C0020. Data from sediment cores and drilling mud caught inside the core liner are shown.

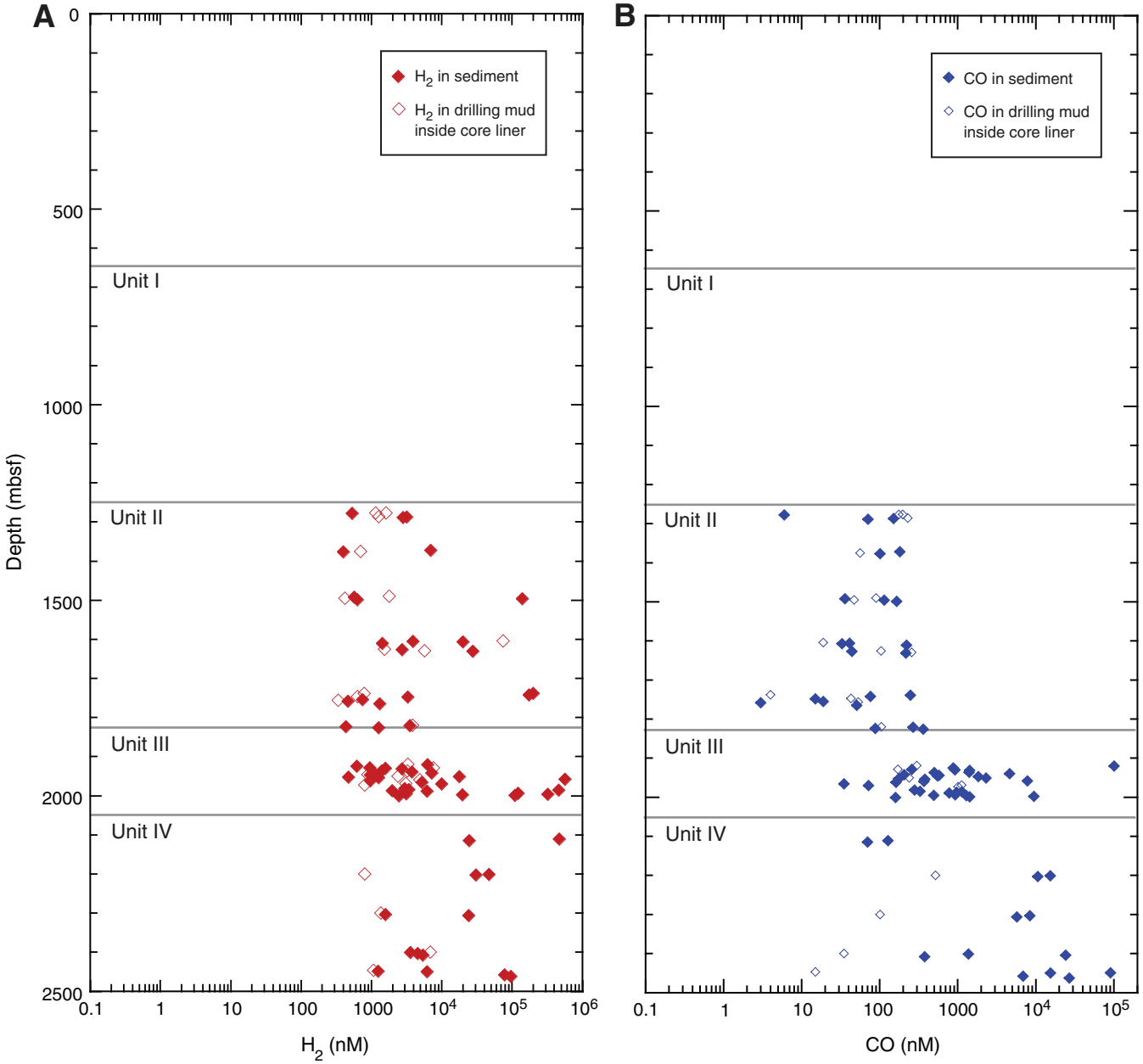

Figure F39. Depth profiles of (**A**) inorganic carbon, (**B**) total organic carbon (TOC), (**C**) total nitrogen (TN), (**D**) total sulfur, and (**E**) molecular TOC/TN ratio, Site C0020. Open symbols = cuttings samples, solid symbols = core samples.

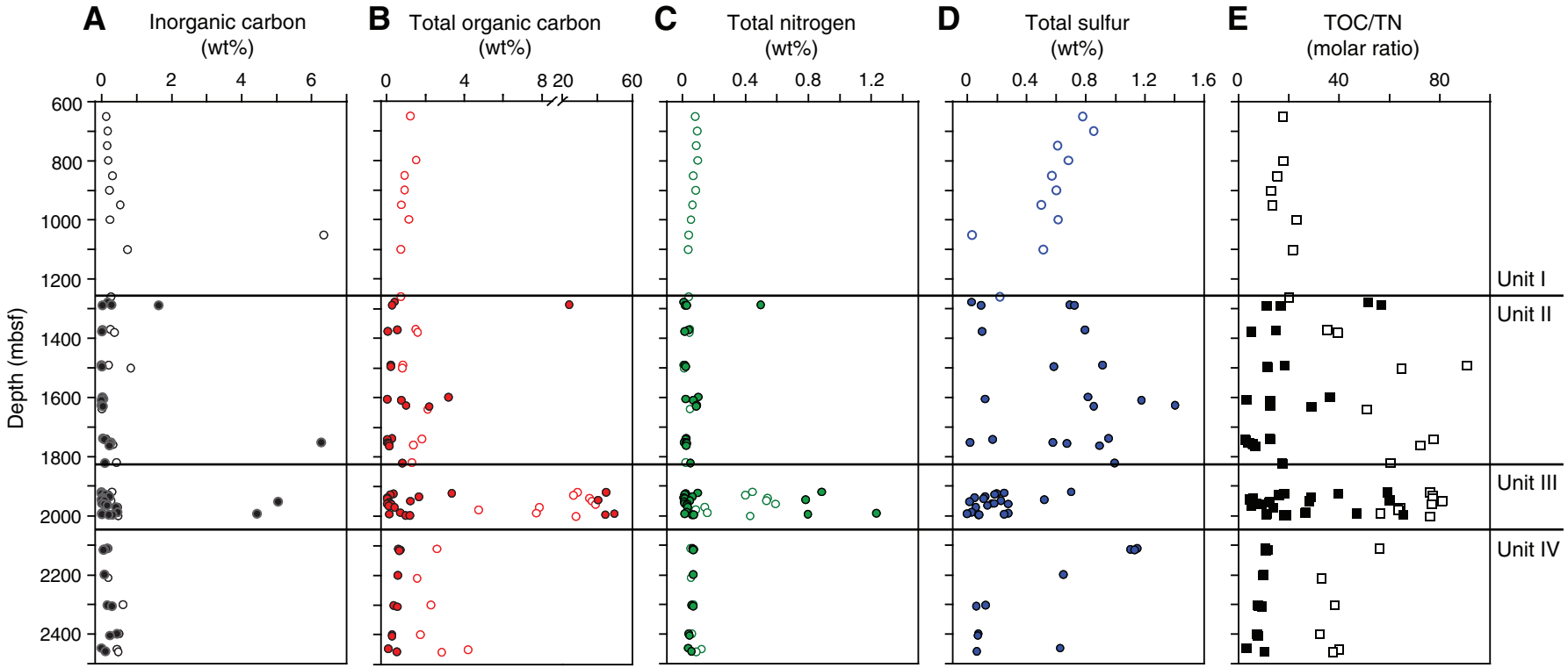

Figure F40. Depth profiles of Rock-Eval pyrolysis parameters, Site C0020. **A.** T_{max}. **B.** S1 – hydrocarbons free/volatile hydrocarbons. **C.** S2 – hydrocarbons liberated by pyrolysis. **D.** S3 – yield on combustion. **E.** Hydrogen index. **F.** Oxygen index. OM = organic matter, HC = hydrocarbon, TOC = total organic carbon. Open circles = cuttings samples, solid circles = core samples. Blue arrows = values from ODP Leg 201 Site 1227 (Peru margin, water depth = 427 m, sediment from 7 to 103 mbsf, TOC = 1–11 wt%; D'Hondt, Jørgensen, Miller, et al., 2003), red arrows = values from IODP Expedition 322 Hole C0011B (Nankai Trough, water depth = 4049 m, sediment from 340 to 858 mbsf, TOC < 0.5 wt%; Underwood et al., 2009).

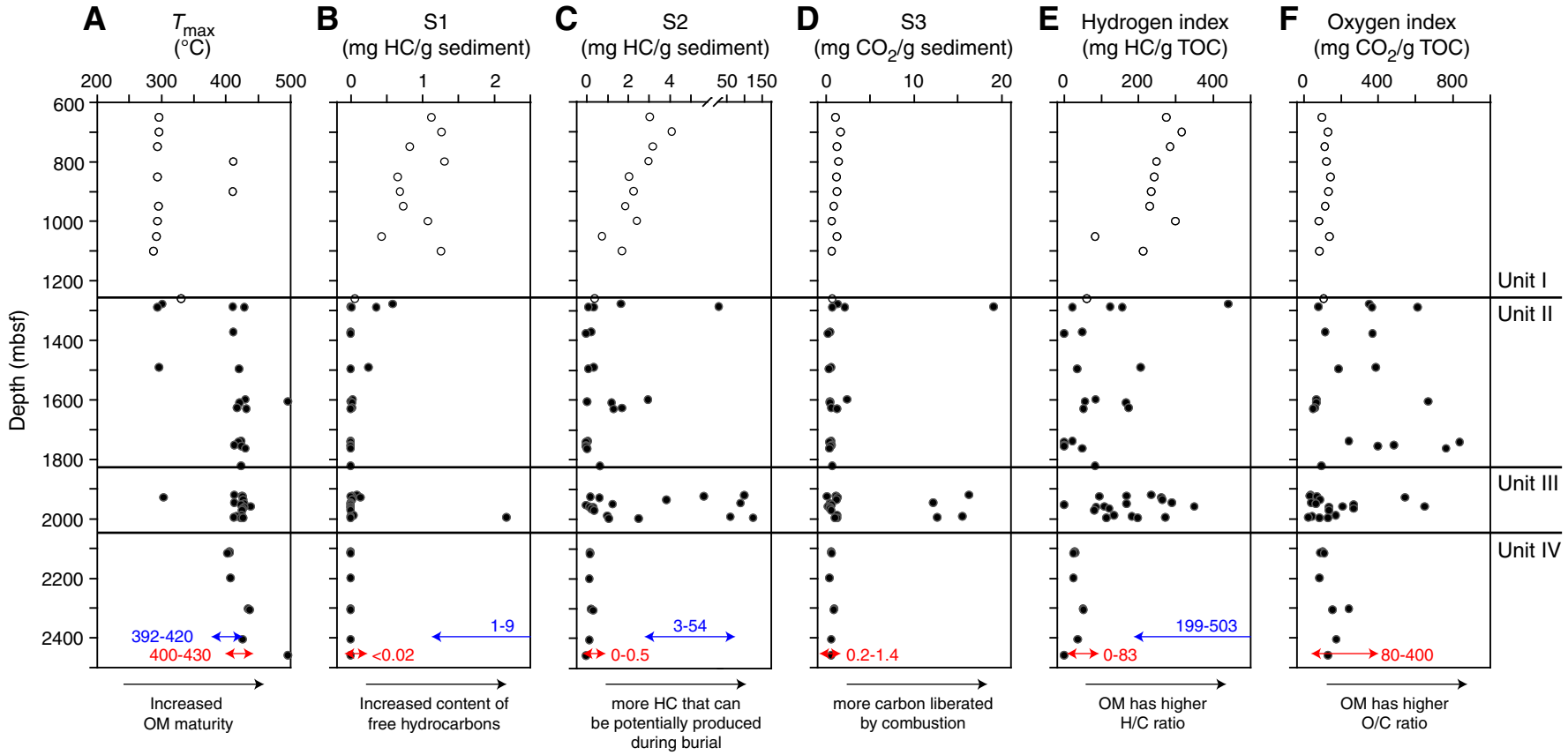

Figure F41. *n*-Alkane *m/z* 85 mass chromatograms, Site C0020. Representative chromatograms for coal, siltstone, and mudstone lithologies. Pr = pristane, Ph = phytane, 19 = C_{19} *n*-alkanes, etc.

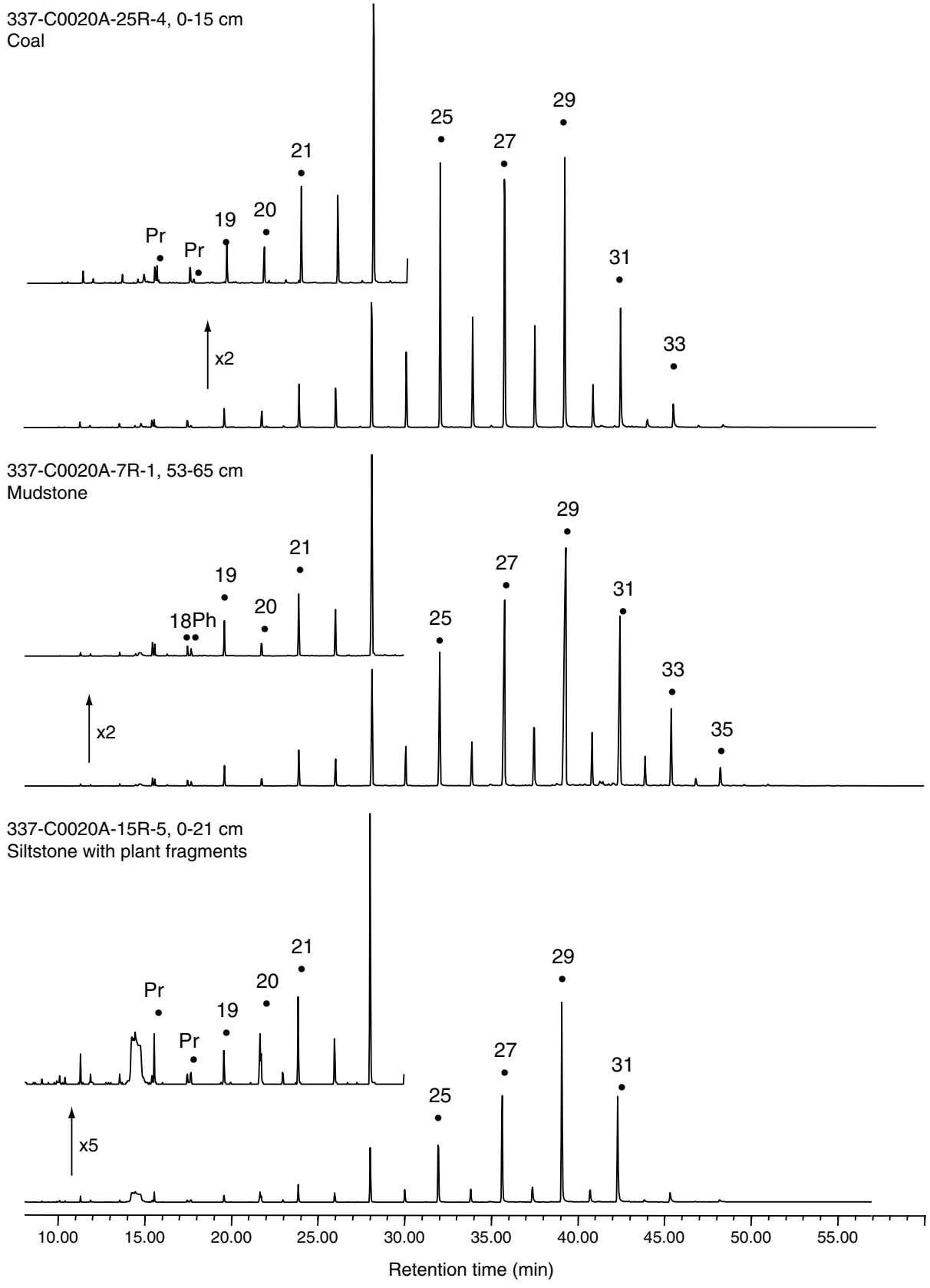

Figure F42. Combined mass chromatograms of the ions *m/z* 178 + 192, Site C0020. Representative chromatograms for coal, siltstone, and mudstone lithologies. P = phenanthrene, 2-MP = 2-methylphenanthrene, etc.

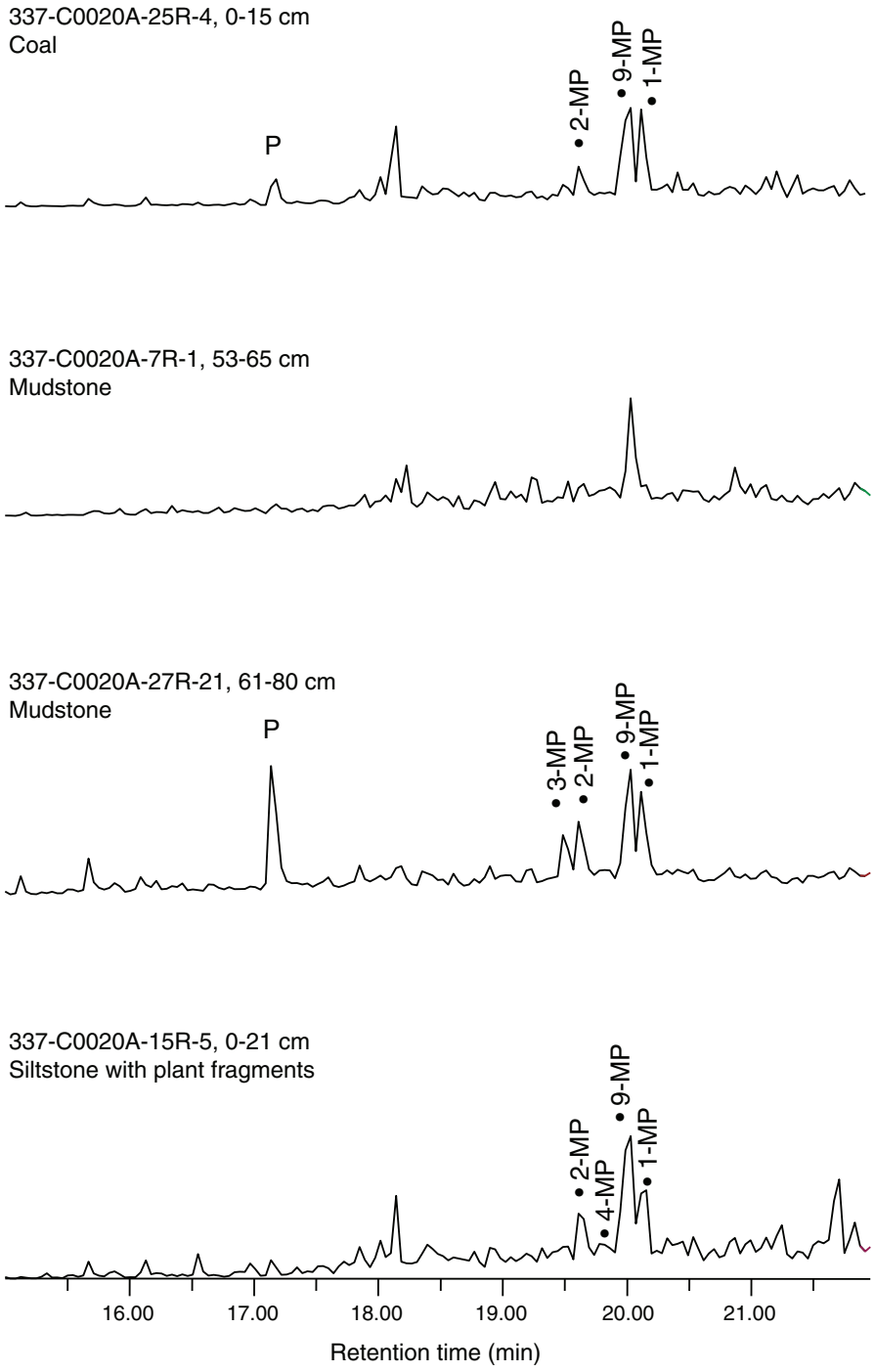

Figure F43. Combined mass chromatograms of the ions *m/z* 202 + 216, Site C0020. Representative chromatograms for coal, siltstone, and mudstone lithologies. Fl = fluoranthene, Py = pyrene, Fl[a] = benzo[a]fluoranthene, etc.

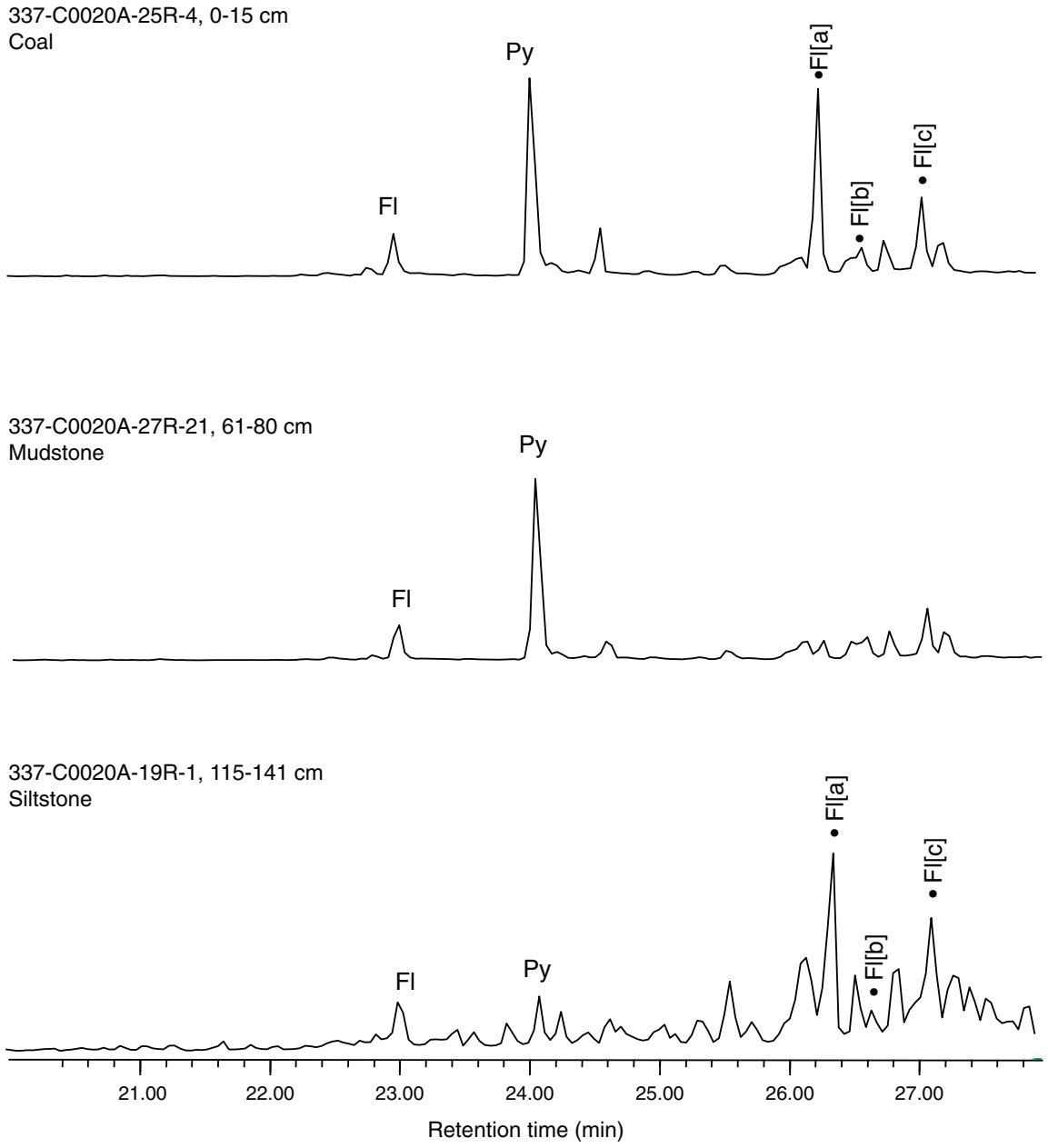

Figure F44. Combined mass chromatograms of the ions *m/z* 117 + 75 showing the trimethylsilyl ethers and esters of *n*-alkanols and *n*-alkanoic acids, respectively, Site C0020. Representative chromatograms for coal, siltstone, and mudstone lithologies. 16:0 = C_{16} *n*-alkanoic acid, 18:0 OH = C_{18} *n*-alkanol, etc., * = interfering peak derived from drilling operations.

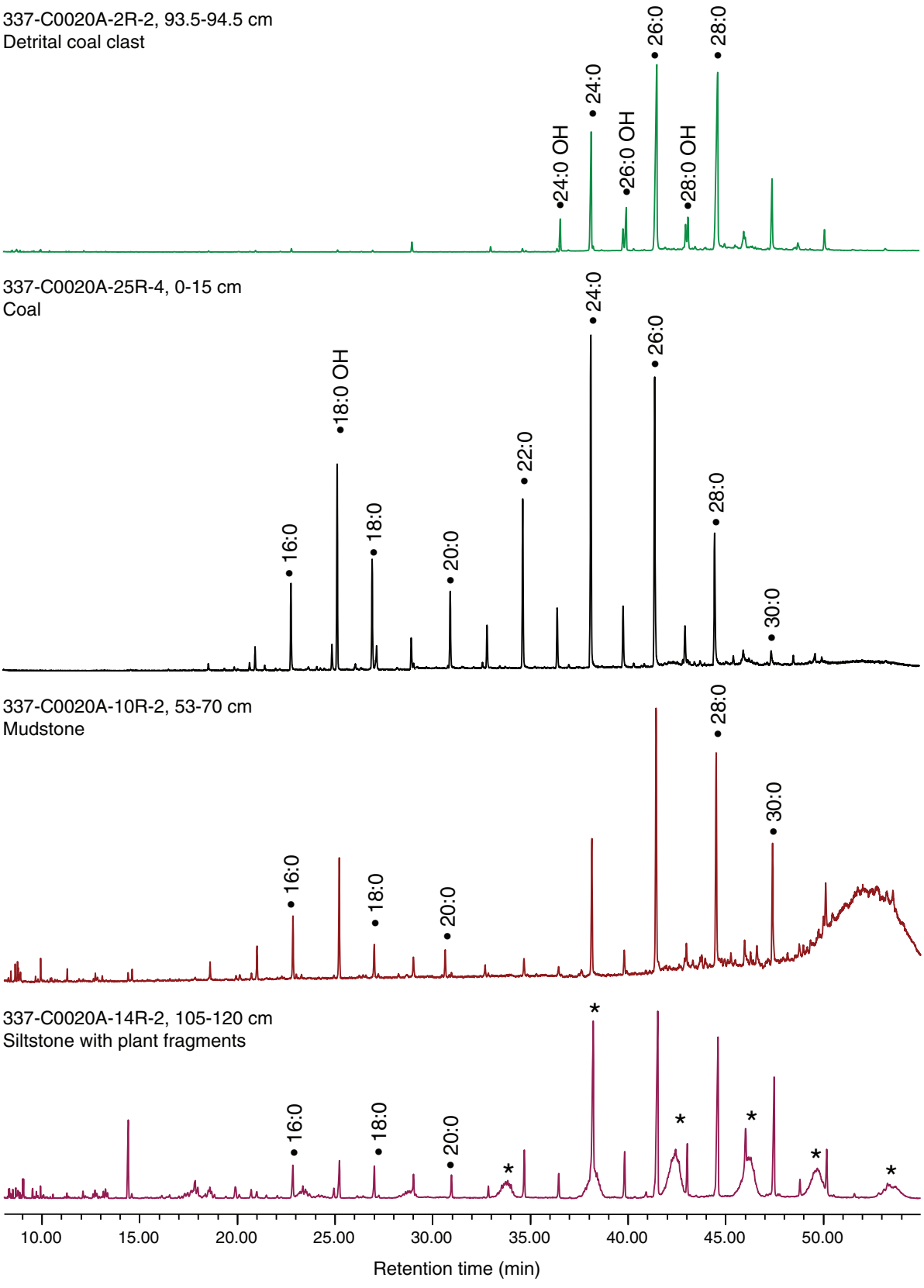

Figure F45. Combined mass chromatograms of the ions *m/z* 117 + 75 showing the trimethylsilyl ethers and esters of *n*-alkanols and *n*-alkanoic acids, respectively, Site C0020. Chromatograms displayed next to carbon preference index (CPI) for *n*-alkanoic acids and *n*-alkanes, where CPI *n*-alkanoic acids = (24:0 + 26:0 + 28:0 + 30:0 + 32:0)/(23:0 + 25:0 + 27:0 + 29:0 + 31:0) and CPI *n*-alkanes = 2 × ([C_{25} + C_{27} + C_{29} + C_{31} + C_{33}]/[C_{24} + C_{26} + C_{28} + C_{30} + C_{32}] + [C_{25} + C_{27} + C_{29} + C_{31} + C_{33}]/[C_{26} + C_{28} + C_{30} + C_{32} + C_{34}]). 18:0 = C18 *n*-alkanoic acid, n25 = C_{25} *n*-alkanes, etc.

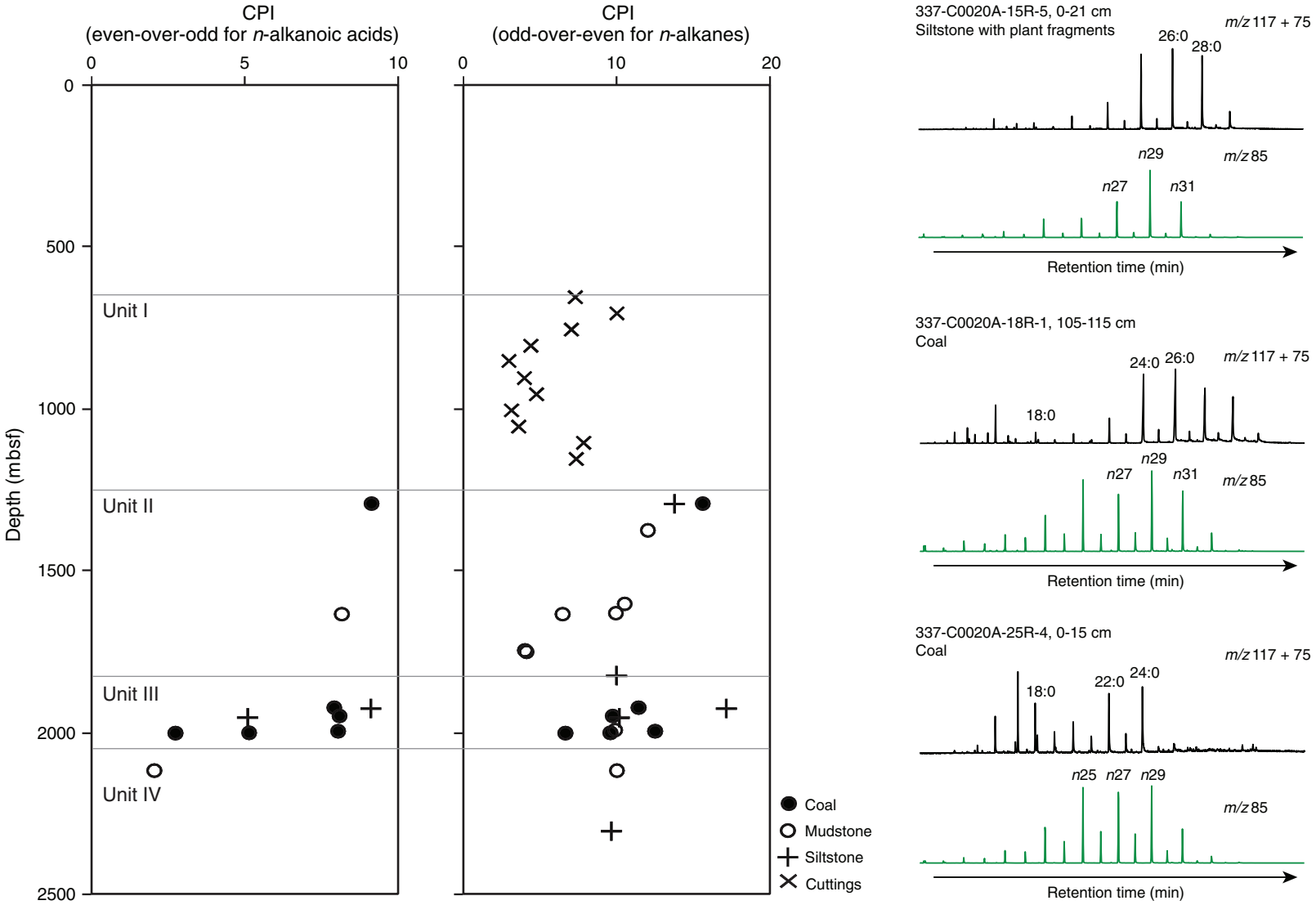

Figure F46. Combined mass chromatograms of the ions *m/z* 117 + 75 showing trimethylsilyl ethers and esters of *n*-alkanols and *n*-alkanoic acids, respectively, Site C0020. Chromatograms are ordered by depth. 18:0 OH = C_{18} *n*-alkanol, i 15:0 = 14-methyl-alkanoic acid, a 15:0 = 13-methyl-alkanoic acid, br = unspecified methyl-branched alkanoic acid, 14:0 = C_{14} *n*-alkanoic acid, 15:0 = C_{15} *n*-alkanoic acid, etc.

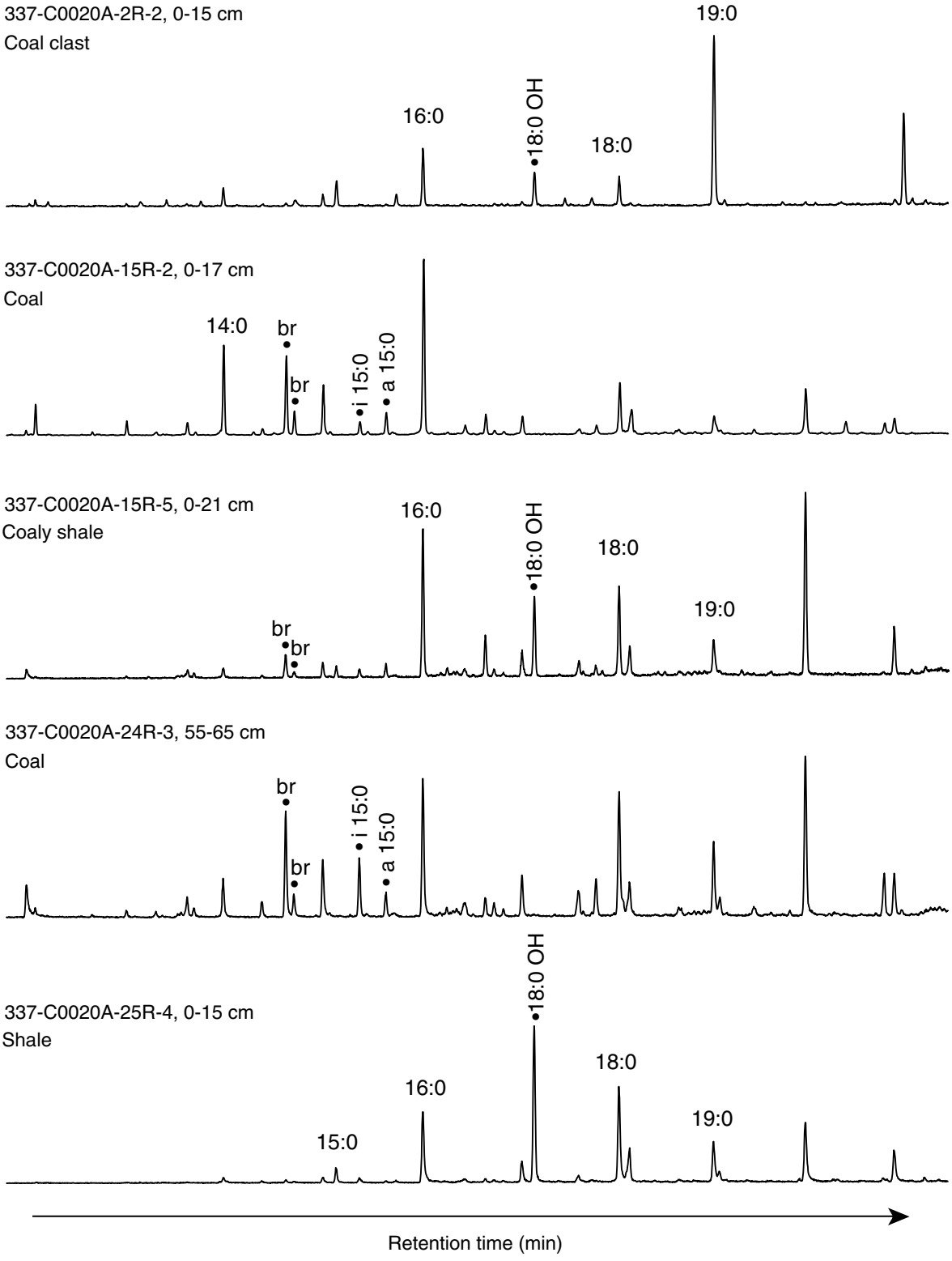

Figure F47. Combined mass chromatograms of the ions *m/z* 215 + 257 showing sterenes and *n*-alkanes. Site C0020. Carbon numbers are noted above peaks. 4,22 = stera-4,22-diene; 5,22 = stera-5,22-diene; Δ4 = ster-4-ene; Δ5 = ster-5-ene, *n*28 = C_{28} *n*-alkanes, etc.

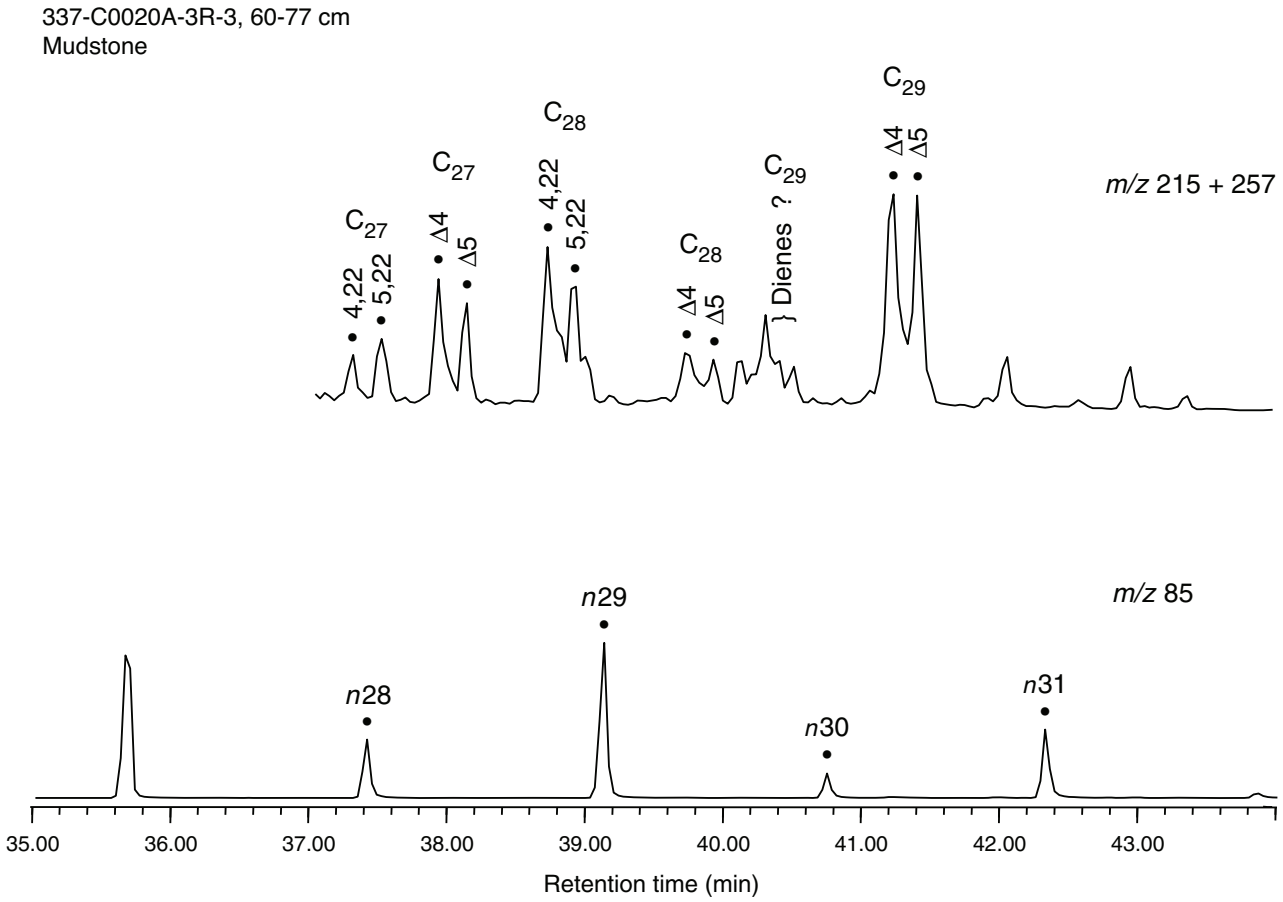

Figure F48. Mass chromatograms of the ions *m/z* 215 and 217 for coal, siltstone, and mudstone lithologies, Site C0020. Carbon numbers are noted above peaks. Δ4 = ster-4-ene; Δ5 = ster-5-ene; ααα R = 5α,14α,17α(H)20(R) steranes; βαα = 5β,14α,17α(H) steranes; αββ R = 5α,14β,17β(H) steranes; ααα S = 5α,14α,17α(S) steranes; αββ S = 5α,14β,17β(S) steranes.

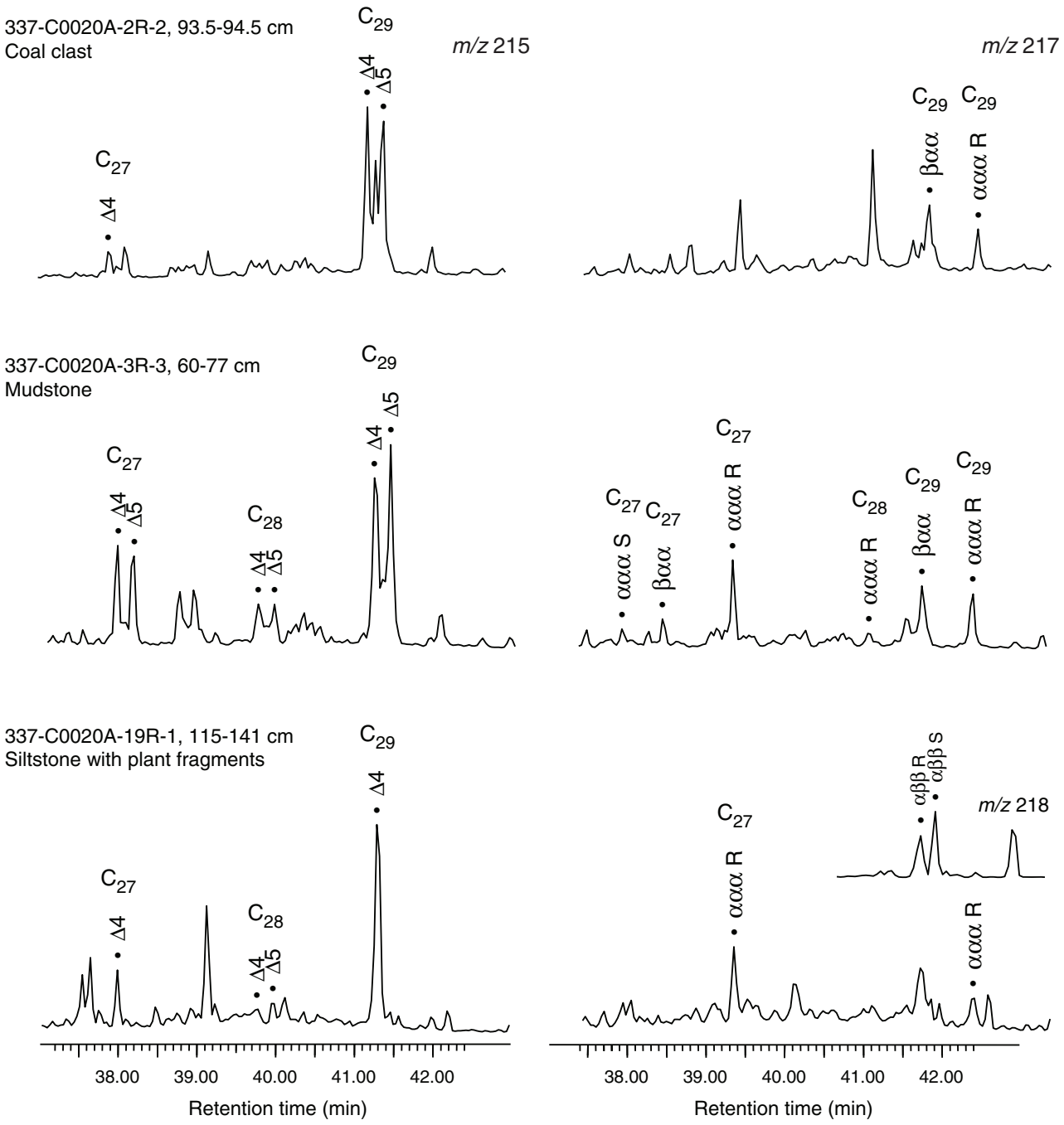

Figure F49. Mass chromatograms of the ions *m/z* 191 for hopanes and other pentacyclic triterpenoids for samples of coal, mudstone, and siltstone, Site C0020. Data are also shown for an oil stained sandstone. αβ = 17α,21β(H) hopane; βα = 17β,21α(H); ββ = 17β,21β(H) hopane; αβ S = 17α,21β(H)22(S) hopane; Δ17 = hop-17-ene; Δ13 = hop-13-ene. Pairs of S and R isomers of the same hopane compound are bracketed on the chromatograms.

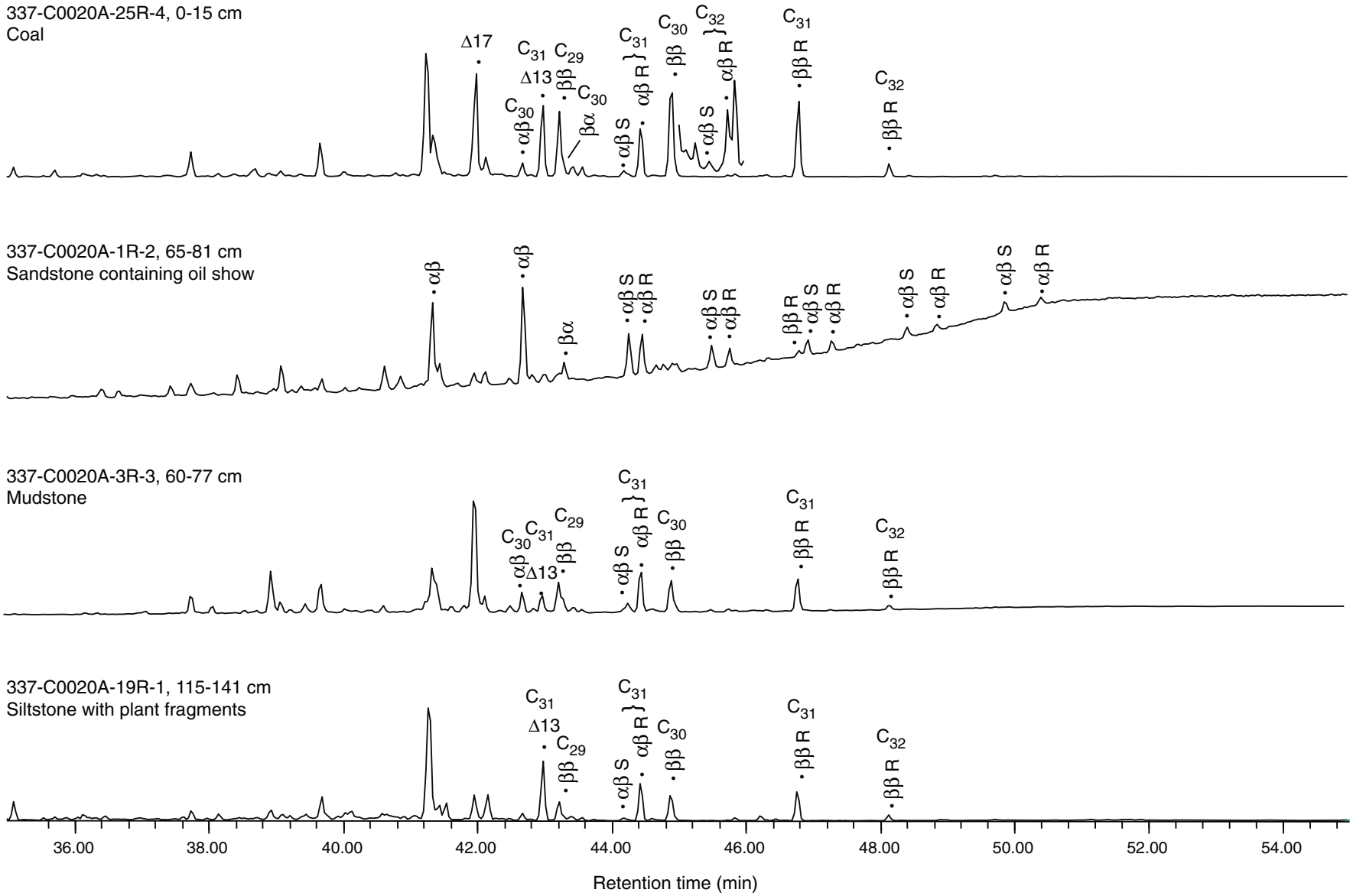

Figure F50. Ratio of C_{29} 5α,14α,17α(H)20(R) sterane to C_{29} Δ^4 and Δ^5 sterenes, Site C0020. Trend lines are shown for predicted values for 22°C/km, 24°C/km, and 26°C/km geothermal gradients; these predictions are derived from data obtained by Amo et al. (2007) and presented in the inset.

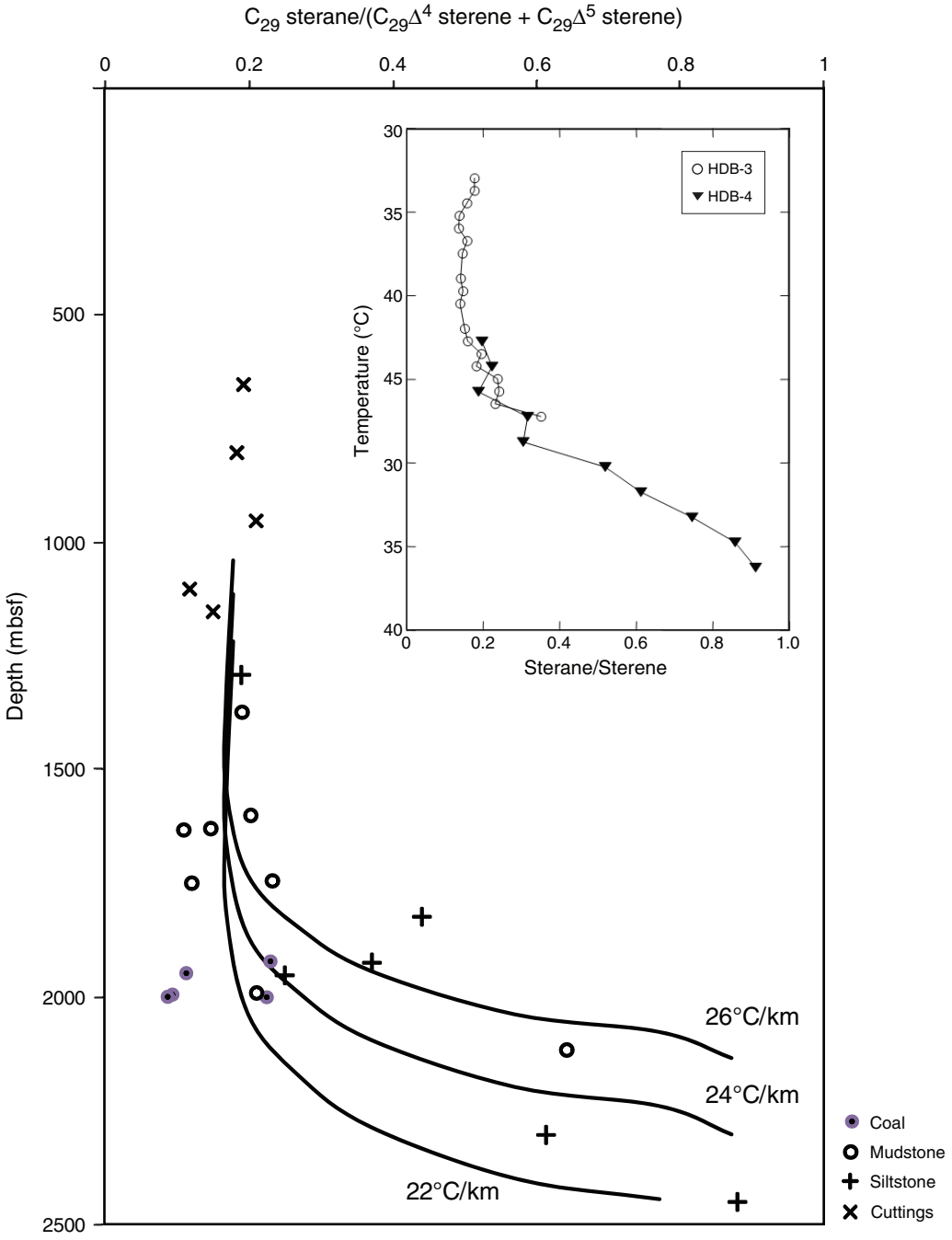

Figure F51. Proportion of C_{29} Δ^4 and Δ^5 sterenes as a proportion of C_{27} to C_{29} Δ^4 and Δ^5 sterene homologs set against backdrop of lithology obtained from cuttings, Site C0020. Blue = mudstone, orange = sandstone, white unfilled region = proportion of siltstone. Doublets of Δ^4 and Δ^5 sterenes are denoted by carbon number. Samples show varying proportions of each carbon number homolog downhole–generally C_{29} isomer lowest in mudstone rich intervals.

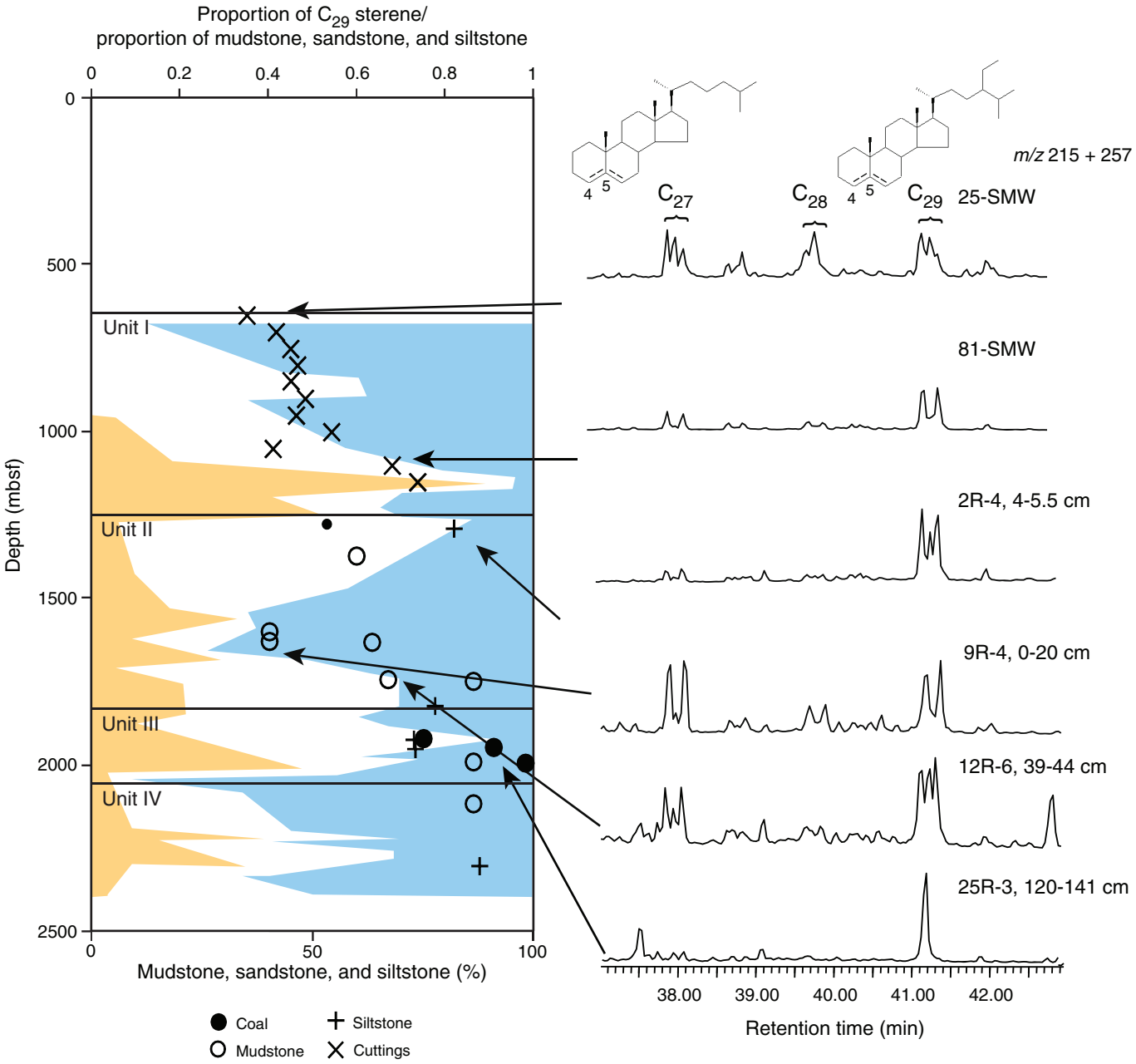

Figure F52. Mass chromatograms of the ions *m/z* 191 for hopanes and other pentacyclic triterpenoids for samples of ASTEX-S SAS (drilling additive), the extract from a sandstone in interval 337-C0020A-16R-2, 12–45 cm, and the extract from a siltstone in interval 337-C0020A-15R-5, 0–21 cm. The sandstone sample contains a hopane distribution that is a mix of the organic-rich lithology above and the SAS drilling additive. αβ = 17α,21β(H) hopane; ββ = 17β,21β(H) hopane.

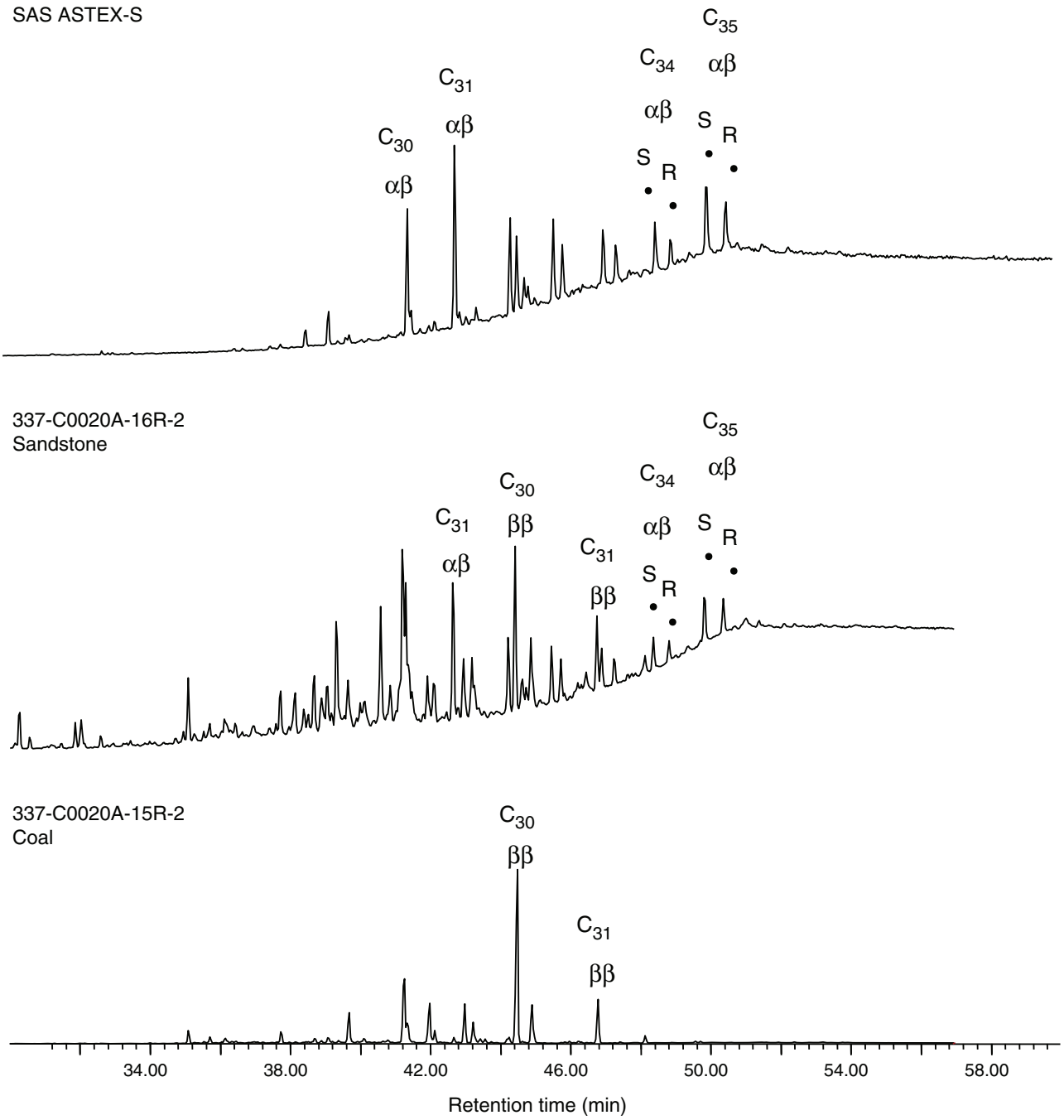

Figure F53. Total ion chromatograms for sequential extraction of cuttings (Sample 337-C0020A-25-SMW). The extract from the exterior is dominated by drilling mud components (marked by *). After cleaning by sonication in solvent, a repeat (second) sonication results in strongly reduced detection of GC-amenable compounds; however, drilling mud components no longer dominate, suggesting that the surface has been cleaned. The subsequent solvent extract obtained from the crushed sample contains far less drilling contaminants. is = standard. ASE = extract obtained from Accelerated Solvent Extractor.

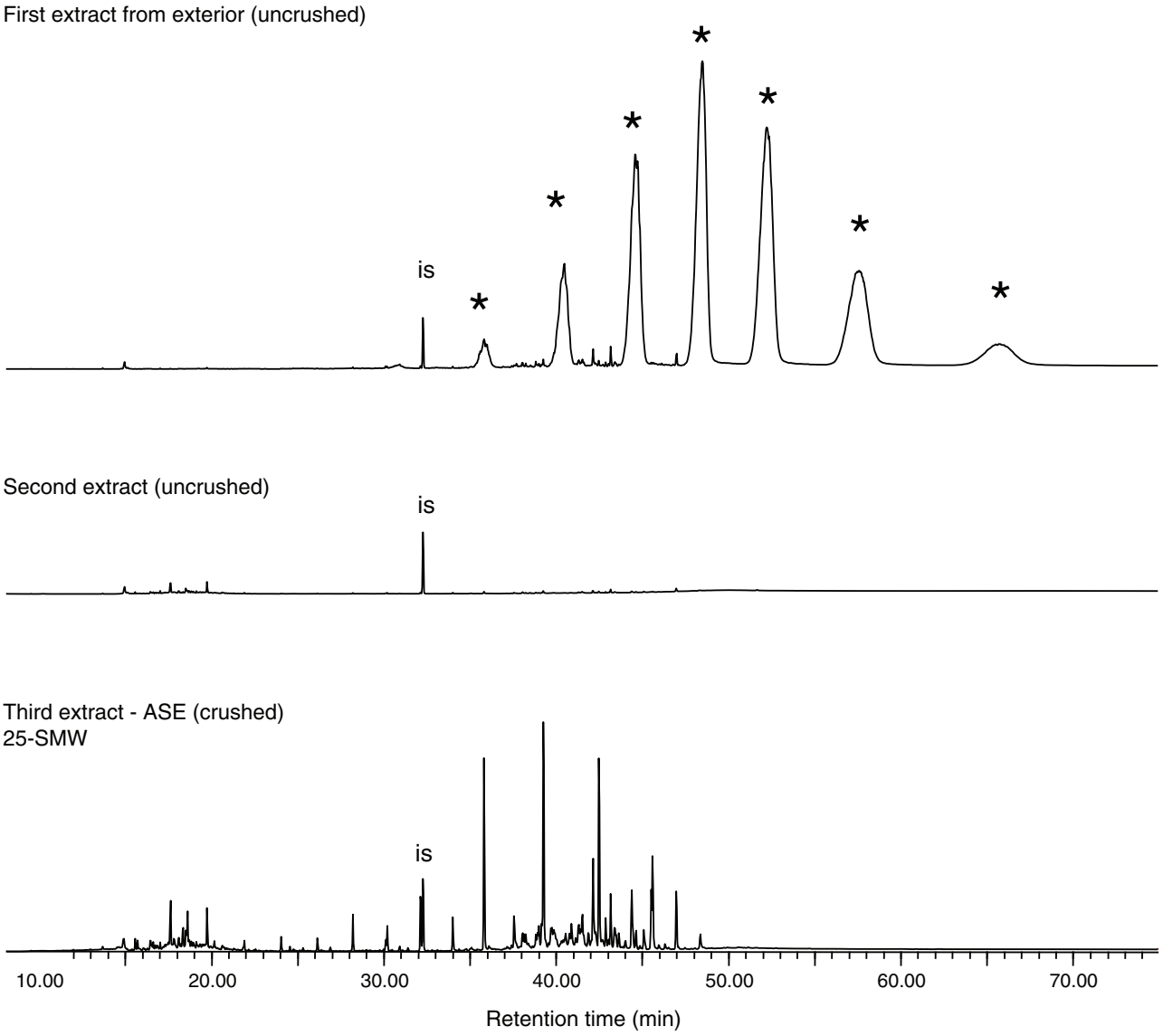

Figure F54. Mass chromatograms of the ions *m/z* 85, 215, and 217 for *n*-alkanes, sterenes and 5-β cholane standard. Comparison of full procedural blanks for the AF_1 fraction (see Fig. **F22** in the "Methods" chapter [Expedition 337 Scientists, 2013b]), Site C0020. No hydrocarbon biomarkers were detected in the procedural blank and there is little evidence of peaks that could interfere with biomarker measurement. is = standard.

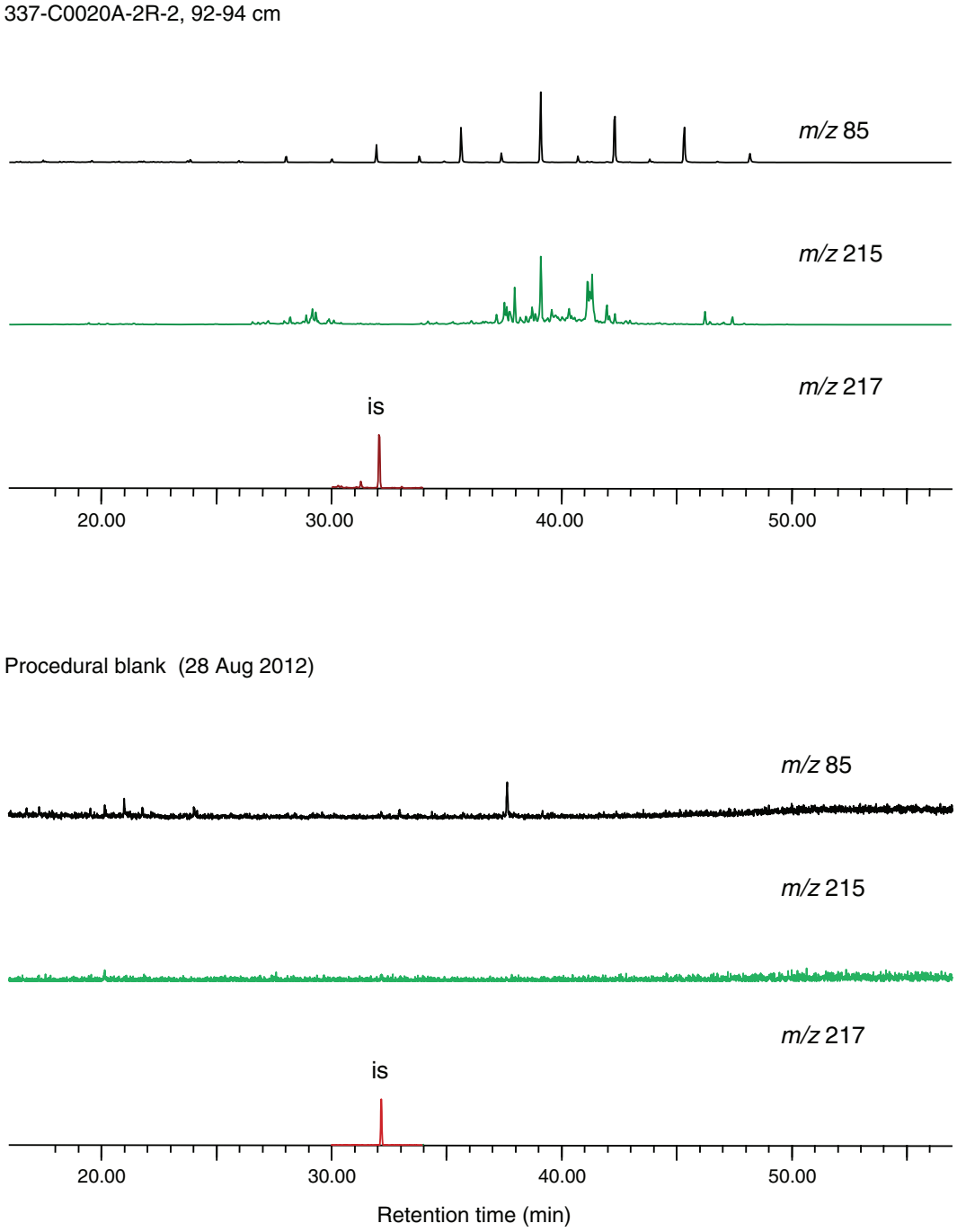

Figure F55. Sampling scheme and flow diagram for various microbiology samples and analyses, Expedition 337. Letters in brackets = sample code (see MBIO_SAMPLE_LIST.XLSX in MBIO in **"Supplementary material"**). MBIO = microbiology, IW = interstitial water, Sed. = sedimentology, PFC = perfluorocarbon, pSRR = potential sulfate reduction rate, H_2ase = hydrogenase, NanoSIMS = nanoscale secondary–ion mass spectrometry, GC-ECD = gas chromatograph–electron capture detector, FCM = flow cytometry, FISH = fluorescence in situ hybridization, PCR = polymerase chain reaction, qPCR = quantitative polymerase chain reaction, T-RFLP = terminal restriction fragment length polymorphism, subst. = substrate, cont. = contaminated.

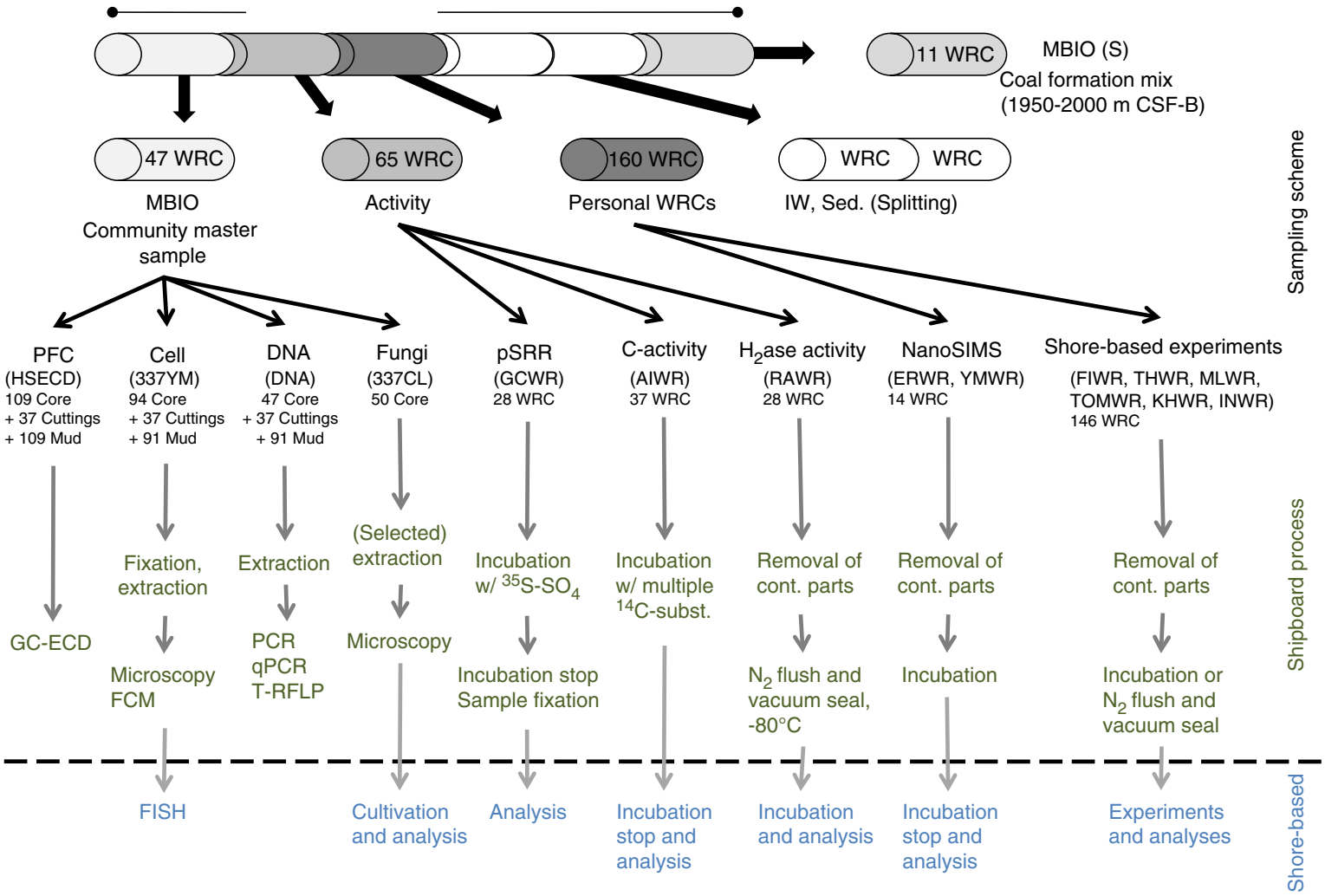

Figure F56. Time course of perfluorocarbon (PFC) concentration monitoring in drilling mud from actively mixed mud tanks (active Tanks 4 and 5), core liner fluid, and drilling mud that had circulated back on board the ship and was sampled in the mud ditch, from 2 August to 9 September 2012 (see *x*-axis) during Expedition 337. The two panels show the same data, but over different PFC concentration (*y*-axis) ranges. PFC was added on 25 days (diamonds). The very high PFC concentrations measured on two dates (upper panel) suggest lack of homogenization because of insufficient mixing at the time of sampling. Dashed blue line (lower panel) = PFC concentration (100 µg/L) assumed in all calculations of drilling mud and contaminant cell intrusion. The line at the bottom displays optimization of the PFC extraction protocol over the course of the expedition. All core samples underwent the final sampling protocol, which included 2 h of preincubation.

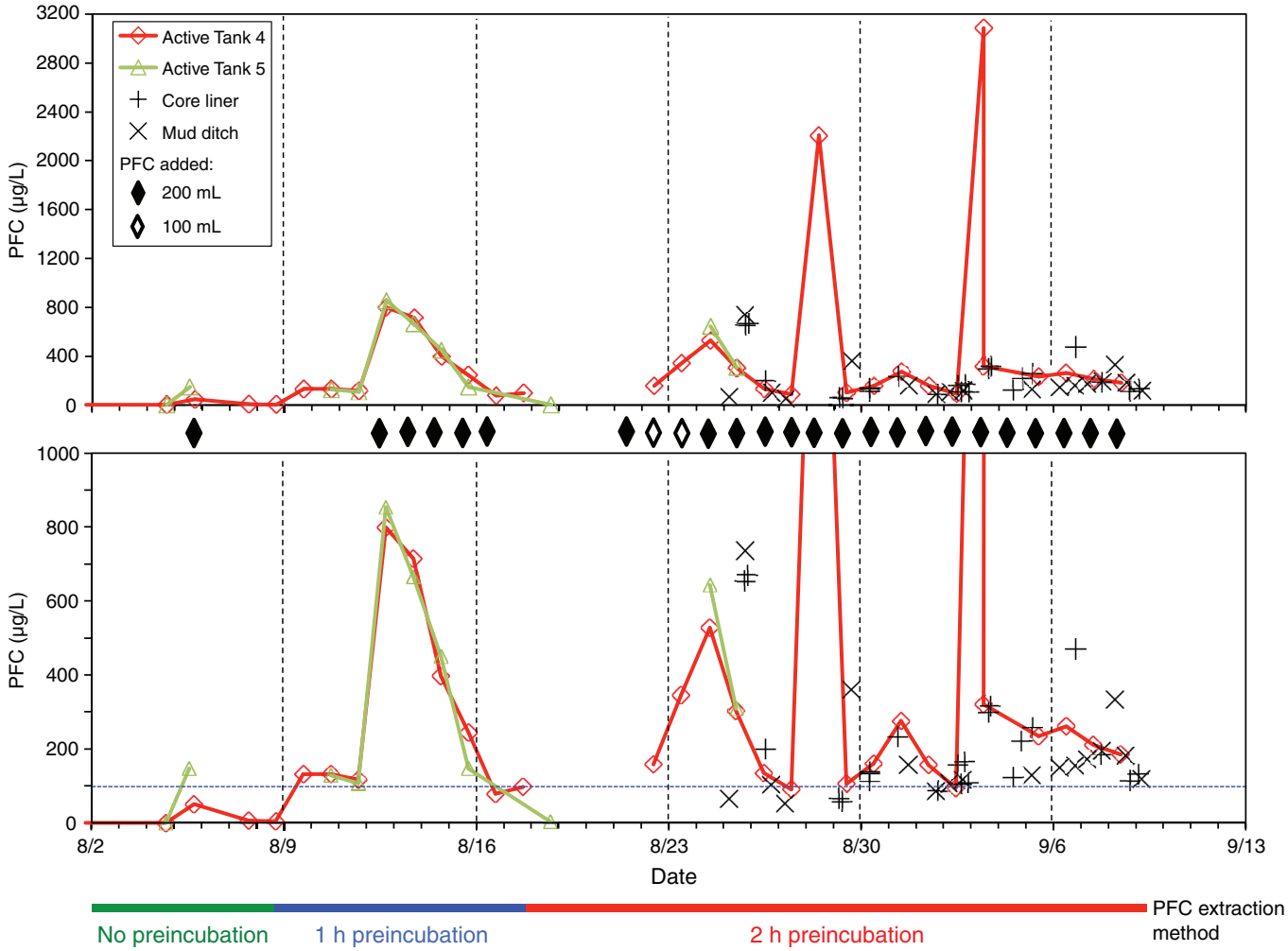

Figure F57. Determination of perfluorocarbon (PFC) detection limit, Expedition 337. PFC in headspace was detected in 182 out of 222 core samples. PFC amounts below 8×10^{-12} g (8 pg) within the volume of headspace gas injected (0.5 cm^3) were not detectable. Thus, we estimated the detection limit of the GC-ECD, indicated by the dashed line, to be 8×10^{-12} g (8 pg).

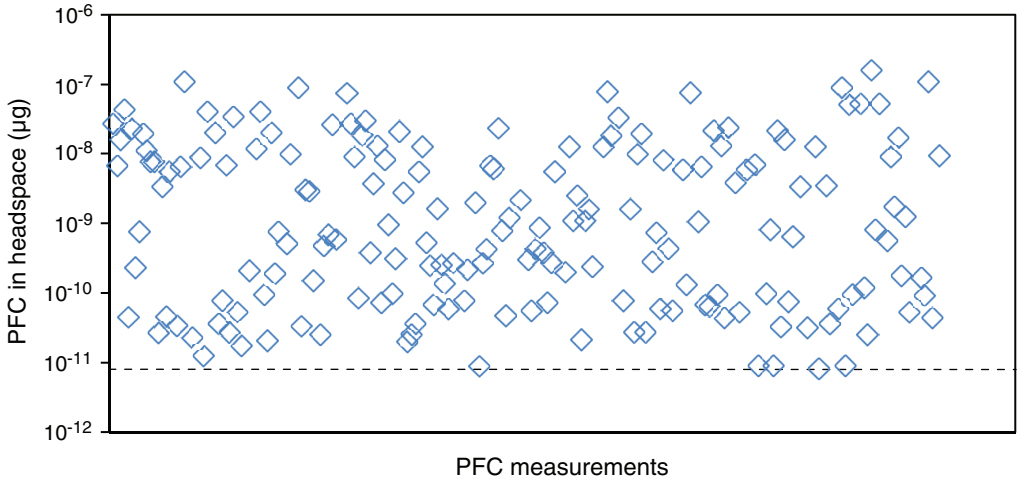

Figure F58. Drilling mud contamination of core samples (µL drilling mud per g sample) plotted against depth, Site C0020. For core samples where PFC was below detection, we show the maximum possible drilling mud contamination, calculated based on the analytical detection limit of 8×10^{-12} g (8 pg) PFC in the injection volume (0.5 cm^3), a PFC concentration in drilling mud of 100 µg/mL, and the amount of sample (g) taken for PFC analyses.

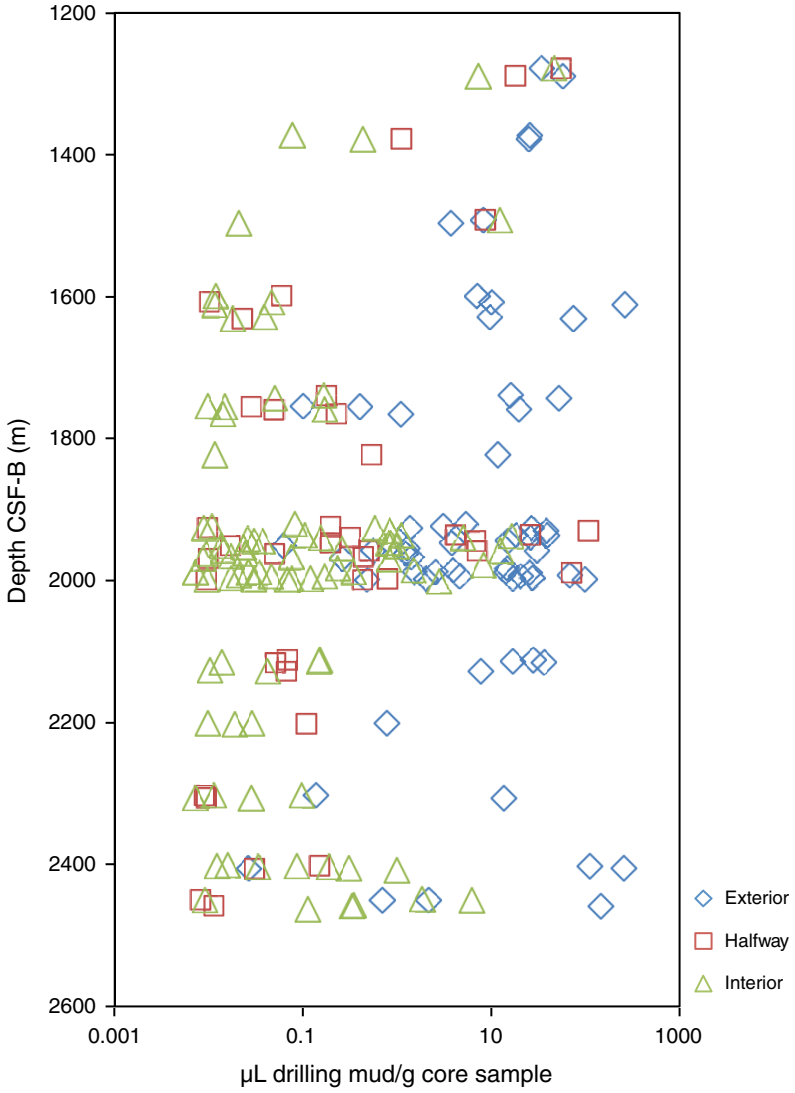

Figure F59. Drilling mud contamination of core interiors (µL drilling mud per g sample from core interior) across different lithologies, Hole C0020A. Data from the entire coring interval were included and organized by lithology. For samples where PFC was below detection (marked by *), we show the estimated maximum drilling mud contamination; as for Figure F58, this was calculated assuming the analytical detection limit of 8×10^{-12} g (8 pg) as PFC value within the GC-ECD injection volume (0.5 cm^3), a PFC concentration in drilling mud of 100 µg/mL, and the amount of sample (g) taken for PFC analyses. Because the analytical detection limit and assumed PFC concentration were constant, the variation in calculated maximum estimates is solely due to differences in the amount of sample (g) used between samples. These considerable variations were caused by (1) inaccuracies in eye-based estimates of sample volumes (our target sample volume was 5 cm^3), (2) variability in sample bulk densities, and (3) failure to obtain target sample volumes from hard samples (e.g., shales) within the short processing times that were necessary to minimize PFC loss to volatilization.

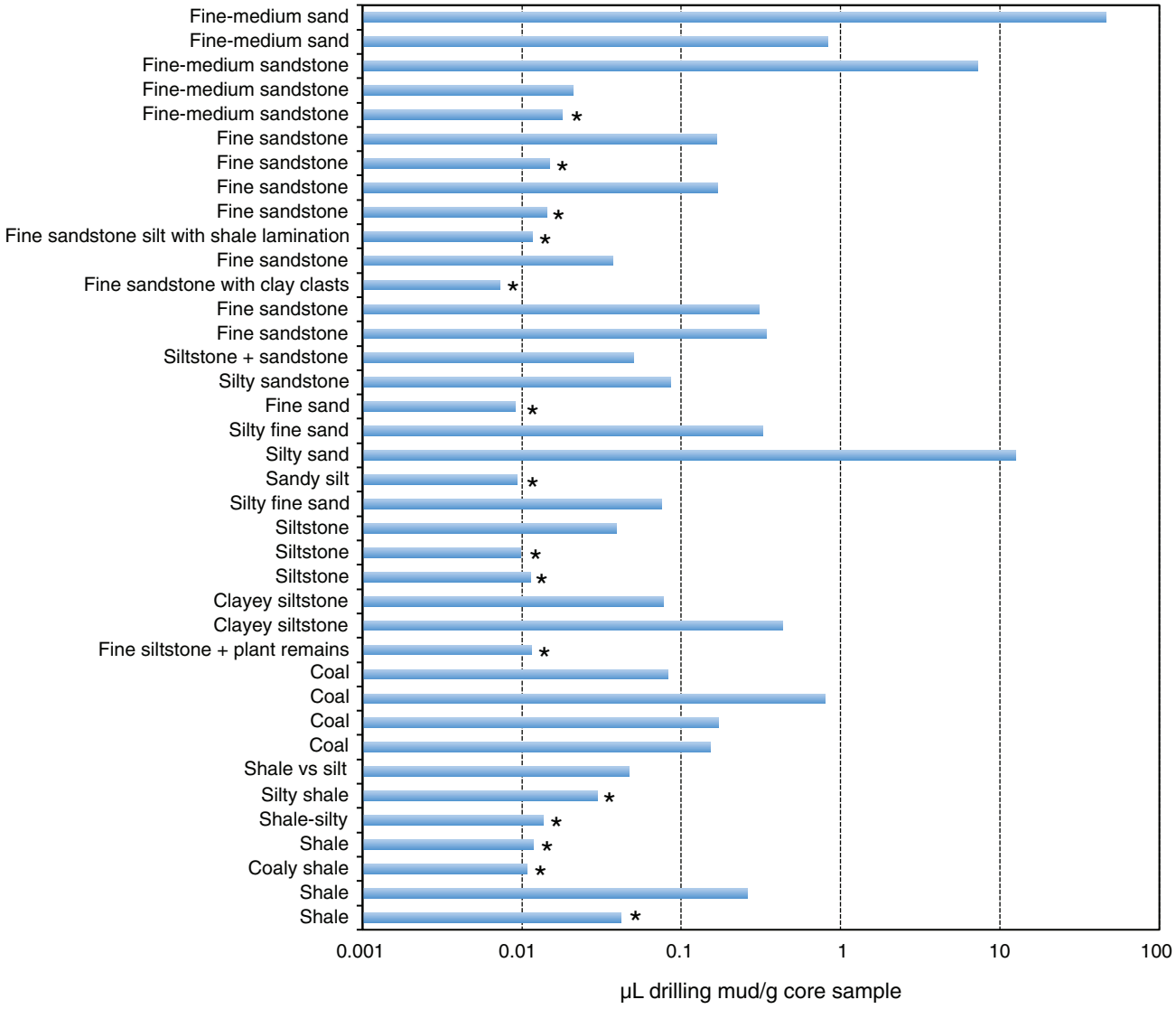

Figure F60. Microbial cell abundance in core samples at Site C0020 quantified by microscopic counts and flow cytometry (FCM). The minimum quantification limit (MQL) of each quantification method is shown as a line for both of the measurements.

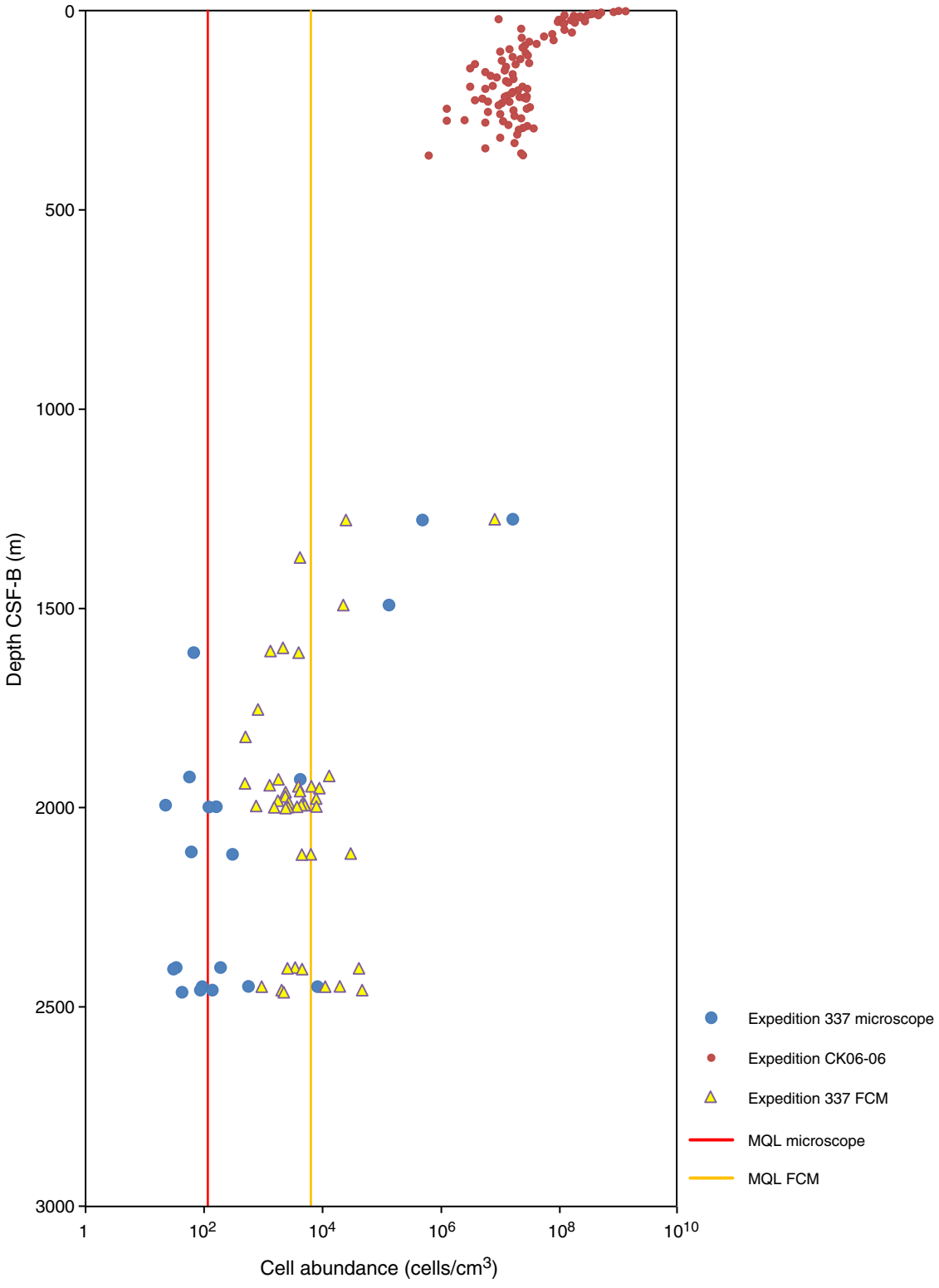

Figure F61. Microscopic image of microbial cells attaching to mineral particles from core Sample 337-C0020A-32R-2, 43–65 cm, at 2458 m CSF-B. Scale bar = 3 µm.

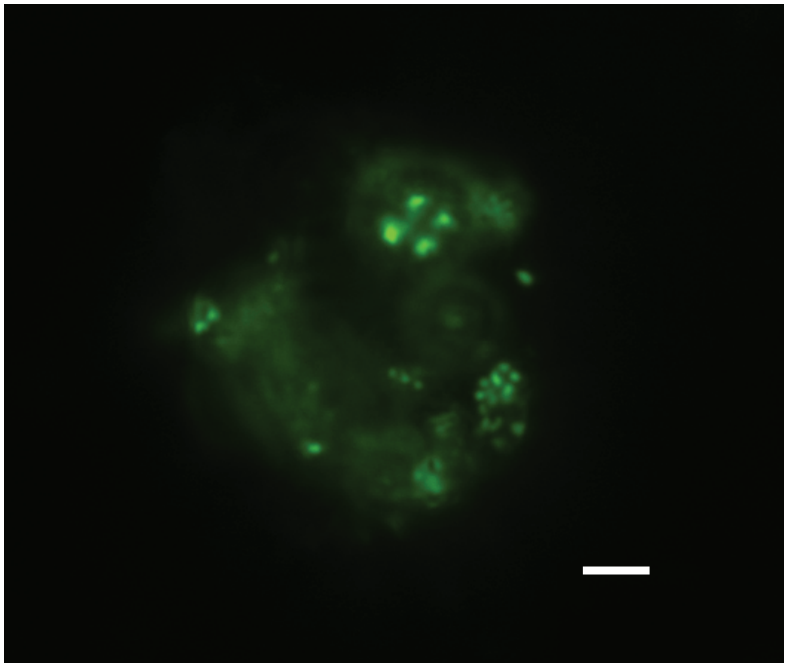

Figure F62. qPCR-based depth distribution of bacterial (red) and archaeal (blue) cell abundance in Hole C0020A core samples. Three different primer mixtures were used for each Bacteria (Bac) and Archaea (Arc). Bac 806Fmod-908R, Bac 908F-1075R, Arc 806F-915R, and Arc 915F-1059R were used with DNA extracted by the chemical lysis method. Bac 27F-338R and Arc 806F-958R were used with DNA extracted by the hot alkaline lysis method.

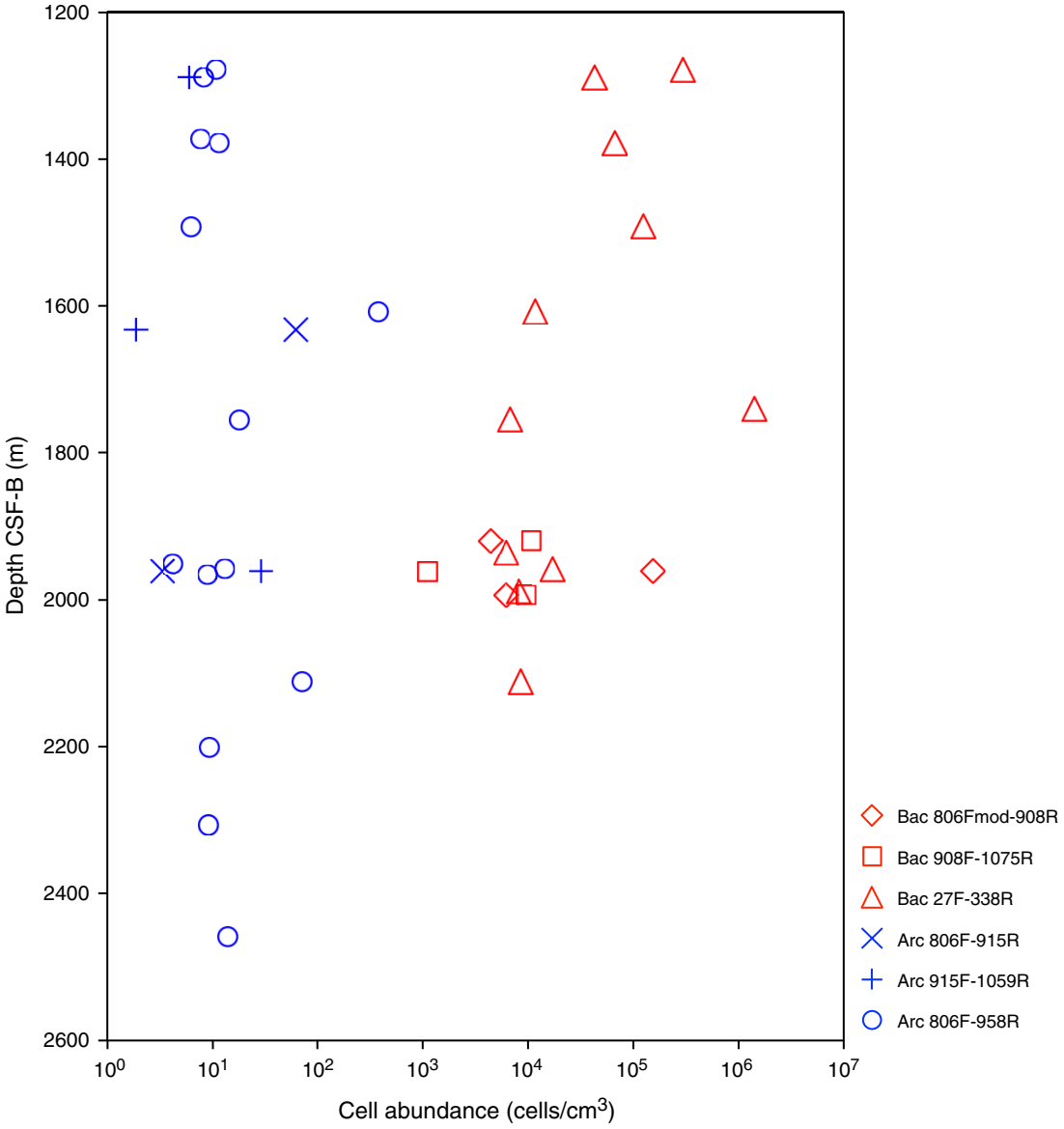

Figure F63. T-RFLP profiles of drilling mud and negative controls for DNA extraction and PCR, Expedition 337. Orange lines = peaks common throughout the drilling period, purple lines = peaks from negative controls for the DNA extraction and PCR. The *y*-axis maximum of each panel is 6000 relative fluorescence units, *x*-axis unit bp = base pairs. LMT = fresh mud water, T-RFs = terminal restriction fragments, NTCE = negative control for DNA extraction, NTCP = negative control for PCR (for exact sample info, see MBIO_SAMPLE_LIST.XLSX in MBIO in **"Supplementary material"**).

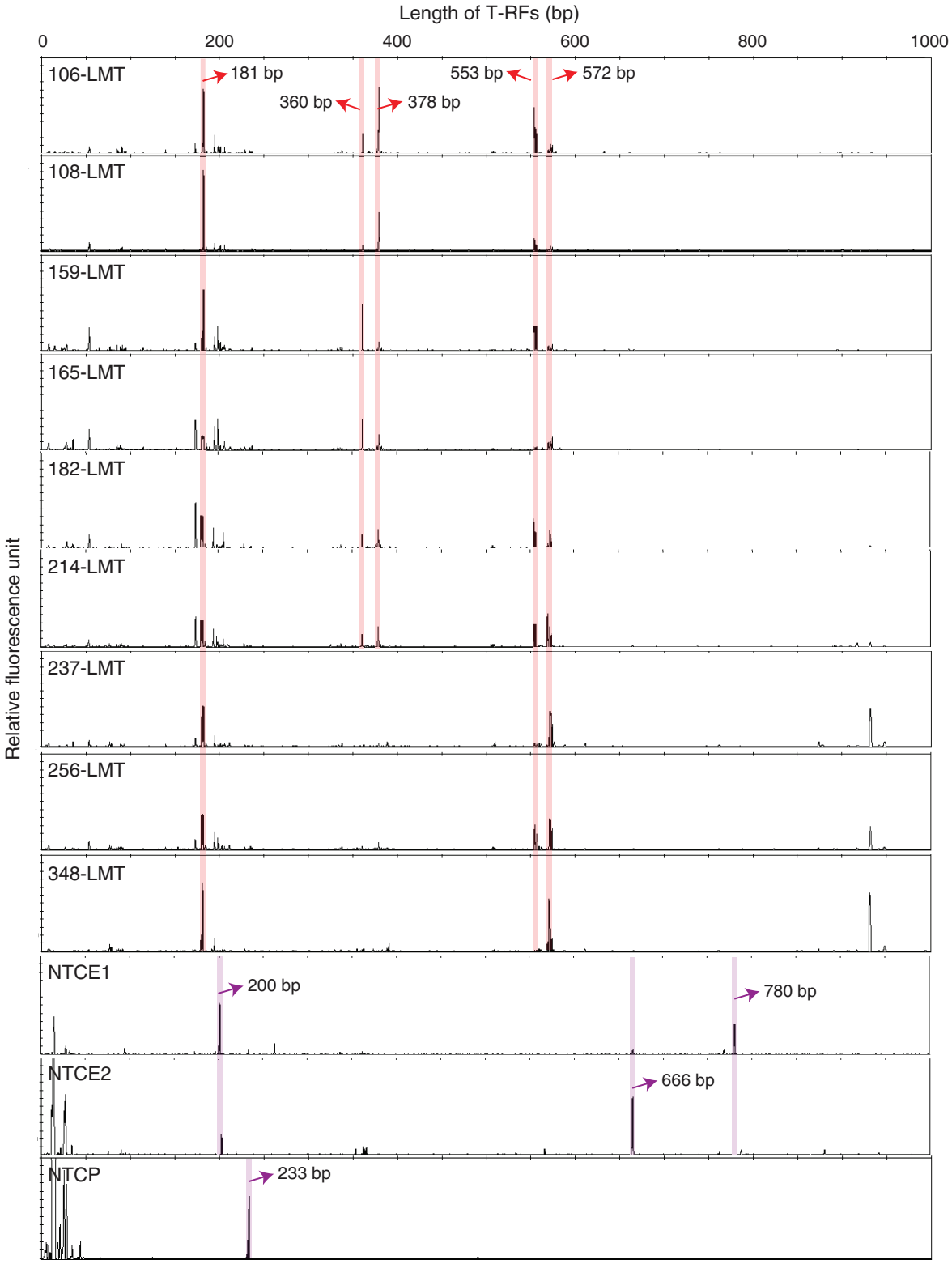

Figure F64. T-RFLP profiles of core samples, Hole C0020A. Orange lines = peaks common through the drilling period, purple lines = peaks from negative controls for the DNA extraction and PCR. Red triangles with the length of terminal restriction fragments (T-RFs) = peaks that only appear from the core sample. The *x*-axis maximum of each panel is 12,000 relative fluorescence units; bp = base pairs (for exact sample info, see MBIO_SAMPLE_LIST.XLSX in MBIO in **"Supplementary material"**).

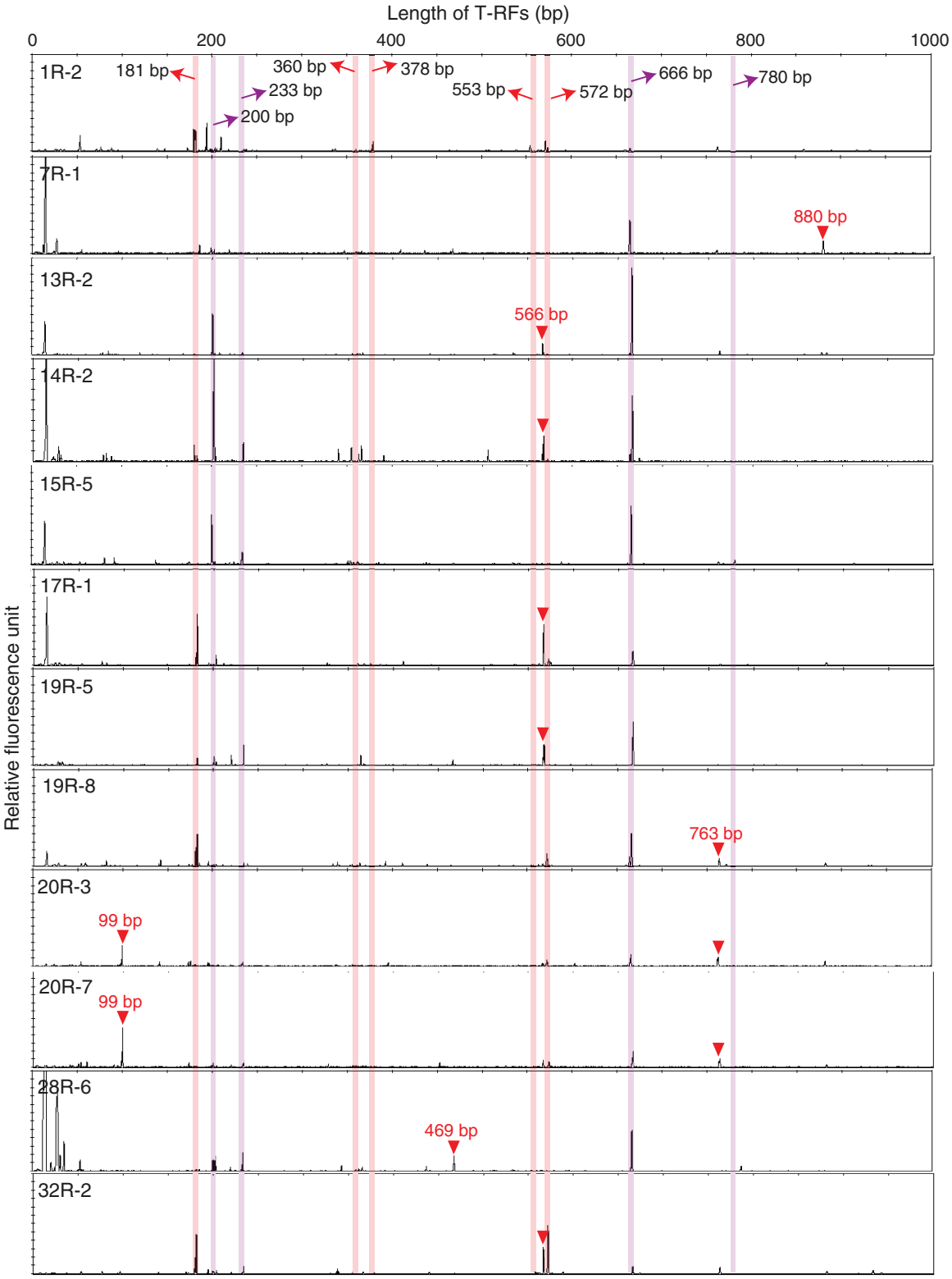

Figure F65. Cells enriched in media targeting (**A**) iron reducers (ferric citrate medium) and (**B**) homoacetogens (H_2/CO_2 plus BES). Scale bar = 10 µm.

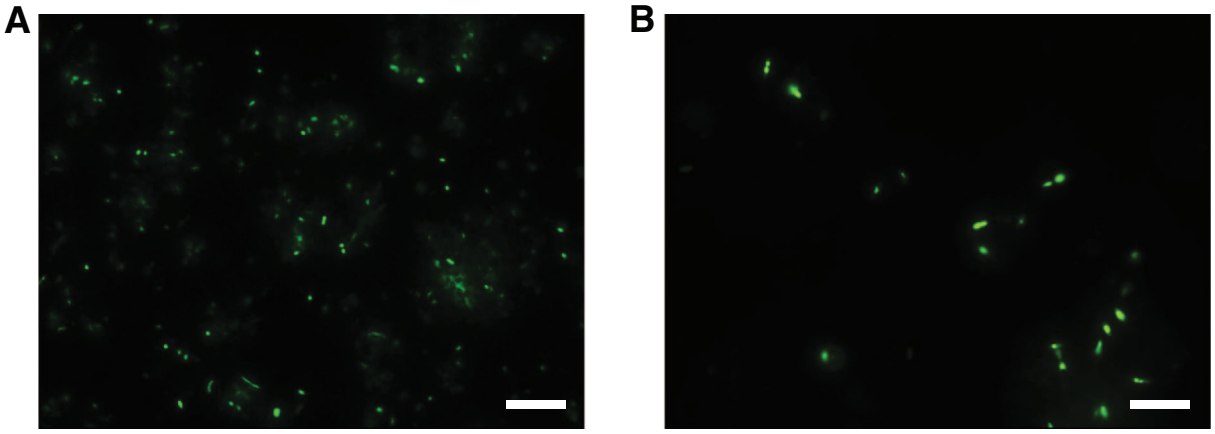

Table T1. Summary of the qualitative XRD analyses of core samples, Site C0020. (Continued on next page.)

Sample ID	Core, section, interval (cm)	Depth CSF-B (m)	Lithology	Quartz	Plagioclase	Alkali feldspars	Mica (muscovite, biotite, phlogophite)	Illite	Glauconite	Chlorite group	Smectite group	Cristobalite	Calcite	Dolomite	Aragonite	Siderite	Lignite	Pyrite	Iron oxides	Pyroxene	Amphibole	Olivine	Garnet	Zircon	Titanite	Monazite	Glaucophane	Kyanite	Evaporite	Zeolite contaminant?	Other synthetic compounds
	337-C0020A-																														
CKY5138900	1R-1	1277.64	Sandstone	x	x	x	x					x			x					x											x
CKY5137600	2R-2	1288.04	Sandstone	x	x	x						x								x					x					x	
CKY5166800	3R-2	1371.39	Siltstone	x	x	x	x	x	x			x						x													
CKY5174100	4R-2	1377.33	Sandstone	x	x	x	x													x									*		
CKY5197600	5R-2	1491.62	Silty sandstone	x	x	x	x	x				x						x			x										x Silver trithorase
CKY5199500	6R-3	1498.41	Silty sandstone	x	x	x	x	x												x											
CKY5202200	7R-1	1599.285	Shale	x	x	x	x	x				*						x			x										
CKY5239900	8L-2	1604.325	Silty shale	x	x	x	x	x				†										x									
CKY5242500	8L-6	1608.21	Clay-rich sandstone	x	x		x					x								x											
CKY5247300	8L-9	1611.98	Siltstone	x	x		x	x				x						x		x					x						
CKY5274300	9R-4	1629.275	Shale	x	x	x	x	x				x						x							x						
CKY5299300	10R-2	1632.25	Siltstone	x	x	x	x											x													
CKY5334200	11R-3	1740.395	Sandstone	x	x		x	x										x		x	x									x	
CKY5345400	12R-5	1753.32	Sandstone	x	x	x												x												x	
CKY5347500	12R-6, 0.1	1753.535	Siltstone	x	x	x	x	x													x										
CKY5348300	12R-6, 5.1	1753.945	Siltstone	x	x	x	x							x		x														x	
CKY5348800	12R-6, 9.2	1754.355	Sandstone	x	x	x	x	x										x		x	x										
CKY5373000	13R-5	1761.88	Sandstone	x	x	x	x		x											x	x				x						
CKY5400500	14R-4	1824.78	Shale	x	x		x	x	x									x		x											
CKY5400700	14R-5	1824.935	Sandstone	x	x	x						x						x		x	x				x						
CKY5400900	14R-7	1826.565	Silty shale	x	x	x	x	x	x											x											
CKY5411800	15R-4	1923.46	Shale	x		x	x	x	x									x		x											
CKY5412700	15R-6	1924.64	Silty shale	x	x	x	x	x	x	x										x					x						
CKY5423900	16R-1	1929.445	Sandstone	x	x	x	x			x						x				x											
CKY5446800	17R-5	1940.445	Shale	x	x	x	x	x	x	x										x											
CKY5513900	19R-7	1957.865	Shale	x	x	x	x	x	x	x		x				x				x		x									
CKY5517900	20R-1	1960.765	Sandstone	x	x	x	x	x		x		x	x																		
CKY5523100	20R-5	1964.615	Silty shale	x	x		x	x		x		x						x		x		x									
CKY5532300	21R-1	1969.905	Shale	x	x		x	x							x	x				x											x Baumstarkite
CKY5544900	22R-2	1975.415	Sandstone	x	x	x						x	x			x				x											
CKY5566200	23R-5	1987.105	Silty shale	x	x	x	x	x	x	x										x											
CKY5580900	24R-2		Siderite nodule	x			x	x						x		x															
CKY5583400	24R-4	1994.27	Sandstone	x	x	x	x	x		x				x						x											
CKY5593500	25R-CC	2002.225	Shale	x			x	x	x													x			x						
CKY5632100	26R-7	2117.765	Shale	x	x		x	x	x			x								x					x						
CKY5632300	27R-4	2204.49	Shale	x	x	x	x	x				x						x		x					x						
CKY5703100	29R-7	2407.46	Sandstone	x	x	x	x	x	x							x				x				x							
CKY5729900	30R-1	2447.425	Shale	x	x	x	x	x	x											x					x						

Table T1 (continued).

Sample ID	Core, section, interval (cm)	Depth CSF-B (m)	Lithology	Quartz	Plagioclase	Alkali feldspars	Mica (muscovite, biotite, phlogophite)	Illite	Glauconite	Chlorite group	Smectite group	Cristobalite	Calcite	Dolomite	Aragonite	Siderite	Lignite	Pyrite	Iron oxides	Pyroxene	Amphibole	Olivine	Garnet	Zircon	Titanite	Monazite	Glaucophane	Kyanite	Evaporite	Zeolite contaminant?	Other synthetic compounds
CKY5732900	30R-4	2449.985	Sandstone	x	x	x		x												x											
CKY5725500	32R-3	2459.905	Sandstone	x	x	x	x	x	x			x	x							x				x							
CKY5725800	32R-6	2463.515	Shale	x	x		x	x	x			x								x					x						
CKY5235900	Mud water			x								*																	x		Graphite, pyrolysite, barite, sylvite, and cuboargite

Note: * = synthetic compounds, † = some synthetic compounds.

Table T2. Summary of the qualitative XRD analyses of cuttings samples, Site C0020. (Continued on next page.)

Sample ID	Cuttings sample	Depth MSF (m)	Quartz	Plagioclase	Alkali feldspars	Mica (muscovite, biotite, phlogophite)	Illite	Glauconite	Chlorite group	Smectite group	Cristobalite	Calcite	Dolomite	Aragonite	Lignite	Pyrite	Iron oxides	Pyroxene	Amphibole	Olivine	Garnet	Zircon	Titanite	Monazite	Glaucophane	Kyanite
	337-C0020A-																									
CKY5037100	24-SMW	641.5	x	x		x	x		x		x					x		x								
CKY5037300	25-SMW	651.5	x	x	x	x	x		x		x					x			x							
CKY5037500	26-SMW	661.5	x	x	x	x	x	x			x					x		x	x	x		x	x	x	x	
CKY5037700	27-SMW	671.5	x	x		x	x	x	x	x	x					x		x	x			x	x			
CKY5037900	28-SMW	681.5	x	x		x	x	x	x	x						x	x	x					x			x
CKY5038100	29-SMW	691.5	x	x	x	x	x		x		x	x				x	x	x				x	x			
CKY5038300	30-SMW	701.5	x	x		x			x		x					x	x	x				x	x			
CKY5038500	31-SMW	711.5	x	x	x	x	x	x	x		x	x				x		x					x			
CKY5038700	32-SMW	721.5	x	x		x	x	x	x		x					x		x					x			
CKY5038900	33-SMW	731.5	x	x	x	x	x	x			x					x		x					x			
CKY5038900	33-SMW	731.5	x	x	x	x	x	x	x		x					x	x	x	x				x			
CKY5039100	34-SMW	741.5	x	x	x	x			x	x	x					x		x	x			x	x	x		x
CKY5039800	35-SMW	751.5	x	x		x			x		x					x		x		x			x			
CKY5039900	36-SMW	761.5	x	x		x	x		x		x					x	x	x			x		x			
CKY5040000	37-SMW	771.5	x	x		x	x		x							x			x				x			
CKY5040100	38-SMW	781.5	x	x					x		x					x	x				x	x	x			
CKY5040200	39-SMW	791.5	x	x		x	x		x		x					x	x						x			
CKY5040300	40-SMW	801.5	x	x		x	x		x		x					x	x						x			x
CKY5045900	41-SMW	811.5	x	x	x	x	x				x					x		x					x			
CKY5046100	42-SMW	821.5	x	x		x	x		x							x							x			
CKY5055700	62-SMW	961.5	x	x		x	x				x	x	x			x		x		x	x	x		x		
CKY5046300	43-SMW	831.5	x	x		x	x		x		x					x		x		x	x	x	x			
CKY5049600	44-SMW	841.5	x	x		x	x		x		x		x			x	x				x		x			
CKY5049800	45-SMW	851.5	x	x		x			x		x		x			x										
CKY5050000	46-SMW	861.5	x	x	x	x	x				x	x						x					x	x		
CKY5050200	53-SMW	871.5	x	x		x			x		x					x	x						x			
CKY5050400	54-SMW	881.5	x	x		x	x			x						x		x					x			
CKY5051000	55-SMW	891.5	x	x		x	x	x	x				x			x							x			
CKY5054500	56-SMW	901.5	x	x		x	x	x	x		x					x										
CKY5054700	57-SMW	911.5	x	x		x	x	x	x							x										
CKY5054900	58-SMW	921.5	x	x		x			x		x		x													
CKY5055100	59-SMW	931.5	x	x		x	x				x		x			x							x			
CKY5055300	60-SMW	941.5	x	x		x			x				x			x							x			
CKY5055500	61-SMW	951.5	x	x		x	x				x		x			x										
CKY5055700	62-SMW	961.5	x	x		x	x						x			x		x								
CKY5071400	63-SMW	971.5	x	x		x	x		x							x		x					x			
CKY5071600	64-SMW	981.5	x	x		x	x		x		x		x			x										
CKY5071800	65-SMW	991.5	x	x		x	x				x		x			x										
CKY5072000	66-SMW	1001.5	x	x		x	x	x			x		x			x										
CKY5072200	67-SMW	1011.5	x	x		x		x	x		x		x			x										
CKY5072400	70-SMW	1021.5	x	x		x	x	x			x		x			x										
CKY5072600	71-SMW	1031.5	x	x	x		x									x										
CKY5072800	72-SMW	1041.5	x	x				x					x			x										
CKY5073000	73-SMW	1051.5	x	x		x							x			x										
CKY5073200	74-SMW	1061.5	x	x									x													
CKY5073400	75-SMW	1071.5	x	x		x	x						x			x				x						
CKY5073600	79-SMW	1081.5	x	x	x			x		x	x		x			x										
CKY5073800	80-SMW	1091.5	x	x				x			x		x			x							x			
CKY5074000	81-SMW	1101.5	x	x		x					x		x			x							x			
CKY5085200	88-SMW	1111.5	x	x	x	x					x		x			x										
CKY5145700	119-SMW	1331.5	x	x	x	x	x				x					x		x								
CKY5194000	136-SMW	1451.5	x	x	X						x			x												
CKY5195500	148-SMW	1488.5	x	x	x	x												x					x			
CKY5211800	158-SMW	1551.5	x	x	x	x	x									x										
CKY5420000	192-SMW	1651.5	x	x	x	x	x				x				x	x		x					x			
CKY5420500	198-SMW	1701.5	x	x		x					x					x		x					x			

Table T2 (continued).

Sample ID	Cuttings sample	Depth MSF (m)	Quartz	Plagioclase	Alkali feldspars	Mica (muscovite, biotite, phlogophite)	Illite	Glauconite	Chlorite group	Smectite group	Cristobalite	Calcite	Dolomite	Aragonite	Lignite	Pyrite	Iron oxides	Pyroxene	Amphibole	Olivine	Garnet	Zircon	Titanite	Monazite	Glaucophane	Kyanite
CKY5421000	207-SMW	1751.5	x	x		x	x									x		x	x							
CKY5421300	212-SMW	1801.5	x	x	x	x	x									x		x					x			
CKY5422000	222-SMW	1871.5	x	x	x	x	x											x		x						
CKY5584500	254-SMW	2001.5	x	x	x	x	x	x	x																	
CKY5586400	261-SMW	2051.5	x	x	x	x	x		x										x							
CKY5588000	267-SMW	2101.5	x	x	x	x	x	x										x								
CKY5635900	274-SMW	2151.5	x	x	x	x	x	x			x							x		x						
CKY5636400	285-SMW	2201.5	x	x	x	x		x								x							x			
CKY5646100	290-SMW	2251.55	x	x	x	x	x											x					x			
CKY5745000	358-SMW	2351.5	x	x	x	x	x											x		x			x			

Table T3. Lithologic units with sediment age information, Hole C0020A.

Unit	Subunit	Core/Cuttings number	Depth interval MSF (m)	Thickness (m)	Lithology	Age
I	a	Samples 337-C0020A-24-SMW through 58-SMW	647–926.5	279.5	Diatom-bearing siltstone and claystone	late–middle Pliocene
	b	Samples 337-C0020A-59-SMW through 88-SMW	926.5–1116.5	190	Semiconsolidated diatom-bearing clayey siltstone with common fine sandstone	middle Pliocene/early Pliocene–late Miocene
	c	Samples 337-C0020A-92-SMW through 95-SMW	1116.5–1236.5	120	Unconsolidated to semiconsolidated sandstone and silty sandstone with rare clayey siltstone	early Pliocene–Miocene
	d	Samples 337-C0020A-97-SMW through 98-SMW	1236.5–1256.5	20	Semiconsolidated clayey siltstone with medium loose sand	early Pliocene–Miocene
II	a	Samples 337-C0020A-98-SMW through 153-SMW; Cores C0020A-1R through 6R	1256.5–1506.5	250	Sandstone and siltstone associated with marine fossiliferous material	Miocene
	b	Samples 337-C0020A-153-SMW through 216-SMW; Cores C0020A-7R through 14R	1506.5–1826.5	320	Organic-rich shale and sandstone associated with plant remains	Miocene
III		Samples 337-C0020A-216-SMW through 261-SMW; Cores C0020A-15R through 25R	1826.5–2046.5	220	Organic-rich sandstone and shale associated with coalbeds	early–middle Miocene
IV	a	Samples 337-C0020A-261-SMW through 384-SMW; Cores C0020A-26R through 29R	2046.5–2426.5	380	Shale and sandstone associated with carbonate and glauconitic material	early Miocene–late Oligocene
	b	Samples 337-C0020A-384-SMW through 391-SMW; Cores C0020A-30R through 32R	2426.5–2466	39.5	Sandstone and shale associated with coalbed	early Miocene–late Oligocene

Table T4. Distribution of dinoflagellate cysts, pollen, and spores in Unit I, Hole C0020A.

			Dinoflagellate cysts																																	Spores							Gymnosperm pollen			Angiosperm pollen											Other organic materials			
Cuttings sample	Depth MSF (m)	Group abundance	*Achomosphaera* spp.	*Bitectodinium tepikiense*	*Brigantedinium cariacoense*	*Brigantedinium majusculum*	*Brigantedinium simplex*	*Brigantedinium* spp.	*Capillicysta fusca*	*Cribroperidinium* spp.	*Evittosphaerula* sp. A	*Filisphaera filifera*	*Hystrichokolpoma* spp.	*Impagidinium aculeatum*	*Impagidinium* spp.	*Lejeunecysta hyalina*	*Lejeunecysta* spp.	*Operculodinium centrocarpum*	*Operculodinium wallii*	*Operculodinium israelianum*	*Operculodinium* spp.	*Polykrikos* spp.	*Selenopemphix nephroides*	*Selenopemphix quanta*	*Selenopemphix* sp. A	*Selenopemphix* sp. B	*Selenopemphix* sp. C	*Selenopemphix* spp.	*Spiniferites* spp.	*Systematophora* spp.	*Tectatodinium pellitum*	*Tuberculodinium vancampoae*	*Votadinium carvum*	*Votadinium spinosum*	*Xandarodinium variabile*	*Deltoidospora* spp.	*Granulatisporites* spp.	*Laevigatosporites* spp.	*Lycopodium* spp.	*Osmunda*	*Polypodium*	Spores undifferentiated	Bisaccate pollen (*Pinus*, *Picea*)	Taxodiaceous pollen	*Tsuga* spp.	*Alnus* spp.	*Carya* spp.	*Castanea*	Compositae (Asteraceae)	*Fagus* spp.	*Juglans*	*Nyssa*	Poaceae	*Pterocarya*	*Symplocos*	*Tilia* spp.	Foraminiferal linings	Fungi	*Pterospumella*	Tardigrade
337-C0020A-																																																												
24-SMW	636.5–646.5	M			5		11	43				1									1		2											2	3			1					8	1													1	1		1
25-SMW	646.5–656.5	G			13		21	119				7						3					1	1											3	1							101	1	2												2			2
26-SMW	656.5–666.5	G	1		1		14	106				12						1			4														1	1		1					105	1	4												2			3
27-SMW	666.5–676.5	G			4	1	21	72				35									3		1	1								1											86		1												2			1
28-SMW	676.5–686.5	M			2		11	41				2				1			1				1								1				3	2				1			19	2	1												1			
29-SMW	686.5–696.5	G					5	90				4	1										2								1				4								102	4	3												4			
30-SMW	696.5–706.5	M					1	43				2												2				1						1	1	1						X	35	3	2												5	1		1
31-SMW	706.5–716.5	G					1	41				1									1			2	1							1			1								91	3	3												3	2		1
32-SMW	716.5–726.5	M					3	54													1														3								32		1												1	1		1
33-SMW	726.5–736.5	M					3	48										1					1												3				1				29	2	2												1			4
34-SMW	736.5–746.5	G					6	70										1			1			1	3										4	1		2					95	1	3					1										
35-SMW	746.5–756.5	G	1		1		6	73	1									1			1		1							X					10								130	5	2												3			2
36-SMW	756.5–766.5	G			1		6	48			X	3									3		1	1											2		1	1				X	71	6	2				1											
37-SMW	766.5–776.5	G			2		15	79	2			1							1		1			1	1						1			2	2								34	2	4															1
38-SMW	776.5–786.5	G					10	44															1	1							1				2			1					112	3	11					1							1			
39-SMW	786.5–796.5	P				2	2	23				1						2					1		2											1					1	X	22	3	5												2	2		
40-SMW	796.5–806.5	M					9	38													1			1				2							1								25	13	1													1		2
41-SMW	806.5–816.5	P					7	20	1			1															1	1						1									18	1													1	2		
42-SMW	816.5–826.5	M		2			1	32	2									2			4										1				1								10	42	1	2		1		1		3	2	2			1			
43-SMW	826.5–836.5	P						19	2			1									1		1	1											3			1		1			17		1				1								1	1		
44-SMW	836.5–846.5	G		1	1		9	68	1			7						5	1		1		1		2			1				2			9	2							38	4	2												4			1
45-SMW	846.5–856.5	P			2		2	18				3											1					1					1		4	1							15		3												3	2		
46-SMW	856.5–866.5	P			3	1	6	29	1			4				1					1			1											4								21	1																1
56-SMW	896.5–906.5	P			1		2	47									1	5	3		3		2											2									9	4	3												6			
57-SMW	906.5–916.5	P					2	17				2																1	1		1				1					2			13	5	2												1			
58-SMW	916.5–926.5	P		1	2		5	32				3						2	1		1				3				1						1	1		2					20	2	2	1											1			1
59-SMW	926.5–936.5	P					5	17										2		2				1					1						2			1	1		1		3		3												2			
60-SMW	936.5–946.5	P						19				3								2	1								2		1				9	1		2		1	3		19	1	4	2				1							2	1		
61-SMW	946.5–956.5	P			1	4	1	22				2											2	2	1			2						1	21								9	1						1							4			
62-SMW	956.5–966.5	P					1	12				2																	1						12							X	5	3	1	3					3						5	1		
63-SMW	966.5–976.5	P						10	1			2											1	2	1										5			1					7	1						2							1		1	
64-SMW	976.5–986.5	M		1		1	1	21				8									1				4										19			3					16	3	2						3				1			2		
65-SMW	986.5–996.5	P						15															3		3	1									7								6	2	3											1				
66-SMW	996.5–1006.5	P				2		18	2			2												1	1			2							6								9	3	4					4							3			
67-SMW	1006.5–1016.5	P			2	1		24	2			1						1					3	3	12			2	1						3			2					8	1	2															
72-SMW	1036.5–1046.5	P			1	2		16		X		1						1						2											2	2							3	1							1						1			
73-SMW	1046.5–1056.5	P						15															2					1							2										1												1			
74-SMW	1056.5–1066.5	P		2				15				1					2	2	1						2			1							4								2	3													2			
75-SMW	1066.5–1076.5	P						2	1																										1																						1			
79-SMW	1076.5–1086.5	P		1		1	2	9				3		1		3	1	1				1		1												1							13	2	2															
80-SMW	1086.5–1096.5	P			1	1		4				5			2				1		1		3					1							1					1			5	1	1						1							1		
81-SMW	1096.5–1106.5	P			1			5	1			6					2						3	1				1							2								1	1			1				1									

Numbers in the taxa columns refer to abundance counts of specimens. Group abundance: B = barren, P = poor (1–75 specimens within a sample), M = moderate (76–125 specimens), G = good (>126). X = reworked.

Table T5. Distribution of dinoflagellate cysts, pollen, and spores in Unit II, Hole C0020A.

Core, section, interval (cm) or cuttings sample	Depth (mbsf)	Group abundance	Dinoflagellate cysts													Spores					Gymnosperms									Angiosperms																																				Other organic materials		
			Brigantedinium majusculum	*Brigantedinium* spp.	*Cleistosphaeridium* spp. undifferentiated	*Filisphaera filifera*	*Lejeunecysta hyalina*	*Lejeunecysta* spp.	*Operculodinium centrocarpum*	*Operculodinium* spp.	*Selenopemphix quanta*	*Selenopemphix* spp.	*Trinovantedinium boreale*	*Tuberculodinium vancampoae*	*Xandarodinium variabile*	Dinocysts undifferentiated	*Deltoidospora* spp.	*Laevigatosporites* spp.	*Osmunda*	*Polypodium*	*Stereisporites* spp.	*Abies*	Bisaccate pollen (*Pinus*, *Picea*)	*Cathaya*	*Cryptomerria*	*Larix*	*Picea*	*Sciadopites* spp.	Taxodiaceous pollen	*Tsuga* spp.	*Acer* spp.	*Aesculiidites* spp.	*Ailanthus* spp.	*Alnus* spp.	Anacardiaceae	*Betula* spp.	Betulaceae/Myricaceae types	*Carpinus* spp	*Carya* spp.	*Castanea*	*Celtis* spp.	*Corylus*	*Fagus* spp.	*Fraxinoipollenites*	*Gingko*	*Ilex*	*Juglans*	*Liquidamber*	*Magnolia*	*Milfordia*	*Nyssa*	*Platanus*	Poaceae	*Polygonum*	*Pterocarya*	*Quercus* (deciduous)	*Quercus* (evergreen)	*Salix*	*Sparganiaceaepollenites*	*Tetracolporopollenites* spp.	*Tilia* spp.	Tricolporate undifferentiated	*Ulmus*/*Zelcova* spp.	*Ulmipollenites*	*Weigela*	Foraminiferal linings	Fungi	Algae
337-C0020A-																																																																					
114-SMW	1276.5–1286.5	P	1	3	1		1				1							1											7					3				1									2																1			1		
1R-CC	1278.58–1278.74	B																																																																	
115-SMW	1286.5–1296.5	B																																																																	
2R-CC	1289.99–1290.09	B																																																																	
116-SMW	1296.5–1306.5	P							2						1		3											8					2		3						1	1								2												1					
117-SMW	1306.5–1316.5	B																																																																	
118-SMW	1316.5–1326.5	B																																																																	
119-SMW	1326.5–1336.5	P		1												1	1	1			1		3						7	1				3		6			1		1		3													2					1		2				1	
121-SMW	1356.5–1366.5	P		3						1			X			1		4	1				2						14					3		5							2					1															2					
3R-4, 95–96	1373.71–1373.72	P		4		1		2										3					1						9					10		4			2			1	2												4	2					1							
129-SMW	1376.5–1386.5	B																																																																	
4R-CC	1378.47–1378.83	M		3				1	1	1					1	2	1	4					2						24					10	2	5						7	9			1							1										2				2	
131-SMW	1386.5–1396.5	B																																																																	
132-SMW	1406.5–1416.5	B																																																																	
134-SMW	1426.5–1436.5	B																																																																	
5R-CC	1492.7–1492.95	M		2						3		2				1		10		1			12			4	2	1	34	3				17		10	1	1	4				1			1		2		1					2				1			2	6					
6R-4, 54–55	1499.12–1499.13	B																																																																	
154-SMW	1506.5–1516.5	B																																																																	
157-SMW	1536.5–1546.5	M															9					1						28					10		16		1	1			3	4			1								1	1		2				1				2		1	
161-SMW	1566.5–1576.5	M		1				2						1				19			1		2						34			1		25		5	9			1		1	6	1	1				3						6	1					1	2		2				
163-SMW	1586.5–1599.5	M															4					1						16		3			23		6		7	1			4	5			1	1								2								5	2				
7R-CC	1600.01–1600.16	G															176											16		4		1	25		24		10	3		2	1	5				1									6					5		20				3	
8L-2, 47–48	1604.68–1604.69	P		2													2	3											12		5			7		12			1	1		1	7		1		5							1	4	2				1			2				3	3
8L-2, 94–95	1605.15–1605.16	M															12											15	2	1			20		11						2	7												1	1		1			4				1			
9R-CC	1629.47–1629.54	B																																																																	
10R-CC	1634.90–1634.91	P		7		1				1		1										1	10			1	5		10	6				1				1					1													1							1					
199-SMW	1716.5–1726.5	P		5		1		3				2				1							17	1		1	6			10				2		6		1									1										1						1					
13R-CC	1766.47–1766.53	M		1					3				X					2					2		1				47					7		6		2	1								1				1				1	5											1	
212-SMW	1795.5–1806.5	P							1											1		1						14					2		1			1																2	1							2					
213-SMW	1806.5–1816.5	P				1				1								2	1				3			1			38					4		9		2								1	1					1				2					2	1	4					

Numbers in the taxa columns refer to abundance counts of specimens. Group abundance: B = barren, P = poor (1–75 specimens within a sample), M = moderate (76–125 specimens), G = good (>126). X = reworked.

Table T6. Distribution of dinoflagellate cysts, pollen, and spores in Unit III, Hole C0020A.

Core, section, interval (cm) or cuttings sample	Depth (mbsf)	Group abundance	Dinoflagellate cysts												Spores							Gymnosperms						
			Bellatudinium hokkaidoanum	*Brigantedinium* spp.	*Cleistosphaeridium* spp. undifferentiated	*Enneadocysta* sp.	*Evittosphaerula* sp. A	*Gelatia inflata*	*Kallosphaeridium* spp.	*Phthanoperidinium* spp.	*Systematophora ancyrea*	*Tectatodinium pellitum*	*Trinovantedinium boreale*	Dinocysts undifferentiated	*Deltoidospora* spp.	*Gleicheniidites*	*Granulatisporites* spp.	*Laevigatosporites* spp.	*Osmunda*	*Stereisporites* spp.	Spores undifferentiated	Bisaccate pollen (*Pinus, Picea*)	*Ephedra*	*Larix*	*Picea*	*Sciadopites* spp.	Taxodiaceous pollen	*Tsuga* spp.
337-C0020A-																												
217-SMW	1826.5–1836.5	P			1						X		X	2				5				4					37	
14R-CC	1827.58–1828.10	G	X							X								9				14					74	
219-SMW	1836.5–1846.5	M									X							10				9					46	
220-SMW	1846.5–1856.5	M		1			1		X	X			X					6		2		2				1	49	
221-SMW	1866.5–1856.5	M													1			12	1			2					52	
15R-1, 104–106	1920.04–1920.06	G																6	3			3					120	
15R-CC	1926.64–1926.85	B																										
16R-CC	1933.40–1933.46	B																										
236-SMW	1936.5–1946.5	G																13	5	1	1	5					64	1
18R-2, 62–63	1947.27–1947.28	M																7				3				1	25	
19R-6, 115–116	1956.81–1956.82	G				X		X		X				1	6	1		18	7			35			3		85	1
19R-7, 119–120	1958.28–1958.29	G																10						3			20	
20R-5, 99–100	1978.63–1978.64	G													1			2				1				2	51	
22R-5, 85–86	1978.49–1978.50	G												2	3			20	5	1		27					99	
23R-2, 73–74	1983.19–1983.20	M																2				5			1	1	56	
23R-5, 55–56	1986.81–1986.82	G													1			15	3			5					70	
23R-CC	1991.08–1991.25	P															1	5	2	1		3					30	
24R-2, 100–101	1997.41–1997.42	G																3	1			6					65	
25R-6, 19–20	2001.59–2002.60	G																	18			3					85	
25R-CC	2002.09–2002.35	G	X									2						20	10				1				26	

Core, section, interval (cm) or cuttings sample	Depth (mbsf)	Angiosperms																													
		Acer spp.	*Aesculiidites* spp.	*Alnus* spp.	*Betula* spp.	Betulaceae/Myricaceae types	*Caprifoliipites* spp.	*Carpinus* spp	*Carya* spp.	*Castanea*	*Castanopsis*	*Celtis* spp.	*Cercidiphyllites*	*Corylus*	*Cupuliferoipollenites pusillus*	*Engelhardtia*	*Ericaceae*	*Fagus* spp.	*Fraxinoipollenites*	*Gingko*	*Gothanipollis*	*Ilex*	*Juglans*	*Liquidamber*	*Malvacipollis*	Myrtaceae	*Nyssa*	*Nyssapollenites explanata*	*Pandaniidites*	*Paraalnipollenites* sp.	*Pasania*
337-C0020A-																															
217-SMW	1826.5–1836.5					9			1					1	1				1	1											
14R-CC	1827.58–1828.10		1	13	2	5		2	4			1	1	1					1			1	2					1			
219-SMW	1836.5–1846.5			3		5				1				1								3					1				
220-SMW	1846.5–1856.5	2		11	3	7			1	2									2	1		2					3				
221-SMW	1866.5–1856.5	1		6	7	1													1			1	1	1					1		
15R-1, 104–106	1920.04–1920.06	2	1	62	9				1			1			5							2	1	9			32				
15R-CC	1926.64–1926.85																														
16R-CC	1933.40–1933.46																														
236-SMW	1936.5–1946.5	2		19	6				1	1				1			3	6	3			5		1			7				1
18R-2, 62–63	1947.27–1947.28	2		2	4	1		1							3		9	4	1			4	1				7				
19R-6, 115–116	1956.81–1956.82			21	10	4		3	2								1	2				4		12	1		1				
19R-7, 119–120	1958.28–1958.29	1		4	7			1	1						2			8				2		1			2				
20R-5, 99–100	1978.63–1978.64			4	10	1		1	1						1		25	3	1					2			8				
22R-5, 85–86	1978.49–1978.50	1		10	14			3	7	2						1	2	1	3			1		5	1	2	28			2	
23R-2, 73–74	1983.19–1983.20	1		3	5																			3							
23R-5, 55–56	1986.81–1986.82	2	2	29	9				3	3	1		7										3	13			25		3		
23R-CC	1991.08–1991.25			5	11	1											1	1						2							
24R-2, 100–101	1997.41–1997.42	5		6	12	1			1	1						1	1				1	2		1			3				1
25R-6, 19–20	2001.59–2002.60	3		13	49																	8		2			15				
25R-CC	2002.09–2002.35	2		13	3		2	3										6					1	16			4	1			

Core, section, interval (cm) or cuttings sample	Depth (mbsf)	Angiosperms																									Other organic materials		
		Platanus	Poaceae	*Polygonum*	*Pterocarya*	*Quercoidites*	*Quercus* (deciduous)	*Quercus* (evergreen)	*Reevsia*	cf. *Rhoipites angustus*	*Rhoipites bradleyi*	*Rhus*	*Salix*	*Sparganiaceaepollenites*	*Striatopollis* sp. A	*Symplocoipollenites*	*Symplocos*	*Talisiipites pulvifluminus*	*Tetracolporopollenites* spp.	*Tilia* spp.	*Tricolpites hians*	Tricolporate undifferentiated	*Trivestibulopollenites* spp.	*Ulmus/Zelcova* spp.	*Ulmipollenites*	*Weigela*	Foraminiferal linings	Fungi	Plant resin
337-C0020A-																													
217-SMW	1826.5–1836.5									1										1		3			2		1		
14R-CC	1827.58–1828.10				4											1						1			6			1	
219-SMW	1836.5–1846.5				1	1				1				1			1			2		1	1						1
220-SMW	1846.5–1856.5			1			2							1			1			2	1	5			1			2	
221-SMW	1866.5–1856.5							1						1						1	1	4		2		1			3
15R-1, 104–106	1920.04–1920.06	13					30	2	4		2	2	2		1			1				2		8					
15R-CC	1926.64–1926.85																												
16R-CC	1933.40–1933.46																												
236-SMW	1936.5–1946.5	4			1		24	16				1	1							2				5					
18R-2, 62–63	1947.27–1947.28	4					20	7					1									1		3					
19R-6, 115–116	1956.81–1956.82	6			3		1					1		1		1				4		1		8					
19R-7, 119–120	1958.28–1958.29	11					62	32					3															1	
20R-5, 99–100	1978.63–1978.64	5					22	17																4				2	
22R-5, 85–86	1978.49–1978.50	16			2		33	5				1		2				1		1				27					
23R-2, 73–74	1983.19–1983.20				1		3																	2					
23R-5, 55–56	1986.81–1986.82	11	1		2		10	12					1	2								1		37					
23R-CC	1991.08–1991.25	3																				1		3					
24R-2, 100–101	1997.41–1997.42	4					81	48	1			1								1		2		4		1		2	
25R-6, 19–20	2001.59–2002.60																							8					
25R-CC	2002.09–2002.35	3			4		5												1	1				2					

Numbers in the taxa columns refer to abundance counts of specimens. Group abundance: B = barren, P = poor (1–75 specimens within a sample), M = moderate (76–125 specimens), G = good (>126). X = reworked.

Table T7. Distribution of dinoflagellate cysts, pollen, and spores in Unit IV, Hole C0020A.

			Dinoflagellate cysts														
Core, section, interval (cm)	Depth CSF-B (m)	Group abundance	*Batiacasphaera micropapillata*	*Bellatudinium hokkaidoanum*	*Brigantedinium* spp.	*Cribroperidinium* spp.	*Diphyes latiusculum*	*Hystrichokolpoma* spp.	cf. *Impagidinium velorum*	*Operculodinium centrocarpum*	*Operculodinium* spp.	*Phthanoperidinium* spp.	*Selenopemphix nephroides*	*Selenopemphix* spp.	*Spiniferites* spp.	*Trinovantedinium boreale*	Dinocysts undifferentiated
337-C0020A-																	
26R-9, 34–35	2119.20–2119.21	G			1					1		X	7			X	4
26R-9, 45–46	2119.31–2119.32	G									1		2	2		X	
28R-4, 13–14	2303.71–2303.72	M				1	2								1		4
29R-2, 75.5–76	2402.15–2402.16	M										X			1		
29R-5, 100.5–101	2405.98–2405.99	M															2
30R-3, 0–42 A	2448.68–2449.1	G		X													
30R-3, 0–42 B	2448.68–2449.1	G															
32R-5, 120–121	2462.31–2462.32	G							1								1
32R-7, 58–59	2464.23–2464.24	G	2					1			1	X					1

	Spores								Gymnosperms							
Core, section, interval (cm)	*Cicatricosisporites*	*Deltoidospora* spp.	*Gleicheniidites*	*Granulatisporites* spp.	*Laevigatosporites* spp.	*Osmunda*	*Stereisporites* spp.	Spores undifferentiated	Bisaccate pollen (*Pinus*, *Picea*)	*Cathaya*	*Ephedra*	*Larix*	*Picea*	*Sciadopites* spp.	Taxodiaceous pollen	*Tsuga* spp.
337-C0020A-																
26R-9, 34–35					2	1			23	2	1	1	4		93	4
26R-9, 45–46		1			3				12	3			4	1	109	2
28R-4, 13–14					10	1			14				1		36	
29R-2, 75.5–76		1		1	1	2			6				2		39	
29R-5, 100.5–101					1		1		10						50	
30R-3, 0–42 A		3			4	1			11				2		77	
30R-3, 0–42 B		3			6	3		1	22			1	8		75	
32R-5, 120–121	X	2	1		5	2			40						91	
32R-7, 58–59		2		1	6				68				2		134	

	Angiosperms																			
Core, section, interval (cm)	*Aesculiidites* spp.	*Alnus* spp.	*Betula* spp.	Betulaceae/Myricaceae types	*Carpinus* spp	*Carya* spp.	*Celtis* spp.	*Engelhardtia*	Ericaceae	*Fagus* spp.	*Fraxinoipollenites*	*Ilex*	*Juglans*	*Lanagiopollis*	*Liquidamber*	*Magnolia*	*Nyssa*	*Paraalnipollenites*	*Platanus*	Poaceae
337-C0020A-																				
26R-9, 34–35	1	2	9		2	1				3	1				9		2		2	
26R-9, 45–46		4	5	1						1	1				7		3		2	
28R-4, 13–14		2	11			3	1	1		5			1		4		1		4	
29R-2, 75.5–76		2	10			3				1	1									
29R-5, 100.5–101		1	10												1		1		1	1
30R-3, 0–42 A		2	13	1		1			3			1	1	1	6			1	6	
30R-3, 0–42 B		10	12	3		1				1		1			4		1		5	
32R-5, 120–121		7	23						1	1					6	1				
32R-7, 58–59		16	20	4		3					3		3	1	18		1			

	Angiosperms																			Other organic materials	
Core, section, interval (cm)	*Porocolpopollenites* sp.	*Pterocarya*	*Quercoidites*	*Quercus* (deciduous)	*Quercus* (evergreen)	*Reevsia*	*Rhus*	*Salix*	*Scabratricolporites*	*Sparganiaceaepollenites*	*Tetracolporopollenites* spp.	*Tilia* spp.	*Tricolpites hians*	Tricolpate undifferentiated	Tricolporate undifferentiated	*Triporopollenites* spp.	*Ulmus/Zelcova* spp.	*Ulmipollenites*	*Weigela*	Foraminiferal linings	Fungi
337-C0020A-																					
26R-9, 34–35		2		6	5		1										20				
26R-9, 45–46		1		1	2		1	1				1					8				1
28R-4, 13–14		3	3					2		2							5				
29R-2, 75.5–76		4															3				
29R-5, 100.5–101									1	1					1		6				
30R-3, 0–42 A		1	1							1	1	1					10	1		1	1
30R-3, 0–42 B		2								8		2					8		1		1
32R-5, 120–121		2	1			1						1	5		1		18				3
32R-7, 58–59	1	3								4			1	3	3	3	8				

Numbers in the taxa columns refer to abundance counts of specimens. Group abundance: M = moderate (76–125 specimens), G = good (>126). X = reworked.

Table T8. Distribution of diatoms in Unit I, Hole C0020A.

Cuttings sample	Depth DRF (m)	Top depth MSF (m)	Bottom depth MSF (m)	Geologic age	Zone/ Subzone	Abundance	Preservation	*Actinocyclus oculatus*	*Crucidenticula* spp.	*Denticulopsis* spp.	*Kisselviella* spp.	*Melosira* spp.	*Neodenticula kamtschatica*	*Neodenticula koizumii*	*Neodenticula seminae*	*Nitzchia pliocena*	*Proboscia curvirostris*	*Thalassiosira oestrupii*
337-C0020A-																		
25-SMW	1865	646.5	656.5	Barren	—	B	—											
35-SMW	1965	746.5	756.5	late Pliocene	upper NPD9	C	M	R						R	F			
40-SMW	2015	796.5	806.5	late Pliocene	upper NPD9	R	P							R	R			
45-SMW	2065	846.5	856.5	late Pliocene	upper NPD9	C	M	R						R	F			
53-SMW	2085	866.5	876.5	Barren	—	B	—											
54-SMW	2095	876.5	886.5	Barren	—	B	—											
55-SMW	2105	886.5	896.5	late Pliocene	NPD9	F	P							F				
56-SMW	2115	896.5	906.5	early Pliocene	NPD8	F	G	R					R	R	X			
61-SMW	2165	946.5	956.5	early Pliocene	NPD8	C	M						F	F	X			
66-SMW	2215	996.5	1006.5	early Pliocene	NPD7Bb	A	G						C					R
74-SMW	2275	1056.5	1066.5	early Pliocene	NPD7Bb	F	M						F					R
75-SMW	2285	1066.5	1076.5	early Pliocene	NPD7Bb	F	G	R					F					R
92-SMW		1116.5	1126.5	Lost														
89-SMW	2335	1126.5	1136.5	Miocene	—	C	M				R	C	X		X			
90-SMW	2345	1136.5	1146.5	Miocene	—	C	M				R	C						
94-SMW	2435	1216.5	1226.5	Barren	—	B	—											
95-SMW	2445	1226.5	1236.5	Miocene	—	R	M				R		X		X			
97-SMW	2455	1236.5	1246.5	Miocene	—	R	P										X	
98-SMW	2465	1246.5	1256.5	Miocene	—	R	P		?	R				X				

NPD = North Pacific diatom. Abundance: A = abundant (≥6 specimens per field of view [FOV] at 400× magnification), C = common (1–5 specimens/FOV at 400×), F = few (1–4 specimens/5 FOVs at 400×), R = rare (1–10 specimens/horizontal traverse at 400×), B = barren, X = contaminant. Preservation: P = poor, M = moderate, G = good. — = barren or indeterminate.

Table T9. Log response of major lithology, Site C0020.

Lithofacies	GR	SP	Resistivity	Density	Neutron porosity
Coal	Low	Low	Very high	Very low	Very high
Sandstone	Low	High	Low	Low	Low
Cemented sandstone	Low	High	Very high	Very high	Very low
Siltstone/Shale	Medium	Low	Medium	Medium	High

GR = gamma ray, SP = spontaneous potential.

Table T10. Major coal layers, Site C0020.

Coal layer	Lith. unit	Depth WMSF (m) Top	Depth WMSF (m) Bottom	Thickness (m)
1	II	1529.5	1530.1	0.6
2	II	1539.4	1539.7	0.3
3	II	1543.4	1544.0	0.6
4	III	1839.1	1840.0	0.9
5	III	1846.3	1846.9	0.6
6	III	1863.7	1864.6	0.9
7	III	1916.2	1923.5	7.3
8	III	1944.4	1947.9	3.5
9	III	1958.4	1958.7	0.3
10	III	1978.8	1979.3	0.5
11	III	1993.7	1994.8	1.1
12	III	1997.5	1998.8	1.3
13	III	2002.3	2003.0	0.7
14	III	2027.0	2028.1	1.1
15	III	2043.9	2045.3	1.4
16	III	2054.7	2055.0	0.3
17	IV	2448.4	2449.3	0.9

Table T11. Fluid sampling points, Site C0020.

Sampling point	Lith. unit	Depth WMSF (m)	Mobility (mD/cP)	Formation pressure (KPa)	Temperature (°C)
1	III	1977.99	50.02	31,979	47
2	III	1901.19	26.13	31,200	46
3	III	1844.03	54.77	30,607	45
4	II	1807.97	207.08	30,235	44
5	II	1489.28	65.10	27,008	39
6	II	1279.52	318.94	24,905	35

Table T12. Drilling mud water, Hole C0020A.

Lith. unit	Mud water sample	Salinity (‰)	Alkalinity (mM)	PO_4 (µM)	NH_4 (mM)	Cl^- (mM)	Br^- (mM)	SO_4^{2-} (mM)	Na^+ (mM)
	337-C0020A-								
Pre	2-LMT	111.38	49.55	BD	BD	1218.68	0.69	27.95	511.49
I	23-LMT	100.91	39.74	31.11	BD	1097.82	0.89	25.71	475.10
II	120-LMW	97.86	44.98	BD	0.97	970.18	0.94	22.96	457.41
II	189-LMW	103.31	49.86	BD	BD	1130.72	0.68	20.52	624.37
III	257-LMW	138.89	77.70	BD	BD	1547.56	0.81	55.96	1146.67
IV	280-LMW	125.69	63.97	BD	BD	1367.33	0.73	49.45	1013.76
IV	373-LMW	127.41	70.03	BD	BD	1394.39	0.83	50.99	1019.80
Post	392-LMT	104.57	46.11	BD	BD	1103.69	0.76	37.96	812.25

LMT = fluid collected at the mud tank. LMW = fluid taken from drilling mud. BD = below detection., ND = not detected.

Lith. unit	Mud water sample	K^+ (mM)	Mg^{2+} (mM)	Ca^{2+} (mM)	B (µM)	Ba (µM)	Fe (µM)	Li (µM)	Mn (µM)	Si (µM)	Sr (µM)
	337-C0020A-										
Pre	2-LMT	847.34	28.18	5.96	299.38	5.15	BD	152.62	BD	119.80	57.78
I	23-LMT	756.11	28.02	5.41	192.76	5.71	9.48	164.10	ND	233.66	13.91
II	120-LMW	642.97	23.82	8.41	176.26	42.60	166.69	151.85	1.69	2305.82	16.82
II	189-LMW	650.04	14.05	6.17	166.12	14.16	151.06	259.81	3.02	2150.94	13.61
III	257-LMW	732.92	5.18	4.30	176.41	9.52	392.30	233.30	5.34	4416.41	17.68
IV	280-LMW	662.50	3.87	4.08	188.57	12.51	464.14	224.34	4.66	5278.75	25.55
IV	373-LMW	668.84	2.23	4.05	237.83	13.72	587.60	191.73	5.71	7202.78	32.98
Post	392-LMT	578.05	1.54	3.50	173.91	14.43	449.15	190.80	3.57	5418.73	28.82

Table T13. Drilling cuttings water, Hole C0020A.

Lith. unit	Cuttings sample	Prep.	Depth MSF (m) Top	Depth MSF (m) Bottom	Salinity (‰)	pH	Alkalinity (mM)	PO_4 (µM)	NH_4 (mM)	Cl^- (mM)	Br^- (mM)	SO_4^{2-} (mM)
	337-C0020A-											
I	56-SMW	Bulk	897	907	71.66	8.41	17.02	9.42	10.22	1170.19	0.83	20.78
I	56-SMW	Clean	897	907	70.04	8.47	15.41	11.64	10.96	1188.39	0.91	20.34
I	66-SMW	Clean	997	1007	72.79	8.29	16.85	13.52	8.01	1177.24	0.85	19.76
I	81-SMW	Bulk	1097	1107	75.93	8.81	16.72	3.64	3.67	1145.22	0.79	23.24
II	114-SMW	Bulk	1276	1286	83.83	11.62	23.69	ND	0.49	1163.19	0.80	18.62
II	128-SMW	Bulk	1367	1377	79.65	8.62	—	3.44	0.71	1129.21	0.79	23.85
II	187-SMW	Bulk	1626	1637	88.65	—	27.92	ND	0.47	1263.45	0.77	23.21
II	197-SMW	Rhizon	1687	1697	97.77	—	24.16	ND	1.23	1514.71	0.85	23.28
II	213-SMW	Bulk	1807	1817	103.30	9.00	23.21	ND	0.76	1513.53	0.84	22.85

Prep. = preparation. — = not analyzed. ND = not detected.

Lith. unit	Cuttings sample	Na^+ (mM)	K^+ (mM)	Mg^{2+} (mM)	Ca^{2+} (mM)	B (µM)	Ba (µM)	Fe (µM)	Li (µM)	Mn (µM)	Si (µM)	Sr (µM)
	337-C0020A-											
I	56-SMW	538.07	635.14	33.54	2.39	176.77	9.82	1.07	96.43	1.38	503.04	31.11
I	56-SMW	543.56	621.15	34.06	2.44	197.27	10.65	0.92	103.11	0.65	661.01	37.90
I	66-SMW	544.31	637.83	32.97	2.27	236.19	12.57	0.92	108.81	0.68	741.27	35.96
I	81-SMW	508.91	691.09	27.66	1.71	100.91	7.02	10.60	70.53	0.72	374.42	21.63
II	114-SMW	479.94	648.38	0.15	62.06	64.98	4.57	5.87	63.58	0.71	292.94	78.85
II	128-SMW	485.81	678.01	21.72	4.60	81.97	5.76	1.26	63.75	1.12	305.55	22.26
II	187-SMW	518.41	752.37	13.95	1.76	76.98	4.26	2.61	68.36	1.07	249.99	10.00
II	197-SMW	740.37	720.67	15.05	4.27	45.11	11.67	1.79	68.12	3.46	271.47	54.18
II	213-SMW	815.00	781.49	10.62	0.76	73.58	4.76	1.91	72.30	0.85	90.60	10.96

Table T14. Interstitial water chemistry from whole-round cores, Hole C0020A.

Lith. unit	Core, section, interval (cm)	Depth CSF-B (m) Top	Depth CSF-B (m) Bottom	Salinity (‰)	pmH	Alkalinity (mM)	PO_4 (µM)	NH_4 (mM)	Cl^- (mM)	Br^- (mM)	SO_4^{2-} (mM)
	337-C0020A-										
II	1R-2, 0–65	1277.77	1278.42	76.80000	7.95	16.87	5.39	6.27	1097.47	0.79	20.17
II	2R-3, 0–60	1288.79	1289.39	70.53000	7.63	17.39	3.26	5.56	817.60	0.86	9.92
II	3R-3, 0–60	1371.99	1372.59	39.42000	8.04	8.97	ND	3.29	690.36	0.99	2.98
II	4R-3, 10–40	1377.545	1377.845	67.88000	0.00	16.93	ND	7.85	1014.84	0.83	15.41
II	5R-3, 39–85	1492.24	1492.7	36.29000	8.30	5.47	ND	2.24	621.00	0.94	2.04
II	6R-2, 15–76	1496.555	1497.165	41.47000	8.55	4.56	ND	2.69	689.21	0.98	2.40
II	8L-5, 35–93	1607.67	1608.09	40.02000	8.46	3.11	ND	2.89	715.92	0.92	2.07
II	8L-9, 16–46	1611.33	1611.63	39.16000	—	6.36	ND	2.89	643.94	0.85	1.65
II	10R-3, 0–37	1632.32	1632.69	39.00000	—	2.10	ND	2.45	572.95	0.89	0.97
II	11R-2, 0–40	1738.88	1739.28	33.48000	—	5.38	ND	2.02	593.26	0.82	1.40
II	11R-5, 23–58	1742.73	1743.08	36.62000	—	3.25	ND	2.34	613.20	0.81	1.50
II	12R-2, 53–75	1748.965	1749.185	41.38491	—	5.47	ND	2.89	689.14	0.83	1.88
II	12R-7, 30–50	1754.835	1755.035	39.65151	—	5.14	ND	2.54	665.07	0.81	2.31
II	13R-2, 4.5–44	1757.907	1758.281	39.86819	9.06	3.24	ND	2.40	638.88	0.83	1.59
II	13R-8, 27–60	1764.811	1765.123	40.73489	—	6.31	ND	2.64	672.91	0.74	2.27
III	15R-7, 18–33	1925.645	1925.795	29.30528	—	4.92	ND	1.35	487.68	0.71	1.14
III	16R-2, 18–77	1929.69	1930.28	42.73913	7.78	14.08	ND	3.20	792.26	0.71	10.51
III	17R-1, 60–100	1936.6	1937	40.24737	—	11.68	ND	1.97	622.23	0.77	4.42
III	17R-4, 65–85	1939.35	1939.55	41.70992	7.58	14.21	ND	2.23	660.30	0.72	4.26
III	17R-9, 25–51	1944.39	1944.65	44.52670	7.87	13.90	ND	2.38	646.72	0.70	4.50
III	19R-9, 30–60	1958.831	1959.108	37.70000	8.17	9.25	ND	1.72	596.61	0.76	5.06
III	20R-3, 23–77	1961.795	1962.335	28.82000	—	4.69	—	1.34	512.36	0.74	1.15
IV	28R-6, 0–30	2306.35	2306.65	—	—	—	—	—	751.51	0.60	11.35
IV	29R-6, 0–76	2405.3	2406.06	26.75935	—	5.71	—	—	459.35	0.48	2.90

— = not analyzed. ND = not detected.

Lith. unit	Core, section, interval (cm)	Na^+ (mM)	K^+ (mM)	Mg^{2+} (mM)	Ca^{2+} (mM)	B (µM)	Ba (µM)	Fe (µM)	Li (µM)	Mn (µM)	Si (µM)	Sr (µM)
	337-C0020A-											
II	1R-2, 0–65	605.67	448.59	40.28	18.39	108.93	12.79	5.08	218.41	6.98	393.03	141.61
II	2R-3, 0–60	663.80	315.26	47.00	25.25	358.17	13.37	24.95	353.34	13.33	643.30	212.10
II	3R-3, 0–60	547.69	65.27	31.85	22.21	465.57	31.12	0.54	92.29	18.74	871.29	176.68
II	4R-3, 10–40	683.50	215.20	46.30	30.75	254.09	18.18	16.83	218.79	25.41	579.46	185.69
II	5R-3, 39–85	502.77	14.30	19.89	30.82	691.89	8.95	1.15	99.52	27.94	866.89	93.90
II	6R-2, 15–76	559.41	39.87	25.26	39.23	348.91	14.97	0.59	106.71	18.51	741.28	124.54
II	8L-5, 35–93	584.29	24.06	16.66	37.25	337.95	28.73	0.90	171.05	7.39	101.70	145.90
II	8L-9, 16–46	574.82	18.19	14.42	34.14	438.61	26.67	0.72	193.99	36.66	447.22	150.18
II	10R-3, 0–37	530.79	10.29	9.90	25.12	262.03	16.60	0.88	162.30	10.19	330.91	99.49
II	11R-2, 0–40	535.67	11.99	12.55	26.22	329.50	42.79	0.80	138.92	9.79	629.37	218.29
II	11R-5, 23–58	559.26	33.30	13.00	26.70	359.11	45.81	0.74	138.43	5.24	458.76	233.83
II	12R-2, 53–75	616.90	31.08	14.32	29.61	162.76	47.18	0.86	141.49	1.05	204.27	281.15
II	12R-7, 30–50	613.36	13.64	14.24	28.48	268.82	56.46	0.96	159.12	1.84	141.26	287.31
II	13R-2, 4.5–44	600.43	22.18	14.79	29.58	202.27	57.25	0.90	160.19	1.78	102.30	300.65
II	13R-8, 27–60	617.71	22.55	14.28	30.87	130.93	54.59	0.77	159.28	0.77	76.18	319.24
III	15R-7, 18–33	466.24	3.31	12.38	15.19	82.97	78.76	0.73	133.84	1.12	124.86	306.82
III	16R-2, 18–77	667.72	57.09	22.51	27.92	207.83	29.67	1.50	303.12	16.76	266.77	497.28
III	17R-1, 60–100	584.37	26.93	17.99	22.72	148.21	29.57	0.59	178.73	2.15	161.85	450.86
III	17R-4, 65–85	630.71	46.97	18.87	23.90	305.59	75.64	1.58	320.28	14.38	296.28	473.94
III	17R-9, 25–51	614.66	30.30	20.11	26.30	310.50	57.48	1.79	400.14	41.28	303.65	440.18
III	19R-9, 30–60	541.04	38.02	13.67	17.98	200.97	64.63	0.88	154.53	1.49	162.72	345.36
III	20R-3, 23–77	463.37	2.34	11.20	14.74	121.61	69.07	3.11	184.89	1.45	106.89	304.78
IV	28R-6, 0–30	650.31	37.32	14.08	36.00	1313.52	38.92	4.60	230.31	1.06	305.83	719.55
IV	29R-6, 0–76	413.48	3.70	7.27	16.89	111.94	25.13	4.72	156.36	0.55	68.89	382.94

Table T15. Formation water, Hole C0020A.

Lith. unit	Sample	Depth WSF (m)	Salinity (‰)	pH	Alkalinity (mM)	PO_4 (µM)	NH_4 (mM)	Cl^- (mM)	Br^- (mM)	SO_4^{2-} (mM)	Na^+ (mM)	K^+ (mM)
	337-C0020A-											
II	398-LWL	1279.5	52.00	7.55	34.39	6.59	2.80	777.05	0.88	7.94	555.50	214.13
II	397-LWL	1489.3	47.67	7.52	12.11	ND	2.72	772.08	0.81	7.94	566.54	158.65
II	396-LWL	1808.0	39.76	7.60	9.68	ND	1.83	669.69	0.84	5.09	549.72	76.50
III	395-LWL	1844.0	69.23	7.72	19.27	ND	2.04	1125.50	0.83	21.77	807.52	344.87
III	394-LWL	1901.5	70.91	7.91	18.45	ND	2.01	1181.22	0.81	23.86	861.65	375.49
III	393-LWL	1978.0	46.64	7.88	12.20	ND	2.31	769.67	0.74	11.42	640.63	137.19

LWL = formation water collected with the Quicksilver probe. ND = not detected.

Lith. unit	Sample	Mg^{2+} (mM)	Ca^{2+} (mM)	B (µM)	Ba (µM)	Fe (µM)	Li (µM)	Mn (µM)	Si (µM)	Sr (µM)
	337-C0020A-									
II	398-LWL	26.93	16.58	715.21	23.58	68.32	92.77	19.21	1592.60	154.10
II	397-LWL	19.73	26.91	913.60	12.08	12.24	98.80	64.92	1386.92	87.56
II	396-LWL	12.02	21.07	820.86	52.70	14.81	154.03	5.98	353.68	255.45
III	395-LWL	11.63	18.01	356.51	26.56	32.37	163.29	8.82	244.28	235.78
III	394-LWL	11.10	15.80	234.58	23.32	15.35	157.37	3.68	228.48	227.78
III	393-LWL	11.33	16.69	403.80	31.32	16.38	174.22	4.32	471.54	331.32

Table T16. Time intervals during which mud gas was recovered from the geological formation, Hole C0020A. (Continued on next page.)

Period of mud-gas recovery				Depth of recovered mud gas MSF (m)	
Start date (2012)	Start time (h)	End date (2012)	End time (h)	Top	Bottom
15 Aug	1107	15 Aug	1202	648.0	694.5
15 Aug	1215	15 Aug	1220	702.0	708.0
15 Aug	1224	15 Aug	1226	712.5	713.5
15 Aug	1555	15 Aug	1607	787.5	798.5
15 Aug	1612	15 Aug	1617	803.0	806.0
15 Aug	1735	15 Aug	1738	822.0	825.0
15 Aug	1745	15 Aug	1754	832.0	837.5
15 Aug	1802	15 Aug	1813	839.5	848.0
15 Aug	1832	15 Aug	1843	852.5	861.5
15 Aug	1850	15 Aug	1914	868.0	886.0
15 Aug	2104	15 Aug	2144	888.0	924.5
16 Aug	1446	16 Aug	1536	1005.5	1035.5
16 Aug	1733	16 Aug	1744	1043.5	1055.0
16 Aug	1747	16 Aug	1751	1055.5	1058.5
16 Aug	1812	16 Aug	1823	1063.0	1076.5
16 Aug	2027	16 Aug	2049	1077.5	1091.0
16 Aug	2055	16 Aug	2127	1093.5	1105.5
16 Aug	2140	16 Aug	2146	1109.5	1114.0
18 Aug	1303	18 Aug	1422	1195.5	1229.5
18 Aug	1452	18 Aug	1521	1233.0	1245.0
18 Aug	1755	18 Aug	1815	1251.5	1257.5
18 Aug	1818	18 Aug	1839	1258.0	1263.0
25 Aug	1344	25 Aug	1355	1267.0	1271.0
26 Aug	0043	26 Aug	0055	1306.5	1314.0
26 Aug	0115	26 Aug	0156	1317.0	1340.5
26 Aug	0159	26 Aug	0224	1341.0	1353.0
26 Aug	0353	26 Aug	0408	1353.5	1360.5
26 Aug	0417	26 Aug	0437	1362.0	1370.0
26 Aug	1339	26 Aug	1354	1381.0	1383.5
26 Aug	1527	26 Aug	1558	1388.5	1397.0
26 Aug	1611	26 Aug	1736	1400.0	1430.5
26 Aug	1741	26 Aug	1858	1431.5	1436.0
26 Aug	1921	26 Aug	1953	1439.0	1448.0
26 Aug	2116	26 Aug	2132	1453.0	1456.0
26 Aug	2146	26 Aug	2217	1457.5	1467.5

Table T16 (continued).

Period of mud-gas recovery				Depth of recovered mud gas MSF (m)	
Start date (2012)	Start time (h)	End date (2012)	End time (h)	Top	Bottom
27 Aug	1026	27 Aug	1033	1503.0	1504.0
27 Aug	1052	27 Aug	1103	1507.0	1518.5
27 Aug	1122	27 Aug	1137	1519.5	1529.0
27 Aug	1151	27 Aug	1220	1529.5	1542.5
27 Aug	1239	27 Aug	1251	1544.0	1551.5
27 Aug	1308	27 Aug	1457	1559.5	1597.5
27 Aug	2028	27 Aug	2032	1602.5	1604.0
31 Aug	0941	31 Aug	0952	1628.0	1629.0
31 Aug	1303	31 Aug	1316	1637.0	1638.5
31 Aug	1506	31 Aug	1804	1641.5	1675.5
31 Aug	1832	31 Aug	1912	1677.0	1696.0
31 Aug	1937	31 Aug	2045	1696.5	1737.0
1 Sep	0818	1 Sep	0835	1765.0	1766.1
1 Sep	1009	1 Sep	1028	1772.0	1775.0
1 Sep	1041	1 Sep	1053	1776.0	1780.0
1 Sep	1109	1 Sep	1211	1781.5	1810.0
1 Sep	1220	1 Sep	1244	1810.5	1820.0
1 Sep	2023	1 Sep	2043	1826.5	1829.5
1 Sep	2103	1 Sep	2123	1830.5	1834.0
1 Sep	2144	1 Sep	2237	1836.5	1848.0
1 Sep	2246	1 Sep	2358	1848.5	1870.5
2 Sep	0016	2 Sep	0132	1873.0	1881.5
2 Sep	0222	2 Sep	0255	1883.0	1886.0
2 Sep	0305	2 Sep	0403	1886.3	1891.0
2 Sep	0439	2 Sep	0722	1893.0	1915.0
2 Sep	1343	2 Sep	1433	1921.5	1928.0
2 Sep	1649	2 Sep	1728	1929.5	1934.0
2 Sep	1952	2 Sep	2033	1937.5	1945.0
2 Sep	2244	2 Sep	2309	1946.0	1950.0
4 Sep	1723	4 Sep	1732	1965.5	1966.5
4 Sep	1833	4 Sep	1855	1969.5	1973.0
5 Sep	0244	5 Sep	0259	1989.5	1991.0
5 Sep	0354	5 Sep	0407	1991.5	1995.0
5 Sep	0718	5 Sep	0741	2000.5	2003.0
5 Sep	0905	5 Sep	1129	2004.0	2032.5
5 Sep	1142	5 Sep	1238	2035.5	2048.5
5 Sep	1255	5 Sep	1714	2049.0	2080.5
5 Sep	1734	5 Sep	1819	2082.0	2087.0
5 Sep	1843	5 Sep	2116	2088.5	2105.0
6 Sep	0407	6 Sep	0422	2116.5	2119.0
6 Sep	0508	6 Sep	0535	2121.5	2124.5
6 Sep	0632	6 Sep	0839	2128.0	2150.5
6 Sep	0851	6 Sep	0946	2152.5	2163.5
6 Sep	1009	6 Sep	1024	2165.0	2168.0
6 Sep	1027	6 Sep	1237	2169.0	2193.5
6 Sep	1310	6 Sep	1319	2195.5	2196.5
7 Sep	0354	7 Sep	0414	2207.0	2209.5
7 Sep	0524	7 Sep	0533	2212.5	2213.5
7 Sep	0550	7 Sep	076	2214.5	2227.5
7 Sep	0721	7 Sep	0819	2230.0	2240.0
7 Sep	0836	7 Sep	0923	2241.0	2259.0
7 Sep	0935	7 Sep	0946	2261.5	2264.0
7 Sep	0959	7 Sep	1032	2266.5	2277.5
7 Sep	1113	7 Sep	1207	2278.5	2300.0
7 Sep	2032	7 Sep	2106	2311.0	2317.0
7 Sep	2119	7 Sep	2253	2317.5	2342.0
7 Sep	2328	8 Sep	0256	2345.0	2379.0
8 Sep	0315	8 Sep	0413	2381.0	2392.5
8 Sep	1155	8 Sep	1251	2412.5	2431.0
8 Sep	1317	8 Sep	1403	2432.0	2440.0
9 Sep	0503	9 Sep	0514	2463.5	2466.0

Data were recorded nonstop during operations, including periods when drilling did not advance into the formation and times without mud flow and/or mud-gas recovery. The latter did not yield meaningful information about gas content of the geological formation and were carefully identified and discarded from the data set, leaving data recorded during times reported here for further data processing. Time is ship local time (UTC + 8 h).

Table T17. Carbon isotopic composition and concentration of methane in mud gas analyzed during on-line mud-gas monitoring using the methane carbon isotope analyzer (MCIA), Hole C0020A.

Depth of on-line monitored mud gas MSF (m)	δ^{13}C-methane (‰ vs. VPDB)	SD δ^{13}C-methane (‰ vs. VPDB)	Methane (ppm)	SD methane (ppm)
648.0	–67.3	0.1	1,190	47
649.0	–67.1	0.4	1,460	61
649.5	–67.0	0.3	1,540	166
650.0	–66.1	0.9	1,220	143
650.5	–66.2	0.9	1,740	211
651.5	–67.2	0.3	2,290	81
652.0	–67.5	0.1	2,530	84
652.5	–67.1	0.1	2,790	129
653.0	–67.0	0.2	3,840	386
654.0	–66.2	0.1	4,730	126
654.5	–66.2	0.2	5,120	125
655.0	–66.2	0.1	5,430	88
655.5	–66.3	0.1	5,780	148
656.0	–66.3	0.1	6,180	132
656.5	–66.1	0.2	7,100	402
656.6	–66.0	0.2	7,970	429
657.0	–66.0	0.1	8,580	47
657.5	–66.2	0.2	8,730	55
658.0	–66.2	0.1	8,900	62
658.5	–66.0	0.1	9,110	30
659.0	–66.2	0.1	9,290	110
660.0	–66.0	0.1	9,620	105
660.5	–66.1	0.1	10,000	185
661.5	–66.2	0.1	12,600	834
662.5	–66.1	0.0	13,300	105
663.5	–66.1	0.1	16,000	1,170
664.0	–66.2	0.2	29,500	8,880
664.5	–66.3	0.1	20,500	839
665.5	–66.2	0.3	17,900	1,880
666.5	–66.1	0.1	17,000	3,480
667.0	–67.8	0.5	398,000	257,000
667.5	–66.6	0.1	138,000	93,400
668.0	–66.0	0.1	81,900	23,900
668.5	–66.7	0.1	260,000	36,400
669.5	–66.1	0.1	86,800	6,630
670.0	–66.3	0.0	164,000	37,500
671.0	–66.2	0.1	126,000	37,200
671.5	–66.3	0.3	96,800	13,800
672.5	–66.5	0.2	157,000	5,540
673.5	–66.1	0.3	96,400	18,500
674.5	–66.1	0.1	121,000	34,300
675.5	–66.2	0.4	123,000	29,000
676.5	–66.1	0.0	92,300	15,500
678.0	–66.3	0.0	134,000	32,600
678.5	–66.1	0.3	95,100	28,100
679.0	–66.3	0.2	123,000	44,200
679.5	–66.2	0.1	91,600	26,400
680.5	–66.3	0.1	114,000	38,300
681.0	–66.3	0.2	83,600	18,400
682.0	–66.4	0.1	127,000	38,000
682.5	–66.2	0.2	78,600	9,230
683.0	–66.5	0.1	147,000	20,400
684.0	–66.1	0.3	89,300	22,500
685.0	–66.2	0.1	99,400	27,300
685.5	–66.4	0.3	170,000	2,750
686.5	–66.1	0.2	79,200	11,200
687.0	–66.7	0.0	172,000	39,800
687.5	–66.3	0.2	145,000	49,300

In general, 100–200 data points were recorded by MCIA per meter of drilled sediment. The actual number of data points per depth interval depends on the rate of penetration. The table reports average values and standard deviations (SDs) for 0.5 m depth intervals. Methane contents in the on-line monitored flow of extracted mud gas are reported as well, but it is important to note that they depend on several factors (rate of penetration, mud flow, mud/headspace ratio in the separator, gas flow into the gas monitoring lab, etc.) and do not directly reflect the in situ concentration of methane in the formation. VPDB = Vienna Peedee belemnite. Only a portion of this table appears here. The complete table is available in **ASCII.**

Table T18. Concentration of hydrocarbon gases in mud gas in Hole C0020A, analyzed during on-line mud-gas monitoring using a GC-FID. (Continued on next two pages.)

Date (2012)	Time (h)	Depth MSF (m)	Concentration in on-line monitored mud gas (ppmv)					
			Methane	Ethane	Propane	*iso*-Butane	*n*-Butane	C_1/C_2
15 Aug	1121	657.0	37,600	4.6	BD	BD	BD	8,240
15 Aug	1141	668.0	126,000	16.9	BD	BD	BD	7,450
15 Aug	1201	692.5	10,600	BD	BD	BD	BD	—
15 Aug	1601	786.5	49,700	6.0	BD	BD	BD	8,260
15 Aug	1841	859.5	1,450	BD	BD	BD	BD	—
15 Aug	1901	877.5	2,600	BD	BD	BD	BD	—
15 Aug	2121	904.5	5,220	2.3	BD	BD	BD	2,320
15 Aug	2141	921.5	207,000	26.6	BD	BD	BD	7,780
16 Aug	1501	1017.5	11,200	BD	BD	BD	BD	—
16 Aug	1520	1023.0	5,398	BD	BD	BD	BD	—
16 Aug	1741	1053.0	22,000	2.9	BD	BD	BD	7,540
16 Aug	1821	1074.5	22,600	2.9	BD	BD	BD	7,800
16 Aug	2041	1086.5	9,270	BD	BD	BD	BD	—
16 Aug	2101	1096.5	12,000	1.7	BD	BD	BD	7,280
16 Aug	2121	1104.0	8,770	BD	BD	BD	BD	—
16 Aug	2141	1106.5	1,540	BD	BD	BD	BD	—
18 Aug	1321	1206.5	11,900	2.4	BD	BD	BD	4,950
18 Aug	1341	1215.0	11,000	2.6	BD	BD	BD	4,240
18 Aug	1401	1221.5	6,840	1.7	BD	BD	BD	4,050
18 Aug	1421	1229.0	12,700	3.2	BD	BD	BD	3,990
18 Aug	1501	1237.5	3,340	BD	BD	BD	BD	—
18 Aug	1521	1245.0	9,180	2.4	BD	BD	BD	3,890
18 Aug	1801	1253.5	5,500	BD	BD	BD	BD	—
18 Aug	1821	1258.5	4,720	BD	BD	BD	BD	—
26 Aug	0120	1320.0	691	BD	BD	BD	BD	—
26 Aug	0141	1332.5	1,320	BD	BD	1.3	BD	—
26 Aug	0200	1345.0	1,200	BD	BD	1.7	BD	—
26 Aug	0221	1353.0	836	BD	BD	BD	BD	—
26 Aug	0401	1358.5	578	BD	BD	BD	BD	—
26 Aug	0421	1362.0	975	BD	BD	BD	BD	—
26 Aug	1341	1381.5	334	BD	BD	BD	BD	—
26 Aug	1541	1391.5	483	BD	BD	BD	BD	—
26 Aug	1621	1402.5	365	BD	BD	BD	BD	—
26 Aug	1710	1426.0	766	BD	BD	BD	BD	—
26 Aug	1741	1431.5	390	BD	BD	BD	BD	—
26 Aug	1801	1433.0	371	BD	BD	BD	BD	—
26 Aug	1821	1434.5	311	BD	BD	BD	BD	—
26 Aug	1841	1435.5	312	BD	BD	BD	BD	—
26 Aug	1921	1439.5	266	BD	BD	BD	BD	—
26 Aug	1941	1445.0	390	BD	BD	BD	BD	—
26 Aug	2121	1455.0	365	BD	BD	BD	BD	—
26 Aug	2201	1466.0	579	BD	BD	BD	BD	—
27 Aug	1101	1515.5	745	BD	BD	BD	BD	—
27 Aug	1201	1534.0	618	BD	BD	BD	BD	—
27 Aug	1242	1545.5	708	BD	BD	BD	BD	—
27 Aug	1320	1566.0	940	BD	BD	BD	BD	—
27 Aug	1341	1572.0	484	BD	BD	BD	BD	—
27 Aug	1401	1582.0	738	BD	BD	BD	BD	—
27 Aug	1454	1597.0	401	BD	BD	BD	BD	—
31 Aug	0941	1628.0	264	0.9	BD	6.6	BD	300
31 Aug	1522	1644.0	443	1.5	0.3	1.8	BD	297
31 Aug	1541	1650.0	795	2.7	0.6	1.9	BD	297
31 Aug	1601	1655.5	616	2.6	0.5	1.5	BD	239
31 Aug	1622	1657.5	312	1.4	BD	1.4	BD	229
31 Aug	1642	1662.0	520	1.8	BD	1.3	BD	290
31 Aug	1702	1665.0	573	1.8	0.3	1.3	BD	325
31 Aug	1721	1669.0	621	2.9	0.5	1.4	BD	216
31 Aug	1741	1672.5	673	2.7	0.4	1.1	BD	248
31 Aug	1801	1675.5	419	1.5	BD	0.8	BD	272
31 Aug	1841	1679.5	734	2.3	BD	0.8	BD	313
31 Aug	1902	1689.5	1,110	2.7	0.4	0.7	BD	415
31 Aug	1941	1703.5	1,030	1.8	BD	0.8	BD	582
31 Aug	2001	1706.5	1,680	3.2	0.5	0.6	BD	522
31 Aug	2021	1718.5	1,870	2.6	BD	0.5	BD	732
31 Aug	2041	1737.0	1,150	1.8	BD	0.5	BD	631
1 Sep	0822	1766.0	566	0.8	BD	BD	BD	690
1 Sep	1021	1775.0	402	0.7	BD	BD	BD	566

Table T18 (continued). (Continued on next page.)

Date (2012)	Time (h)	Depth MSF (m)	Concentration in on-line monitored mud gas (ppmv)					
			Methane	Ethane	Propane	*iso*-Butane	*n*-Butane	C_1/C_2
1 Sep	1042	1776.5	304	0.7	BD	BD	BD	422
1 Sep	1121	1791.2	1,100	1.2	BD	BD	BD	927
1 Sep	1141	1798.5	879	1.0	BD	BD	BD	906
1 Sep	1201	1800.0	835	1.9	BD	BD	BD	446
1 Sep	1221	1811.0	673	1.4	BD	BD	BD	498
1 Sep	1241	1820.0	767	1.1	BD	BD	BD	717
1 Sep	2041	1829.5	539	0.6	BD	BD	BD	913
1 Sep	2122	1834.0	632	0.9	BD	BD	BD	744
1 Sep	2201	1839.0	1,210	1.3	BD	BD	BD	923
1 Sep	2221	1844.5	1,214	1.6	BD	BD	BD	764
1 Sep	2301	1853.5	797	0.9	BD	BD	BD	886
1 Sep	2322	1859.5	958	1.1	BD	BD	BD	895
1 Sep	2341	1867.0	1,840	1.8	BD	BD	BD	1,040
2 Sep	0030	1876.5	778	1.5	BD	BD	BD	505
2 Sep	0101	1880.0	725	0.9	BD	BD	BD	788
2 Sep	0122	1881.0	550	1.0	BD	BD	BD	556
2 Sep	0242	1884.0	472	0.9	BD	BD	BD	542
2 Sep	0322	1888.5	531	0.9	BD	BD	BD	611
2 Sep	0342	1890.0	353	0.8	BD	BD	BD	465
2 Sep	0402	1891.0	300	BD	BD	BD	BD	—
2 Sep	0442	1893.0	348	0.7	BD	BD	BD	527
2 Sep	0501	1896.0	502	0.5	BD	BD	BD	1,000
2 Sep	0521	1900.5	620	0.7	BD	BD	BD	850
2 Sep	0541	1905.0	363	1.5	BD	BD	BD	236
2 Sep	0602	1906.5	397	0.8	BD	BD	BD	509
2 Sep	0622	1908.5	483	1.2	BD	BD	BD	417
2 Sep	0642	1912.0	535	0.9	BD	BD	BD	575
2 Sep	0702	1912.5	328	BD	BD	BD	BD	—
2 Sep	0721	1915.0	599	0.8	BD	BD	BD	798
2 Sep	1402	1923.0	4,660	3.0	BD	BD	BD	1,540
2 Sep	1422	1925.5	1,500	2.0	BD	BD	BD	739
2 Sep	1702	1932.5	430	1.2	BD	BD	BD	361
2 Sep	1722	1934.0	504	0.8	BD	BD	BD	655
2 Sep	2002	1940.0	499	1.4	BD	BD	BD	359
2 Sep	2022	1944.0	713	1.8	BD	BD	BD	401
2 Sep	2302	1949.0	2,590	1.9	BD	BD	BD	1,370
5 Sep	0402	1995.0	1,610	1.0	BD	BD	BD	1,550
5 Sep	0722	2000.5	576	BD	BD	BD	BD	—
5 Sep	1021	2012.0	403	0.6	BD	BD	BD	708
5 Sep	1042	2015.5	642	0.8	BD	BD	BD	782
5 Sep	1102	2021.5	886	0.9	BD	BD	BD	996
5 Sep	1122	2032.0	2,430	1.8	BD	BD	BD	1,340
5 Sep	1200	2038.5	674	BD	BD	BD	BD	—
5 Sep	1221	2040.1	2,490	2.0	BD	BD	BD	1,230
5 Sep	1301	2050.5	756	0.8	BD	BD	BD	933
5 Sep	1321	2055.0	1,490	1.5	BD	BD	BD	1,010
5 Sep	1342	2059.5	864	1.1	BD	BD	BD	823
5 Sep	1402	2062.0	747	0.9	BD	BD	BD	812
5 Sep	1421	2064.0	651	1.0	BD	BD	BD	658
5 Sep	1442	2065.5	417	0.6	BD	BD	BD	652
5 Sep	1529	2072.0	506	0.8	BD	BD	BD	641
5 Sep	1633	2077.5	346	0.9	BD	BD	BD	377
5 Sep	1652	2079.5	365	0.7	BD	BD	BD	515
5 Sep	1742	2083.0	397	0.8	BD	BD	BD	516
5 Sep	1802	2085.5	419	1.1	BD	BD	BD	378
5 Sep	1903	2093.0	515	1.0	BD	BD	BD	510
5 Sep	1922	2094.5	371	1.0	BD	BD	BD	379
5 Sep	1942	2096.0	304	0.8	BD	BD	BD	376
5 Sep	2002	2097.5	377	1.0	BD	BD	BD	366
5 Sep	2022	2100.5	447	1.1	BD	BD	BD	406
5 Sep	2041	2103.0	430	1.1	BD	BD	BD	394
5 Sep	2102	2104.5	302	0.9	BD	BD	BD	351
6 Sep	0422	2119.0	438	1.4	BD	BD	BD	322
6 Sep	0522	2123.0	420	1.0	BD	BD	BD	412
6 Sep	0642	2129.0	359	1.1	BD	BD	BD	329
6 Sep	0702	2131.5	403	1.1	BD	BD	BD	373
6 Sep	0722	2134.5	445	1.2	BD	BD	BD	383
6 Sep	0742	2139.0	600	1.9	BD	BD	BD	316
6 Sep	0801	2143.5	581	2.0	BD	BD	BD	288

Table T18 (continued).

Date (2012)	Time (h)	Depth MSF (m)	Concentration in on-line monitored mud gas (ppmv)					C_1/C_2
			Methane	Ethane	Propane	*iso*-Butane	*n*-Butane	
6 Sep	0821	2147.0	513	1.7	BD	BD	BD	306
6 Sep	0901	2156.0	1,020	2.8	BD	BD	BD	367
6 Sep	0921	2160.0	712	2.4	BD	BD	BD	300
6 Sep	0940	2162.5	746	2.5	0.5	BD	BD	297
6 Sep	1021	2167.0	608	1.8	BD	BD	BD	332
6 Sep	1042	2172.0	739	2.4	0.4	BD	BD	304
6 Sep	1102	2176.5	660	2.0	BD	BD	BD	324
6 Sep	1121	2180.0	505	1.7	BD	BD	BD	292
6 Sep	1140	2185.0	665	2.1	BD	BD	BD	317
6 Sep	1201	2188.5	572	2.2	BD	BD	BD	266
6 Sep	1221	2190.5	480	1.8	BD	BD	BD	274
7 Sep	0401	2208.5	425	1.6	BD	BD	BD	265
7 Sep	0601	2215.0	530	1.7	BD	BD	BD	317
7 Sep	0622	2219.5	542	1.8	BD	BD	BD	301
7 Sep	0641	2220.5	355	1.4	BD	BD	BD	248
7 Sep	0702	2227.0	943	2.7	BD	BD	BD	348
7 Sep	0721	2230.0	435	1.4	BD	BD	BD	309
7 Sep	0800	2234.0	623	2.2	BD	BD	BD	282
7 Sep	0737	2234.0	730	2.5	BD	BD	BD	296
7 Sep	0841	2242.0	636	2.3	BD	BD	BD	279
7 Sep	0902	2249.0	1,080	3.4	BD	BD	BD	314
7 Sep	0922	2259.0	1,400	4.2	BD	BD	BD	332
7 Sep	0941	2263.5	927	3.2	BD	BD	BD	291
7 Sep	1001	2267.5	738	2.1	BD	BD	BD	353
7 Sep	1021	2275.0	1,220	3.8	BD	BD	BD	324
7 Sep	1120	2277.5	1,130	3.5	BD	BD	BD	319
7 Sep	1141	2284.5	1,120	3.4	BD	BD	BD	331
7 Sep	1202	2299.0	1,250	3.7	BD	BD	BD	333
7 Sep	2042	2312.5	398	1.4	BD	BD	BD	286
7 Sep	2101	2316.5	604	1.9	BD	BD	BD	320
7 Sep	2122	2318.5	405	1.3	BD	BD	BD	309
7 Sep	2142	2323.5	781	2.3	BD	BD	BD	338
7 Sep	2202	2329.5	802	2.2	BD	BD	BD	370
7 Sep	2222	2333.5	705	2.2	BD	BD	BD	326
7 Sep	2242	2340.0	940	3.0	BD	BD	BD	310
7 Sep	2350	2349.0	640	2.3	BD	BD	BD	273
8 Sep	0022	2355.0	719	2.8	BD	BD	BD	256
8 Sep	0041	2357.0	603	2.1	BD	BD	BD	290
8 Sep	0102	2361.0	622	2.4	BD	BD	BD	259
8 Sep	0122	2364.5	620	2.5	BD	BD	BD	252
8 Sep	0142	2367.0	530	2.4	BD	BD	BD	220
8 Sep	0202	2369.5	563	2.2	BD	BD	BD	254
8 Sep	0222	2373.0	588	2.5	BD	BD	BD	234
8 Sep	0242	2376.0	673	2.8	BD	BD	BD	238
8 Sep	0322	2382.5	599	2.6	BD	BD	BD	234
8 Sep	0342	2386.0	608	2.9	BD	BD	BD	210
8 Sep	0402	2390.0	689	2.9	BD	BD	BD	238
8 Sep	1202	2414.5	648	2.1	BD	BD	BD	315
8 Sep	1222	2424.5	493	1.7	BD	BD	BD	288
8 Sep	1242	2430.0	644	2.3	BD	BD	BD	286
8 Sep	1322	2432.5	380	1.5	BD	BD	BD	253
8 Sep	1342	2437.0	630	2.5	BD	BD	BD	256
8 Sep	1402	2440.0	566	2.2	BD	BD	BD	261

BD = below detection. — = values cannot be calculated. Time was recorded as ship local time (UTC + 8 h).

Table T19. Concentration of hydrocarbon gases in headspace samples taken from cuttings, Hole C0020A.

Cuttings sample	Depth MSF (m)		Concentration in headspace (ppmv)						Concentration in interstitial water (μM)				
	Top	Bottom	Methane	Ethane	Propane	*iso*-Butane	*n*-Butane	C_1/C_2	Methane	Ethane	Propane	*iso*-Butane	*n*-Butane
337-C0020A-													
25-SMW	646.5	656.5	1130	1.1	BD	1.9	BD	994	146	0.15	BD	0.24	BD
30-SMW	696.5	706.5	1360	1.2	BD	2.4	BD	1170	180	0.15	BD	0.32	BD
35-SMW	746.5	756.5	1480	1.4	BD	1.7	BD	1070	170	0.16	BD	0.20	BD
40-SMW	796.5	806.5	1870	1.7	BD	1.7	BD	1090	199	0.18	BD	0.18	BD
45-SMW	846.5	856.5	2690	1.7	BD	1.7	BD	1580	249	0.16	BD	0.15	BD
56-SMW	896.5	906.5	2760	2.1	BD	1.7	BD	1320	336	0.26	BD	0.21	BD
61-SMW	946.5	956.5	985	0.8	BD	1.5	BD	1290	192	0.15	BD	0.29	BD
66-SMW	996.5	1006.5	2250	2.5	BD	1.6	BD	911	178	0.20	BD	0.13	BD
73-SMW	1046.5	1056.5	2120	2.0	BD	1.4	BD	1060	181	0.17	BD	0.12	BD
81-SMW	1096.5	1106.5	1190	1.2	BD	5.0	BD	994	71.4	0.07	BD	0.30	BD
90-SMW	1196.5	1206.5	173	BD	BD	0.5	BD	—	15.2	BD	BD	0.04	BD
98-SMW	1256.5	1266.5	126	0.4	BD	0.4	BD	312	8.20	0.03	BD	0.03	BD
116-SMW	1296.5	1306.5	149	0.4	BD	2.3	BD	382	13.3	0.03	BD	0.21	BD
122-SMW	1346.5	1356.5	67.1	0.3	BD	2.8	BD	—	23.4	0.11	BD	0.96	BD
124-LMW	1356.5	1366.5	16.0	BD	BD	3.3	BD	—	7.54	BD	BD	1.55	BD
131-SMW	1396.5	1406.5	99.8	0.4	BD	4.3	BD	245	32.3	0.13	BD	1.39	BD
139-LMW	1419.5	1429.5	29.5	BD	BD	3.6	BD	—	11.8	BD	BD	1.42	BD
136-SMW	1446.5	1456.5	39.9	0.4	BD	2.0	BD	96	44.7	0.47	BD	2.29	BD
144-LMW	1481.5	1491.5	9.10	BD	BD	4.0	BD	—	3.23	BD	BD	1.41	BD
153-SMW	1496.5	1506.5	54.3	0.4	BD	4.1	BD	125	4.80	0.04	BD	0.37	BD
158-SMW	1546.5	1556.5	335	2.4	BD	3.0	BD	139	29.9	0.22	BD	0.27	BD
170-SMW	1596.5	1606.5	64.3	1.2	BD	2.8	BD	52	6.76	0.13	BD	0.30	BD
172-LMW	1606.5	1616.5	31.4	BD	BD	3.1	BD	—	12.1	BD	BD	1.21	BD
192-SMW	1646.5	1656.5	587	16.3	0.9	3.6	0.7	36	56.2	1.56	0.09	0.34	0.07
196-LMW	1658.5	1668.5	114	1.4	BD	12.7	BD	84	31.0	0.37	BD	3.43	BD
198-SMW	1696.5	1706.5	680	8.1	0.4	3.4	BD	84	158	1.87	0.08	0.78	BD
205-LMW	1736.5	1746.5	39.9	0.2	BD	5.4	BD	164	13.2	0.08	BD	1.78	BD
207-SMW	1746.5	1756.5	107	1.4	BD	2.6	BD	79	40.1	0.51	BD	0.98	BD
212-SMW	1796.5	1806.5	177	0.8	BD	2.6	BD	217	29.1	0.13	BD	0.43	BD
215-LMW	1820.0	1829.5	4020	3.0	BD	3.3	BD	1330	1420	1.06	BD	1.15	BD
220-SMW	1846.5	1856.5	545	4.6	BD	4.3	BD	117	85.0	0.72	BD	0.67	BD
226-SMW	1896.5	1906.5	75.9	0.7	BD	5.0	BD	108	9.04	0.08	BD	0.60	BD
228-LMW	1919.0	1928.5	3180	2.2	BD	4.9	BD	1450	1060	0.73	BD	1.65	BD
242-SMW	1946.5	1956.5	2430	13.6	1.2	2.3	0.5	178	138	0.77	0.07	0.13	0.03
254-SMW	1996.5	2006.5	170	3.1	0.3	5.4	0.3	54	63.7	1.18	0.10	2.03	0.11
261-SMW	2046.5	2056.5	665	7.8	0.7	13.1	5.4	85	226	2.66	0.24	4.45	1.83
267-SMW	2096.5	2106.5	63.5	2.9	2.0	12.5	6.4	22	20.6	0.95	0.63	4.05	2.08
274-SMW	2146.5	2156.5	46.2	3.9	4.0	8.5	3.2	12	9.17	0.77	0.79	1.69	0.64
285-SMW	2196.5	2206.5	32.6	0.5	0.4	2.3	0.4	61	3.84	0.06	0.05	0.27	0.05
290-SMW	2246.5	2256.5	285	10.9	1.1	3.0	BD	26	78.0	2.99	0.29	0.81	BD
352-SMW	2296.5	2306.5	39.4	4.8	1.1	5.2	0.8	8	11.2	1.36	0.31	1.47	0.24
358-SMW	2346.5	2356.5	230	20.0	2.2	3.3	0.3	11	37.2	3.23	0.35	0.53	0.05
369-SMW	2396.5	2406.5	20.1	1.2	BD	2.0	BD	17	5.23	0.31	BD	0.51	BD
390-SMW	2446.5	2456.5	423	14.5	0.6	2.6	BD	29	53.4	1.83	0.07	0.33	BD
391-SMW	2456.0	2466.0	214	12.7	0.6	3.9	BD	17	16.6	0.98	0.05	0.30	BD

Both concentrations in headspace and interstitial water are reported. The C_1/C_2 ratios were also calculated. SMW = solids taken from mud water, LMW = fluid taken from drilling mud water. BD = below detection. — = values cannot be calculated.

Table T20. Concentration of hydrocarbon gases in headspace samples and void gases taken from sediment cores, Hole C0020A. (Continued on next page.)

Core, section, interval (cm)	Depth CSF-B (m)	Concentration in headspace samples (ppmv)						Concentration in interstitial water (μM)					
		Methane	Ethane	Propane	*iso*-Butane	*n*-Butane	C_1/C_2	Methane	Ethane	Propane	*iso*-Butane	*n*-Butane	
337-C0020A-													
1R-1, 123–127	1277.75	845	1.28	BD	0.82	BD	661	473	0.71	BD	0.46	BD	
2R-1, 126–140	1287.38	1,050	119	2.86	4.86	5.40	8.89	1,730	195	4.69	7.97	8.86	
3R-2, 71–75	1371.97	1,980	2.38	BD	3.22	0.61	830	1,500	1.80	BD	2.44	0.46	
4R-2, 99–103	1377.43	2,290	2.36	BD	2.46	BD	969	1,340	1.38	BD	1.44	BD	
5R-2, 39–43	1491.82	13,400	8.12	BD	2.07	BD	1,650	2,960	1.79	BD	0.46	BD	
6R-1, 136.5–140.5	1496.39	18,500	11.0	BD	0.88	BD	1,680	5,680	3.38	BD	0.27	BD	
8L-3, 79.5–80	1605.96	1,940	4.80	BD	BD	BD	404	970	2.40	BD	BD	BD	
8L-5, 19.5–20	1607.36	2,830	7.25	BD	0.92	BD	391	1,570	4.01	BD	0.51	BD	
8L-9, 16–17	1611.34	5,580	21.3	0.34	1.30	0.32	262	2,550	9.74	0.15	0.60	0.14	
9R-1, 139–143	1626.91	621	3.57	BD	0.40	BD	174	326	1.87	BD	0.21	BD	
10R-1, 137–141	1630.89	2,150	15.4	0.42	1.52	0.62	140	1,410	10.1	0.28	1.00	0.41	
11R-1, 134–138	1738.86	2,670	3.46	BD	0.72	BD	771	1,290	1.68	BD	0.35	BD	
11R-4, 142–146	1742.48	3,010	9.07	BD	1.23	BD	332	2,600	7.83	BD	1.06	BD	
12R-1, 139.5–143.5	1748.42	12,500	19.0	BD	0.62	BD	658	2,890	4.40	BD	0.14	BD	
12R-7, 0–4	1754.56	2,370	8.03	BD	0.90	BD	295	1,320	4.45	BD	0.50	BD	
13R-1, 140–144	1757.92	1,720	5.35	BD	0.99	BD	322	1,370	4.25	BD	0.79	BD	
13R-7, 137–141	1764.98	1,410	5.63	0.33	1.13	BD	250	919	3.67	0.22	0.74	BD	
14R-1, 137–141	1821.39	2,190	6.94	BD	1.10	BD	316	2,940	9.29	BD	1.47	BD	
14R-5, 23–27	1824.09	2,760	11.0	0.65	0.70	BD	251	953	3.79	0.22	0.24	BD	
14R-5, 91.5–95.5	1825.79	1,590	1.94	BD	BD	BD	820	771	0.94	BD	BD	BD	
15R-1, 135.5–139.5	1920.38	158,000	97.1	2.18	1.77	0.87	1,630	271,000	167	3.75	3.04	1.50	
15R-6, 136–140	1925.44	4,570	13.0	0.65	0.39	BD	353	3,010	8.52	0.43	0.25	BD	
16R-1, 97–101	1929.49	712	1.63	BD	1.13	BD	437	607	1.39	BD	0.96	BD	
16R-2, 73–77	1930.26	572	11.4	0.53	2.53	1.65	50.3	211	4.20	0.20	0.93	0.61	
16R-3, 97–101	1931.27	1,260	5.59	BD	4.37	1.56	225	970	4.32	BD	3.38	1.20	
16R-4, 98–102	1932.29	1,560	1.86	BD	1.12	BD	840	644	0.77	BD	0.46	BD	
17R-1, 137–141	1937.39	2,260	2.75	BD	0.36	BD	824	1,220	1.49	BD	0.20	BD	
17R-4, 137–141	1940.09	1,130	13.0	0.58	0.65	0.60	86.4	397	4.59	0.20	0.23	0.21	
17R-6, 62–66	1941.51	262	0.30	BD	BD	BD	880	257	0.29	BD	BD	BD	
17R-8, 116.5–120.5	1944.12	440	3.53	BD	0.39	0.45	125	184	1.48	BD	0.16	0.19	
18R-1, 111–115	1946.63	219,000	198	5.53	1.59	0.48	1,100	84,200	76.4	2.13	0.61	0.18	
19R-1, 137–141	1951.39	24,600	66.8	2.65	1.49	0.34	368	30,800	83.8	3.33	1.86	0.43	
19R-3, 137–141	1953.56	823	0.81	BD	0.42	BD	1,010	290	0.29	BD	0.15	BD	
19R-4, 86–90	1954.46	1,030	2.81	0.27	1.48	0.26	366	449	1.23	0.12	0.64	0.12	
19R-7, 137–141	1958.48	1,190	26.1	2.04	0.88	0.27	45.4	1,690	37.1	2.90	1.25	0.38	
20R-2, 62–66	1961.55	5,270	7.35	0.38	0.41	BD	717	1,680	2.34	0.12	0.13	BD	
20R-6, 47–51	1965.67	2,810	1.60	BD	BD	BD	1,760	2,000	1.14	BD	BD	BD	
21R-1, 138–142	1970.40	3,650	9.98	0.70	1.37	0.39	366	1,830	5.02	0.35	0.69	0.19	
22R-4, 0–4	1977.21	1,340	1.42	BD	0.32	BD	948	708	0.75	BD	0.17	BD	
23R-1, 92–96	1982.44	18,600	102	4.42	1.34	0.59	183	12,100	66.0	2.87	0.87	0.39	
23R-3, 136–140	1985.24	3,230	19.0	1.13	1.05	BD	170	1,680	9.88	0.59	0.55	BD	
23R-4, 96.5–100.5	1986.24	19,800	119	5.92	2.55	1.37	167	7,870	47.2	2.35	1.01	0.54	
23R-5, 101–105	1987.29	3,210	24.3	1.64	2.45	0.90	132	2,120	16.0	1.08	1.62	0.60	
23R-8, 0–4	1989.50	817	8.27	3.06	3.21	3.28	98.8	551	5.58	2.06	2.16	2.21	
24R-1, 97–101	1991.99	339	0.62	BD	2.54	BD	546	115	0.21	BD	0.86	BD	
24R-3, 71.5–75.5	1993.95	15,000	61.7	2.83	1.51	0.28	244	3,700	15.2	0.69	0.37	0.07	
25R-1, 137–141	1996.39	1,040	16.9	1.59	2.45	1.61	61.3	1,110	18.1	1.70	2.62	1.72	
25R-2, 137–141	1997.80	301,000	460	11.1	3.63	1.22	654	194,000	297	7.14	2.34	0.79	

Table T20 (continued).

Core, section, interval (cm)	Depth CSF-B (m)	Concentration in headspace samples (ppmv)						Concentration in interstitial water (μM)				
		Methane	Ethane	Propane	*iso*-Butane	*n*-Butane	C_1/C_2	Methane	Ethane	Propane	*iso*-Butane	*n*-Butane
25R-3, 137–141	1999.21	1,640	18.5	1.20	1.11	0.47	88.5	1,440	16.2	1.05	0.97	0.41
25R-5, 136.5–140.5	2001.38	198,000	348	8.32	2.81	0.92	570	120,000	210	5.03	1.70	0.55
26R-2, 0–4	2111.41	14,900	50.4	11.9	3.68	4.87	296	10,900	36.7	8.65	2.68	3.55
26R-4, 136–140	2114.90	34,300	129	27.2	8.06	10.8	266	12,200	45.6	9.63	2.85	3.82
26R-7, 0–4	2117.11	8,070	46.5	12.1	4.95	6.51	174	6,040	34.8	9.06	3.70	4.87
27R-2, 0–4	2201.02	7,100	35.0	3.39	1.77	1.41	203	13,200	65.3	6.32	3.30	2.64
27R-3, 140–144	2203.22	12,400	60.7	5.90	2.76	3.04	205	11,700	57.1	5.55	2.60	2.86
28R-2, 137–141	2302.80	1,640	11.8	0.54	0.35	BD	139	1,290	9.33	0.43	0.28	BD
28R-5, 137–141	2306.38	2,190	39.7	1.93	BD	BD	55.1	1,690	30.7	1.49	BD	BD
29R-1, 136.5–140.5	2401.39	15.3	0.86	BD	0.48	BD	17.9	6.23	0.35	BD	0.19	BD
29R-3, 134–137	2403.52	2,330	12.9	0.47	0.85	BD	181	2,250	12.5	0.46	0.82	BD
29R-7, 136.5–140.5	2408.14	2,660	18.0	1.03	1.45	BD	148	851	5.75	0.33	0.47	BD
30R-3, 0–4	2448.70	73,400	810	24.1	0.83	1.03	90.7	100,000	1,100	32.8	1.13	1.40
30R-4, 0–4	2449.72	2,020	26.0	1.24	0.62	BD	77.6	1,870	24.1	1.15	0.58	BD
32R-1, 141–145	2457.93	4,670	19.3	0.74	0.52	BD	242	3,550	14.7	0.57	0.39	BD
32R-6, 67–71	2463.63	7,240	108	8.26	1.29	0.98	66.8	4,060	60.8	4.63	0.72	0.55
32R-10, 0–10	2466.53	548	6.66	1.03	7.69	5.03	82.3	326	3.97	0.61	4.58	3.00
Concentration in void gas samples (ppmv):												
22R-3 59–59	1976.41	751,000	2,330	10.3	4.20	2.70	322					
22R-4 17–17	1977.36	577,000	1,560	4.60	4.00	3.80	371					
22R-5 32–32	1977.96	832,000	2,470	6.20	5.80	1.50	337					
22R-5 77–77	1978.41	840,000	2,570	6.30	5.80	2.00	326					

BD = below detection.

Table T21. Background control on the hydrocarbon gas content of drilling mud entering Hole C0020A.

Mud tank sample	Date (2012)	Time (h)	Sample weight (g)	Concentration in headspace (ppmv)						
				Methane	Ethane	Propane	*iso*-Butane	*n*-Butane	Propylene	Ethylene
337-C0020A-										
106-LMT	26 Aug	1235	5.02	4.9	BD	BD	3.6	BD	BD	BD
107-LMT	26 Aug	1235	5.23	5.2	BD	BD	3.1	BD	BD	BD
108-LMT	26 Aug	1236	4.94	4.6	3.6	BD	4.7	BD	BD	BD
109-LMT	26 Aug	1236	4.90	4.6	3.0	BD	5.4	BD	BD	BD
159-LMT	27 Aug	0610	5.33	10.0	BD	BD	3.0	BD	BD	BD
165-LMT	28 Aug	0523	5.06	5.7	BD	BD	3.6	BD	BD	BD
167-LMT	31 Aug	0343	5.25	9.8	BD	BD	2.9	BD	BD	BD
185-LMT	31 Aug	0438	4.71	10.8	2.3	BD	4.2	BD	BD	BD
214-LMT	1 Sep	0551	5.18	90.2	0.2	BD	4.2	BD	BD	BD
229-LMT	2 Sep	0611	4.94	47.6	BD	BD	8.0	11.5	BD	0.3
237-LMT	3 Sep	0408	5.06	55.8	BD	BD	2.8	BD	BD	BD
239-LMT	4 Sep	0557	5.04	12.4	BD	BD	4.8	BD	BD	BD
256-LMT	5 Sep	0603	4.80	60.8	BD	BD	5.9	BD	BD	BD
348-LMT	7 Sep	0450	4.77	31.6	BD	BD	5.2	BD	BD	BD

The composition of hydrocarbon gases was analyzed in samples taken from the drilling mud tank using the headspace technique, ~5 mL of drilling mud and 20 mL headspace vials. LMT = fresh mud water collected at mud tank. BD = below detection. Time was recorded as ship local time (UTC + 8 h).

Table T22. Concentration of oxygen, argon, nitrogen, carbon monoxide, and hydrogen in mud gas in Hole C0020A, analyzed during on-line mud-gas monitoring using the process gas mass spectrometer (PGMS).

Depth MSF (m)	Concentration of on-line monitored mud gas (%)				
	Oxygen	Argon	Nitrogen	Carbon monoxide	Hydrogen
1005.5	20.8	0.93	78.1	2.4E–03	2.0
1006	19.8	0.87	70.6	6.4E–04	1.2
1006.5	19.7	0.87	69.6	7.0E–04	1.1
1007	20.0	0.87	69.7	6.2E–04	1.2
1007.5	19.8	0.87	70.8	4.4E–04	1.2
1008	19.8	0.87	70.4	3.4E–04	1.1
1008.5	19.6	0.88	70.1	6.1E–04	1.1
1009	19.8	0.86	70.3	4.7E–04	1.1
1009.5	19.5	0.86	69.2	3.8E–04	1.2
1010	20.0	0.86	70.4	7.3E–04	1.1
1010.5	19.7	0.87	70.1	3.9E–04	1.2
1011	19.9	0.86	69.9	6.0E–04	1.2
1011.5	19.6	0.87	70.9	6.9E–04	1.1
1012	19.5	0.86	68.9	6.9E–04	1.3
1012.5	19.8	0.86	70.5	8.4E–04	1.1
1013	19.8	0.87	70.0	1.0E–03	1.2
1013.5	19.8	0.87	71.2	6.3E–04	1.1
1014	19.7	0.86	71.4	1.1E–03	1.2
1014.5	19.8	0.88	70.0	8.7E–04	1.1
1016	19.7	0.88	71.6	1.2E–03	1.2
1016.5	19.7	0.87	70.5	1.1E–03	1.1
1017	19.6	0.86	71.1	9.7E–04	1.0
1017.5	19.7	0.87	70.6	1.1E–03	1.1
1018	19.7	0.86	71.3	1.2E–03	1.1
1018.5	19.6	0.88	71.1	1.2E–03	1.1
1019	19.7	0.86	71.4	1.2E–03	1.1
1019.5	19.9	0.86	71.0	1.3E–03	1.1
1020	19.6	0.87	70.7	1.2E–03	1.1
1020.5	19.6	0.88	70.3	1.3E–03	1.2
1021	19.7	0.86	71.3	1.4E–03	1.1
1021.5	19.8	0.87	71.0	9.5E–04	1.2
1022	19.9	0.88	70.6	5.0E–04	1.2
1022.5	19.8	0.87	70.4	4.2E–04	1.1
1023	19.8	0.87	70.2	4.7E–04	1.1
1023.5	19.9	0.89	70.6	4.1E–04	1.2
1024	19.9	0.88	69.9	5.8E–04	1.1
1024.5	19.8	0.87	71.0	7.3E–04	1.2
1025	19.8	0.89	70.6	5.6E–04	1.3
1025.5	20.1	0.87	71.7	5.2E–04	1.3
1026	19.8	0.86	70.8	4.0E–04	1.2
1026.5	19.9	0.89	70.7	6.4E–04	1.2
1027	19.8	0.87	70.3	7.3E–04	1.1
1027.5	20.0	0.88	70.1	6.9E–04	1.3
1028	20.0	0.88	70.6	6.1E–04	1.1
1028.5	19.9	0.86	70.3	4.9E–04	1.2
1029	19.9	0.87	70.7	7.8E–04	1.1
1029.5	19.8	0.88	70.8	7.3E–04	1.2
1030	19.7	0.86	70.5	6.8E–04	1.2
1030.5	19.7	0.87	71.7	7.6E–04	1.1
1031	19.9	0.88	71.0	8.0E–04	1.2
1031.5	19.9	0.87	70.5	7.1E–04	1.2
1032	19.7	0.87	70.8	5.8E–04	1.2
1032.5	19.6	0.89	70.8	6.4E–04	1.2
1034.5	19.8	0.87	71.2	7.9E–04	1.2
1035	19.7	0.89	71.1	8.7E–04	1.1
1035.5	19.8	0.86	71.3	8.3E–04	1.2
1044	19.9	0.85	72.9	6.1E–04	1.2
1044.5	19.6	0.88	71.0	8.9E–04	1.2
1045	19.7	0.89	71.2	1.0E–03	1.1
1045.5	19.7	0.87	70.3	1.0E–03	1.2
1046	19.8	0.87	71.1	9.2E–04	1.2

On-line monitoring of mud gas by PGMS only started at 1005.5 m MSF because of insufficient gas flow to the instrument during the first day of mud-gas monitoring (15 August 2012). Only a portion of this table appears here. The complete table is available in **ASCII.**

Table T23. Concentration of nitrogen, oxygen, argon, and carbon monoxide in mud gas in Hole C0020A, analyzed during on-line mud-gas monitoring using GC-TCD.

Date (2012)	Time (h)	Concentration in mud gas (%)			
		Nitrogen	Oxygen	Argon	Carbon monoxide
15 Aug	2309	77.1	19.9	0.925	2.90E–03
21 Aug	2334	79.0	21.2	0.942	
26 Aug	1646	79.5	21.1	0.947	
27 Aug	1429	79.5	20.9	0.946	2.97E–03
2 Sep	0005	79.7	21.0	0.950	3.28E–03
5 Sep	1505	80.6	21.0	0.960	2.74E–03
5 Sep	1609	79.3	20.8	0.944	3.27E–03
7 Sep	2326	79.2	21.0	0.943	

Time was recorded in ship local time (UTC + 8 h).

Table T24. Concentrations of molecular hydrogen and carbon monoxide in interstitial water of sediment cores of Hole C0020A, determined by the extraction method.

Core, section, interval (cm)	Depth CSF-B (m)	H_2 (μM)	CO (nM)
337-C0020A-			
1R-1, 123–127	1278	0.54	6.00
2R-1, 136–140	1287	3.23	151
2R-2, 136–139	1289	2.82	71.0
3R-2, 71–75	1372	6.99	181
4R-2, 99–103	1377	0.40	101
5R-2, 39–43	1492	0.57	36.0
6R-1, 136.5–140.5	1496	140	114
6R-3, 137–141	1499	0.63	165
8R-3, 79.5–80	1606	3.88	41.0
8R-5, 19.5–20	1607	20.0	33.0
8R-9, 15–17	1611	1.43	221
9R-1, 139–143	1627	2.73	44.0
10R-1, 137–141	1631	27.9	216
11R-1, 134–138	1739	201	248
11R-4, 142–146	1742	174	76.0
12R-1, 139.5–143.5	1748	3.33	15.0
12R-7, 0–4	1755	0.75	19.0
13R-1, 140–144	1758	0.46	3.00
13R-7, 137–141	1765	1.32	51.0
14R-1, 136–140	1821	3.51	268
14R-4, 23–27	1824	0.44	88.0
14R-5, 91.5–95.5	1826	1.27	362
15R-1, 135.5–139.5	1920	6.30	101,000
15R-6, 136–140	1925	0.62	879
16R-1, 97–101	1929	0.95	258
16R-2, 73–77	1930	1.58	919
16R-3, 97–101	1931	2.76	1,420
17R-1, 137–141	1937	1.41	502
17R-4, 137–141	1940	3.80	4,620
17R-6, 62–66	1942	7.21	206
17R-8, 116.5–120.5	1944	1.14	575
18R-1, 111–115	1947	0.97	1,830
19R-1, 137–141	1951	17.7	2,310
19R-3, 137–141	1953	0.48	175
19R-4, 86–90	1954	1.27	379
19R-7, 137–141	1958	562	7,840
20R-2, 62–66	1962	0.97	162
20R-6, 47–51	1966	5.24	35.0
21R-1, 138–142	1970	9.94	72.0
23R-3, 136–140	1985	3.42	329
23R-1, 92–96	1982	3.00	280
23R-4, 96.5–100.5	1986	460	1,130
23R-5, 101–105	1987	1.98	969
23R-8, 0–4	1989	6.26	779
24R-1, 97–101	1995	3.15	494
24R-3, 71.5–75.5	1994	123	926
25R-1, 137–141	1996	322	1,280
25R-2, 137–141	1998	19.9	9,450
25R-3, 137–141	1999	110	1,420
25R-5, 156.5–140.5	2001	2.49	160
26R-2, 0–4	2111	465	128
26R-4, 136–140	2115	24.4	70.0
27R-2, 0–4	2201	46.9	15,400
27R-3, 140–144	2203	30.8	10,600
28R-2, 137–141	2303	1.58	8,410
28R-5, 137–141	2306	24.3	5,740
29R-1, 136.5–140.5	2401	3.55	1,380
29R-3, 134–137	2404	4.60	24,200
29R-7, 136.5–140.5	2408	5.43	377
30R-3, 0–4	2449	1.25	90,700
30R-4, 0–4	2450	6.19	15,500
32R-1, 141–145	2458	78.0	6,900
32R-6, 67–71	2463	95.7	27,000

Table T25. Concentrations of molecular hydrogen and carbon monoxide in drilling sand that filled the void space between sediment cores and core liners in Hole C0020A, determined by the extraction method.

Core	H_2 (μM)	CO (nM)
337-C0020A-		
1R	1.62	198
1R	1.15	176
2R	1.28	229
4R	0.70	56
5R	1.79	90
6R	0.42	47
8L	74.6	19
9R	1.54	104
10R	5.67	257
11R	0.78	4
12R	0.63	43
13R	0.33	53
14R	3.83	105
15R	3.30	298
16R	7.65	171
17R	3.26	1,410
18R	0.89	548
22R	0.79	1,010
19R	2.41	239
20R	4.84	370
21R	3.09	1,120
27R	0.79	518
28R	1.37	101
29R	6.93	35
30R	1.07	15

Table T26. Concentrations of molecular hydrogen and carbon monoxide in interstitial water of sediment cores of Hole C0020A, determined by the incubation method. (Continued on next page.)

Core, section, interval (cm)	Depth CSF-B (m)	*t* = 0 (ppmv)		*t* = 1 (ppmv)		*t* = 2 (ppmv)	
		H_2	CO	H_2	CO	H_2	CO
337-C0020A-							
1R-1, 123–127	1278	0.4	0.1	35.5	0.30	51.6	1.20
2R-1, 136–140	1287	0.8	1.6	14.8	14.8	22.5	1.20
2R-2, 136–139	1289	0.9	BD	12.3	0.50	1040	1.90
3R-2, 71–75	1372	2.3	0.8	46.5	0.60	292	8.10
4R-2, 99–103	1377	1.2	0.0	4.00	0.60	1790	1.90
5R-2, 39–43	1492	2.0	0.0	24.6	0.70	783	5.50
6R-1, 136.5–140.5	1496	0.8	0.1	260	8.10	447	12.9
6R-3, 137–141	1499	2.5	0.3	25.2	1.40	77.1	3.60
8R-3, 79.5–80	1606	1.0	0.1	13.1	1.60	6.60	1.80
8R-5, 19.5–20	1607	0.4	BD	8.30	1.70	21.5	1.70
8R-9, 15–17	1611	0.7	0.2	2.40	1.40	0.40	0.70
9R-1, 139–143	1627	0.3	BD	88.2	0.40	77.7	0.00
10R-1, 137–141	1631	5.1	1.9	761	0.90	473	1.00
11R-1, 134–138	1739	2.0	0.2	2250	0.10	2420	0.50
11R-4, 142–146	1742	2.6	0.0	1080	2.20	1480	2.10
12R-1, 139.5–143.5	1748	2.7	BD	460	3.80	439	4.30
12R-7, 0–4	1755	1.3	0.0	486	14.5	549	15.3
13R-1, 140–144	1758	2.6	0.3	107	0.70	98.4	0.70
13R-7, 137–141	1765	1.6	0.0	41.8	0.30	39.1	1.00
14R-1, 136–140	1821	1.5	2.0	510	1.40	219	1.20
14R-4, 23–27	1824	1.5	0.9	28.6	0.10	1.80	BD
14R-5, 91.5–95.5	1826	0.7	0.1	2560	4.70	2310	1.00
15R-1, 135.5–139.5	1920	BD	2.7	4.40	19.8	25.9	19.0
15R-6, 136–140	1925	0.4	2.0	1370	5.80	1725	3.60
16R-1, 97–101	1929	1.0	0.0	1.50	2.20	14.9	3.60
16R-2, 73–77	1930	1.1	0.8	BD	4.00	6.80	3.50
16R-3, 97–101	1931	1.1	2.0	208	6.00	1060	4.60
16R-4, 98–102	1932	1.2	0.1	13.7	1.10	6.80	3.50
17R-1, 137–141	1937	1.7	0.8	18.2	2.20	1070	2.50
17R-4, 137–141	1940	0.2	1.1	31.7	7.60	38.1	6.70
17R-6, 62–66	1942	1.6	0.1	50.6	1.40	149	1.20

Table T26 (continued).

Core, section, interval (cm)	Depth CSF-B (m)	t = 0 (ppmv)		t = 1 (ppmv)		t = 2 (ppmv)	
		H_2	CO	H_2	CO	H_2	CO
17R-8, 116.5–120.5	1944	0.4	BD	8.00	2.70	14.7	1.00
18R-1, 111–115	1947	2.7	18.4	68.2	58.8	65.9	45.3
19R-1, 137–141	1951	1.9	0.1	4.90	2.80	2.80	0.50
19R-3, 137–141	1953	0.3	0.0	74.7	2.00	171	2.30
19R-4, 86–90	1954	BD	0.0	31.7	2.10	45.3	0.70
19R-7, 137–141	1958	5.5	1.0	115	46.9	69.1	33.9
20R-2, 62–66	1962	2.5	0.0	7.30	0.40	3.70	0.20
20R-6, 47–51	1966	0.4	0.1	5.10	0.10	1.60	0.00
21R-1, 138–142	1970	BD	0.0	72.6	0.80	61.5	0.40
22R-4, 0–4	1978	BD	0.0	236	3.30	1150	6.60
23R-1, 92–96	1982	0.4	0.4	54.4	13.8	61.9	6.40
23R-3, 136–140	1985	BD	0.1	35.8	16.8	105	15.3
23R-4, 96.5–100.5	1986	BD	0.7	80.8	3.20	66.4	0.40
23R-8, 0–4	1989	BD	0.1	62.9	10.2	202	7.60
24R-1, 97–101	1995	1.1	0.1	10.7	3.80	1450	3.40
25R-1, 137–141	1996	BD	0.8	264	17.6	426	1.50
25R-2, 137–141	1998	BD	2.6	10.2	68.3	82.4	39.9
25R-3, 137–141	1999	0.1	0.4	77.8	11.1	49.3	3.60
25R-5, 156.5–140.5	2001	BD	5.0	149	95.6	378	66.6
26R-2, 0–4	2111	1.0	0.3	876	1.50	237	1.50
26R-4, 136–140	2115	2.2	0.3	306	1.10	6.80	0.00
26R-7, 0–4	2117	0.1	0.1	1310	4.80	1430	15.3
27R-2, 0–4	2201	1.1	BD	76.8	1.50	175	1.10
27R-3, 140–144	2203	9.0	0.2	6.40	0.20	6.50	0.40
28R-2, 137–141	2303	1.1	0.0	824	10.0	1050	22.1
28R-5, 137–141	2306	6.4	0.2	77.9	1.90	77.5	9.10
29R-1, 136.5–140.5	2401	3.0	0.0	41.6	0.70	62.7	BD
29R-3, 134–137	2404	2.4	0.2	137	3.10	3170	12.5
29R-7, 136.5–140.5	2408	0.3	0.0	54.8	0.50	53.5	1.80
30R-3, 0–4	2449	0.7	1.6	1.90	0.20	0.60	BD
30R-4, 0–4	2450	0.7	0.0	27.8	0.80	30.8	1.10
32R-1, 141–145	2458	0.2	0.1	2200	19.8	1610	11.8
32R-6, 67–71	2463	0.7	0.0	70.7	0.00	256	11.7
32R-1, 141–145 control	2458	BD	BD	1520	12.6	3060	19.8
32R-6, 67–71 control	2463	BD	0.0	259	18.0	125	13.9

BD = below detection.

Table T27. Radon data, Site C0020.

Date (2012)	Time (h)	^{222}Rn (Bq/m^3)
20 Aug	0120	—
20 Aug	0130	7
20 Aug	0140	9
20 Aug	0150	2
20 Aug	0200	12
20 Aug	0210	4
20 Aug	0220	4
20 Aug	0230	7
20 Aug	0240	5
20 Aug	0250	17
20 Aug	0300	16
20 Aug	0310	7
20 Aug	0320	21
20 Aug	0330	6
20 Aug	0340	21
20 Aug	0350	18
20 Aug	0400	9
20 Aug	0410	0
20 Aug	0420	7
20 Aug	0430	7
20 Aug	0440	14
20 Aug	0450	0
20 Aug	0500	11
20 Aug	0510	4
20 Aug	0520	9
20 Aug	0530	0
20 Aug	0540	8
20 Aug	0550	0
20 Aug	0600	11
20 Aug	0610	17
20 Aug	0620	4
20 Aug	0630	6
20 Aug	0640	9
20 Aug	0650	8
20 Aug	0700	5
20 Aug	0710	14
20 Aug	0720	7
20 Aug	0730	5
20 Aug	0740	8
20 Aug	0750	3
20 Aug	0800	3
20 Aug	0810	4
20 Aug	0820	2
20 Aug	0830	9
20 Aug	0840	14
20 Aug	0850	22
20 Aug	0900	11
20 Aug	0910	4
20 Aug	0920	1
20 Aug	0930	4
20 Aug	0940	14
20 Aug	0950	6
20 Aug	1000	7
20 Aug	1010	9
20 Aug	1020	7
20 Aug	1030	2
20 Aug	1040	2
20 Aug	1050	2
20 Aug	1100	5
20 Aug	1110	5
20 Aug	1120	26
20 Aug	1130	0
20 Aug	1140	3
20 Aug	1150	0
20 Aug	1200	0
20 Aug	1210	12

Time is UTC + 1 h. — = no data. Only a portion of this table appears here. The complete table is available in **ASCII.**

Table T28. Concentrations of methane, ethane, propane, *n*-butane, hydrogen, and carbon monoxide together with C_1/C_2 ratios in fluid samples obtained from Hole C0020A by DFA.

Sampling bottle	Depth WRF (m)	Depth WMSF (m)	CH_4 (mM)	C_2H_6 (μM)	C_3H_8 (nM)	*n*-C_4H_{10} (nM)	C_1/C_2	H_2 (μM)	CO (nM)
1.06	2488.0	1279.5	32.4	10.8			3000	10.6	1150
1.05	2697.8	1489.3	19.4	9.30	476	150	2090	493	6700
1.04	3016.5	1808.0	30.9	19.0	143		1630	130	3020
1.03	3052.5	1844.0	19.9	9.58		123	2080	35.6	857
1.02	3110.0	1901.5	17.3	6.50	60		2660	12.6	919
1.01	3186.5	1978.0	39.6	17.4		337	2280	12.6	2310

Table T29. Contents of total carbon (TC), carbonate, inorganic carbon, total organic carbon (TOC), total nitrogen (TN), total sulfur (TS), and atomic TOC/TN ratio in the core samples, Hole C0020A.

Core, section, interval (cm)	Depth CSF-B (m) Top	Depth CSF-B (m) Bottom	Lithology	Inorganic carbon (wt%)	$CaCO_3$ (wt%)	TN (wt%)	TC (wt%)	TS (wt%)	TOC (wt%)	TOC/TN (molar ratio)
337-C0020A-										
1R-2, 65–81	1278.4	1278.6	Sandstone	0.2	1.5	0.0	0.6	0.0	0.4	52
2R-2, 93.5–94	1288.3	1288.3	Coal clast	0.3	2.4	0.5	25	0.7	24	57
2R-3, 60–81	1289.4	1289.6	Sandstone	0.0	0.3	0.0	0.3	0.1	0.3	17
2R-4, 4–5.5	1289.6	1289.7	Sandstone	1.6	14	0.0	1.9	0.7	0.3	11
3R-3, 60–77	1372.6	1372.8	Siltstone	0.0	0.2	0.0	0.6	0.8	0.6	15
4R-3, 64–77	1378.1	1378.2	Sandstone	0.0	0.1	0.0	0.1	0.1	0.1	5
5R-3, 24–39	1492.1	1492.2	Sandstone	BD	BD	0.0	0.3	0.9	0.3	18
6R-2, 0–15	1496.4	1496.6	Sandstone	0.0	0.1	0.0	0.3	0.6	0.3	11
7R-1, 53–65	1599.5	1599.7	Shale	0.0	0.3	0.1	3.3	0.8	3.2	36
8L–5, 20–35	1607.4	1607.5	Shale	0.1	0.4	0.0	0.1	0.1	0.1	3
8L–9, 0–16	1611.2	1611.3	Siltstone	BD	BD	0.1	0.8	1.2	0.8	13
9R-4, 0–20	1628.4	1628.6	Shale	BD	BD	0.1	1.0	1.4	1.0	13
10R-2, 53–70	1631.4	1631.6	Shale	0.0	0.3	0.1	2.2	0.9	2.2	29
11R-3, 0–18	1739.6	1739.8	Sandstone	0.0	0.3	0.0	0.3	1.0	0.3	12
11R-5, 58–75	1743.1	1743.3	Siltstone	0.1	0.8	0.0	0.2	0.2	0.1	3
12R-6, 39–44	1753.8	1753.9	Siltstone	6.3	52	0.0	6.3	0.0	0.1	4
12R-7, 15–30	1754.7	1754.8	Sandstone	0.3	2.2	0.0	0.4	0.6	0.1	4
13R-2, 44–59	1758.4	1758.5	Sandstone	0.2	2.0	0.0	0.4	0.7	0.1	6
13R-8, 60–77	1765.6	1765.8	Sandstone	0.2	1.8	0.0	0.4	0.9	0.2	7
14R-2, 105–120	1822.5	1822.6	Sandstone	0.1	0.9	0.1	0.9	1.0	0.8	18
15R-2, 0–17	1920.4	1920.6	Coal	0.0	0.0	0.9	45	0.7	45	59
15R-5, 0–21	1923.6	1923.8	Coaly shale	0.0	0.0	0.1	3.4	0.3	3.4	40
15R-7, 33–41	1925.8	1925.9	Sandstone	BD	BD	0.0	0.4	0.2	0.4	18
16R-2, 0–18	1929.5	1929.7	Sandstone	0.1	1.0	0.0	0.3	0.2	0.2	16
17R-1, 45–60	1936.5	1936.6	Shale	0.2	1.9	0.1	1.9	0.1	1.7	29
17R-4, 85–95	1939.6	1939.7	Sandstone	0.0	0.2	0.0	0.1	0.1	0.1	6
17R-9, 10–25	1944.2	1944.4	Sand	0.0	0.3	0.0	0.1	0.1	0.1	5
18R-1, 105–115	1946.6	1946.7	Coal	0.0	0.1	0.8	41	0.5	41	60
19R-1, 115–141	1951.2	1951.4	Shale	0.1	0.7	0.1	1.3	0.2	1.2	28
19R-5, 0–27	1954.5	1954.8	Cemented sandstone	5.1	42	0.0	5.2	0.0	0.2	12
19R-8, 60–77	1959.1	1959.3	Sandstone	0.0	0.1	0.0	0.1	0.2	0.1	7
19R-9, 0–20	1959.3	1959.5	Sandstone	0.0	0.1	0.0	0.1	0.2	0.1	5
20R-3, 0–13	1961.6	1961.7	Siltstone	0.1	0.7	0.0	0.4	0.3	0.3	9
20R-7, 62–76	1966.3	1966.5	Sand	0.2	1.4	0.0	0.3	0.1	0.1	5
21R-4, 32–42	1971.7	1971.8	Sand	0.4	3.4	0.0	0.9	0.1	0.5	14
23R-8, 0–15	1989.5	1989.6	Siltstone	0.5	3.8	0.0	1.2	0.0	0.7	27
24R-3, 55–65	1993.8	1993.9	Coal	0.0	0.1	1.2	50	0.3	50	47
25R-1, 75–91	1995.8	1995.9	Cemented sandstone	4.5	37	0.0	4.6	BD	0.2	11
25R-2, 70–85	1997.1	1997.3	Coal	0.0	0.1	0.8	45	0.3	45	65
25R-3, 120–141	1999.0	1999.2	Coaly shale	0.3	2.6	0.1	1.3	0.1	1.0	18
25R-4, 0–15	1999.2	1999.4	Shale	0.2	1.8	0.1	1.4	0.1	1.2	19
26R-2, 0–9	2111.4	2111.5	Shale	0.2	1.4	0.1	0.8	1.2	0.6	11
26R-6, 0–15	2115.7	2115.8	Shale	0.1	0.6	0.1	0.8	1.1	0.7	12
26R-7, 84–101	2117.9	2118.1	Shale	0.1	0.5	0.1	0.7	1.1	0.7	11
27R-2, 61–80	2201.6	2201.8	Siltstone	0.1	0.8	0.1	0.7	0.7	0.6	10
28R-3, 0–24	2302.8	2303.1	Siltstone/Siderite?	0.2	1.3	0.1	0.6	0.1	0.4	8
28R-6, 30–45	2306.7	2306.9	Sandstone/Siderite?	0.3	2.5	0.1	0.9	0.1	0.6	9
29R-2, 17.5–27	2401.6	2401.7	Sandstone	0.5	3.7	0.1	0.7	0.1	0.3	7
29R-5, 59–81	2405.6	2405.8	Sandstone	0.2	2.0	0.1	0.6	0.1	0.3	8
30R-4, 6–23	2449.8	2449.9	Sandstone	BD	BD	0.0	0.1	0.6	0.1	3
32R-2, 43–65	2458.4	2458.6	Sandstone	0.1	1.1	0.1	0.7	0.1	0.5	10

BD = below detection.

Table T30. Contents of total carbon (TC), carbonate, inorganic carbon, total organic carbon (TOC), total nitrogen (TN), total sulfur (TS), and atomic TOC/TN ratio in the cuttings samples, Hole C0020A.

Cuttings sample	Depth MSF (m) Top	Depth MSF (m) Bottom	Lithology	Inorganic carbon (wt%)	$CaCO_3$ (wt%)	TN (wt%)	TC (wt%)	TS (wt%)	TOC (wt%)	TOC/TN (molar ratio)
337-C0020A-										
25-SMW	646.5	656.5	Silty clay	0.1	1.1	0.1	1.4	0.8	1.2	18
30-SMW	696.5	706.5	Silty clay	0.2	1.4	0.1	0.0	0.9	NV	NV
35-SMW	746.5	756.5	Silty clay	0.2	1.4	0.1	0.0	0.6	NV	NV
40-SMW	796.5	806.5	Silty clay	0.2	1.6	0.1	1.7	0.7	1.5	18
45-SMW	846.5	856.5	Clayey silt	0.3	2.6	0.1	1.3	0.6	1.0	15
56-SMW	896.5	906.5	Silty clay	0.2	1.9	0.1	1.2	0.6	1.0	13
61-SMW	946.5	956.5	Clay-silt	0.5	4.5	0.1	1.3	0.5	1.0	14
66-SMW	996.5	1006.5	Silt-clay	0.2	2.0	0.1	1.4	0.6	1.2	23
73-SMW	1046.5	1056.5	Clayey silt with some fine sand	6.4	53	0.0	6.0	0.0	NV	NV
81-SMW	1096.5	1106.5	Cayey silt with fine sand	0.8	6.3	0.0	1.5	0.5	0.8	22
98-SMW	1256.5	1266.5	Cayey silt with some fine sand	0.3	2.2	0.0	1.0	0.2	0.7	20
128-SMW	1366.5	1376.5	Silt	0.3	2.1	0.1	1.8	ND	1.5	35
129-SMW	1376.5	1386.5	Clayey silt	0.4	3.1	0.1	2.0	ND	1.6	39
152-SMW	1486.5	1496.5	Clayey silt	0.2	1.7	0.0	1.1	ND	0.9	91
153-SMW	1496.5	1506.5	Sandy silt	0.8	7.0	0.0	1.7	ND	0.8	65
188-SMW	1636.5	1646.5	Silty clay	0.0	0.2	0.1	2.2	ND	2.1	51
206-SMW	1736.5	1746.5	Clayey silt	0.1	1.1	0.0	2.0	ND	1.9	78
208-SMW	1756.5	1766.5	Clayey silt	0.3	2.7	0.0	1.7	ND	1.4	72
216-SMW	1816.5	1826.5	Clayey silt	0.4	3.7	0.0	1.8	ND	1.3	60
234-SMW	1916.5	1926.5	Coal	0.3	2.4	0.5	29	ND	29	76
235-SMW	1926.5	1936.5	Coal	0.2	1.8	0.4	27	ND	27	77
236-SMW	1936.5	1946.5	Coal	0.2	1.3	0.5	36	ND	36	77
242-SMW	1946.5	1956.5	Coal	0.3	2.3	0.5	37	ND	37	81
243-SMW	1956.5	1966.5	Coal	0.2	1.4	0.6	39	ND	39	77
249-SMW	1966.5	1976.5	Silty sand	0.5	3.9	0.1	8.4	ND	8.0	64
250-SMW	1976.5	1986.5	Silty sand	0.4	3.6	0.1	5.2	ND	5.0	64
252-SMW	1986.5	1996.5	Silty sand	0.4	3.3	0.2	8.1	ND	8.0	57
254-SMW	1996.5	2006.5	Coal to sand	0.5	4.0	0.4	29	ND	28	76
270-SMW	2106.5	2116.5	Silty clay	0.2	1.6	0.1	2.8	ND	3.0	56
286-SMW	2206.5	2216.5	Silty clay	0.2	1.6	0.1	1.8	ND	2.0	33
352-SMW	2296.5	2306.5	Silty clay	0.6	5.1	0.1	2.9	ND	2.3	38
369-SMW	2396.5	2406.5	Silty shale	0.5	4.2	0.1	2.3	ND	1.8	32
390-SMW	2446.5	2456.5	Clayey silt	0.4	3.7	0.1	4.6	ND	4.2	40
391-SMW	2456.0	2466.0	Silty shale	0.5	3.9	0.1	3.3	ND	2.9	37

NV = no valid value, ND = not determined.

Table T31. Characterization of the type and maturity of organic matter in the cuttings samples, Hole C0020A.

Cuttings sample	Depth MSF (m) Top	Depth MSF (m) Bottom	Lithology	S1 (mg HC/g)	S2 (mg HC/g)	S3 (mg CO_2/g)	T_{max} (°C)*	HI (mg HC/g TOC)	OI (mg CO_2/g TOC)	PI	PC (wt%)	RC (wt%)
337-C0020A-												
25-SMW	646.5	656.5	Silty clay	1.1	3.0	1.1	297	276	100	0.27	0.39	0.71
30-SMW	696.5	706.5	Silty clay	1.3	4.1	1.7	297	317	130	0.24	0.51	0.79
35-SMW	746.5	756.5	Silty clay	0.8	3.2	1.3	295	286	114	0.21	0.38	0.74
40-SMW	796.5	806.5	Silty clay	1.3	3.0	1.5	412	249	121	0.31	0.41	0.79
45-SMW	846.5	856.5	Clayey silt	0.7	2.0	1.2	295	243	145	0.24	0.27	0.57
56-SMW	896.5	906.5	Silty clay	0.7	2.3	1.3	411	234	134	0.23	0.30	0.67
61-SMW	946.5	956.5	Clay-silt	0.7	1.9	0.9	296	231	116	0.28	0.25	0.56
66-SMW	996.5	1006.5	Silt-clay	1.1	2.4	0.7	295	299	81	0.31	0.32	0.49
73-SMW	1046.5	1056.5	Clayey silt with some fine sand	0.4	0.8	1.3	293	83	138	0.36	0.15	0.77
81-SMW	1096.5	1106.5	Clayey silt with fine sand	1.3	1.7	0.7	288	214	85	0.42	0.28	0.53
98-SMW	1256.5	1266.5	Clayey silt with some fine sand	0.1	0.4	0.7	331	60	107	0.12	0.07	0.60

* = minimum value of this parameter is 300°C. HC = hydrocarbon, TOC = total organic carbon, HI = hydrogen index, OI = oxygen index, PI = production index, PC = pyrolyzable carbon, RC = residual organic carbon.

Table T32. Characterization of the type and maturity of organic matter in the core samples, Hole C0020A.

Core, section, interval (cm)	Depth CSF-B (m)		Lithology	S1 (mg HC/g)	S2 (mg HC/g)	S3 (mg CO_2/g)	T_{max} (°C)*	HI (mg HC/g TOC)	OI† (mg CO_2/g TOC)	PI	PC (wt%)	RC (wt%)
	Top	Bottom										
337-C0020A-												
1R-2, 65–81	1278.4	1278.6	Sandstone	0.6	1.7	1.3	302	442	353	0.26	0.2	0.1
2R-2, 93.5–94	1288.3	1288.3	Coal clast	0.0	29	19	411	124	80	0.00	3.4	20
2R-3, 60–81	1289.4	1289.6	Sandstone	0.4	0.3	0.8	295	157	367	0.52	0.1	0.1
2R-4, 4–5.5	1289.6	1289.7	Sandstone	0.0	0.1	2.2	429	22	614	0.16	0.1	0.3
3R-3, 60–77	1372.6	1372.8	Siltstone	0.0	0.2	1.0	412	49	116	0.01	0.0	0.4
4R-3, 64–77	1378.1	1378.2	Sandstone	0.0	0.0	0.3	607	0	371	0.00	0.0	0.1
5R-3, 24–39	1492.1	1492.2	Sandstone	0.3	0.3	0.6	297	206	388	0.43	0.1	0.1
6R-2, 0–15	1496.4	1496.6	Sandstone	0.0	0.1	0.4	421	36	186	0.00	0.0	0.2
7R-1, 53–65	1599.5	1599.7	Shale	0.0	3.0	2.4	431	85	69	0.01	0.4	3.1
8L-5, 20–35	1607.4	1607.5	Shale	0.0	0.0	0.5	497	57	671	0.00	0.0	0.1
8L-9, 0–16	1611.2	1611.3	Siltstone	0.0	1.2	0.5	422	167	67	0.02	0.1	1.0
9R-4, 0–20	1628.4	1628.6	Shale	0.0	1.7	0.6	418	173	60	0.01	0.2	1.0
10R-2, 53–70	1631.4	1631.6	Shale	0.0	1.3	1.3	432	52	50	0.00	0.2	2.3
11R-3, 0–18	1739.6	1739.8	Sandstone	0.0	0.1	0.6	424	23	242	0.00	0.0	0.2
11R-5, 58–75	1743.1	1743.3	Siltstone	0.0	0.0	0.4	420	0	840	0.00	0.0	0.0
12R-7, 15–30	1754.7	1754.8	Sandstone	0.0	0.0	0.7	414	0	486	0.00	0.0	0.1
13R-2, 44–59	1758.4	1758.5	Sandstone	0.0	0.0	0.6	425	0	400	0.00	0.0	0.1
13R-8, 60–77	1765.6	1765.8	Sandstone	0.0	0.0	0.5	431	50	767	0.00	0.0	0.0
14R-2, 105–120	1822.5	1822.6	Sandstone	0.0	0.7	0.8	424	83	96	0.00	0.1	0.7
15R-2, 0–17	1920.4	1920.6	Coal	0.1	100	16	414	234	38	0.00	9.4	33
15R-5, 0–21	1923.6	1923.8	Coaly shale	0.0	5.7	1.2	426	168	34	0.00	0.6	2.8
15R-7, 33–41	1925.8	1925.9	Sandstone	0.0	0.2	0.1	427	95	70	0.00	0.0	0.2
16R-2, 0–18	1929.5	1929.7	Sandstone	0.1	0.6	1.3	304	262	546	0.18	0.1	0.1
17R-1, 45–60	1936.5	1936.6	Shale	0.0	3.9	1.3	428	264	86	0.01	0.4	1.1
18R-1, 105–115	1946.6	1946.7	Coal	0.0	89	12	414	290	39	0.00	8.6	22
19R-1, 115–141	1951.2	1951.4	Shale	0.0	1.3	0.5	429	168	64	0.00	0.1	0.6
19R-5, 0–27	1954.5	1954.8	Cemented sandstone	0.0	0.0	0.7	424	0	269	0.00	0.0	0.2
19R-8, 60–77	1959.1	1959.3	Sandstone	0.0	0.1	0.3	439	108	208	0.00	0.0	0.1
19R-9, 0–20	1959.3	1959.5	Sandstone	0.0	0.1	0.3	547	350	650	0.00	0.0	0.0
20R-3, 0–13	1961.6	1961.7	Siltstone	0.0	0.3	0.5	429	86	135	0.00	0.0	0.3
20R-7, 62–76	1966.3	1966.5	Sandstone	0.0	0.2	0.51	427	121	268	0.00	0.0	0.2
21R-4, 32–42	1971.7	1971.8	Sandstone	0.0	0.4	0.6	426	82	136	0.00	0.1	0.4
23R-8, 0–15	1989.5	1989.6	Siltstone	0.0	1.0	1.3	425	134	171	0.04	0.1	0.6
24R-3, 55–65	1993.8	1993.9	Coal	0.0	62	15	417	182	46	0.00	6.4	28
25R-2, 70–85	1997.1	1997.3	Coal	2.2	126	13	413	273	27	0.02	12	35
25R-3, 120–141	1999.0	1999.2	Coaly shale	0.0	1.1	1.3	424	114	131	0.00	0.1	0.8
25R-4, 0–15	1999.2	1999.4	Shale	0.0	3.0	1.1	428	198	84	0.00	0.3	1.0
26R-2, 0–9	2111.4	2111.5	Shale	0.0	0.2	0.6	406	28	102	0.00	0.0	0.6
26R-6, 0–15	2115.7	2115.8	Shale	0.0	0.2	0.6	406	30	90	0.00	0.0	0.6
26R-7, 84–101	2117.9	2118.1	Shale	0.0	0.2	0.7	403	25	109	0.00	0.0	0.6
27R-2, 61–80	2201.6	2201.8	Siltstone	0.0	0.1	0.4	408	25	85	0.00	0.0	0.5
28R-3, 0–24	2302.8	2303.1	Siltstone/siderite?	0.0	0.2	1.0	435	51	244	0.00	0.1	0.4
28R-6, 30–45	2306.7	2306.9	Sandstone/siderite?	0.0	0.3	0.9	437	53	157	0.00	0.1	0.5
29R-5, 59–81	2405.6	2405.8	Sandstone	0.0	0.1	0.6	427	37	174	0.00	0.0	0.3
32R-2, 43–65	2458.4	2458.6	Sandstone	0.0	0.0	0.6	497	0	131	0.00	0.0	0.5

* = minimum value of this parameter is 300°C. † = values of OI in excess of 300 are not likely to be representative. HC = hydrocarbon, TOC = total organic carbon, HI = hydrogen index, OI = oxygen index, PI = production index, PC = pyrolyzable carbon, RC = residual organic carbon.

Table T33. *n*-Alkane data obtained from core samples, Hole C0020A.

Core, section, interval (cm)	Depth CSF-B (m) Top	Depth CSF-B (m) Bottom	Lithology	C_{17} to C_{34} *n*-alkanes (µg/g sed)	CPI	Pr/Ph	C_{18}/Ph
337-C0020A-							
2R-2, 93.5–94	1288.3	1288.3	Coal clast	1.8	16	—	2.6
15R-2, 0–17	1920.4	1920.6	Coal	1.8	11	3.2	3.5
18R-1, 105–115	1946.6	1946.7	Coal	2.0	10	2.5	3.5
24R-3, 55–65	1993.8	1993.9	Coal	2.1	12	5.8	2.0
25R-3, 120–141	1999	1999.2	Coal	0.4	10	0.6	0.1
25R-4, 0–15	1999.2	1999.4	Coal	13.4	7	1.7	3.5
2R-4, 4–5.5	1289.6	1289.7	Sandstone (rippled)	0.7	14	0.5	1.3
14R-2, 105–120	1822.5	1822.6	Siltstone	1.0	10	0.8	0.2
15R-5, 0–21	1923.6	1923.8	Siltstone	0.7	17	3.3	0.9
19R-1, 115–141	1951.2	1951.4	Siltstone	0.7	10	2.7	0.7
28R-3, 0–24	2302.8	2303.1	Siltstone	1.2	10	0.4	0.1
3R-3, 60–77	1372.6	1372.8	Mudstone	0.4	12	0.5	0.4
7R-1, 53–65	1599.5	1599.7	Mudstone	0.2	11	2.2	0.8
9R-4, 0–20	1628.4	1628.6	Mudstone	0.4	10	0.0	0.1
10R-2, 53–70	1631.4	1631.6	Mudstone	0.0	6	1.0	1.9
11R-5, 58–75	1743.1	1743.3	Mudstone	0.4	4	1.0	1.3
12R-7, 15–30	1754.7	1754.8	Mudstone	0.1	4	0.3	0.9
23R-8, 0–15	1989.5	1989.6	Mudstone	0.1	10	1.3	4.9
26R-2, 0–9	2111.4	2111.5	Shale	1.4	11	0.3	0.1

Carbon preference index (CPI), pristane/phytane ratio, and C_{18}/phytane ratio are discussed in the text. CPI = 2 × ([C_{25} + C_{27} + C_{29} + C_{31} + C_{33}]/[C_{24} + C_{26} + C_{28} + C_{30} +C_{32}]) + ([C_{25} + C_{27} + C_{29} + C_{31} + C_{33}]/[C_{26} + C_{28} + C_{30} + C_{32} +C_{34}]); Pr/Ph = ratio of pristane to phytane measured on *m/z* 85 ion chromatogram; C_{18}/Ph = ratio of C_{18} *n*-alkane to phytane measured on *m/z* 85 ion chromatogram.

Table T34. *n*-Alkanoic acid data obtained from core samples, Hole C0020A.

Core, section, interval	Depth CSF-B (m) Top	Depth CSF-B (m) Bottom	Lithology	Conc. C_{14} to C_{32} *n*-alkanoic acids (µg/g sed)	Conc. C_{16} + C_{18} *n*-alkanoic acids (µg/g sed)	Conc. C_{15} + C_{16} methyl-alkanoic acids (µg/g sed)	CPI-*n*-acids
337-C0020A-							
2R-2, 93.5–94	1288.3	1288.3	Coal clast	25	0.02	0.01	9
15R-2, 0–17	1920.4	1920.6	Coal	532	18	13	8
18R-1, 105–115	1946.6	1946.7	Coal	260	6	4	8
24R-3, 55–65	1993.8	1993.9	Coal	53	0.75	1	8
25R-3, 120–141	1999	1999.2	Coal	7	0.10	0.04	5
25R-4, 0–15	1999.2	1999.4	Coal	5	0.19	0.03	3
2R-4, 4–5.5	1289.6	1289.7	Siltstone (rippled)	—	—	—	—
14R-2, 105–120	1822.5	1822.6	Siltstone	—	—	—	—
15R-5, 0–21	1923.6	1923.8	Siltstone	35	0.30	0.10	9
19R-1, 115–141	1951.2	1951.4	Siltstone	44	0.29	0.15	5
28R-3, 0–24	2302.8	2303.1	Siltstone	—	—	—	—
3R-3, 60–77	1372.6	1372.8	Mudstone	—	—	—	—
7R-1, 53–65	1599.5	1599.7	Mudstone	—	—	—	—
9R-4, 0–20	1628.4	1628.6	Mudstone				
10R-2, 53–70	1631.4	1631.6	Mudstone	1	0.02	—	8
11R-5, 58–75	1743.1	1743.3	Mudstone	—	—	—	—
12R-7, 15–30	1754.7	1754.8	Mudstone	—	—	—	—
23R-8, 0–15	1989.5	1989.6	Mudstone	—	—	—	—
26R-2, 0–9	2111.4	2111.5	Shale	2	0.22	0.33	2

CPI = carbon preference index. CPI-*n*-alkanoic acids = [24:0 + 26:0 + 28:0 + 30:0 + 32:0]/[23:0 + 25:0 + 27:0 + 29:0 + 31:0] and CPI *n*-alkanes = 2 × ([C_{25} + C_{27} + C_{29} + C_{31}+ C_{33}]/[C_{24} + C_{26} + C_{28} + C_{30} + C_{32}]) + ([C_{25} + C_{27} + C_{29} + C_{31}+ C_{33}]/[C_{26} + C_{28} + C_{30} + C_{32} +C_{34}]).

Table T35. Steroid data obtained from core samples, Hole C0020A.

Core, section, interval	Depth CSF-B (m)		Lithology	C_{29} Δ^4 and Δ^5 sterenes (µg/g sed)	C_{29} sterane (µg/g sed)	C_{29} sterane/sterene	Δ^4 and Δ^5 sterenes (%)			5α(H),14α(H),17α(H) 22(R) steranes (%)		
	Top	Bottom					C_{27}	C_{28}	C_{29}	C_{27}	C_{28}	C_{29}
337-C0020A-												
2R-2, 93.5–94	1288.3	1288.3	Coal clast	0.58	0.28	0.48	32	14	54	16	7	76
15R-2, 0–17	1920.4	1920.6	Coal	2.45	0.56	0.23	19	6	75	17	7	75
18R-1, 105–115	1946.6	1946.7	Coal	1.52	0.17	0.11	6	4	91	10	30	59
24R-3, 55–65	1993.8	1993.9	Coal	1.85	0.17	0.09	0.5	2	98	6	3	91
25R-3, 120–141	1999	1999.2	Coal	0.13	0.01	0.09	7	7	86	32	17	51
25R-4, 0–15	1999.2	1999.4	Coal	0.22	0.05	0.22	2	2	96	1	4	95
2R-4, 4–5.5	1289.6	1289.7	Siltstone (rippled)	0.17	0.03	0.19	11	7	82	17	13	71
14R-2, 105–120	1822.5	1822.6	Siltstone	0.25	0.11	0.44	11	12	78	28	5	66
15R-5, 0–21	1923.6	1923.8	Siltstone	0.13	0.05	0.37	9	18	73	5	18	78
19R-1, 115–141	1951.2	1951.4	Siltstone	0.43	0.11	0.25	14	13	73	9	26	65
28R-3, 0–24	2302.8	2303.1	Siltstone	0.52	0.32	0.61	6	7	88	7	4	89
30R-3, 6–23			Black laminated sandstone			0.88	5	33	63	17	42	41
3R-3, 60–77	1372.6	1372.8	Mudstone	0.28	0.05	0.19	27	13	60	19	18	63
7R-1, 53–65	1599.5	1599.7	Mudstone	0.07	0.01	0.20	16	8	76	8	18	74
9R-4, 0–20	1628.4	1628.6	Mudstone	0.52	0.08	0.15	38	21	40	43	19	39
10R-2, 53–70	1631.4	1631.6	Mudstone	0.03	0.00	0.11	26	10	63	22	35	43
11R-5, 58–75	1743.1	1743.3	Mudstone	0.04	0.01	0.23	20	13	67	33	19	48
12R-7, 15–30	1754.7	1754.8	Mudstone	0.05	0.01	0.12	35	20	46	58	24	18
23R-8, 0–15	1989.5	1989.6	Mudstone	0.05	0.01	0.21	19	14	67	31	33	36
26R-2, 0–9	2111.4	2111.5	Shale	0.62	0.40	0.64	10	6	84	25	3	72

Table T36. *n*-Alkane, sterene, and sterane data for drill cuttings, Hole C0020A.

Cuttings sample	Depth MSF (m)		*n*-alkanes (µ/g sed)	CPI	C_{29} Δ^4 and Δ^5 sterenes (µg/g sed)	C_{29} sterane (µg/g sed)	C_{29} sterane/sterene	Δ^4 and Δ^5 sterenes (%)			5α(H),14α(H),17α(H) 22(R) steranes (%)		
	Top	Bottom						C_{27}	C_{28}	C_{29}	C_{27}	C_{28}	C_{29}
337-C0020A-													
25-SMW	646.5	656.5	0.5	7	0.001	0.0002	0.19	34	31	35	25	29	46
30-SMW	696.5	706.5	0.1	10	0.001	0.0005	0.44	32	26	42	24	31	45
35-SMW	746.5	756.5	1.3	7	0.002	0.002	0.90	38	17	45	27	27	46
40-SMW	796.5	806.5	0.9	4	0.005	0.001	0.18	38	15	47	23	26	51
45-SMW	846.5	856.5	0.4	3	0.002	0.001	0.46	40	15	45	19	28	54
56-SMW	896.5	906.5	0.4	4	0.004	0.002	0.45	35	16	48	19	25	56
61-SMW	946.5	956.5	0.1	5	0.004	0.001	0.21	41	13	46	26	25	49
66-SMW	996.5	1006.5	0.1	3	0.002	0.001	0.43	36	10	54	22	22	56
73-SMW	1046.5	1056.5	0.02	4	0.0001	5E–5	0.41	46	13	41	30	24	46
81-SMW	1096.5	1106.5	0.3	8	0.004	0.0005	0.12	22	10	68	19	18	62
98-SMW	1256.5	1266.5	0.9	7	0.009	0.001	0.15	14	13	74	16	22	62

CPI = carbon preference index. CPI = 2 × ([C_{25} + C_{27} + C_{29} + C_{31}+ C_{33}]/[C_{24} + C_{26} + C_{28} + C_{30} +C_{32}]) + ([C_{25} + C_{27} + C_{29} + C_{31}+ C_{33}]/[C_{26} + C_{28} + C_{30} + C_{32} +C_{34}]).

Table T37. Schedule of PFC additions to drilling mud tanks, Expedition 337.

Addition				
Date (2012)	Time (h)	Tank	Volume added (cm^3)	Remarks
5 Aug	1730	ACT4	100	
	1730	ACT5	100	
10 Aug	NA	NA	NA	
12 Aug	NA	ACT4	100	
		ACT5	100	
		RSV2	200	
		RSV3	200	
		RSV4	200	
		RSV5	200	
13 Aug	NA	ACT4 or 5?	100	
14 Aug	NA	ACT4 or 5?	100	
15 Aug	NA	ACT4 or 5?	100	Drilling, only cuttings sampling
16 Aug	NA	ACT4 or 5?	100	Drilling, only cuttings sampling
21 Aug	1400	ACT4	50	
		ACT5	50	
		RSV2	100	
		RSV4	100	
		RSV5	100	
		RSV6	100	
		RSV7	100	
22 Aug	NA	ACT4	50	
		ACT5	50	
23 Aug	NA	ACT4	50	
		ACT5	50	
24 Aug	0700	ACT4	100	
		ACT5	100	
25 Aug	0700	ACT4	100	ACT4 and ACT5 in circulation
		ACT5	100	
26 Aug	0700	ACT4	100	Coring, ACT4 in circulation
		ACT5	100	
27 Aug	0700	ACT4	200	Coring, ACT4 in circulation
28 Aug	0700	ACT4	200	Coring, ACT4 in circulation
29 Aug	0700	ACT4	200	Coring, ACT4 in circulation
30 Aug	0700	ACT4	200	Coring, ACT4 in circulation
31 Aug	0700	ACT4	200	Coring, ACT4 in circulation
1 Sep	0700	ACT4	200	Coring, ACT4 in circulation
2 Sep	0700	ACT4	200	Coring, ACT4 in circulation
3 Sep	0700	ACT4	200	Coring, ACT4 in circulation
4 Sep	0700	ACT4	200	Coring, ACT4 in circulation
5 Sep	0700	ACT4	200	Coring, ACT4 in circulation
6 Sep	0700	ACT4	200	Coring, ACT4 in circulation
7 Sep	0700	ACT4	200	Coring, ACT4 in circulation
8 Sep	0630	ACT4	200	Coring, ACT4 in circulation

Time was recorded as ship local time (UTC + 8 h). ACT = active tank, RSV = reserve tank. NA = information not available.

Table T38. Overview of PFC concentrations and microbial cell counts in fresh mud water from active drilling tanks, mud water retrieved from core liners, and from the mud ditch, Expedition 337. (Continued on next page.)

Sample number*	PFC (µg/L)	Cell counts (x10^8 cells/mL)	Fluid source	Date collected (2012)	Time collected (h UTC)	Remarks
337-C0020A-						
1-LMT	0.020	ND		1 Aug		Fresh mud water
2-LMT	0.002	ND	ACT4	4 Aug		Fresh mud water
3-LMT	0.001	ND	ACT5	4 Aug		Fresh mud water
4-LMT	0.285	ND	RSV2	4 Aug		Fresh mud water
5-LMT	0.894	ND	RSV3	4 Aug		Fresh mud water
6-LMT	4.259	ND	RSV4	4 Aug		Fresh mud water
7-LMT	0.020	ND	RSV5	4 Aug		Fresh mud water
8-LMT	49.991	ND	ACT4	5 Aug	1730	Fresh mud water; 2 h collection
9-LMT	147.044	ND	ACT5	6 Aug	1330	Fresh mud water; 20 h collection
10-LMT	9.853	ND		7 Aug		Fresh mud water
11-LMT	6.545	ND		8 Aug		Fresh mud water
12-LMT	4.155	ND		9 Aug		Fresh mud water
13-LMT	131.537	2.08	ACT4	10 Aug		Fresh mud water
14-LMT	128.464	4.20	ACT5	10 Aug		Fresh mud water
15-LMT	117.031	4.63	ACT4	11 Aug		Fresh mud water
16-LMT	106.795	8.37	ACT5	11 Aug		Fresh mud water
17-LMT	798.537	2.13	ACT4	12 Aug		Fresh mud water; PFC peak saturated
18-LMT	854.460	2.71	ACT5	12 Aug		Fresh mud water; PFC peak saturated
19-LMT	714.336	1.39	ACT4	13 Aug		Fresh mud water
20-LMT	664.852	1.77	ACT5	13 Aug		Fresh mud water
21-LMT	396.955	1.35	ACT4	14 Aug		Fresh mud water
22-LMT	449.354	3.36	ACT5	14 Aug		Fresh mud water
23-LMT	244.964	1.10	ACT4	15 Aug		Mud water; just before drilling
49-LMT	146.010	3.30	ACT5	15 Aug		Fresh mud water
76-LMT	79.577	5.45	ACT4	16 Aug		Fresh mud water
86-LMT	96.665	ND		17 Aug		Fresh mud water
87-LMT	1.744	ND		17 Aug	1700	LCM
99-LMT	2.385	ND	ACT5	18 Aug		Fresh mud water
103-LMT	158.250	1.03	ACT4	22 Aug	1045	Fresh mud water
104-LMT	345.623	3.82	ACT4	23 Aug	1100	Fresh mud water
106-LMT	527.824	1.60	ACT4	24 Aug	1200	Fresh mud water
107-LMT	643.345	2.58	ACT5	24 Aug	1200	Fresh mud water
108-LMT	301.740	2.05	ACT4	25 Aug	1100	Fresh mud water
109-LMT	309.481	1.68	ACT5	25 Aug	1100	Fresh mud water
110-LMW	736.870	1.84	Ditch	25 Aug	1815	Mud water
112-LMW	653.768	ND	Core 1R	25 Aug	1822	Mud water
113-LMW	669.667	ND	Core 2R	25 Aug	2123	Mud water
124-LMW	65.774	4.09	Ditch	26 Aug	0430	Mud water
126-LMT	134.432	ND	ACT4	26 Aug	1100	Fresh mud water
127-LMW	199.373	ND	Core 4R	26 Aug	1225	Mud water
139-LMW	103.690	0.97	Ditch	26 Aug	1725	Mud water
142-LMW	64.742	ND	Core 5R	29 Aug	2012	Mud water
143-LMW	57.950	ND	Core 6R	29 Aug	2012	Mud water4
144-LMW	52.312	3.01	Ditch	27 Aug	0545	Mud water
159-LMT	89.606	ND	ACT4	27 Aug	1100	Fresh mud water
165-LMT	2208.350	2.03	ACT4	28 Aug	1100	Fresh mud water; PFC peak saturated
167-LMT	104.448	ND	ACT4	29 Aug	1100	Fresh mud water
172-LMW	361.029	ND	Ditch	29 Aug	1529	Mud water
173-LMW	113.541	ND	Section 8L-2	30 Aug	0730	Mud water
175-LMW	133.958	ND	Section 8L-4	30 Aug	0730	Mud water
177-LMW	138.822	ND	Section 8L-6	30 Aug	0730	Mud water
179-LMW	136.973	ND	Section 8L-8	30 Aug	0730	Mud water
182-LMT	160.278	ND	ACT4	30 Aug	1100	Fresh mud water
183-LMW	232.820	ND	Core 9R	31 Aug	0813	Mud water
185-LMT	275.022	ND	ACT4	31 Aug	1100	Fresh mud water
196-LMW	156.499	ND	Ditch	31 Aug	1715	Mud water
214-LMT	94.159	ND	ACT4	1 Sep	1810	Fresh mud water; 1809.5–1810.5 m
215-LMW	86.246	ND	Core 14R	1 Sep	1843	Mud water
218-LMW	85.741	ND	Ditch	1 Sep	1733	Mud water
223-LMW	107.491	ND	Ditch	2 Sep	0513	Mud water
228-LMW	156.447	ND	Core 15R	2 Sep	1230	Mud water
229-LMT	105.716	ND	ACT4	2 Sep	1100	Fresh mud water; 1923.5 m
230-LMW	165.691	ND	Core 16R	2 Sep	1540	Mud water
231-LMW	165.691	ND	Core 17R	2 Sep	1838	Mud water
232-LMW	107.771	1.24	Core 18R	2 Sep	2153	Mud water

Table T38 (continued).

Sample number*	PFC (µg/L)	Cell counts (x10^8 cells/mL)	Fluid source	Date collected (2012)	Time collected (h UTC)	Remarks
233-LMW	116.544	ND	Ditch	2 Sep	1657	Mud water
237-LMT	3085.210	ND	ACT4	3 Sep	1100	Fresh mud water; 1950 m MSF; weak mixing—mud pump stopped at pull out of the hole; PFC peak saturated
238-LMW	122.833	ND	Core 19R	4 Sep	1233	Mud water
239-LMT	319.940	ND	ACT4	3 Sep	1100	Fresh mud water; 1957.5 m MSF
240-LMW	299.634	ND	Core 20R	3 Sep	1504	Mud water
241-LMW	316.227	ND	Core 21R	3 Sep	1708	Mud water
245-LMW	238.167	ND		4 Sep		Mud water
246-LMW	221.642	ND	Core 22R	4 Sep	2015	Mud water
253-LMW	127.651	ND	Ditch	5 Sep	0508	Mud water
256-LMT	234.161	1.39	ACT4	5 Sep	1100	Fresh mud water
263-LMW	257.343	ND	Core 25R	5 Sep	0544	Mud water
269-LMW	148.804	ND	Ditch	6 Sep	0508	Mud water
279-LMT	261.613	ND	ACT4	6 Sep	1100	Fresh mud water; 2190.5 m MSF
282-LMW	471.133	ND	Core 27R	6 Sep	1915	Mud water
283-LMW	155.400	ND	Ditch	6 Sep	1836	Mud water
284-LMW	171.310	ND	Ditch	7 Sep	0524	Mud water
348-LMT	210.457	ND	ACT4	7 Sep	1100	Fresh mud water
349-LMW	185.390	ND	Core 28R	7 Sep	1800	Mud water
356-LMW	194.162	ND	Ditch	7 Sep	1826	Mud water
368-LMW	333.666	ND	Ditch	8 Sep	0515	Mud water
372-LMT	184.257	ND	ACT4	8 Sep	1100	Fresh mud water
386-LMW	182.243	ND	Ditch	8 Sep	1523	Mud water
387-LMW	113.235	ND	Core 30R	9 Sep	1848	Mud water
388-LMW	132.163	ND	Core 32R liner	9 Sep		Mud water
389-LMW	117.860	ND	Ditch	9 Sep	0717	Mud water

* = see MISC_MATERIAL_SAMPLE_LIST.XLSX in GEOCHEM in **"Supplementary material."** Cell counts varied considerably over the duration of the expedition (mean = 2.66×10^8, standard deviation = 1.68×10^8 cells/cm^3) but consistently exceeded 1×10^8 cells/cm^3. LMT = fresh mud water collected at mud tank; LMW = fluid taken from drilling mud or mud water. Mud was collected from the ditch after circulation back on board the ship. PFC = perfluorocarbon, used as a tracer. ACT = active tank, RSV = reserve tank. LCW = lost circulation material. ND = not determined.

Table T39. Drilling mud and predicted contamination with nonindigenous cells in cuttings, compared to data from direct cell counts, Expedition 337.

Sample number*	Depth MSF (m)	Concentration (µL drilling mud/ g cuttings)	Drilling mud in pore water (%)	Predicted contamination (cells/cm^3)	Direct cell counts (cells/cm^3)
337-C0020A-					
25-SMW	646.5	46.4	10.9	1.9E+07	1.6E+07
30-SMW	696.5	57.4	14.6	2.4E+07	2.6E+07
35-SMW	746.5	59.7	15.4	2.5E+07	3.4E+07
40-SMW	796.5	52.2	13.8	2.2E+07	3.0E+07
45-SMW	846.5	72.3	19.1	3.1E+07	2.4E+07
56-SMW	896.5	49.4	13.1	2.1E+07	3.2E+07
61-SMW	946.5	32.8	9.5	1.5E+07	6.7E+07
66-SMW	996.5	ND	ND	ND	ND
73-SMW	1046.5	18.1	5.2	8.1E+06	4.7E+07
81-SMW	1096.5	239.8	86.8	1.2E+08	4.3E+07
90-SMW	1196.5	6.2	2.4	3.1E+06	ND
98-SMW	1256.5	18.5	5.7	8.6E+06	ND
116-SMW	1296.5	42.5	12.4	1.9E+07	ND
122-SMW	1346.5	89.4	36.3	4.5E+07	ND
124-SMW	1356.5	141.4	75.3	7.6E+07	ND
131-SMW	1396.5	75.3	32.4	3.8E+07	ND
136-SMW	1446.5	43.4	30.9	2.5E+07	ND
153-SMW	1496.5	28.0	10.2	1.3E+07	ND
158-SMW	1546.5	44.4	13.2	2.0E+07	ND
170-SMW	1596.5	297.3	91.4	1.3E+08	ND
192-SMW	1646.5	422.5	137.3	1.9E+08	ND
198-SMW	1696.5	303.1	124.4	1.5E+08	ND
205-SMW	1736.5	214.7	83.3	1.1E+08	ND
207-SMW	1746.5	54.7	22.8	2.8E+07	ND
212-SMW	1796.6	496.5	269.5	2.7E+08	ND
220-SMW	1846.5	21.5	9.6	1.1E+07	ND
226-SMW	1896.5	20.9	7.4	1.0E+07	ND
242-SMW	1946.5	207.9	62.9	8.6E+07	ND
254-SMW	1996.5	138.9	56.8	7.1E+07	ND
261-SMW	2046.5	289.3	139.4	1.5E+08	ND
267-SMW	2096.5	0.2	0.1	1.2E+05	ND
274-SMW	2146.5	263.8	91.4	1.3E+08	ND
285-SMW	2196.5	663.3	298.9	3.4E+08	ND
290-SMW	2246.5	1039.0	424.4	5.3E+08	ND
352-SMW	2296.5	314.4	136.9	1.6E+08	ND
358-SMW	2346.5	317.0	146.7	1.7E+08	ND
369-SMW	2396.5	357.6	118.2	1.7E+08	ND
390-SMW	2446.5	203.8	60.5	9.2E+07	ND
391-SMW	2456	175.7	79.8	9.0E+07	ND

* = see MISC_MATERIAL_SAMPLE_LIST.XLSX in GEOCHEM in "Supplementary material." ND = not determined.

Table T40. Overview of core samples analyzed for contamination using perfluorocarbon (PFC) tracer, calculated quantitative estimates of drilling fluid and contaminant cell intrusion, and lithologic characteristics of the respective samples, Hole C0020A. (Continued on next four pages.)

Core, section, interval (cm)	Depth CSF-B (m)	Cross-sectional location	Concentration (µg PFC/cm³ sediment)	Concentration (µL drilling fluid/g sediment)	Drilling fluid in pore water (%)	Predicted contamination (cells/cm³)	Lithology	Remarks
337-C0020A-								
1R-2, 65–81	1278.42	IN	9.5E–03	46.3	26.5	2.5E+07	Fine–medium sand	
1R-2, 65–81	1278.42	H	1.1E–02	55.4	31.7	3.0E+07		
1R-2, 65–81	1278.42	EX	7.1E–03	34.6	19.7	1.9E+07		
2R-3, 60–81	1289.39	IN	1.4E–03	7.3	3.4	3.8E+06	Fine–medium sandstone	
2R-3, 60–81	1289.39	H	3.6E–03	18.3	8.4	9.6E+06		
2R-3, 60–81	1289.39	EX	1.1E–02	57.2	26.3	3.0E+07		
3R-3, 60–77	1372.59	IN	1.6E–05	0.1	0.0	4.1E+04	Clayey siltstone	
3R-3, 60–77	1372.59	EX	5.2E–03	25.6	12.4	1.4E+07		
4R-3, 64–77	1378.09	IN	8.7E–05	0.4	0.2	2.3E+05	Clayey siltstone	
4R-3, 64–77	1378.09	H	2.3E–04	1.1	0.6	6.0E+05	Sandstone	
4R-3, 64–77	1378.09	EX	5.0E–03	25.0	13.5	1.3E+07	Siltstone	
5R-3, 24–39	1492.09	IN	2.4E–03	12.4	5.4	6.3E+06	Fine–medium sandstone	
5R-3, 24–39	1492.09	H	1.7E–03	8.7	3.8	4.4E+06		
5R-3, 24–39	1492.09	EX	1.6E–03	8.2	3.6	4.2E+06		
6R-2, 0–15	1496.41	IN	4.4E–06	0.0	0.0	1.2E+04	Fine–medium sandstone	
6R-2, 0–15	1496.41	EX	7.8E–04	3.8	2.2	2.1E+06		
7R-1, 53–65	1599.53	IN	[2.4E–06]	0.0	0.0	6.5E+03	Shale	
7R-1, 53–65	1599.53	H	1.2E–05	0.1	0.0	3.3E+04		
7R-1, 53–65	1599.53	EX	1.5E–03	7.2	3.9	3.9E+06		
8L–5, 20–35	1607.36	IN	9.5E–06	0.1	0.0	2.5E+04	Shale vs. silt	
8L–5, 20–35	1607.36	H	[2.0E–06]	0.0	0.0	5.4E+03		
8L–5, 20–35	1607.36	EX	2.0E–03	10.1	4.9	5.4E+06		
8L–9, 0–16	1611.17	IN	[2.2E–06]	0.0	0.0	5.9E+03	Fine siltstone + plant remains	
8L–9, 0–16	1611.17	EX	5.1E–02	262.6	122.6	1.4E+08		
9R-4, 0–20	1628.34	IN	7.9E–06	0.0	0.0	2.1E+04	Siltstone	
9R-4, 0–20	1628.34	EX	1.9E–03	9.7	4.9	5.1E+06		
10R-2, 53–70	1631.44	IN	[3.2E–06]	0.0	0.0	8.6E+03	Fine–medium sandstone	
10R-2, 53–70	1631.44	H	4.1E–06	0.0	0.0	1.1E+04		
10R-2, 53–70	1631.44	EX	1.3E–02	74.6	27.6	3.6E+07		
11R-2, 0–40	1738.88	OUT	1.4E–02	68.3	32.6	3.6E+07	Fine–medium sandstone	
11R-3, 0–18	1739.63	IN	3.3E–05	0.2	0.1	8.8E+04	Fine sandstone	
11R-3, 0–18	1739.63	H	3.5E–05	0.2	0.1	9.4E+04		
11R-3, 0–18	1739.63	EX	3.2E–03	16.2	7.7	8.5E+06		
11R-5, 58–75	1743.08	IN	9.9E–06	0.1	0.0	2.6E+04	Siltstone + sandstone	
11R-5, 58–75	1743.08	EX	1.0E–02	52.0	24.6	2.7E+07		
12R-6, 39–44	1753.82	IN	[2.6E–06]	0.0	0.0	6.8E+03	Siltstone	
12R-6, 39–44	1753.82	EX	2.6E–05	0.1	0.3	6.9E+04		
12R-7, 15–30	1754.69	IN	[3.2E–06]	0.0	0.0	8.5E+03	Fine sandstone	
12R-7, 15–30	1754.69	H	6.1E–06	0.0	0.0	1.6E+04		
12R-7, 15–30	1754.69	EX	8.6E–05	0.4	0.3	2.3E+05		
12R-7, 30–50	1754.84	OUT	4.6E–03	21.2	14.7	1.2E+07	Fine sandstone	
13R-2, 4.5–44	1757.91	OUT	1.2E–02	56.3	39.1	3.2E+07	Silty fine sandstone	
13R-2, 44–59	1758.31	IN	3.7E–05	0.2	0.1	9.7E+04	Fine sandstone	
13R-2, 44–59	1758.31	H	1.1E–05	0.1	0.0	2.8E+04		
13R-2, 44–59	1758.31	EX	4.3E–03	19.7	13.7	1.1E+07		
13R-8, 60–76	1765.16	IN	[3.0E–06]	0.0	0.0	8.1E+03	Fine sandstone	

Table T40 (continued). (Continued on next page.)

Core, section, interval (cm)	Depth CSF-B (m)	Cross-sectional location	Concentration (μg PFC/cm³ sediment)	Concentration (μL drilling fluid/g sediment)	Drilling fluid in pore water (%)	Predicted contamination (cells/cm³)	Lithology	Remarks
13R-8, 60–76	1765.16	H	4.8E–05	0.2	0.2	1.3E+05		
13R-8, 60–76	1765.16	EX	2.3E–04	1.1	0.7	6.2E+05		
14R-2, 105–120	1822.46	IN	[2.6E–06]	0.0	0.0	6.9E+03	Fine sandstone silt with shale lamination	
14R-2, 105–120	1822.46	H	1.2E–04	0.5	0.4	3.2E+05		
14R-2, 105–120	1822.46	EX	2.6E–03	11.6	9.0	6.9E+06		
14R-3, 0–45	1821.41	OUT	2.0E–02	88.8	73.1	5.3E+07	Fine sandstone	
15R-2, 0–17	1920.40	IN	1.1E–05	0.1	0.0	2.9E+04	Coal	
15R-2, 0–17	1920.40	EX	7.0E–04	5.4	2.5	1.9E+06		
15R-5, 0–21	1923.64	IN	[2.4E–06]	0.0	0.0	6.5E+03	Coaly shale	
15R-5, 0–21	1923.64	H	4.4E–05	0.2	0.2	1.2E+05		
15R-5, 0–21	1923.64	EX	7.0E–04	3.1	3.1	1.9E+06		
15R-5, 21–40	1923.85	OUT	5.2E–06	0.0	0.0	1.4E+04		
15R-7, 18–33	1925.65	IN	1.3E–04	0.6	0.1	3.3E+05	Silty fine sand	
15R-7, 18–33	1925.65	EX	2.9E–04	1.4	0.9	7.8E+05		
15R-7, 33–41	1925.80	IN	[1.9E–06]	0.0	0.01	5.1E+03		
15R-7, 33–41	1925.80	H	[2.1E–06]	0.0	0.0	5.6E+03		
15R-7, 33–41	1925.80	EX	5.7E–03	26.6	17.6	1.5E+07		
16R-2, 0–18	1929.51	IN	1.7E–04	0.8	0.5	4.6E+05	Fine–middle sand	
16R-2, 0–18	1929.51	H	2.2E–02	107.0	62.4	5.9E+07		
16R-2, 0–18	1929.51	EX	8.0E–03	38.7	22.6	2.1E+07		
16R-2, 18–77	1929.69	EX	2.6E–03	12.5	6.9	6.9E+06		
17R-1, 45–60	1936.45	IN	2.2E–05	0.1	0.1	5.9E+04		From sand layer
17R-1, 45–60	1936.45	H	5.6E–03	26.1	18.1	1.5E+07	Layers of middle sand + silty shale	From sand layer
17R-1, 45–60	1936.45	EX	8.5E–03	39.5	27.4	2.3E+07		From sand layer
17R-1, 45–60	1936.45	IN	2.4E–04	1.1	0.8	6.3E+05		From coal layer
17R-1, 45–60	1936.45	H	9.1E–04	4.2	2.9	2.4E+06		From coal layer
17R-1, 45–60	1936.45	EX	3.9E–03	18.3	12.7	1.0E+07		From coal layer
17R-1, 60–100	1936.60	EX	2.0E–05	0.1	0.1	5.3E+04	Middle sand + clay clasts/layers	
17R-1, 137–141	1937.37	IN	3.2E–03	16.3	7.8	8.6E+06		
17R-4, 65–85	1939.35	EX	1.0E–03	4.9	2.9	2.7E+06	Cemented sandstone with mud clasts	
17R-4, 85–95	1939.55	IN	3.3E–05	0.2	0.1	8.7E+04		
17R-4, 85–95	1939.55	H	6.6E–05	0.3	0.2	1.8E+05		
17R-4, 85–95	1939.55	EX	5.5E–03	26.1	15.3	1.5E+07		
17R-4, 137–141	1940.07	IN	1.1E–03	5.1	3.0	2.8E+06		
17R-6, 62–66	1941.49	IN	5.6E–06	0.0	0.0	1.5E+04		
17R-8, 116.5–120.5	1944.10	IN	6.5E–06	0.0	0.0	1.7E+04		
17R-9, 10–25	1944.24	IN	7.7E–06	0.0	0.0	2.0E+04	Fine sandstone	
17R-9, 10–25	1944.24	H	1.4E–03	6.8	3.9	3.7E+06		
17R-9, 10–25	1944.24	EX	3.1E–03	15.1	8.7	8.3E+06		
17R-9, 25–51	1944.39	EX	3.5E–04	1.6	1.1	9.4E+05		
18R-1, 105–115	1946.55	IN	9.8E–05	0.8	0.3	2.6E+05	Coal	
18R-1, 105–115	1946.55	H	2.4E–05	0.2	0.1	6.4E+04		
18R-1, 105–115	1946.55	EX	4.6E–04	3.8	1.5	1.2E+06		
18R-1, 111–115	1946.61	IN	1.1E–04	0.9	0.3	2.8E+05		
19R-1, 85–115	1950.85	EX	3.4E–05	0.2	0.1	9.0E+04	Silty shale-organic matter rich + fine sand	
19R-1, 115–141	1951.15	IN	[3.1E–06]	0.0	0.0	8.2E+03		
19R-1, 115–141	1951.15	H	[3.8E–06]	0.0	0.0	1.0E+04		
19R-1, 115–141	1951.15	EX	1.4E–05	0.1	0.1	3.8E+04		
19R-1, 137–141	1951.37	IN	2.3E–04	1.0	0.9	6.0E+05		

Table T40 (continued). (Continued on next page.)

Core, section, interval (cm)	Depth CSF-B (m)	Cross-sectional location	Concentration (µg PFC/cm³ sediment)	Concentration (µL drilling fluid/g sediment)	Drilling fluid in pore water (%)	Predicted contamination (cells/cm³)	Lithology	Remarks
19R-3, 137–141	1953.37	IN	[4.8E–06]	0.0	0.0	1.3E+04		
19R-4, 86–90	1954.16	IN	5.4E–05	0.3	0.2	1.4E+05	Shale	
19R-5, 0–27	1954.13	EX	3.4E–04	1.3	10.5	9.2E+05	Silt/carbonate cemented silt	
19R-7, 137–141	1957.91	IN	1.5E–03	6.9	5.9	4.1E+06		
19R-8, 60–77	1958.44	IN	2.7E–06	0.0	0.0	7.2E+03	Sand with plant remains	
19R-8, 60–77	1958.44	H	9.5E–05	0.5	0.2	2.5E+05		
19R-8, 60–77	1958.44	EX	1.1E–04	0.6	0.2	2.9E+05		
19R-9, 0–20	1958.55	IN	2.5E–03	12.6	6.3	6.7E+06	Silty sand	
19R-9, 0–20	1958.55	H	1.4E–03	7.1	3.6	3.8E+06		
19R-9, 0–20	1958.55	EX	6.1E–03	30.5	15.2	1.6E+07		
19R-9, 30–60	1958.85	EX	2.1E–04	1.1	0.5	5.6E+05		
20R-2, 62–66	1961.53	IN	[5.3E–06]	0.0	0.0	1.4E+04		
20R-3, 0–13	1961.57	IN	[2.0E–06]	0.0	0.0	5.4E+03	Sandy silt	
20R-3, 0–13	1961.57	H	1.1E–05	0.1	0.0	2.9E+04		
20R-3, 0–13	1961.57	EX	2.7E–04	1.2	0.8	7.1E+05		
20R-3, 23–77.5	1961.80	EX	1.3E–03	5.8	3.8	3.4E+06		
20R-6, 47–51	1965.65	IN	4.0E–06	0.0	0.0	1.1E+04		
20R-7, 0–52	1965.69	EX	1.0E–04	0.5	0.4	2.8E+05	Organic-rich silty shale	
20R-7, 62–76	1966.31	IN	1.7E–05	0.1	0.1	4.5E+04	Silty fine sand	
20R-7, 62–76	1966.31	H	10.0E–05	0.4	0.4	2.7E+05		
20R-7, 62–76	1966.31	EX	3.2E–04	1.4	1.2	8.6E+05		
21R-1, 138–142	1970.38	IN	1.8E–04	0.8	0.6	4.9E+05		
21R-4, 0–32	1969.00	EX	2.5E–05	0.1	0.1	6.7E+04		
21R-4, 32–42	1969.32	IN	[2.0E–06]	0.0	0.0	5.3E+03	Fine sand vs. coaly layers	
21R-4, 32–42	1969.32	H	[2.3E–06]	0.0	0.0	6.0E+03		
21R-4, 32–42	1969.32	EX	5.9E–05	0.3	0.2	1.6E+05		
22R-4, 0–4	1977.19	IN	1.8E–03	8.3	6.2	4.8E+06		
23R-1, 95–96	1982.45	IN	5.2E–05	0.2	0.2	1.4E+05		
23R-1, 95–96	1982.45	OUT	3.3E–03	14.7	12.5	8.7E+06		
23R-3, 139–140	1985.19	IN	3.4E–04	1.5	1.3	8.9E+05		
23R-3, 139–140	1985.19	OUT	8.7E–04	3.9	3.4	2.3E+06		
23R-5, 99.5–100.5	1987.13	IN	7.6E–06	0.0	0.0	2.0E+04		
23R-5, 99.5–100.5	1987.13	OUT	3.4E–04	1.5	1.6	9.2E+05		
23R-6, 48–76	1987.64	EX	2.3E–06	0.0	0.0	6.2E+03	Shale with plant remains + coaly shale (?)	
23R-6, 75–76	1987.91	IN	5.9E–06	0.0	0.0	1.6E+04		
23R-6, 75–76	1987.91	OUT	5.8E–04	2.6	2.7	1.5E+06		
23R-7, 0–1	1987.90	IN	7.6E–05	0.3	0.3	2.0E+05		
23R-7, 0–1	1987.90	OUT	3.2E–03	14.3	12.6	8.5E+06		
23R-8, 0–15	1989.27	IN	[1.6E–06]	0.0	0.0	4.2E+03	Silt with plant remains	
23R-8, 0–15	1989.27	H	1.6E–02	71.9	54.2	4.2E+07		
23R-8, 0–15	1989.27	EX	5.6E–03	25.4	19.2	1.5E+07		
24R-1, 100–101	1992.00	IN	[4.3E–06]	0.0	0.0	1.2E+04		
24R-1, 100–101	1992.00	OUT	1.4E–02	68.4	37.4	3.7E+07		
24R-3, 55–65	1993.77	IN	2.1E–05	0.2	0.1	5.6E+04	Coal	
24R-3, 55–65	1993.77	EX	5.7E–04	4.7	1.5	1.5E+06		
24R-3, 74.5–75.5	1993.96	IN	5.7E–06	0.1	0.0	1.5E+04		
24R-3, 74.5–75.5	1993.96	OUT	2.5E–03	20.6	6.8	6.8E+06		
25R-1, 140–141	1996.40	IN	[3.7E–06]	0.0	0.0	9.8E+03		
25R-1, 140–141	1996.40	OUT	5.9E–03	27.5	18.3	1.6E+07		

Table T40 (continued). (Continued on next page.)

Core, section, interval (cm)	Depth CSF-B (m)	Cross-sectional location	Concentration (µg PFC/cm³ sediment)	Concentration (µL drilling fluid/g sediment)	Drilling fluid in pore water (%)	Predicted contamination (cells/cm³)	Lithology	Remarks
25R-2, 70–85	1997.11	IN	1.7E–05	0.1	0.1	4.5E+04		
25R-2, 70–85	1997.11	H	1.8E–04	0.8	0.7	4.7E+05		
25R-2, 70–85	1997.11	EX	4.5E–04	2.0	1.9	1.2E+06		
25R-2, 140–141	1997.81	IN	2.7E–05	0.1	0.1	7.2E+04		
25R-2, 140–141	1997.81	OUT	3.8E–03	17.1	15.8	1.0E+07		
25R-3, 120–141	1999.02	IN	[2.2E–06]	0.0	0.0	5.9E+03		
25R-3, 120–141	1999.02	H	[2.2E–06]	0.0	0.0	5.8E+03		
25R-3, 120–141	1999.02	EX	1.1E–04	0.5	0.5	3.0E+05		
25R-3, 140–141	1999.22	IN	1.6E–05	0.1	0.1	4.2E+04		
25R-3, 140–141	1999.22	OUT	2.3E–03	1.0	9.7	6.2E+06		
25R-4, 0–15	1999.23	IN	[7.0E–06]	0.0	0.0	1.9E+04	Silty shale	
25R-4, 0–15	1999.23	H	9.9E–05	0.4	0.5	2.6E+05		
25R-4, 0–15	1999.23	EX	2.3E–02	98.2	105.4	6.1E+07		
25R-5, 139.5–140.5	2001.39	IN	6.0E–04	2.8	1.9	1.6E+06		
25R-5, 139.5–140.5	2001.39	OUT	7.9E–03	36.9	24.6	2.1E+07		
26R-2, 0–9	2111.38	IN	3.4E–05	0.2	0.1	9.0E+04	Coal ?	
26R-2, 0–9	2111.38	H	1.5E–05	0.1	0.1	4.0E+04	Shale	
26R-2, 0–9	2111.38	EX	6.2E–03	27.9	21.5	1.7E+07		
26R-4, 139–140	2114.85	IN	3.3E–05	0.2	0.1	8.8E+04		
26R-4, 139–140	2114.85	OUT	3.8E–03	17.2	12.8	1.0E+07	Shale	
26R-6, 0–15	2115.58	IN	[3.0E–06]	0.0	0.0	8.0E+03	Shale-silty	
26R-6, 0–15	2115.58	H	1.1E–05	0.1	0.0	3.0E+04		
26R-6, 0–15	2115.58	EX	8.0E–03	35.9	25.9	2.1E+07		
26R-7, 0–1	1226.97	IN	[2.3E–06]	0.0	0.0	6.1E+03		
26R-7, 0–1	1226.97	OUT	8.6E–04	3.9	2.7	2.3E+06		
26R-7, 84–101	1227.81	IN	[9.3E–06]	0.0	0.0	2.5E+04	Shale	
26R-7, 84–101	1227.81	H	1.5E–05	0.1	0.1	3.9E+04		
26R-7, 84–101	1227.81	EX	1.7E–03	7.7	5.6	4.5E+06		
27R-2, 0–1	2201.00	IN	[6.5E–06]	0.0	0.0	1.7E+04		
27R-2, 0–1	2201.00	OUT	2.9E–03	12.8	11.3	7.7E+06		
27R-2, 61–80	2201.61	IN	2.2E–06	0.0	0.0	5.8E+03	Silt	
27R-2, 61–80	2201.61	H	2.4E–05	0.1	0.1	6.5E+04		
27R-2, 61–80	2201.61	EX	1.7E–04	0.8	0.7	4.7E+05		
27R-3, 143–144	2203.23	IN	4.2E–06	0.0	0.0	1.1E+04		
27R-3, 143–144	2203.23	OUT	5.8E–03	26.1	21.6	1.5E+07		
28R-2, 140–141	2302.81	IN	2.1E–05	0.1	0.1	5.6E+04		
28R-2, 140–141	2302.81	OUT	3.4E–03	15.6	11.2	9.0E+06		
28R-3, 0–24	2302.82	IN	[2.9E–06]	0.0	0.1	7.8E+03	Siltstone	
28R-3, 0–24	2302.82	EX	3.6E–05	0.1	0.6	9.5E+04		
28R-3, 0–24	2302.82	H	2.3E–06	0.0	0.0	6.1E+03		
28R-3, 24–75	2303.06	EX	4.8E–04	1.8	7.3	1.3E+06		
28R-5, 140–141	2306.39	IN	[6.3E–06]	0.0	0.0	1.7E+04		
28R-5, 140–141	2306.39	OUT	2.6E–03	11.8	9.1	7.0E+06		
28R-6, 0–30	2306.39	EX	9.1E–06	0.0	0.0	2.4E+04	Fine sandstone with clay clasts	
28R-6, 30–45	2306.69	IN	[1.6E–06]	0.0	0.0	4.3E+03	Fine sandstone with clay clasts	
28R-6, 30–45	2306.69	EX	3.0E–03	13.5	10.9	8.1E+06		
28R-6, 30–45	2306.69	H	2.1E–06	0.0	0.0	5.6E+03		
29R-1, 139.5–140.5	2401.40	IN	[3.5E–06]	0.0	0.0	9.4E+03		
29R-1, 139.5–140.5	24001.40	OUT	1.1E–03	4.8	3.9	2.8E+06		

Table T40 (continued).

Core, section, interval (cm)	Depth CSF-B (m)	Cross-sectional location	Concentration (µg PFC/cm³ sediment)	Concentration (µL drilling fluid/g sediment)	Drilling fluid in pore water (%)	Predicted contamination (cells/cm³)	Lithology	Remarks
29R-2, 17.5–27	2401.58	IN	1.9E–05	0.1	0.1	5.1E+04	Silty sandstone	
29R-2, 17.5–27	2401.58	H	3.3E–05	0.2	0.1	8.8E+04		
29R-2, 17.5–27	2401.58	EX	2.5E–02	112.7	90.6	6.7E+07		
29R-2, 27–47	2401.68	EX	2.7E–06	0.0	0.0	7.3E+03		
29R-3, 137–138	2403.54	IN	[8.2E–06]	0.0	0.1	2.2E+04		
29R-3, 137–138	2403.54	OUT	1.8E–02	72.2	102.2	4.7E+07		
29R-3, 138–141	2403.55	IN	4.7E–05	0.2	0.3	1.2E+05		
29R-3, 138–141	2403.55	OUT	1.6E–02	63.7	90.1	4.1E+07		
29R-5, 59–81	2405.57	IN	6.9E–05	0.3	0.3	1.8E+05	Fine sandstone	
29R-5, 59–81	2405.57	H	6.8E–06	0.0	0.0	1.8E+04		
29R-5, 59–81	2405.57	EX	5.6E–02	254.3	206.3	1.5E+08		
29R-5, 81–101	2405.79	EX	[5.9E–06]	0.0	0.0	1.6E+04	Fine sand	
29R-7, 139.5–140.5	2408.15	IN	2.5E–04	1.0	1.8	6.8E+05		
29R-7, 139.5–140.5	2408.15	OUT	1.7E–02	65.3	114.1	4.4E+07		
30R-3, 0–1	2448.68	IN	4.2E–04	1.9	1.6	1.1E+06		
30R-3, 0–1	2448.68	OUT	4.0E–03	17.5	15.4	1.1E+07		
30R-4, 0–1	2449.70	IN	1.4E–03	6.3	5.8	3.8E+06		
30R-4, 0–1	2449.70	OUT	4.4E–03	19.5	18.0	1.2E+07		
30R-4, 44–81	2450.14	EX	1.6E–04	0.7	0.7	4.2E+05		
30R-4, 6–23	2449.76	IN	[2.1E–06]	0.0	0.0	5.5E+03	Fine sand	
30R-4, 6–23	2449.76	H	[1.9E–06]	0.0	0.0	5.0E+03		
30R-4, 6–23	2449.76	EX	4.9E–04	2.2	2.0	1.3E+06		
32R-1, 144–145	2457.94	IN	7.8E–05	0.3	0.3	2.1E+05	Fine sandstone	
32R-1, 144–145	2457.94	OUT	1.4E–04	0.6	0.6	3.7E+05	Silty shale	
32R-2, 43–65	2458.38	IN	7.6E–05	0.3	0.3	2.0E+05		
32R-2, 43–65	2458.38	H	2.6E–06	0.0	0.0	6.9E+03		
32R-2, 43–65	2458.38	EX	3.4E–02	147.4	140.4	9.0E+07		
32R-6, 70–71	2463.64	IN	2.6E–05	0.1	0.1	6.9E+04		
32R-6, 70–71	2463.64	OUT	3.1E–03	13.6	13.3	8.3E+06		

Samples in which PFC was below detection, values were calculated assuming the detection amount (8 pg) and are shown in brackets. BD = below detection. IN = innermost part of core, H = halfway between liner and core center, EX = outer centimeter of core after removal of contaminated outer surface, OUT = contaminated outer surface of core that is in contact with core liner.

Table T41. Overview of samples used for DNA extraction and target groups analyzed by quantitative and conventional PCR, Hole C0020A. This table is available in an **oversized format.**

Table T42. Overview of the samples incubated with ^{35}S-labeled Na_2SO_4 (aqueous solution), Hole C0020A.

Core, section	Depth CSF-B (m)	A/B/C/D sample	Incubation (MBq)	Headspace gas	Incubation			
					Start date (2012)	End date (2012)	Period (days)	Temperature (°C)
337-C0020A-								
1R-1	1276.70	A, B	3.7	N_2	26 Aug	5 Sep	10	25
1R-1	1276.70	C, D	3.7	N_2/CH_4	26 Aug	5 Sep	10	25
2R-2	1287.82	A, B	3.7	N_2	26 Aug	5 Sep	10	25
2R-2	1287.82	C, D	3.7	N_2/CH_4	26 Aug	5 Sep	10	25
3R-2	1371.89	A, B	3.7	N_2	27 Aug	6 Sep	10	25
3R-2	1371.89	C, D	3.7	N_2/CH_4	27 Aug	6 Sep	10	25
6R-1	1495.00	A, B	3.7	N_2	29 Aug	8 Sep	10	25
6R-1	1495.00	C, D	3.7	N_2/CH_4	29 Aug	8 Sep	10	25
8R-5	1607.16	A, B	3.7	N_2	31 Aug	10 Sep	10	35
8R-5	1607.16	C, D	3.7	N_2/CH_4	31 Aug	10 Sep	10	35
9R-1	1625.50	A, B	3.7	N_2	1 Sep	11 Sep	10	35
9R-1	1625.50	C, D	3.7	N_2/CH_4	1 Sep	11 Sep	10	35
10R-1	1630.12	A, B	3.7	N_2	1 Sep	11 Sep	10	35
10R-1	1630.12	C, D	3.7	N_2/CH_4	1 Sep	11 Sep	10	35
11R-1	1738.75	A, B	3.7	N_2	2 Sep	12 Sep	10	35
11R-1	1738.75	C, D	3.7	N_2/CH_4	2 Sep	12 Sep	10	35
13R-4	1760.44	A, B	3.7	N_2	2 Sep	12 Sep	10	35
13R-4	1760.44	C, D	3.7	N_2/CH_4	2 Sep	12 Sep	10	35
14R-2	1822.36	A, B	3.7	N_2	2 Sep	12 Sep	10	35
14R-2	1822.36	C, D	3.7	N_2/CH_4	2 Sep	12 Sep	10	35
15R-3	1921.93	A, B	3.7	N_2	3 Sep	13 Sep	10	35
15R-3	1921.93	C, D	3.7	N_2/CH_4	3 Sep	13 Sep	10	35
15R-6	1924.06	A, B	3.7	N_2	3 Sep	13 Sep	10	35
15R-6	1924.06	C, D	3.7	N_2/CH_4	3 Sep	13 Sep	10	35
16R-3	1930.28	A, B	3.7	N_2	3 Sep	13 Sep	10	35
16R-3	1930.28	C, D	3.7	N_2/CH_4	3 Sep	13 Sep	10	35
18R-1	1945.63	A, B	3.7	N_2	5 Sep	15 Sep	10	35
18R-1	1945.63	C, D	3.7	N_2/CH_4	5 Sep	15 Sep	10	35
19R-1	1950.00	A, B	3.7	N_2	5 Sep	15 Sep	10	35
19R-1	1950.00	C, D	3.7	N_2/CH_4	5 Sep	15 Sep	10	35
20R-5	1965.06	A, B	3.7	N_2	5 Sep	15 Sep	10	35
20R-5	1965.06	C, D	3.7	N_2/CH_4	5 Sep	15 Sep	10	35
22R-5	1977.84	A, B	3.7	N_2	5 Sep	15 Sep	10	35
22R-5	1977.84	C, D	3.7	N_2/CH_4	5 Sep	15 Sep	10	35
23R-3	1984.13	A, B	3.7	N_2	6 Sep	16 Sep	10	45
23R-3	1984.13	C, D	3.7	N_2/CH_4	6 Sep	16 Sep	10	45
25R-2	1997.46	A, B	3.7	N_2	6 Sep	16 Sep	10	45
25R-2	1997.46	C, D	3.7	N_2/CH_4	6 Sep	16 Sep	10	45
25R-3	1998.65	A, B	3.7	N_2	6 Sep	16 Sep	10	45
25R-3	1998.65	C, D	3.7	N_2/CH_4	6 Sep	16 Sep	10	45
26R-4	2113.46	A, B	3.7	N_2	7 Sep	17 Sep	10	45
26R-4	2113.46	C, D	3.7	N_2/CH_4	7 Sep	17 Sep	10	45
27R-1	2200.83	A, B	3.7	N_2	7 Sep	17 Sep	10	45
27R-1	2200.83	C, D	3.7	N_2/CH_4	7 Sep	17 Sep	10	45
28R-4	2304.78	A, B	3.7	N_2	8 Sep	18 Sep	10	45
28R-4	2304.78	C, D	3.7	N_2/CH_4	8 Sep	18 Sep	10	45
28R-5	2305.29	A, B	3.7	N_2	8 Sep	18 Sep	10	45
28R-5	2305.29	C, D	3.7	N_2/CH_4	8 Sep	18 Sep	10	45
29R-5	2405.45	A, B	3.7	N_2	9 Sep	19 Sep	10	45
29R-5	2405.45	C, D	3.7	N_2/CH_4	9 Sep	19 Sep	10	45
30R-2	2448.56	A, B	7.4	N_2	11 Sep	20 Sep	9	45
30R-2	2448.56	C, D	7.4	N_2/CH_4	11 Sep	20 Sep	9	45
30R-3	2449.38	A, B	3.7	N_2	10 Sep	20 Sep	10	45
30R-3	2449.38	C, D	3.7	N_2/CH_4	10 Sep	20 Sep	10	45
32R-1	2456.63	A, B	3.7	N_2	10 Sep	20 Sep	10	45
32R-1	2456.63	C, D	3.7	N_2/CH_4	10 Sep	20 Sep	10	45
Coal formation mix	1950–2000	A, B	3.7	N_2	15 Sep	20 Sep	5	45
Coal formation mix	1950–2000	C, D	3.7	N_2/CH_4	15 Sep	20 Sep	5	45
Drilling mud: 337-C0020A-								
772-LMT	Active mud tank	A, B	2.1	N_2	14 Sep	20 Sep	6	25
772-LMT	Active mud tank	C, D	2.1	N_2/CH_4	14 Sep	20 Sep	6	25

Table T43. Observed microorganisms under light microscopy, Hole C0020A.

Core, section, interval (cm)	Top depth (mbsf)	Bottom depth (mbsf)	H_2O (mL)	Conc. (%)	Incubation date (2012)	Observation date (2012)	Incubation period (d)	Fungal sporelike
Seawater					4 Sep	12 Sep	8	+
337-C0020A-								
245-LMW	1955.5	1965.5	15	13.3	4 Sep	12 Sep	8	—
242-SMW	1946.5	1956.5	15	33.3	4 Sep	13 Sep	9	—
7R-1, 53.0–65.0	1599.5	1599.7	14	7.1	27 Aug	11 Sep	15	—
8L-5, 20.0–35.0	1607.4	1607.5	13	23.1	30 Aug	11 Sep	12	+
8L-9, 0.0–16.0	1611.2	1611.3	13	23.1	30 Aug	11 Sep	12	—
10R-2, 53.0–70.0	1631.4	1631.6	13	7.7	31 Aug	11 Sep	11	+
13R-1, 75.0–85.0	1757.3	1757.4	13	30.8	1 Sep	11 Sep	10	+
14R-2, 45.0–55.0	1821.9	1822	6	16.7	4 Sep	13 Sep	9	+
15R-3, 0.0–20.0	1920.8	1921	14	28.6	4 Sep	12 Sep	8	+
15R-5, 0.0–21.0	1923.6	1923.8	10	20	2 Sep	12 Sep	10	+
15R-7, 33.0–41.0	1925.8	1925.9	13	7.7	2 Sep	12 Sep	10	—
20R-7, 62.0–76.0	1966.3	1966.5	13	19.2	4 Sep	12 Sep	8	+
25R-2, 70.0–85.0	1997.1	1997.3	5	20	5 Sep	13 Sep	8	—
25R-3, 120.0–141.0	1999	1999.2	5	30	5 Sep	13 Sep	8	—
27R-2, 61.0–80.0	2201.6	2201.8	10	25	6 Sep	13 Sep	7	—
28R-3, 0.0–24.0	2302.8	2303.1	10	25	7 Sep	13 Sep	6	+
28R-6, 30.0–45.0	2306.7	2306.9	10	20	7 Sep	13 Sep	6	—
30R-4, 6.0–23.0	2449.8	2449.9	8	12.5	8 Sep	13 Sep	5	—
Seawater control								

+ = observed, with more + added for a greater abundance; — = not observed.